

Copyright

by

Leo A. Joyce

2012

**The Dissertation Committee for Leo Anthony Joyce Certifies that this is the
approved version of the following dissertation:**

**Molecular Sensing Paradigms: Enantioselective Recognition of Chiral
Carboxylic Acids and Interfacial Sensing**

Committee:

Eric Anslyn, Supervisor

Brent Iverson

Dionicio Siegel

Jennifer Brodbelt

Walter Fast

**Molecular Sensing Paradigms: Enantioselective Recognition of Chiral
Carboxylic Acids and Interfacial Sensing**

by

Leo Anthony Joyce, B.S.

Dissertation

Presented to the Faculty of the Graduate School of

The University of Texas at Austin

in Partial Fulfillment

of the Requirements

for the Degree of

Doctor of Philosophy

The University of Texas at Austin

August 2012

Dedication

To Katie, for loving, supporting and challenging me.

Acknowledgements

First and foremost, I would like to thank Professor Eric Anslyn for all of the support you have given me during graduate school. You are truly an inspiration. If I am half as successful as you are, professionally as well as personally, I will consider myself very lucky. I also want to thank Dr. Mark S. Maynor, for getting the carboxylate sensing project started. The determination and courage that he showed on a daily bases still motivates me to make the most out of all situations. You may be gone, but you will never be forgotten. I would also like to thank Professor Katsuhiko Ariga for allowing me to spend the summer doing summer research in Japan, and Professor Scott Miller for hosting me while collaborating at Yale. The members of the Anslyn research group, past and present, deserve a special thanks for tremendous help in my time at UT. Whether it was giving encouragement, helping to interpret results, or chatting about any topic under the sun, you all have helped make my time in graduate school enjoyable.

I would next like to thank my family, since you have all been so integral to my success. Katie-thanks for being my constant source of inspiration, and always bringing out the best in me. Mom-thanks for helping me realize my potential by never letting me accept less than my best effort. Dad-I want to thank you for showing me that hard work and dedication really do pay off. Kevin and Michael-thank you for providing a constant source of friendship and encouragement. Sara-thank you for reminding me to enjoy the good things that happen in life. Lauri, Nolan and Olivia-thanks for continually reminding me the value of family. Rick and Debbie-thanks for taking me into your family, and teaching me to be open-minded. Kimber-thanks for keeping me level headed. Without you, none of this would have been possible.

I would finally like to thank all of my coworkers and friends, with whom I have shared so many great experiences. Group members Michelle, Reid, Pedro, Jeff, Katharine, Alex, Hannah, Brette, John and Diana deserve special recognition for always putting up with my shenanigans. Former groups member Shagufta Shabbir was instrumental in acclimating me to the inner workings of Anslyn group, and deserves a special thanks. For always being there to listen and offer helpful suggestions, I would like to thank Rachel Butorac, Tom Barton, Sarah Stranahan, and Little Mike. All of the Iverson members who provided a constant source of comic relief also helped immensely. Also, thanks to Chelsea Martinez and “Wild Bill” Metola for proofreading this work. Gumnuts played a major supporting role in the creation of this work.

Molecular Sensing Paradigms: Enantioselective Recognition of Chiral Carboxylic Acids and Interfacial Sensing

Leo Anthony Joyce, Ph.D.

The University of Texas at Austin, 2012

Supervisor: Eric V. Anslyn

Determining the presence of an analyte of interest, and finding the enantiomeric purity of chiral molecules are challenging tasks. This work in molecular recognition is carried out routinely by many different researchers, including both academic as well as industrial research groups. The following dissertation presents original research directed toward two different areas of interest to the molecular recognition community: enantioselective sensing in solution, and sensing at a defined interfacial environment. This work begins with a review of the non-chromatographic ways that the enantiomeric purity of chiral carboxylic acids is determined, presented in Chapter 1.

Carboxylic acids are important functional groups, both for organic synthesis as well as pharmaceutical drug development. Chapter 2 presents efforts that have been made to rapidly assess both the enantiomeric purity and identity of chiral carboxylic acids, utilizing the technique of exciton-coupled circular dichroism (ECCD). A twist is imparted on a complex, and can be correlated with the absolute configuration of the stereocenter. The enantiomeric composition can be rapidly determined.

After creating the assay, the focus of the work shifted toward applying this system to new classes of analytes. Chapter 3 covers chemo- and enantioselective differentiation

of α -amino acids, and continues to discuss the expansion to β -homoamino acids. Then a synthetic substrates was tested, and a series of reactions screened to determine if any enantioselectivity had been imparted by a Baeyer-Villiger oxidation. Finally, the enantiomeric composition of a biaryl atropisomer, a compound lacking a stereocenter, was determined. The signal produced from this assay is at a relatively short wavelength, and efforts were undertaken to push this signal to longer wavelength. Chapter 4 is a compendium of the lessons that were learned upon attempting to create a self-assembled sensing system.

The final chapter details work that was done in collaboration with Professor Katsuhiko Ariga at the National Institute of Materials Science in Tsukuba, Japan. In this chapter, an indicator displacement assay was carried out for the first time at the air-water interface. This contribution opens the door for sensing to be carried out at defined regions, rather than free in bulk solution.

Table of Contents

List of Schemes	xiv
List of Figures	xvii
List of Tables.....	xxix
Chapter 1: Enantioselective Sensing of Chiral Carboxylic Acids by Non-Chromatographic Methods	1
1.1. Introduction	1
1.1.2. Chiral Chromatography	3
1.2. Nuclear Magnetic Resonance Spectroscopy	5
1.2.1. ¹ H NMR.....	7
1.2.1.1. Amide Bond Formation.....	7
1.2.1.2. Ester Bond Formation	12
1.2.1.3. Salt Formation	15
1.2.1.4. Hydrogen Bonding Receptors	18
1.2.2. ¹⁹ F NMR	23
1.2.3. ³¹ P NMR	25
1.2.4. ⁷⁷ Se NMR	30
1.3. Optical Spectroscopy.....	33
1.3.1. Fluorescence Spectroscopy	34
1.3.2. Ultraviolet/Visible Spectroscopy	48
1.4. Concluding Remarks	54
1.5. References for Chapter 1	55
Chapter 2: A Simple Method for the Determination of Enantiomeric Excess and Identity of Chiral Carboxylic Acids	61
2.1. Introduction	61
2.2. Enantioselective Indicator Displacement Assays.....	62
2.2.1. eIDAs Performed With Metal-Based Hosts	66
2.3 eIDA Design Criteria	71

2.3.1. Host Synthesis and Properties	72
2.3.2. Indicator Selection.....	74
2.3.3. Binding Studies	75
2.3.4. Indicator Displacement	77
2.4. Exciton-Coupled Circular Dichroism.....	80
2.4.1. Optical Sensor Based on ECCD	82
2.4.2. Design Criteria	84
2.4.3. X-ray Analysis.....	86
2.4.4. CD Analysis	88
2.4.5. Analysis of the CD Data.....	91
2.4.6. Determination of Unknown ee Values	99
2.5. Concluding Remarks	101
2.6. Experimental	101
2.6.1. Materials and Methods	101
2.6.2. Host Synthesis	102
2.6.3. X-ray Structure of 2.34.....	102
2.6.3.1. Experimental Details	102
2.6.3.2. Crystal Parameters.....	104
2.6.4. Buffer Solution	112
2.6.5. Binding of 2.32.....	113
2.6.6. Binding of 2.33.....	113
2.6.7. Binding of 2.36.....	114
2.6.8. Binding of 2.38.....	115
2.6.9. Binding of 2.40.....	116
2.6.10. Guest Repetitions	117
2.6.11. Analysis of Unknown 2.32 Samples	118
2.6.12. Analysis of Unknown 2.36 Samples	119
2.6.13. Analysis of Unknown 2.38 Samples	121
2.7. References for Chapter 2	122

Chapter 3: Applications of The Copper(II)-Based Host to Amino Acid Differentiation and Synthetic Methodology Development	126
3.1. Introduction	126
3.2. Design Criteria For Amino Acid Recognition	128
3.2.1. Boc-Protected α -Amino Acids.....	129
3.2.2. Boc-Protected β -Homoamino Acids	136
3.2.3. Combined Amino Acid Guests	141
3.3. Application To Synthetic Methodology Development.....	143
3.3.1. Asymmetric Baeyer-Villiger Oxidation	143
3.3.1.1. Selection, Synthesis, and Initial Studies of Ketone Substrate	145
3.3.1.2. Peptide Catalyst Library Synthesis	150
3.3.1.3. Screening For Enantioselectivity	152
3.3.2. Resolution of Atropisomeric Biaryls Through Selective Bromination.....	154
3.3.2.1. CD Analysis	157
3.3.2.2. Calculation of ee For Unknown Samples.....	159
3.4. Concluding Remarks	163
3.5. Experimental	164
3.5.1. Materials and Methods	164
3.5.2. CD Titrations.....	164
3.5.2.1. N-Boc Proline Binding.....	164
3.5.2.2. N-Boc Methionine Binding	165
3.5.2.3. N-Boc Alanine Binding.....	166
3.5.2.4. N-Boc Histidine Repetitions	168
3.5.2.5. N-Boc Serine Repetitions.....	168
3.5.2.6. N-Boc Phenylalanine Repetitions	168
3.5.2.7. N-Boc Valine Repetitions	168
3.5.2.8. N-Boc Tryptophan Repetitions	169
3.5.2.9. N-Boc Leucine Repetitions	169
3.5.2.10. N-Boc Tyrosine Repetitions.....	169

3.5.2.11. N-Boc Asparagine Repetitions	170
3.5.2.12. N-Boc- β -Homoleucine Binding	170
3.5.2.13. N-Boc- β -Homoalanine Binding	170
3.5.2.14. N-Boc- β -Homophenylalanine Repetitions	172
3.5.2.15. N-Boc- β -Homovaline Repetitions	173
3.5.3. Baeyer-Villiger Reactions	173
3.6. References for Chapter 3	174
Chapter 4: Progress Toward the Creation of Self-Assembled Chiral Carboxylic Acid	
Receptors	178
4.1. Introduction	178
4.1.1. Dynamic Multi-Component Assemblies	178
4.2. Self-Assembled Imine-Metal Complex	181
4.2.1. Design Criteria	182
4.2.2. Complex Formation	183
4.2.3. X-ray Analysis	186
4.2.4. Incorporation of Additional Aldehydes	188
4.2.5. Incorporation of Additional Transition Metals	195
4.2.6. Incorporation of Additional Amines	197
4.2.7. Reversibility of the System	201
4.3. Concluding Remarks	205
4.4. Future Directions	206
4.5. Experimental Data	208
4.5.1. Materials and Methods	208
4.5.2. Formation of Complex 4.9	208
4.5.3. Crystal Growth for X-ray Analysis	209
4.5.4. X-ray Structural Parameters	209
4.5.4.1. Complex 4.9	209
4.5.4.2. Complex 4.17	214
4.5.4.3. Complex 4.18	225
4.5.4.4. Complex 4.19	234

4.5.4.5. Complex 4.20	246
4.5.4.6. Complex 4.21	255
4.5.4.7. Complex 4.23	264
4.6. References For Chapter 4	274
Chapter 5: Mechanically-Controlled Indicator Displacement Assay	277
5.1. Introduction	277
5.2. Introduction to the Air-Water Interface	278
5.3. Design Criteria	281
5.4. The Interfacial Receptor	282
5.5. Observation of FRET	285
5.6. Monolayer Formation	287
5.7. Matrix Lipid Selection	291
5.7.1. Cholesterol Acetate	292
5.7.2. Dipalmitoylphosphatidylcholine	293
5.7.3. Methyl Stearate	295
5.8. Indicator Binding	297
5.9. Fluorescence Properties of Matrix Monolayers	303
5.10. Guest Displacement	306
5.11. Concluding Remarks	308
5.12. Experimental	309
5.12.1. Materials and Methods	309
5.12.2. Host Synthesis	311
5.13. References for Chapter 5	316
Bibliography	320
Vita	333

List of Schemes

- Scheme 1.1.** Formula for calculating enantiomeric excess (*ee*). 3
- Scheme 1.2.** Derivatization of indoprofene **1.2** with (*R*)-1-methylbenzyl amine to create diastereomers of **1.4** amenable to NMR *ee* analysis..... 8
- Scheme 1.3.** Derivatization of α -methoxyundecanoic acid **1.8** with (*S*)-1-(1-maphthyl)ethylamine to create diastereomers of **1.10** that can be analyzed by NMR..... 10
- Scheme 1.4.** Derivatization of α -disubstituted carboxylic acid **1.11** with (*R*)-phenylglycine methyl ester to create amide **1.13**. 11
- Scheme 1.5.** A) Derivatizing agent for ^{19}F NMR analysis of enantiomeric purity. B) Representative synthesis of β -chiral carboxylic acid **1.47** through Michael addition and subsequent amide hydrolysis..... 25
- Scheme 1.6.** Derivatization protocol to create phenol **1.52** through coupling of carboxylic acid **1.50** and aniline **1.51**..... 27
- Scheme 1.7.** Determination of epimerization for the conversion of **1.64** to **1.65** by way of selenone derivatization..... 33
- Scheme 1.8.** One-step synthesis of receptor **1.77** from commercially available starting materials. 40
- Scheme 2.1.** Schematic representation of an eIDA between a chiral host and each enantiomer of a chiral guest. In this example, the preferred diastereomer is formed between the *R*-guest and the chiral host..... 63
- Scheme 2.2.** Chemical structures of components of the colorimetric eIDA to find the enantiomeric excess of phenyllactic acid **2.5**. 65

Scheme 2.3. Additional chiral host 2.8 and indicator chrome azurol S 2.9 ; part of a second generation eIDA for <i>ee</i> of amino acid guests.....	68
Scheme 2.4. Chemical structures for the hosts and guests used by the Wolf group in their eIDA.....	70
Scheme 2.5. Helically chiral guests formed by derivatizing either amino acids (2.17) or amino alcohols (2.18).....	71
Scheme 2.6. Synthesis of chiral derivatized amino acid complex 2.23	73
Scheme 2.7. Derivatization protocol of the Canary group for absolute configuration assignment for chiral amino acids.	83
Scheme 2.8. (A) Rapid interconversion between two helical structures. (B) The equilibrium is towards one of the diastereomers by addition of a chiral carboxylate guest.....	85
Scheme 3.1. Structures of α - and β -amino acids.....	127
Scheme 3.2. Components for differentiation of amino acids by an IDA: rhodium host 3.1 , indicators galloxyanine (3.2) xylenol orange (3.3), and calcein blue (3.4).	128
Scheme 3.3. A) Representation of the Baeyer-Villiger oxidation of a ketone to the corresponding ester. B) The Miller lab's development of a peptide-catalyzed asymmetric epoxidation reaction of alkenes.	144
Scheme 3.4. Preliminary enantioselective Baeyer-Villiger oxidation reaction, catalyzed by a peptide catalyst.	145
Scheme 3.5. Synthesis of 3-phenylcyclobutanone substrate for asymmetric Baeyer-Villiger reaction.....	146
Scheme 3.6. Kinetic resolution of atropisomeric biaryl species through a peptide-catalyzed bromination reaction.	155

Scheme 4.1. Three-component assembly formation of complex 4.3 from 2-pyridinecarboxaldehyde 4.1 , bis(2-pyridylmethyl)amine 4.2 , and zinc triflate.	180
Scheme 4.2. Brønsted acid-catalyzed dehydration of 4.3 to give iminium ion 4.5 , and subsequent nucleophilic addition of an alcohol to give complex 4.6 .	181
Scheme 4.3. Proposed structure of complex 4.9 , self-assembled from 4.7 and 4.8 .	183
Scheme 4.4. Proposed formation of self-assembled receptor 4.25 , with an open coordination site to bind a carboxylate guest.	199
Scheme 4.5. Envisioned reversibility of complex 4.9 through the addition of aldehyde 4.13 , forming 4.17	202
Scheme 4.6. Envisioned reversibility of complex 4.9 through the addition of tris-amine ligand 4.8 , forming complex 4.9	204
Scheme 5.1. A) Schematic representation of the FRET between a fluorescein donor and a rhodamine acceptor. B) Chemical structures of FRET pair methylesculetin 5.1 and carboxyfluorescein 5.2	283
Scheme 5.2. Proposed synthetic scheme of receptor 5.3 beginning from commercially available Rink Amide Resin.....	284
Scheme 5.3. Schematic representation of the multi channel photo detector (MCPD) used to gather UV/Vis or fluorescence data at the air-water interface.	304

List of Figures

- Figure 1.1.** Chemical structure of analyte **1.1**, whose diastereomeric composition was calculated with NMR techniques. 6
- Figure 1.2.** Chemical structures of amides **1.5-1.7** with known configurations that were applied in this study 9
- Figure 1.3.** A) Model explaining change in chemical shift of the indicated protons as a result of anisotropy. In this model, the phenyl is directed to the left. B) Change in chemical shift across the scope of analytes tolerated with this method. 12
- Figure 1.4.** A) Derivatization protocol for carboxylic acid guest **1.18** with enantiopure (*S*)-alcohol **1.19** to form ester **1.20**. B) Equilibrium between two possible conformers **I** and **II** of ester **1.20**. 13
- Figure 1.5.** A sample of the range of guests used for absolute stereochemistry determination with the secondary alcohol derivatization protocol. . 14
- Figure 1.6.** Chemical structure of prochiral carboxylic acid **1.25** that was analyzed using derivitizing agent **1.26**. 15
- Figure 1.7.** Chemical structures of diamine **1.27** that was used to form a diastereomeric salt with carboxylic acid guests such as **1.28** and **1.29**. 16
- Figure 1.8.** Chemical structures of chiral carboxylic acid receptor **1.30** and mandelic acid **1.31** that were used in these studies. 17
- Figure 1.9.** Structures of chiral carboxylic acid receptor **1.32**, used to determine the *ee* of chiralcarboxylic acids such as **1.33-1.35**. 18

Figure 1.10. A) Hydrogen bonding host 1.36 used for enantioselective sensing of carboxylic acids. B) Proposed mode of interaction of the receptor and carboxylic acid guest.....	19
Figure 1.11. Calix[4]azacrowns 1.37 and 1.38 used for enantioselective recognition of guests 1.31 and 1.39	20
Figure 1.12. Macrocyclic host 1.40 used for enantioselective recognition of chiral carboxylic acids, such as 1.41	22
Figure 1.13. Chiral ¹⁹ F derivatizing agent 1.40 , and chiral carboxylic acids 1.41 and 1.42 that were analyzed.....	24
Figure 1.14. Chemical structures of chiral phosphorous-containing helicenes 1.48 and 1.49 that were used to measure chiral substrates with remote stereocenters, such as chiral carboxylic acid 1.50	26
Figure 1.15. Chemical structures of TADDOL-derivative 1.53 and its complex 1.54 with carboxylic acid 1.34	29
Figure 1.16. Chemical structures of diamine-phosphine complexes 1.55 and 1.56 , and the P(V) complex formed from S ₈ addition to the complex from receptor 1.51 and guest 1.34	30
Figure 1.17. Chemical structures of chiral selenone 1.58 , and the carboxylic acids 1.59 , 1.60 , and 1.61 that were analyzed with this probe.	31
Figure 1.18. Additional chiral selenones that were used to enantioselectively differentiate 1.22 and 1.41	32
Figure 1.19. Chemical structures of bis-BINOL complexes 1.67-1.70 applied as enantioselective sensors of mandelic acid 1.31	35
Figure 1.20. Chemical structures of new guest 1.71 , and monomeric BINOL host 1.72	37

Figure 1.21. Boronic acid-based sensor 1.73 , and newly applied chiral α -hydroxy carboxylic acid analyte 1.74	39
Figure 1.22. Chiral salen-based enantioselective polymer sensors 1.78 and 1.79	41
Figure 1.23. 1,8-Diacridylnaphthalene sensor 1.80 used for enantioselective fluorescence sensing of guests such as 1.81 and 1.82	43
Figure 1.24. A) Chemical structure of new 1,8-diacridylnaphthalene host 1.83 . B) One-dimensional flexibility that is possessed by this host.....	44
Figure 1.25. Chemical structures of macrocyclic structures 1.84-1.87	46
Figure 1.26. Aggregation-induced emission hosts 1.88 and 1.89 that form highly fluorescent precipitates or suspensions with a single enantiomer of a chiral carboxylic acid guest.....	47
Figure 1.27. Chemical structures of calix[4]crown hosts 1.89 and 1.90 , used for colorimetric enantioselective recognition of phenylglycine species 1.91	49
Figure 1.28. Chiral calixarene sensors 1.93 and 1.94	50
Figure 1.29. Host structure used for colorimetric enantioselective discrimination of 1.31	52
Figure 1.30. Colorimetric host 1.96 , used for enantioselective sensing of chiral carboxylic acids such as 1.97	53
Figure 1.31. A) Chemical structure of chiral host 1.98 . B) Proposed binding mode for the carboxylate anion and the electron rich thiourea receptor....	54
Figure 2.1. A) Displacement of indicator 2.4 from host complex 2.6 by addition of amino acid guests. B) Absorbance at 653 nm of complex 2.6 by addition of D- of L-valine. C) Absorbance as a function of <i>ee</i> for leucine with each enantiomer of the host.....	67

Figure 2.2. CD spectrum recorded for complex 2.23 (0.3mM) in CH ₃ CN.	74
Figure 2.3. Indicators screened for color change upon binding copper(II).	75
Figure 2.4. A) Titration of host 2.23 (0-165 μM) into indicator 2.29 (10 μM) in default buffer (75% MeCN, H ₂ O with 20 mM HEPES pH=7.416). B) Difference in absorbance of the host:indicator complex at 602 nm.	76
Figure 2.5. A) Titration of (<i>R</i>)- 2.32 (0-1.3 mM) into host 2.23 (65.1 μM) and indicator 2.29 (10 μM) in the default buffer. B) Change in absorbance at 602 nm upon addition of either (<i>R</i>)- 2.32 (♦), (<i>S</i>)- 2.32 (■), (<i>R</i>)- 2.33 (◆), or (<i>S</i>)- 2.33 (■).	79
Figure 2.6. A) The splitting observed when the excited states of two chromophores, i and j, are coupled. B) The CD spectrum (top) and the UV/Vis spectrum (bottom) that result from the summation of these states. C) The spatial orientation of two chromophores in a clockwise direction, leading to a positive first CE.	82
Figure 2.7. Two different views of copper complex 2.34 . Displacement ellipsoids are scaled to 50% probability, and counterions are omitted for clarity.	87
Figure 2.8. (A) Addition of each enantiomer of 2.32 (1.0mM) to a solution containing 2.34 (0.5mM) in buffer. (B) Chemical structures for chiral carboxylate guests 2.35-2.39	89
Figure 2.9. Change in CD signal at 238 nm with addition of indicated enantiomer of 2.32	90
Figure 2.10. CD spectra for (<i>S</i>)-enantiomer of indicated guest (1.0 mM) and host 2.34 (0.5 mM) in buffer.	91

Figure 2.11. Two-dimensional LDA plot showing the response of each carboxylate guest.	93
Figure 2.12. Newman-type projections for host 2.34 with each enantiomer of 2.32 guest, with the M-propeller giving a (+) chirality for the orientation of the electronic dipole moments of the quinoline chromophores.	94
Figure 2.13. (A) Chemical structures for additional guests applied to this study. (B) CD spectra recorded for the indicated guests (1.0 mM) and the host (0.5 mM) in buffer.	96
Figure 2.14. A) Acid-catalyzed ester hydrolysis used by Taft to quantify steric size. B) Equation used to calculate Taft parameter E_s . C) Taft parameters for selected substituent groups.	97
Figure 2.15. Graph of the CD signal for the (<i>S</i>)-enantiomer of indicated guest as a function of the difference in the E_s values of the medium and small groups.	99
Figure 2.16. CD signal at 238 nm for a solution containing 2.32 (1.0 mM) and host 2.34 (0.5 mM) in buffer as a function of <i>ee</i>	100
Figure 2.17. Top: CD spectra of host 2.34 (0.5 mM) upon addition of each enantiomer of 2.33 (0-2 mM) in buffer. Bottom: Change in CD signal at 238 nm recorded during this titration.	114
Figure 2.18. Top: CD spectra of host 2.34 (0.5 mM) upon addition of each enantiomer of 2.36 (0-2 mM) in buffer. Bottom: Change in CD signal at 238 nm recorded during this titration.	115
Figure 2.19. Top: CD spectra of host 2.34 (0.5 mM) upon addition of each enantiomer of 2.38 (0-2 mM) in buffer. Bottom: Change in CD signal at 238 nm recorded during this titration.	116

Figure 2.20. Top: CD spectra of host 2.34 (0.5 mM) upon addition of each enantiomer of 2.40 (0-2 mM) in buffer. Bottom: Change in CD signal at 238 nm recorded during this titration.	117
Figure 2.21. Graph relating the <i>ee</i> values of samples to the CD signals that were recorded. A value of 100% corresponds to 100% <i>R</i> , while -100% corresponds to 100% <i>S</i>	118
Figure 2.22. Graph relating the <i>ee</i> values of samples to the CD signals that were recorded. A value of 100% <i>ee</i> corresponds to 100% <i>R</i> , while -100% <i>ee</i> corresponds to 100% <i>S</i>	120
Figure 2.23. Graph relating the <i>ee</i> values of samples to the CD signals that were recorded. A value of 100% <i>ee</i> corresponds to 100% <i>R</i> , while -100% <i>ee</i> corresponds to 100% <i>S</i>	121
Figure 3.1. CD spectrum of host 2.34 (0.5 mM) with indicated enantiomer of Boc-proline (1.0 mM) in the default buffer (75% acetonitrile, 25% water with 20 mM HEPES buffer at pH 7.4).	130
Figure 3.2. Model predicting the complex helicity with the guest bound, with the D-amino acid leading to a <i>P</i> -type helix and the L-amino acid preferring the <i>M</i> -type.	131
Figure 3.3. CD signal with addition of increasing amounts of indicated enantiomer of Boc-protected proline (0-2 mM) into host 2.34 (0.5 mM) in default buffer.	132
Figure 3.4. CD spectra of host 2.34 (0.5 mM) with indicated enantiomer of three different guests (1.0 mM) in the default buffer.	133
Figure 3.5. Two-dimensional LDA plot depicting the response of host 2.34 to each of the Boc-protected amino acid guests.	134

Figure 3.6. CD spectra of host 2.34 (0.5 mM) with indicated guest (1.0 mM) in the default buffer.	137
Figure 3.7. CD spectra for each enantiomer of each indicated guest (1.0 mM) and host 2.34 (0.5 mM) in default buffer.	138
Figure 3.8. CD signal at 238 nm for titration of each enantiomer of β -homoleucine (0-2 mM) into a solution containing host 2.34 (0.5 mM) in default buffer.	139
Figure 3.9. Two-dimensional LDA plot depicting the response of host 2.34 to each enantiomer of Boc-protected β -homoamino acid guest.	141
Figure 3.10. Two-dimensional LDA plot depicting the response of host 2.34 to each enantiomer of the α - and β -homoamino acid guests.	142
Figure 3.11. CD spectra for indicated enantiomer of guest (1.0 mM) and host 2.34 (0.5 mM) in default buffer.	148
Figure 3.12. Newman projections explaining the discrepancy between orientation in the steric model and the CIP model.	149
Figure 3.13. CD signal at 238 nm for a solution containing guest 3.12 (1.0 mM) and host 2.34 (0.5 mM) in default buffer as a function of <i>ee</i>	150
Figure 3.14. Peptide library that was constructed for screening of Baeyer-Villiger oxidations.	152
Figure 3.15. CD spectra recorded for host 2.34 (0.5 mM) and synthetic guests dissolved in buffer.	154
Figure 3.16. Possible docking model for the biaryl substrate to the peptide catalyst that explains the enantioselectivity of bromination.	156
Figure 3.17. CD spectra recorded for biaryl guest 3.14 (1.0 mM) by itself, and with 2.34 (0.5 mM) in default buffer.	158

- Figure 3.18.** A) CD spectra for guest **3.14** (1.0 mM) and host **2.34** (0.5 mM) with indicated *ee* values. B) The CD spectrum at 241 nm plotted against *ee* of the solution..... 159
- Figure 3.19.** The CD spectrum at 241 nm plotted against *ee* of the solution the biaryl solution, with the trendline and equation included. 162
- Figure 3.20.** Top: CD spectra of host **1** (0.5 mM) upon addition of each enantiomer of N-Boc-Methionine (0-2 mM) in default buffer. Bottom: Change in CD signal at 238 nm recorded for this titration..... 166
- Figure 3.21.** Top: CD spectra of host **1** (0.5 mM) upon addition of each enantiomer of N-Boc-Alanine (0-2 mM) in default buffer. Bottom: Change in CD signal at 238 nm recorded for this titration. 167
- Figure 3.22.** Top: CD spectra of host **1** (0.5 mM) upon addition of each enantiomer of N-Boc- β -Alanine (0-2 mM) in default buffer. Bottom: Change in CD signal at 238 nm recorded for this titration. 172
- Figure 4.1.** Structural similarity of carboxylic acid host **2.34** and the proposed structure of a self-assembled receptor. 182
- Figure 4.2.** ^1H NMR spectra recorded (all in CD_3CN) for 2-pyridinecarboxaldehyde **4.7** alone, (bottom panel), the tris-imine formed between **4.7** and tris-amine **4.8** (middle panel), and these two components with $\text{Zn}(\text{OTf})_2$ (top panel)..... 185
- Figure 4.3.** Crystal structure of complex **4.9**, viewed from the side (A) and the top (B). Displacement ellipsoids are scaled to 50%, and counterions removed for clarity. C) Structural representation of the complex. 187

Figure 4.4. A) ¹H NMR spectra recorded for benzaldehyde **4.10** alone, (bottom panel), the tris-imine formed between **4.10** and tris-amine **4.8** (middle panel), and these two components with Zn(OTf)₂ (top panel) in CD₃CN. B) Chemical structures for aldehydes **4.10-4.12** used in this study. 190

Figure 4.5. Chemical structure for substituted pyridines **4.13-4.16** used for complex formation. 191

Figure 4.6. A) Crystal structure of complex **4.17**. Displacement ellipsoids are scaled to 50%, and counterions omitted for clarity. B) Structural representation of this complex. 192

Figure 4.7. A) Crystal structure of complex **4.18**. Displacement ellipsoids are scaled to 50%, and counterions omitted for clarity. B) Structural representation of this complex. 193

Figure 4.8. A) Crystal structure of complex **4.19**. Displacement ellipsoids are scaled to 50%, and counterions omitted for clarity. B) Structural representation of this complex. 194

Figure 4.9. A) Crystal structure of complex **4.20**. Displacement ellipsoids are scaled to 50%, and counterions omitted for clarity. B) Structural representation of this complex. 196

Figure 4.10. Crystal structure of the iron (II) complex with aldehyde **4.7**, viewed from the side. Displacement ellipsoids are scaled to 50%, and counterions omitted for clarity. 197

Figure 4.11. A) Structure of tris-amine **4.22**. B) Crystal structure of complex **4.23**. Displacement ellipsoids are scaled to 50%, and counterions omitted for clarity. C) Structural representation of the complex. 198

Figure 4.12. ^1H NMR spectra recorded for 2-pyridinecarboxaldehyde 4.7 alone, (bottom panel), the bis-imine formed between 4.7 and bis-amine 4.18 (middle panel), and these two components with $\text{Zn}(\text{OTf})_2$ (top panel) in CD_3CN	201
Figure 4.13. ^1H NMR spectra recorded for aldehyde 4.13 alone, (bottom panel), complex 4.9 (middle panel), and one equivalent of 4.13 added to 4.9 (top panel), in CD_3CN	203
Figure 4.14. ^1H NMR spectra recorded for complex 4.22 alone, (bottom panel), and this complex with the addition of one equivalent of 4.8 (top panel), in CD_3CN	205
Figure 4.15. Chemical structures of tris- and tetra-amine templates that could possibly be applied to complex formation.	207
Figure 5.1. Binding constants measured for phosphate and guanidinium (a) in disperse aqueous solutions, (b) at micellar or bilayer surfaces, and (c) at air-water interface.	279
Figure 5.2. Top: Illustration of the FRET signal turned on by external compression. Bottom: Schematic representation of the MC-IDA.....	281
Figure 5.3. (A) Absorption spectrum of the host and fluorescence spectrum of indicator ($\lambda_{\text{ex}}=363\text{nm}$) in chloroform:methanol (4:1 v/v). (B) Fluorescence spectra of indicator (5 μM) before and after addition of host ($\lambda_{\text{ex}}=363\text{nm}$).....	286
Figure 5.4. Representation of the Langmuir-Blodgett trough, indicating the water subphase (A), the bars to compress the monolayer (B), and the Wilhelmy plate to read the surface pressure (C).	288

Figure 5.5. Surface pressure-area (π - A) isotherms measured for the host at various concentrations in the spreading solution at 20°C.....	289
Figure 5.6. AFM height images of the monolayer formed by the host that was transferred to a freshly cleaved mica substrate at a surface pressure of 10 mN/m.....	291
Figure 5.7. A) (π - A) isotherm measured for mixed monolayer of host and cholesterol acetate (5.4) on pure water at 20°C. Right: Molecular area as a function of host percent in the matrix at 5 mN/m intervals.....	293
Figure 5.8. Left: (π - A) isotherm measured for mixed monolayer of host and dipalmitoylphosphatidylcholine (5.X) on pure water at 20°C. Right: Molecular area as a function of host percent in the matrix at 5 mN/m intervals.	295
Figure 5.9. Left: (π - A) isotherm measured for mixed monolayer of host and methyl stearate (5.X) on pure water at 20°C. Right: Molecular area as a function of host percent in the matrix at 5 mN/m intervals.	297
Figure 5.10. Left: (π - A) isotherms of the host matrix with indicator in the water subphase at 20°C. Right: Binding curves for the indicator at indicated surface pressures. The value of ΔA represents the difference between the value with dissolved guest and pure water.....	299
Figure 5.11. (π - A) isotherms of the mixed monolayer with indicator at the noted molar ratio, recorded at 20°C.....	301
Figure 5.12. AFM height images of monolayer films of host and indicator dissolved in the spreading solution, transferred to a freshly cleaved mica substrate at surface pressures of 10 mN/m (A) or 20 mN/m (B).....	302

Figure 5.13. Fluorescence spectra of the monolayers of the host indicator complex under various different conditions; (A) 1:5 ratio of host to indicator formed at indicated surface pressures; (B) various ratios of indicator in the spreading solution at a surface pressure of 20 mN/m. 305

Figure 5.14. (A) Matrix monolayer fluorescence uorescence spectra changing upon addition of D-glucose to the subphase. (B) Plot of the fluorescence ratio (I_{525}/I_{450}) with increasing amounts of glucose added. 308

List of Tables

Table 2.1. Errors for the <i>ee</i> calculations of unknown guests related to the difference in their CD signal magnitude.	101
Table 2.2. Crystal data and refinement for 2.34	104
Table 2.3. Atomic coordinates ($\times 10^4$) and equivalent isotropic displacement parameters ($\text{\AA}^2 \times 10^3$) for 1. <i>U</i> (eq) is defined as one third of the trace of the orthogonalized <i>U</i> ^{<i>ij</i>} tensor.	105
Table 2.4. Bond lengths [\AA] and angles [$^\circ$] for 2.34	106
Table 2.5. Anisotropic displacement parameters ($\text{\AA}^2 \times 10^3$) for 1. The anisotropic displacement factor exponent takes the form: $-2\pi^2 [h^2 a^*2U^{11} + \dots + 2 h k a^* b^* U^{12}]$	108
Table 2.6. Hydrogen coordinates ($\times 10^4$) and isotropic displacement parameters ($\text{\AA}^2 \times 10^3$)for 2.34	110
Table 2.7. Torsion angles [$^\circ$] for 2.34	111
Table 2.8. Hydrogen bonds for 1 [\AA and $^\circ$].	112
Table 2.9. Results of the analysis of the eight unknown samples. The average absolute error was determined to be 3.2% for these eight samples.	119
Table 2.10. Results of the analysis of eight unknown samples. The average absolute error was determined to be 4.1% for these eight samples.	120
Table 2.11. Results of the analysis of eight unknown samples. The average absolute error was determined to be 4.1% for these eight samples.	122
Table 3.1. CD signals recorded for each unknown, the % <i>ee</i> values calculated and actual, and the error that was found.	160

Table 3.2. CD signals recorded for each unknown, the % ee values calculated and actual, and the error that was found.	163
Table 4.1. Crystal data and structure refinement for complex 4.9	209
Table 4.2. Atomic coordinates (x 10 ⁴) and equivalent isotropic displacement parameters (Å ² x 10 ³) for 4.9 . U(eq) is defined as one third of the trace of the orthogonalized U ^{ij} tensor.	211
Table 4.3. Bond lengths [Å] and angles [°] for 4.9	211
Table 4.4. Anisotropic displacement parameters (Å ² x 10 ³) for 4.9 . The anisotropic displacement factor exponent takes the form: $-2\pi^2 [h^2 a^{*2} U^{11} + \dots + 2 h k a^* b^* U^{12}]$	213
Table 4.5. Hydrogen coordinates (x 10 ⁴) and isotropic displacement parameters (Å ² x 10 ³) for 4.9	213
Table 4.6. Torsion angles [°] for 4.9	214
Table 4.7. Crystal data and structure refinement for 4.17	215
Table 4.8. Atomic coordinates (x 10 ⁴) and equivalent isotropic displacement parameters (Å ² x 10 ³) for 4.17 . U(eq) is defined as one third of the trace of the orthogonalized U ^{ij} tensor.	216
Table 4.9. Bond lengths [Å] and angles [°] for 4.17	218
Table 4.10. Anisotropic displacement parameters (Å ² x 10 ³) for 4.17 . The anisotropic displacement factor exponent takes the form: $-2\pi^2 [h^2 a^{*2} U^{11} + \dots + 2 h k a^* b^* U^{12}]$	220
Table 4.11. Hydrogen coordinates (x 10 ⁴) and isotropic displacement parameters (Å ² x 10 ³) for 4.17	222
Table 4.12. Torsion angles [°] for 4.17	223
Table 4.13. Hydrogen bonds for 4.17 [Å and °].	224

Table 4.14. Crystal data and structure refinement for 4.18 .	225
Table 4.15. Atomic coordinates ($\times 10^4$) and equivalent isotropic displacement parameters ($\text{\AA}^2 \times 10^3$) for 4.18 . $U(\text{eq})$ is defined as one third of the trace of the orthogonalized U^{ij} tensor.	226
Table 4.16. Bond lengths [\AA] and angles [$^\circ$] for 4.18 .	228
Table 4.17. Anisotropic displacement parameters ($\text{\AA}^2 \times 10^3$) for 4.18 . The anisotropic displacement factor exponent takes the form: $-2\pi^2 [h^2 a^{*2} U^{11} + \dots + 2hk a^* b^* U^{12}]$	230
Table 4.18. Hydrogen coordinates ($\times 10^4$) and isotropic displacement parameters ($\text{\AA}^2 \times 10^3$) for 4.18 .	232
Table 4.19. Torsion angles [$^\circ$] for 4.18 .	232
Table 4.20. Crystal data and structure refinement for 4.19 .	235
Table 4.21. Atomic coordinates ($\times 10^4$) and equivalent isotropic displacement parameters ($\text{\AA}^2 \times 10^3$) for 4.19 . $U(\text{eq})$ is defined as one third of the trace of the orthogonalized U^{ij} tensor.	236
Table 4.22. Bond lengths [\AA] and angles [$^\circ$] for 4.19 .	238
Table 4.23. Anisotropic displacement parameters ($\text{\AA}^2 \times 10^3$) for 4.19 . The anisotropic displacement factor exponent takes the form: $-2\pi^2 [h^2 a^{*2} U^{11} + \dots + 2hk a^* b^* U^{12}]$	240
Table 4.24. Hydrogen coordinates ($\times 10^4$) and isotropic displacement parameters ($\text{\AA}^2 \times 10^3$) for 4.19 .	242
Table 4.25. Torsion angles [$^\circ$] for 4.19 .	244
Table 4.26. Crystal data and structure refinement for 4.20 .	247

Table 4.27. Atomic coordinates ($\times 10^4$) and equivalent isotropic displacement parameters ($\text{\AA}^2 \times 10^3$) for 4.20 . $U(\text{eq})$ is defined as one third of the trace of the orthogonalized U^{ij} tensor.	248
Table 4.28. Bond lengths [\AA] and angles [$^\circ$] for 4.20	249
Table 4.29. Anisotropic displacement parameters ($\text{\AA}^2 \times 10^3$) for 4.20 . The anisotropic displacement factor exponent takes the form: $-2\pi^2 [h^2 a^{*2} U^{11} + \dots + 2 h k a^* b^* U^{12}]$	251
Table 4.30 Hydrogen coordinates ($\times 10^4$) and isotropic displacement parameters ($\text{\AA}^2 \times 10^3$) for 4.20	252
Table 4.31. Torsion angles [$^\circ$] for 4.20	253
Table 4.32. Crystal data and structure refinement for 4.21	256
Table 4.33. Atomic coordinates ($\times 10^4$) and equivalent isotropic displacement parameters ($\text{\AA}^2 \times 10^3$) for 4.21 . $U(\text{eq})$ is defined as one third of the trace of the orthogonalized U^{ij} tensor.	257
Table 4.34. Bond lengths [\AA] and angles [$^\circ$] for 4.21	258
Table 4.35. Anisotropic displacement parameters ($\text{\AA}^2 \times 10^3$) for 4.21 . The anisotropic displacement factor exponent takes the form: $-2\pi^2 [h^2 a^{*2} U^{11} + \dots + 2 h k a^* b^* U^{12}]$	260
Table 4.36. Hydrogen coordinates ($\times 10^4$) and isotropic displacement parameters ($\text{\AA}^2 \times 10^3$) for 4.21	261
Table 4.37. Torsion angles [$^\circ$] for 4.21	262
Table 4.38. Crystal data and structure refinement for 4.23	264
Table 4.39. Atomic coordinates ($\times 10^4$) and equivalent isotropic displacement parameters ($\text{\AA}^2 \times 10^3$) for 4.23 . $U(\text{eq})$ is defined as one third of the trace of the orthogonalized U^{ij} tensor.	265

Table 4.40. Bond lengths [\AA] and angles [$^\circ$] for 4.23	267
Table 4.41. Anisotropic displacement parameters ($\text{\AA}^2 \times 10^3$) for 4.23 . The anisotropic displacement factor exponent takes the form: $-2\pi^2 [h^2 a^{*2} U^{11} + \dots + 2 h k a^* b^* U^{12}]$	269
Table 4.42. Hydrogen coordinates ($\times 10^4$) and isotropic displacement parameters ($\text{\AA}^2 \times 10^3$) or 4.23	271
Table 4.43. Torsion angles [$^\circ$] for 4.23	272

Chapter 1: Enantioselective Sensing of Chiral Carboxylic Acids by Non-Chromatographic Methods

1.1. INTRODUCTION

An important task in synthetic organic chemistry is the determination of the enantiomeric purity of chiral compounds. An increasingly large share of the pharmaceutical drugs that are available today possess chirality.¹ For instance, 37% of the total sales of therapeutics in 2005 were not only chiral, but sold as single-enantiomers.² These chiral compounds have the potential to show enantiospecific profiles in regards to their physiological properties in the human body. Thus, each enantiomer must be tested by itself before being approved for use by the FDA.³ The need for this requirement is demonstrated by the case of thalidomide.⁴ This pharmaceutical agent was given to pregnant women in the early 1960s, as a means of treating morning sickness. One of the enantiomers of this compound, the (*R*)-enantiomer, had the desired affect of relieving morning sickness. The (*S*)-enantiomer, however, was teratogenic and caused severe birth defects in a large subset of the children born when these pregnancies were brought to term. It was later revealed that thalidomide racemizes in the body,⁴ but this example highlights the need to analyze the enantiomeric composition of a drug candidate.

In order to avoid the tedious separation and wasteful discarding of undesired material, many advances have been made in the field of asymmetric synthesis. The main goal of this field is to create synthetic methods that selectively give one enantiomer of a compound in large excess over the other.⁵⁻⁷ The importance of this task is evidenced by the 2001 Nobel Prize, awarded to Knowles, Noyori, and Sharpless for the advances they had made in chiral catalysis.⁸ Asymmetric synthesis necessitates some sort of chiral

entity in order to direct enantioselective product formation, typically an auxiliary or catalyst.

Traditional reaction optimization in asymmetric synthesis was carried out in the past by initially selecting a transformation of interest. A catalyst was then designed to facilitate the particular reaction. This catalyst was then synthesized and applied to the aforementioned target reaction. The success of the reaction was determined by analyzing the products, and optimization of the catalyst structure was made as necessary to further optimize the reaction. This process would then be repeated until the desired high *ee* outcome had been achieved. The iterative nature of this approach has recently given way to the use of parallel synthesis in a high-throughput screening (HTS) fashion. In this approach, large libraries of catalysts are created through combinatorial synthesis.⁹⁻¹⁴ These libraries are often composed of structurally similar reagents, since they can be readily synthesized using similar reaction conditions. The sheer volume of reactions that can be carried out increases the chance of making a serendipitous and unforeseen discovery. The discovery time can be decreased substantially, since the synthesis can be carried out very rapidly. This approach often does not rely on rational design, so many of the assumptions that are made during the traditional approach to catalyst design are not a source of detriment to HTS. These assumptions, such as cooperative effects or competing pathways, play no role in steering catalyst discovery. Thus, incorrect assumptions do not set back the discovery process.

Of the range of chiral substrates, carboxylic acids are functional groups that have found wide application. Chiral carboxylic acids are widely found in pharmaceutical drugs, and they can be found as intermediates during the synthesis of complex natural products.¹⁵⁻¹⁸ To this end, numerous catalytic methodologies to enantioselectively synthesize chiral carboxylic acids have been reported. The attention paid to this

functional group by the synthetic community makes it an important target to assess enantiomeric purity.

The analysis of enantiomeric composition is done by calculating the abundance of one enantiomer over the other. This ratio is known as enantiomeric excess (*ee*), with a higher *ee* value representing a more successful asymmetric synthesis. The value, calculated using the formula in **Scheme 1.1**, is often reported as the absolute value to avoid the use of negative numbers. It is necessary to employ a chiral medium in order to determine *ee*, since enantiomers have the same physical properties in an achiral environment. Chiral chromatography has been one of the most widely used methods for enantiomeric separation.

$$ee = \left(\frac{[R] - [S]}{[R] + [S]} \right) \times 100$$

Scheme 1.1. Formula for calculating enantiomeric excess (*ee*).

1.1.2. Chiral Chromatography

Chromatography is a common analytical laboratory technique to separate a mixture of compounds.¹⁹⁻²¹ The two most common chromatographic means for separation are high-pressure liquid chromatography (HPLC) and gas chromatography (GC). The compound of interest is carried by a mobile phase that subsequently passes through a stationary phase. Molecules often have different affinities for the stationary phase, based on physical properties such as polarity, and will thus partition differently between the two. This differential partitioning leads to inequivalent elution times, and the ability to separate the species. This method can be extended to chiral separations by incorporating a chiral stationary phase. In this direct approach, the chiral species is

chemically adsorbed to the stationary phase of the column. A number of chiral stationary phases have been prepared, composed of various materials such as cyclodextrins,²² macrocyclic antibiotics,²³ saccharides,²⁴ chiral crown ethers,²⁵ or proteins.²⁶ The chromatographic determination of *ee* has proven to be very accurate, with an average error of approximately 1-2%.²⁷ Accuracy notwithstanding, there are several drawbacks that limit the use of HPLC for asymmetric synthesis.

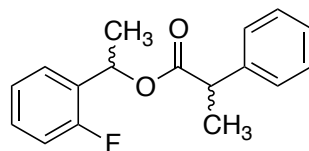
The major drawbacks with chiral chromatography as a means to determine *ee* are related to the practical application of this method. First, chromatography is a particularly slow means of analysis. It is only possible to analyze a single sample at one time, since this method is inherently serial in nature. This was not as much of a limitation using a traditional catalyst design model, but is very detrimental to HTS. Using modern combinatorial methods, it is possible to run thousands of samples every day. A single HPLC operating continuously for a 24 hour period can only analyze around 150 samples,⁹ creating a significant backlog of samples. Some advancements have been made by multiplexing HPLC columns,^{28,29} but these methods are not yet sufficient to meet the demand of HTS. Another drawback is that the columns are costly, and no single column works for every class of analyte. These columns can lose their resolution over time, meaning columns are constantly in need of replacement. A new method must be created for every different analyte, since subtle changes can have large effects in separation efficiency. For these reasons, there is substantial interest in elucidating a faster and more efficient method to rapidly assess enantiomeric purity of chiral compounds.

This chapter will focus on several of the non-chromatographic methods that have been applied specifically to the enantioselective sensing of chiral carboxylic acids. The analysis method will be presented, along with an explanation and critique of practical

application potential for the system. The analysis techniques that have found the broadest use are NMR spectroscopy, and optical sensing methods. The NMR techniques will span a range of nuclei, including ^1H , ^{19}F , ^{31}P , and ^{77}Se . The optical sensing methods that have been used most frequently used are fluorescence, and ultraviolet/visible (UV/vis) spectroscopies.

1.2. NUCLEAR MAGNETIC RESONANCE SPECTROSCOPY

One of the earliest non-chromatographic techniques to be applied to enantioselective recognition utilized nuclear magnetic resonance (NMR) spectroscopy. A chiral auxiliary is used to convert the enantiomeric substrate into diastereomeric complexes. This approach hinges on the magnetically non-equivalent diastereotopic protons in a chiral molecule, initially observed by Cram.³⁰ The general application of this technique spans a broad range of tasks, provided that sufficient difference in chemical shifts is observed that allows baseline resolution of the diastereomeric peaks. Hence, the integrated ratio of these diastereomer peaks is directly related to the enantiomeric composition of the starting analyte. The first application of this strategy was realized by Raban and Mislow.³¹ They were interested in finding a ^1H NMR method for the determination of the *ee* of chiral esters **1.1**. They began by subjecting this species, synthesized from 1-(O-fluorophenyl)-ethanol and 2-phenylpropanoyl chloride, to analysis using chiral chromatography. The chromatographic analysis revealed a ratio of products of 67/33.



1.1

Figure 1.1. Chemical structure of analyte **1.1**, whose diastereomeric composition was calculated with NMR techniques.

The methyl resonances showed up in the ^1H NMR spectrum as two doublets, split by the methine protons on the vicinal carbon. Their chemical shifts were sufficiently different to give appropriate resolution, centered at 8.63 and 8.54 ppm. Integration of these methyl peaks gave a direct way to measure the diastereomeric composition. This analysis gave an enantiomeric ratio of 68/32, in good agreement with the chromatographic analysis.

There are two main ways that NMR sensing is applied to enantioselective recognition: chiral derivatizing agents and chiral solvating agents. The use of derivatizing agents requires synthetic manipulation of the analyte in order to create diastereomeric products. These products are formed and purified in advance of the analysis step. One major concern for this procedure is avoiding potential racemization of the analyte during the derivatization step. In contrast to derivatizing agents, chiral solvating agents rely on *in situ* formation of diastereomeric complexes. This *in situ* complex formation allows the analysis of enantiomeric composition to be performed directly, without extra time consuming synthesis and purification. While the ^1H nucleus has found the widest application, several other nuclei have also been applied to enantioselective recognition. This section begins with the application of ^1H NMR. The

focus will then turn toward alternative nuclei that have been studied, namely ^{19}F , ^{31}P , and ^{77}Se .

1.2.1. ^1H NMR

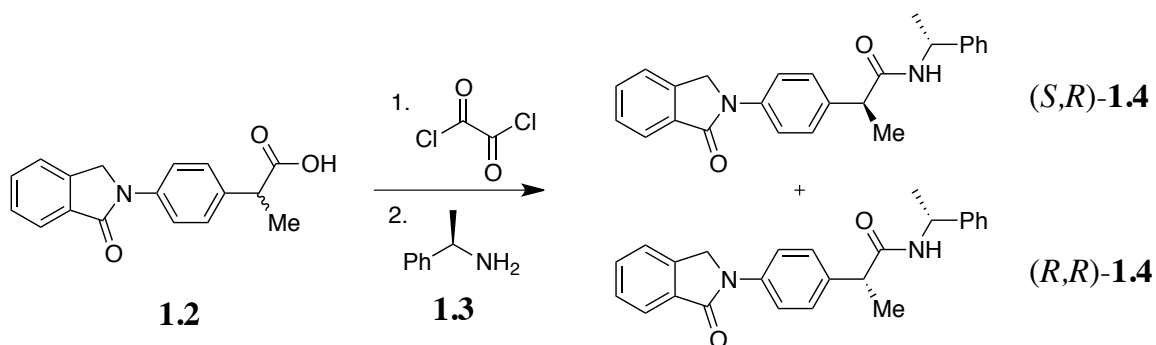
The most widely applied NMR spectroscopic analysis is performed on the proton nucleus. This spin $\frac{1}{2}$ nucleus has a high natural abundance, and thus the analysis can be performed rapidly and reliably. Several methods have been reported for ^1H NMR that make use of both the techniques of chiral derivatization and chiral solvating agents. This section will begin with a discussion of the derivatization, and then move to chiral solvating agents. These solvating agents interact with the chiral carboxylic acid either by transfer of the acidic proton to form an electrostatic pair, or by formation of host:guest complexes through supramolecular interactions.

The initial and widest application of carboxylic acids in chiral discrimination using ^1H NMR relied on a single enantiomer of these carboxylic acids to function as chiral derivatizing agents. In this approach, an enantiopure chiral carboxylic acid is used to form either an amide or ester with an amine or alcohol, respectively.³² Integration of the corresponding peaks on the newly formed diastereomers can be related to the original enantiomeric composition of this amine or alcohol. This analysis method can also be applied in the opposite direction by using an enantiopure amine or alcohol to derivatize a chiral carboxylic acid. Thus, the diastereomers that form between the enantiopure amine or alcohol and the carboxylic acid are representative of the enantiomeric composition of the starting carboxylic acids.

1.2.1.1. Amide Bond Formation

One of the earliest applications of this protocol was reported by the Forgiione group.³³ These researchers were interested in determining the absolute configuration of

the anti-inflammatory agent indoprofene **1.2** (**Scheme 1.2**). Derivatization of this species with enantiomerically pure (*R*)-1-methylbenzyl amine **1.3** creates diastereomeric amide products (*S,R*)- and (*R,R*)-**1.4**. This derivatization, unfortunately, could not be done without first converting the carboxylic acid **1.2** to an acid chloride. This requirement adds extra steps to the process, further slowing down analysis.



Scheme 1.2. Derivatization of indoprofene **1.2** with (*R*)-1-methylbenzyl amine to create diastereomers of **1.4** amenable to NMR *ee* analysis.

The researchers began by studying the observed non-equivalence of three other phenylethylamides of known configuration. These three compounds, shown in **Figure 1.2**, were formed by derivatizing the starting carboxylic acid with amine **1.3** as described in **Scheme 1.2**. The NMR spectra were recorded for the diastereomeric complexes, and non-equivalent methyl resonances were observed for the methyl group in amine **1.3** after derivatization. This behavior was noted for each amide **1.5-1.7**, with an average difference in chemical shift of 0.05 ppm. The (*R,R*)-diastereomer showed a downfield shift of this resonance, while an upfield shift was observed for the (*S,R*)-diastereomer. While it was possible to resolve the small difference in chemical shift for these peaks, the researchers were further able to increase the difference in the chemical shifts to 0.61 ppm using the lanthanide shift reagent $\text{Eu}(\text{fod})_3$. It was determined based on the NMR

evidence recorded that the derivatized indoprofene product was the (*S,R*)-stereoisomer, and thus the absolute stereochemistry of the stereocenter in indoprofene was found to be (*S*).

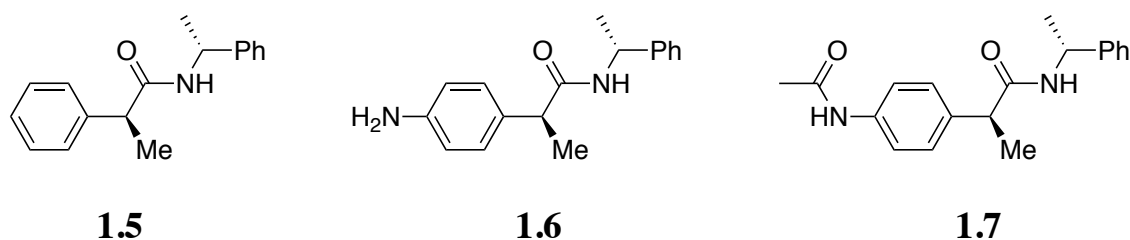
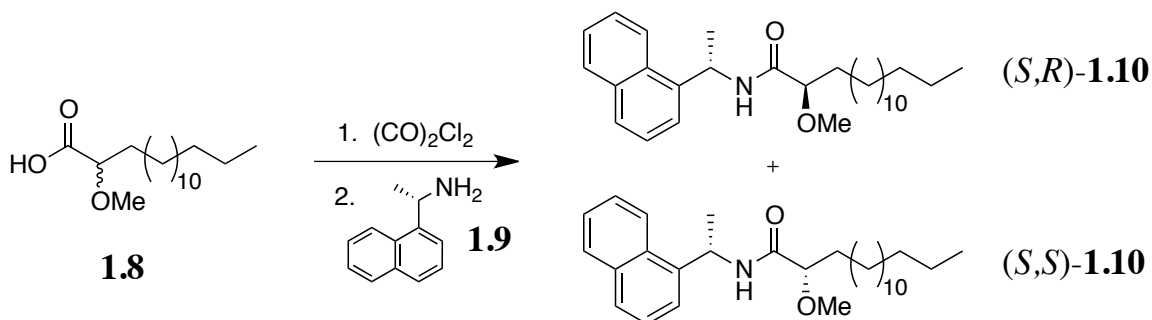


Figure 1.2. Chemical structures of amides **1.5-1.7** with known configurations that were applied in this study

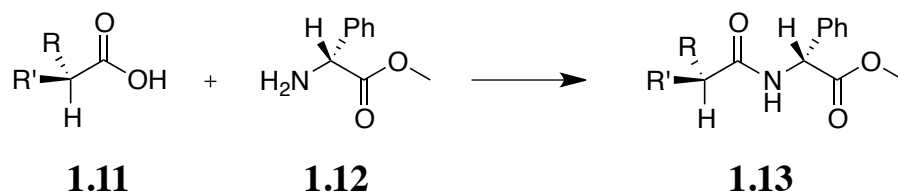
In a similar approach, Carballeira and coworkers reported a substituted ethylamine compound as a chiral derivatization agent for α -methoxy fatty acids.³⁴ These natural products had been isolated from aquatic species, and demonstrated promising antimicrobial activity against Gram-positive bacteria.³⁵ The fatty acids could be synthesized by methylating their α -hydroxy fatty acid counterparts, but there was concern that the stereocenter could be racemized during the course of the reaction. Thus, they sought to monitor the stereochemistry throughout the reaction by the use of ¹H NMR spectroscopy. Following the derivatization model presented earlier, the authors converted α -methoxy fatty acid **1.8** into the corresponding acid chloride with oxalyl chloride, then an amide by addition of (*S*)-1-(1-maphthyl)ethylamine **1.9**. This process led to a mixture of (*S,R*)- and (*S,S*)-diastereomers of **1.10**, as shown in **Scheme 1.3**. In monitoring these product signals, it was determined that the methoxy singlet was the best suited to distinguish the two isomers. The methoxy group of the (*S,R*)-diastereomer was found to resonate at 3.37 ppm, while the (*R,R*)-diastereomer was shifted upfield to 3.16

ppm. This difference in chemical shift of 0.21 ppm is sufficient to achieve baseline resolution, and thus differentiate these species.



Scheme 1.3. Derivatization of α -methoxyundecanoic acid **1.8** with (S) -1-(1-naphthyl)ethylamine to create diastereomers of **1.10** that can be analyzed by NMR.

In a slightly different approach relying on amide bond formation, the Kasumi group developed a chiral anisotropic shift reagent to rapidly assess absolute configuration of substituted carboxylic acid derivatives.^{36,37} This process is based on derivatization of the chiral carboxylic acid with an enantiopure methyl ester of phenylglycine (**1.12**) through PYBOP coupling conditions, as shown in **Scheme 1.4**. The conformation shown for amide product **1.13** is biased according to the structural features built in to this compound. First, structural studies in peptide chemistry have shown that the amide has a preference for the *s-trans* conformation. Also, the polar ester group prefers to be *anti*- to the carbonyl group of the derivatized carboxylic acid. Finally, a hydrogen bond is formed between the amide proton and the carbonyl of the methyl ester. The synergy of these three features biases the molecule toward the conformation that is shown in **1.13**. This assumption has been verified both by X-ray crystallography as well as additional NOE studies.



Scheme 1.4. Derivatization of α -disubstituted carboxylic acid **1.11** with (*R*)-phenylglycine methyl ester to create amide **1.13**.

The magnetic inequivalence of the substituent groups on the stereocenter of the carboxylic acid portion is further enhanced by the phenyl ring on the phenylglycine methyl ester derivatizing agent. Protons located on the group that is on the same side as the phenyl ring, those on the R group in **Scheme 1.4**, have a more upfield shift than the protons on the other group marked R'. This shift is a manifestation of the diamagnetic anisotropic effect of the benzene ring. The authors surmise this in the model they present for this interaction, shown in **Figure 1.3A**. Here, the total change in the chemical shift is the difference between the shifts for the two enantiomers of the starting material. They have applied this method to a variety of substrates, such as α,α -disubstituted carboxylic acids ((*S*)-**1.14**), β,β -disubstituted propionic acids ((*R*)-**1.15**), α -oxysubstituted- α,α -disubstituted acetic acids (**1.16**), and α -oxysubstituted- α -monosubstituted acetic acids (**1.17**). In each of these cases, the absolute stereochemistry was rapidly assessed based on direction of the shift of the protons. The values of the amount of change in chemical shift of the signals are also included in **Figure 1.3B**. The authors postulate that this method can be applied to a wider range of compounds that have no carboxylic acid fragment, but where one can be readily installed.

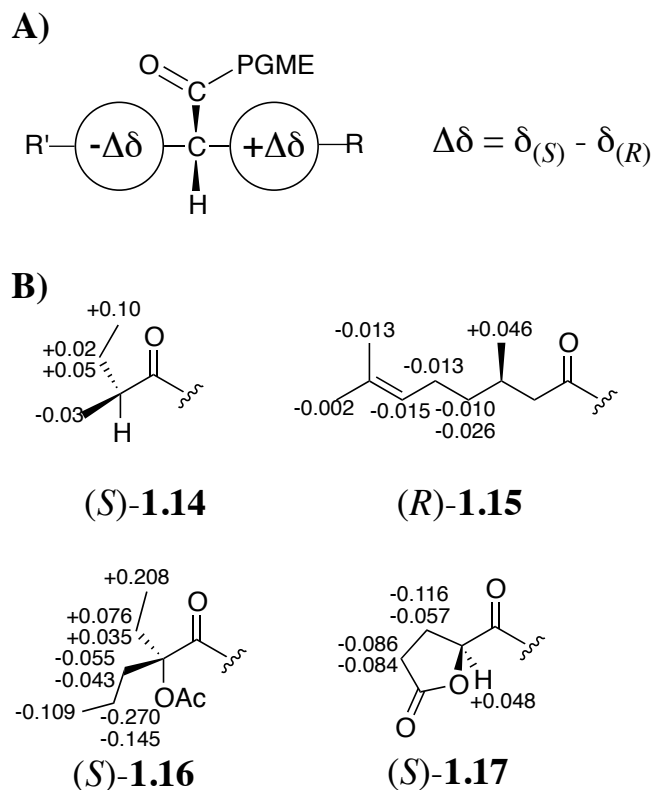


Figure 1.3. A) Model explaining change in chemical shift of the indicated protons as a result of anisotropy. In this model, the phenyl is directed to the left. B) Change in chemical shift across the scope of analytes tolerated with this method.

1.2.1.2. Ester Bond Formation

The Riguera group used ester formation between the (*S*)-enantiomer of the carboxylic acid guest **1.18** and (*S*)-enantiomer of the chiral secondary alcohol **1.19**, shown in **Figure 1.4A**.³⁸ This coupling was promoted by DCC and DMAP, and the ester was initially studied to determine the conformation of the product. Two conformations, namely **I** and **II**, were thought to exist in equilibrium. Through the use of both theoretical calculations, as well as the chemical shift considerations, the authors concluded that there is a preference for conformation **I**, where the hydrogen atoms depicted in **Figure 1.4B** are

located anti-periplanar. This means that the protons on the methyl group are located on the same side as the aromatic ring, and will feel the anisotropy of this ring. This has the effect of shifting this signal upfield to weaker field, while the ethyl group is seen further downfield than the methyl signal. The opposite trend is observed for the other enantiomer of the carboxylic acid, corroborating the conformational assignment.

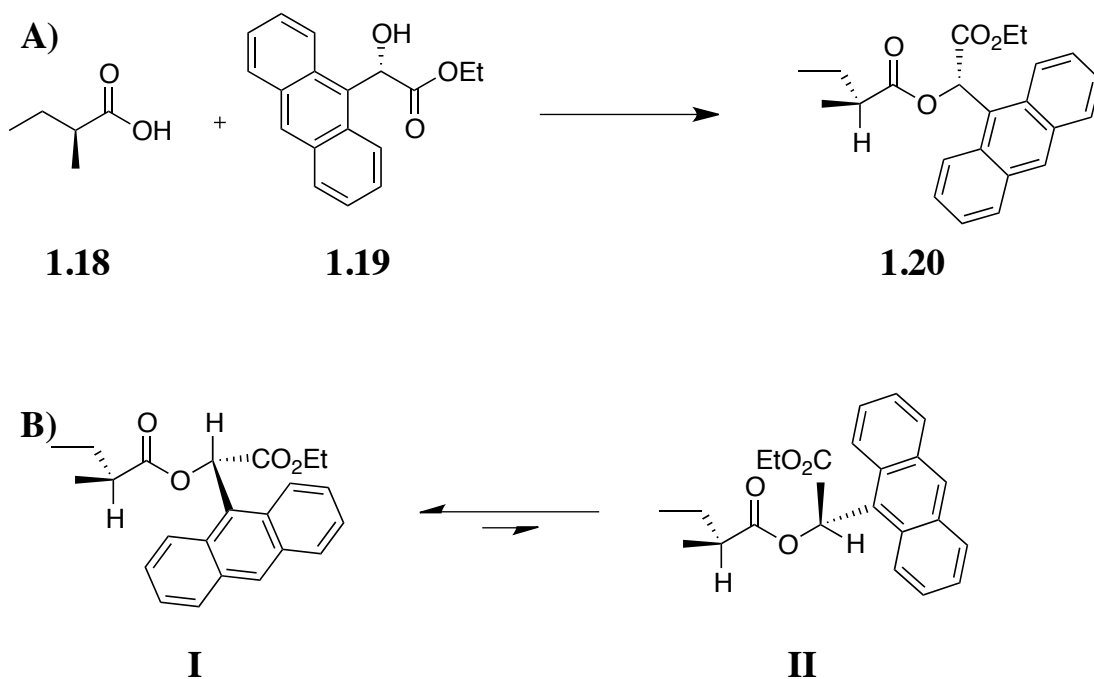


Figure 1.4. A) Derivatization protocol for carboxylic acid guest **1.18** with enantiopure (*S*)-alcohol **1.19** to form ester **1.20**. B) Equilibrium between two possible conformers **I** and **II** of ester **1.20**.

This method was applied to a large range of carboxylic acid guests, including stereocenters containing alkyl groups, halogens, heteroatoms, and various ring structures. A sample of the guest range is shown in **Figure 1.5**, and it was found that they all follow the same general trend. The opposite enantiomer of the chiral alcohol **1.19** showed a reversed trends of anisotropy induced chemical shifts for the same enantiomer of the

carboxylic acid guests. The same was true when considering the opposite enantiomers of the carboxylic acid guests with a single enantiomer of the chiral alcohol **1.19**. The authors also tested a range of chiral secondary alcohols, and found several suitable examples. This method allowed the absolute configuration of the chiral carboxylic acid guest to be assessed quickly and easily.

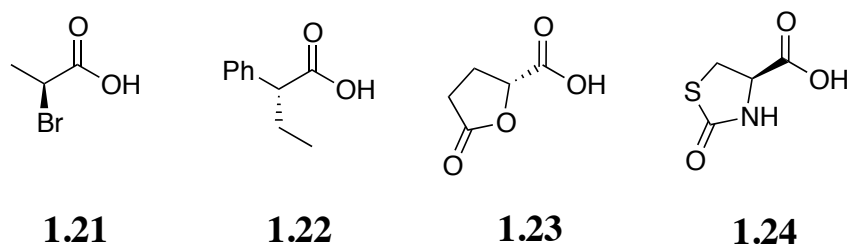


Figure 1.5. A sample of the range of guests used for absolute stereochemistry determination with the secondary alcohol derivatization protocol.

All of the previous reports are geared towards enantiodifferentiation of chiral carboxylic acids with vastly different sized groups attached to the stereocenter. While it is important to be able to distinguish these species, Parker was interested in determining the absolute stereochemistry of α -deuterated carboxylic acids.³⁹ The size difference between the hydrogen and deuterium is very subtle, and differentiating these species is not a trivial exercise. The author addressed this task by derivatizing a prochiral carboxylic acid, such as butanoic acid **1.25** with the (*R*)-enantiomer of the methyl ester of mandelic acid **1.26**. Indeed, it was observed that there was a moderate chemical shift difference of 0.12 ppm for these diastereotopic protons. This was repeated across a variety of prochiral carboxylic acids, and it was found that the *pro-S* hydrogen resonates further downfield than its *pro-R* counterpart. Thus, the absolute configuration of the

monodeuterated products could be assigned by monitoring the location of the peak that disappears as deuterium is incorporated.

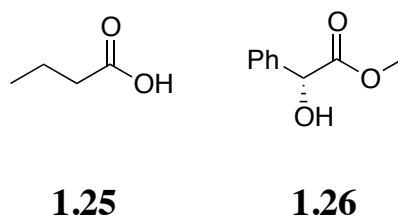


Figure 1.6. Chemical structure of prochiral carboxylic acid **1.25** that was analyzed using derivitizing agent **1.26**.

1.2.1.3. Salt Formation

The previous examples were focused on derivatizing the carboxylic acid by formation of an amide or an ester. While these techniques have proven accurate for determination of absolute configuration, they are limited in scope. The derivatization step is undesirable, since it adds extra synthetic steps to the process. This step is accompanied by an extra purification, further complicating the analysis. These methods are unable to form the amide or ester bond directly, and must proceed with either initial acid chloride formation or use of peptide coupling reagents. Finally, this route is susceptible to epimerization of the stereocenter during the synthetic modification process. In order to avoid this derivatization, it was envisioned that NMR analysis could proceed through formation of diastereomeric salts. Direct addition of a basic amine species to the carboxylic acid deprotonates it to form a salt, whose non-equivalent resonances can be integrated to determine the enantiomeric excess.

To this end, the compound 1,2-diphenyl-diaminoethane **1.27** was selected by Parker and coworkers to act as a base for salt formation (**Figure 1.7**).⁴⁰ Upon addition of two equivalents of carboxylic acid analyte **1.28**, the maximum difference in the chemical

shift of 0.17 ppm was observed for the methine proton. It was determined that the (*R,R*)-enantiomer of diamine **1.27** caused the (*R*)-enantiomer of the carboxylic acid guest to shift further downfield than the (*S*)-enantiomer. From these data, the difference in chemical shift was plotted as a function of enantiomeric excess. A linear correlation was discovered, and allowed for the determination of absolute configuration concurrently with *ee*. The authors demonstrated that this method is general, and could be extended to α -halogenated carboxylic acids (**1.29**) that are susceptible to racemization during other methods of analysis.

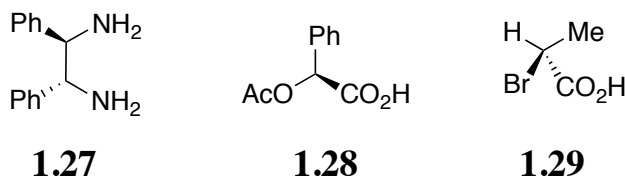


Figure 1.7. Chemical structures of diamine **1.27** that was used to form a diastereomeric salt with carboxylic acid guests such as **1.28** and **1.29**.

The Zhang group designed and synthesized a chiral C_2 symmetric macrocycle **1.28** to serve as an receptor for chiral carboxylic acids (**Figure 1.8**).⁴¹ This species possesses two basic nitrogen atoms, and it was determined that this complex binds carboxylic acids with a 1:2 stoichiometry. The NMR results suggest that the aliphatic nitrogen atoms likely deprotonate the carboxylic acid functional groups, resulting in the formation of a diastereomeric salt complex. Receptor **1.30** was titrated into a solution containing a racemic mixture of mandelic acid guest **1.31**. The difference in chemical shifts between the protons gradually increases, with (*R*)-**1.31** giving the furthest upfield shift. This increasing difference in chemical shift obtained a maximum value when two equivalents of the acid had been added to the receptor, and began to decrease at higher

concentrations. The largest difference observed between the signals was noted as 0.62 ppm, making integration of these peaks for enantiomeric excess determination easy. The integrations were taken for a variety of samples of **1.29** with varying *ee* values, and the calculated values were within $\pm 1\%$ of the actual values.

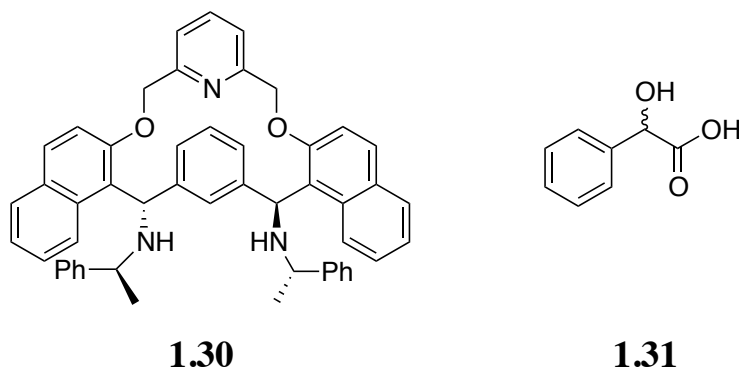


Figure 1.8. Chemical structures of chiral carboxylic acid receptor **1.30** and mandelic acid **1.31** that were used in these studies.

Zhang *et al* also described a new diamine derivative of (*S*)-phenylethylamine to serve as a chemical shift reagent for carboxylic acids through salt formation.⁴² This receptor (**1.32**), shown in **Figure 1.9**, possesses a chiral secondary amine to deprotonate the carboxylic acid guest and form a 1:1 diastereomeric salt complex. The signals of the methine proton on the α -carbon of a variety of guests **1.33-1.35** were observed to shift upfield, evidencing deprotonation and formation of the carboxylate anion. Using mandelic acid guest **1.31**, it was found that the difference in chemical shift for the derivatized enantiomeric carboxylic acids was 0.083 ppm, and was found in a region that didn't contain any other interfering signals. Integration of the diastereomeric methine peaks allowed for the determination of *ee*, which was carried out with a $\pm 1\%$ overall error. The accuracy of this assignment helped to demonstrate the application of this system to *ee* determination.

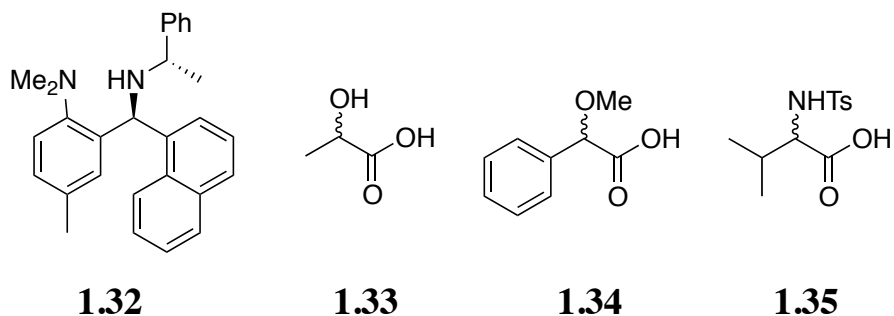


Figure 1.9. Structures of chiral carboxylic acid receptor **1.32**, used to determine the *ee* of chiral carboxylic acids such as **1.33-1.35**.

1.2.1.4. Hydrogen Bonding Receptors

The previous set of receptors were applied to enantioselective sensing of chiral carboxylic acids, but the broad application of these methods have some limiting drawbacks. Firstly, these species work by deprotonation of the carboxylic acid substrate. This strategy would be less likely to work if the analyte of interest contains other acidic sites that could be deprotonated. For instance, one published report showed that an amine base was capable of deprotonating an amide proton in a secondary sulfonamide.⁴¹ Additionally, this strategy could not be applied to molecules that contain internal basic sites. These species, such as amino acids, would require protection to avoid an intramolecular acid-base reaction. For this reason, it was desirable to create further supramolecular sensors. These sensors are based on hydrogen bonding as an attractive interaction, and avoid the pitfalls that come from full deprotonation.

To this end, Ema and Sakai designed macrocyclic receptor (*R*)-**1.36** that contains both hydrogen bond donors and acceptors.⁴³ A nitro group was introduced to the phenyl ring in order to strengthen the donor ability of the closest amides, and 1,1'-binaphthalene-2,2'-diol (BINOL) was selected as the chiral discriminating group (**Figure 1.10A**). This type of cavity had been reported previously by Hamilton to serve as an effective scaffold

for binding acidic guest molecules.⁴⁴ NMR studies of the receptor and a carboxylic acid guest indicated that the complex forms three hydrogen bonds as shown in **Figure 1.10B**, assigned based on the change in chemical shift of the carboxylic acid and two amide protons. The change in the chemical shifts was used to find binding constants for this association, and the (*S*)-enantiomer of the carboxylic acid guest was found to bind preferentially. The difference in the peaks corresponding to each enantiomer of the carboxylic acid guest was found to be around 0.1 ppm, sufficient to achieve baseline resolution of these species.

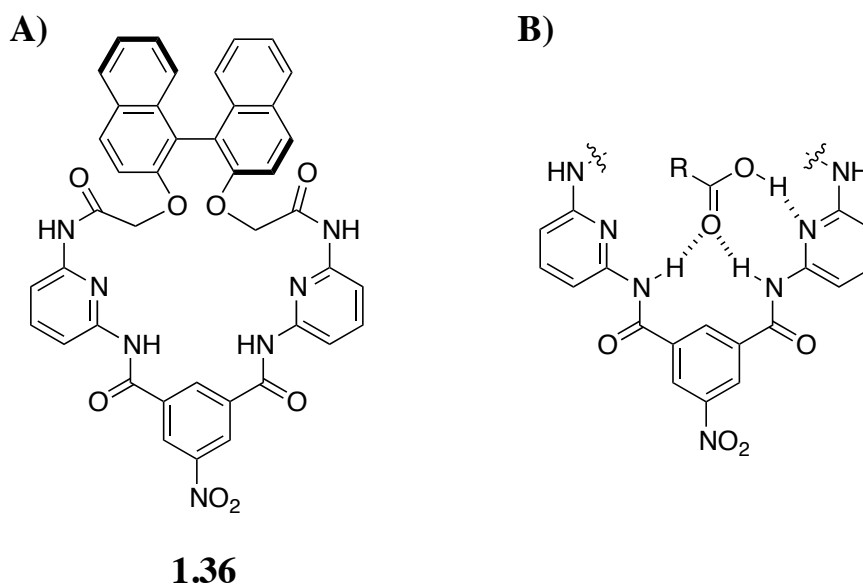


Figure 1.10. A) Hydrogen bonding host **1.36** used for enantioselective sensing of carboxylic acids. B) Proposed mode of interaction of the receptor and carboxylic acid guest.

The Sirit group designed and synthesized two new chiral calix[4]azacrown macrocycles **1.35** and **1.36** that were capable of enantiodifferentiation of chiral carboxylic acids (**Figure 1.11**).⁴⁵ Calixarenes are advantageous in their efficiency and

selectivity of binding, and have been shown to bind a variety of cations, anions, and neutral molecules.^{46,47} Upon addition of this host to racemic mandelic acid guest **1.31**, the methine peaks of the guest shifted upfield. This upfield shift was accompanied by a downfield shift of several of the calixarene peaks, evidencing complexation by multiple hydrogen bonds. It is thought that the carbonyl interacts with the tertiary azacrown nitrogen, as well as making π - π contact interactions between the phenyl group and the calixarene. The complex formed for guests **1.31** and dibenzoyltartaric acid **1.39** was found to be 1:1, and the peak separation was observed at a maximum of 0.06 ppm. The binding constants calculated for this interaction showed enhanced binding to the (*R*)-enantiomer of carboxylic acid guests.

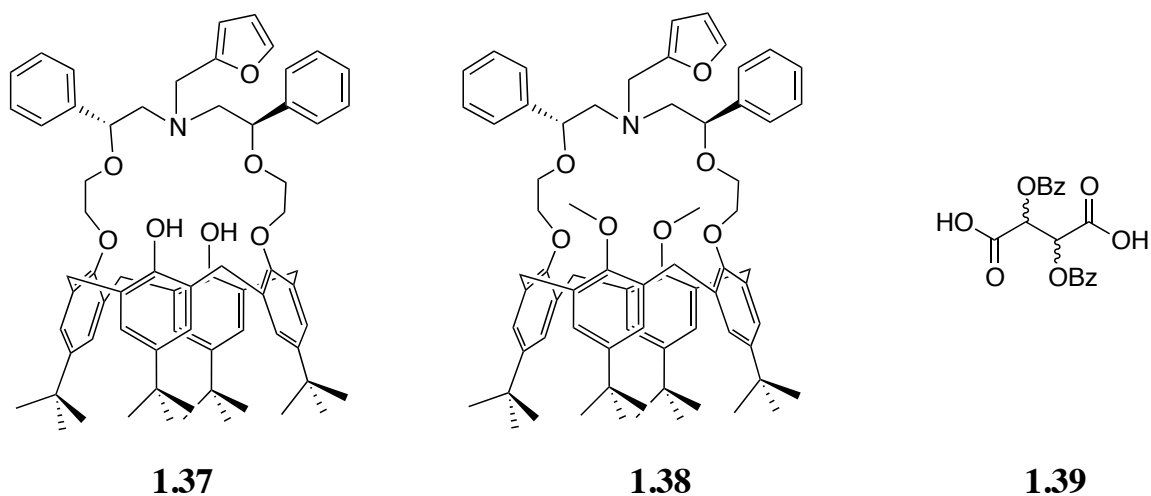


Figure 1.11. Calix[4]azacrowns **1.37** and **1.38** used for enantioselective recognition of guests **1.31** and **1.39**.

Tanaka *et al* reported the synthesis of macrocyclic receptor **1.40**, and used it as a chiral shift reagent for carboxylic acids (**Figure 1.12**).⁴⁸ This molecule was synthesized to contain both hydrogen bond donating and accepting groups, so as to enhance

interactions with the guests. When receptor **1.40** was added to a racemic mixture of chlorinated mandelic acid derivative **1.41**, the methine proton α - to the carbonyl shifted upfield and split into two peaks. This difference in the methine peak continued to get larger until 0.4 equivalents of the receptor had been added, however with increased receptor line broadening became an issue. In order to avoid broadening, 0.2 equivalents of the receptor were added relative to the guest. When these ratios were used the difference between these two peaks characteristic of the starting enantiomers was 0.204 ppm. The macrocycle was further determined to accommodate four equivalents of a variety of carboxylic acid guests that were studied. The (*S*)-enantiomer was found to shift further upfield than the corresponding (*R*)-enantiomer, meaning that the absolute configuration can also be easily determined. Integration of the two peaks allowed for the *ee* value to be readily calculated.

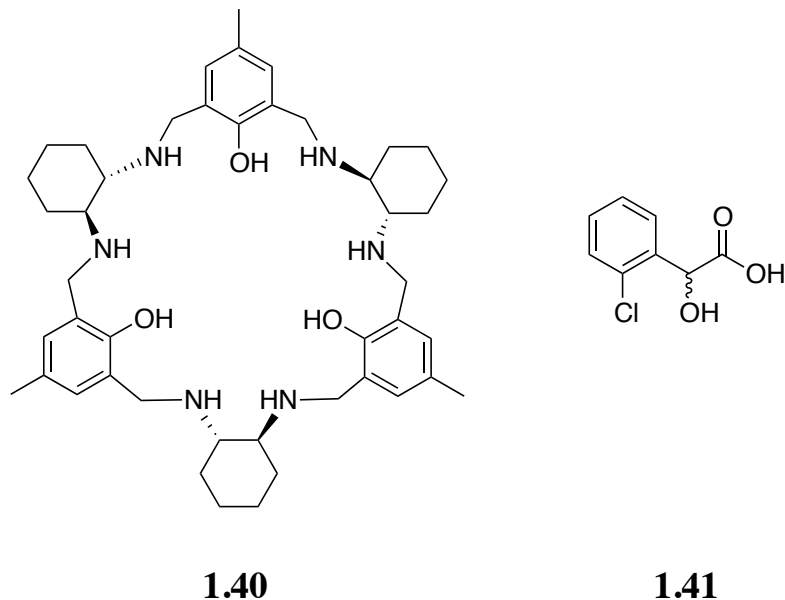


Figure 1.12. Macrocyclic host **1.40** used for enantioselective recognition of chiral carboxylic acids, such as **1.41**.

The previously presented examples show the utility of both chiral derivatization and the chiral shift reagents in identifying not only the absolute configuration, but also the *ee* of chiral carboxylic acids in ^1H NMR spectrometry. While these methods are very useful, there are a few drawbacks overall that limit the general applicability. First of all, there are many different types of protons in many of the guests that were studied. This condition means that overlap of signals is much more likely, thus limiting the range of guests that can be used. Additionally, it is often difficult to create baseline separation between the peaks of the guests that are studied. The proton spectrum covers only around 12 ppm, and it can be very difficult to create a resolvable difference between these newly created diastereotopic peaks. For these reasons, several other nuclei have been examined to determine enantiomeric composition with NMR spectrometry.

1.2.2. ^{19}F NMR

Fluorine NMR is attractive as a means to determine enantiomeric composition of chiral carboxylic acids for many reasons. First, the ^{19}F nucleus is spin $\frac{1}{2}$, analogous to the proton, and thus very responsive to NMR.⁴⁹ Additionally, it has a high magnetogyric ratio, and a natural occurrence of 100%. The observed range of chemical shifts seen for this nucleus is much greater than the range seen for the proton, around 1000 ppm. Organic compounds also contain few if any fluorine atoms, meaning that the spectrum of this nucleus should be free from additional signals that interfere with analysis. For these reasons, ^{19}F NMR has been seen application in the determination of enantiomeric purity of chiral carboxylic acids.

One of the first reports of using ^{19}F NMR to enantioselectively differentiate chiral carboxylic acids was reported by Mosher and coworkers.⁵⁰ Chiral carboxylic acids had previously been prepared for derivatization of a chiral amine to determine the enantiomeric purity of the amine through amide bond formation.⁵¹ This report by Mosher was one of the first to reverse the order of analysis. To this end, enantiopure 2,2,2-trifluoro-1-phenylethylamine **1.42** was prepared (**Figure 1.13**). This reagent was used to derivatize chiral carboxylic acids, such as **1.43** and **1.44**, through DCC coupling to form the corresponding amides. These diastereomeric amides were expected to have different chemical shifts, similar to the previously reported ^1H NMR examples. It was indeed observed that the chemical shifts of the diastereomers were different, with a difference of 0.089 ppm for diastereomers of derivatized **1.43**. This modest difference in chemical shifts is sufficient to achieve baseline separation, but a larger range of shifts is still desirable.

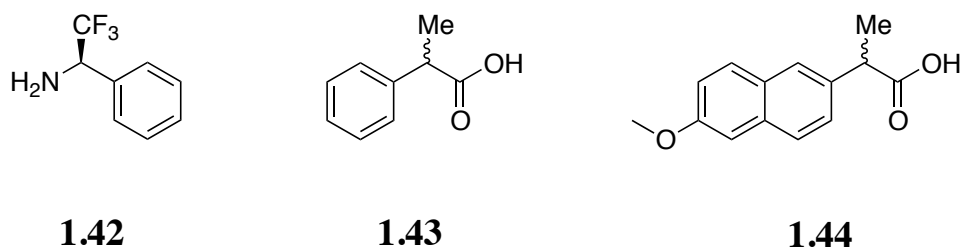
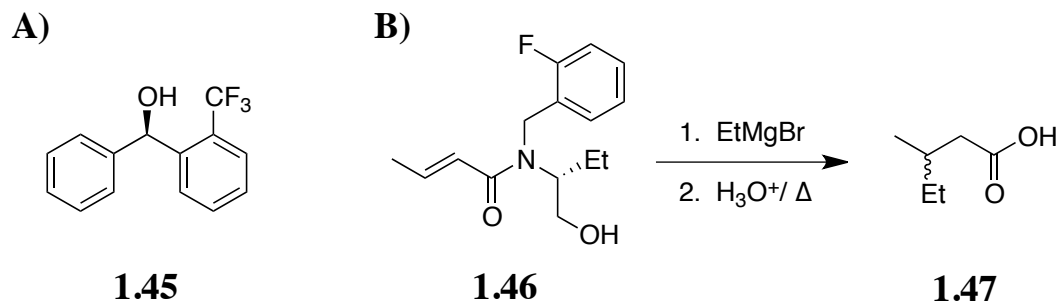


Figure 1.13. Chiral ¹⁹F derivatizing agent **1.40**, and chiral carboxylic acids **1.41** and **1.42** that were analyzed.

Rather than forming an amide, Brown *et al* focused on the creation of esters from a fluorine-containing alcohol.⁵² This alcohol **1.45** was readily synthesized (**Scheme 1.5A**), and applied to determine the enantiomeric composition of a variety of synthetic β -chiral carboxylic acids. The acids were synthesized through the Michael addition of a Grignard reagent to an α,β -unsaturated amide, followed by acidic hydrolysis (**Scheme 1.5B**). The optical rotation was measured, and correlated to an *ee* value according to values that are known in the literature. The ¹⁹F NMR spectrum was then recorded after derivatization through DCC-promoted coupling, and baseline resolution was achieved for both of the diastereomeric products. Integration of the peaks was facile for determining the relative amounts of each enantiomer of the chiral acid. For example, optical rotation revealed that carboxylic acid **1.47** had been synthesized with 90% *ee*. The corresponding derivatized ester was determined to be 87.5% *ee* by integrating the diastereomeric ¹⁹F NMR peaks, giving an overall error in analysis of 2.5%. This error was typical across the 15 substrates tested, giving an average overall error of 3.0%.



Scheme 1.5. A) Derivatizing agent for ^{19}F NMR analysis of enantiomeric purity. B) Representative synthesis of β -chiral carboxylic acid **1.47** through Michael addition and subsequent amide hydrolysis.

1.2.3. ^{31}P NMR

While ^{19}F NMR has found some application in determining the *ee* of chiral carboxylic acids, it is limited by the difficulty of preparing the fluorinated reagent in high enantiomeric purity. To overcome this limitation, one of the other nuclei that scientists have relied on is phosphorous. Much like both ^1H and ^{19}F , ^{31}P is a spin $\frac{1}{2}$ nucleus that has a natural abundance of 100%.⁵³ Many biologically important species contain phosphorous, adding to its potential application. These species cover a wide range of chemical shifts of around 400 ppm, but the location of the signal is more influenced by paramagnetism than by nuclear diamagnetic shielding. One detriment of ^{31}P NMR is the presence of an inconsistent nuclear Overhauser effect, meaning that integration of the peaks does not always provide a way to correlate relative abundances like is inherent for ^1H and ^{19}F . Despite these limitations, reports have been published detailing the application of ^{31}P NMR to enantiomeric composition determination.

In order to synthesize a molecule that possessed a chiral pocket that could be applied to asymmetric catalysis, the Katz group reported chiral helicene-based molecule.⁵⁴ This species was found to catalyze the addition of diethylzinc to aldehydes to

create enantioenriched alcohols, but it was envisioned that the addition of phosphorous trichloride would create phosphine complex **1.48** in **Figure 1.14**. This complex was readily synthesized, then applied as a derivatizing reagent to create diastereomers to be differentiated by ^{31}P NMR spectroscopy.⁵⁵ The location of this probe deep within the chiral cavity of the helicene was postulated to increase the tolerance of the host to more remote stereocenters. Thus, the stereocenters of the bound guest, indicated as X in **1.48**, are expected to be oriented to promote a variety of diastereomeric interactions with the helicene. This was indeed observed when chiral alcohols were bound directly to the phosphorous, allowing analysis of stereocenters that were further away from the alcohol binding site.

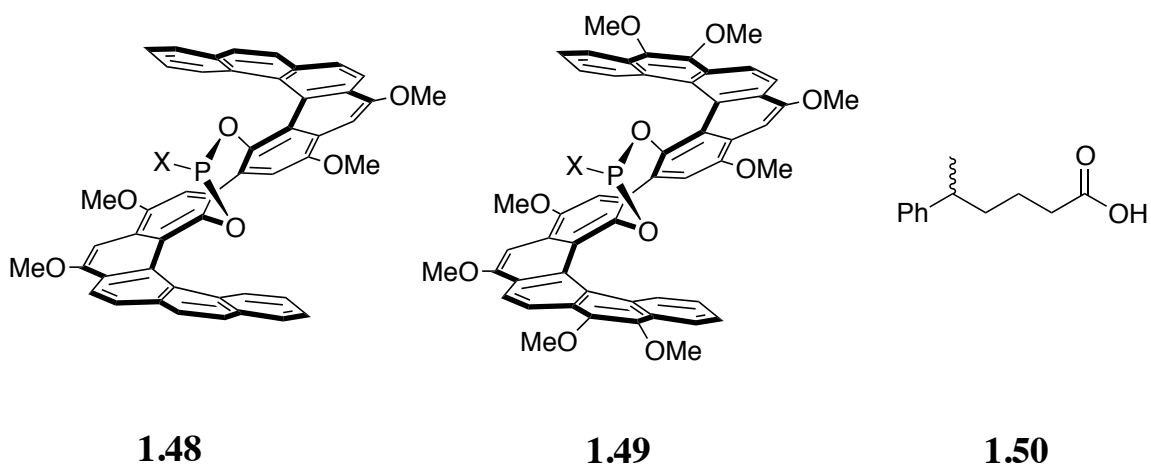
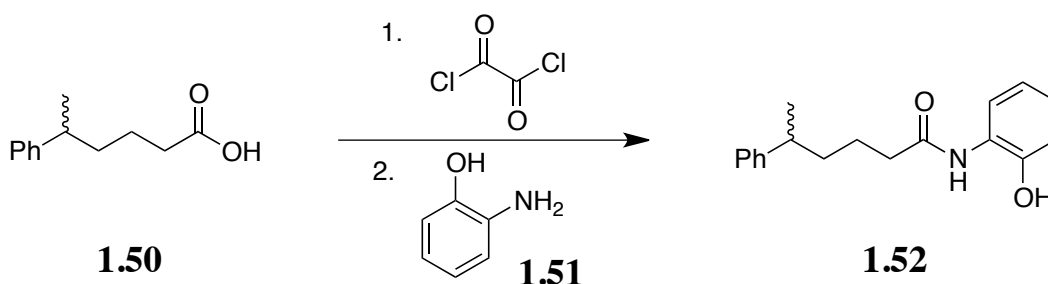


Figure 1.14. Chemical structures of chiral phosphorous-containing helicenes **1.48** and **1.49** that were used to measure chiral substrates with remote stereocenters, such as chiral carboxylic acid **1.50**.

The free carboxylic acid unfortunately did not interact directly with receptor **1.48**, so it was necessary to transform this species into a known binding phenol in order to make this analysis method suitable. To this end, the authors relied on amide bond

formation to create the phenol. Carboxylic acid **1.50** was coupled to a rigid 2-aminophenol linker **1.51** after forming the subsequent acid chloride (**Scheme 1.6**). Analysis of the diastereomeric complex formed from **1.52** and helicene **1.48** facilitated the separation of 0.42 ppm between these peaks. Indeed, this method is quite sensitive to analysis of chiral carboxylic acids with a stereocenter located several bonds away from the binding site.



Scheme 1.6. Derivatization protocol to create phenol **1.52** through coupling of carboxylic acid **1.50** and aniline **1.51**.

This reagent was sensitive to analysis of remote chirality over a wide range of substrates, including amines, alcohols, phenols, and carboxylic acids. There are some important drawbacks to **1.48** it would be desirable to overcome. First, the synthesis forms a small but reliable amount of byproduct. This byproduct is formed in approximately 5%, and requires an additional purification step to be removed. This species is also quite light sensitive, so the purification must be done in the dark. Additionally, this procedure requires that the carboxylic acid analyte be derivatized before analysis can be performed. This adds one more undesirable step to the analysis, further complicating matters. To avoid these limitations, the authors reported the synthesis of alternative helicene **1.49**.⁵⁶ This species is not only easier to obtain

synthetically, it allows the carboxylic acids to be analyzed without additional derivatization. For the acid **1.50**, analysis with the new helicene **1.49** led to a separation of the chemical shifts of the peaks of diastereomers formed from underivatized carboxylic acids. These peaks were separated by 0.45 ppm, comparable to the separation observed for derivatized acids **1.52**.

Alexakis and coworkers reported a method for the determination of enantiomeric composition of chiral carboxylic acids through the use of a TADDOL-phosphorous complex (**1.53**).⁵⁷ These species have been widely applied as chiral ligands in asymmetric synthesis,^{58,59} and it was hypothesized that the complexes formed when a chiral carboxylic acid is added would lead to a chemical shift difference between these diastereomers. To this end, the ³¹P NMR spectrum was recorded for complex **1.54**, derived from *O*-methylmandelic acid **1.34** and TADDOL-phosphorous complex **1.53** (**Figure 1.15**). For these species, the difference in chemical shift was found to be 2.31 ppm. The observed difference is very large, one of the largest observed thus far. Distinct peaks were recorded for enantiomers of β -chiral species, but the differences in chemical shift were relatively modest. Nonetheless, the large difference in chemical shift should render this system viable for rapid assessment of *ee*, though the authors did not explore this task.

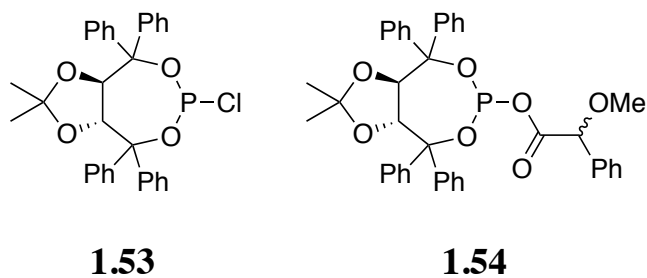


Figure 1.15. Chemical structures of TADDOL-derivative **1.53** and its complex **1.54** with carboxylic acid **1.34**.

The same authors further revised their carboxylic acid sensor to contain a diamine phosphine instead of TADDOL.⁶⁰ To this end, two phosphine complexes **1.55** and **1.56** were prepared (**Figure 1.16**). The former, **1.55**, was successfully applied for the intended purpose of differentiating the complexes formed from the enantiomeric carboxylic acids. When this species was derivatized with the chiral carboxylic acid **1.34**, a significant difference in chemical shift of 6.46 ppm was noted for the resultant diastereomers. In many cases, a better resolution has been achieved from the ³¹P NMR spectrum. In some cases, the authors oxidized the phosphine complex from P(III) to P(V) by addition of S₈. The complex formed from the addition of S₈ (**1.57**) was envisioned to aid in the analysis by helping to accentuate differences in chemical shift for stereoisomeric complexes. The sulfur-containing P(V) analogs gave inconsistent results, promoting a greater difference sometimes while a smaller difference others.

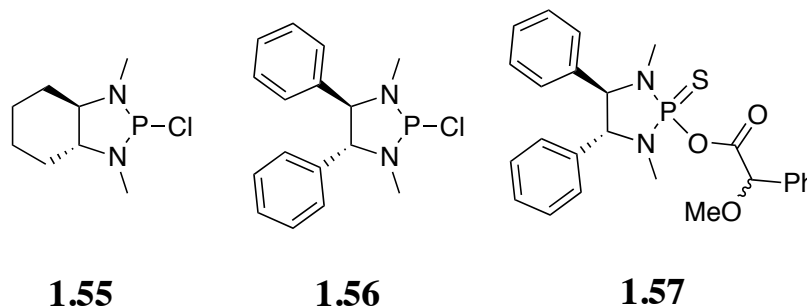


Figure 1.16. Chemical structures of diamine-phosphine complexes **1.55** and **1.56**, and the P(V) complex formed from S_8 addition to the complex from receptor **1.51** and guest **1.34**.

1.2.4. ^{77}Se NMR

Many studies in both organic and biochemical systems have utilized the NMR properties of the ^{77}Se nucleus. This nucleus has a relatively high natural abundance of 7.5%, in addition to having a sensitivity that is greater than many other nuclei.⁶¹⁻⁶³ Plus, it is the same spin $\frac{1}{2}$ nucleus that is observed for ^1H , ^{19}F , and ^{31}P . Another remarkable feature of ^{77}Se NMR is the extremely large range of observed chemical shifts, covering around 3400 ppm.⁶⁴ This nucleus is extremely sensitive to the electronic environment in which it resides, with many orders of magnitude greater than the other nuclei such as ^{31}P . In particular, the incorporation of ^{77}Se as a selenocarbonyl allows access to a shift that spans 80% or the possible range, or approximately 2600 ppm.⁶⁵ All of these advantages made the study of this nucleus attractive for determination of enantiomeric purity.

Some of the earliest examples of ^{77}Se being used to determine enantiomeric purity of chiral carboxylic acids were reported by Silks and coworkers.⁶⁶ These researchers constructed chiral selenone **1.58**, and used DCC methodology to derivatize this scaffold with carboxylic acids such as **1.59** (Figure 1.17). Even with the stereocenter four carbons removed from the carbonyl, the probe was sensitive enough to achieve baseline resolution of the diastereomeric NMR signals. Interestingly enough, the researchers then

used this probe to study the α -deuteration of prochiral carboxylic acid **1.60**. Four different peaks were observed in the ^{77}Se NMR, one corresponding to the fully protonated, two corresponding individually to enantiomers of the mono-deuterated, and one for the fully deuterated adduct. Remarkably, this nucleus is sensitive enough to discern these four structurally very similar but different species.

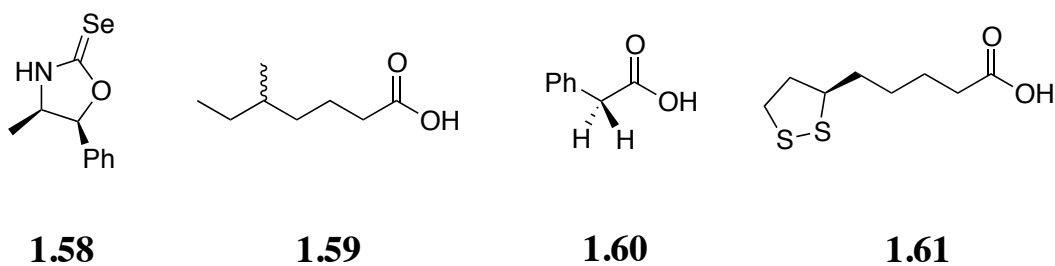


Figure 1.17. Chemical structures of chiral selenone **1.58**, and the carboxylic acids **1.59**, **1.60**, and **1.61** that were analyzed with this probe.

The authors then turned their attention to evaluating lipoic acid (**1.61**), an analyte for which previous attempts to distinguish enantiomers had failed.⁶⁷ The chiral selenone **1.58** was able to differentiate the two different enantiomers of this species, and the resonances of these enantiomers were separated by 0.119 ppm in the ^{77}Se NMR spectrum. After proving the utility of this selenone toward remote enantioselective sensing of chiral carboxylic acids, the authors focused on determining the best structure of the selenone to promote the largest differentiation of mandelic acid guest **1.31**. To this end, a variety of chiral selenones were synthesized and subsequently derivatized with a racemic mixture of the acid chloride of **1.31**.⁶⁸ Chiral selenones **1.62** and **1.63** (**Figure 1.18**) were found to give the best differentiation of the enantiomers of **1.31**, differing at the largest by 45.6 ppm. These probes were then used to determine the *ee* values for **1.22**, both as a challenge to find the *ee* and to study if racemization of the stereocenter occurred. In each

case the error in *ee* was less than 2%, further demonstrating the accuracy of this approach.

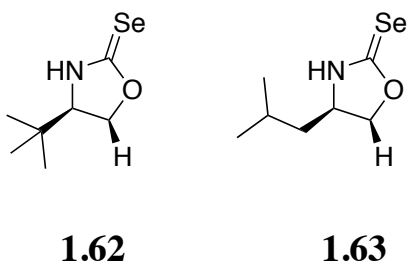
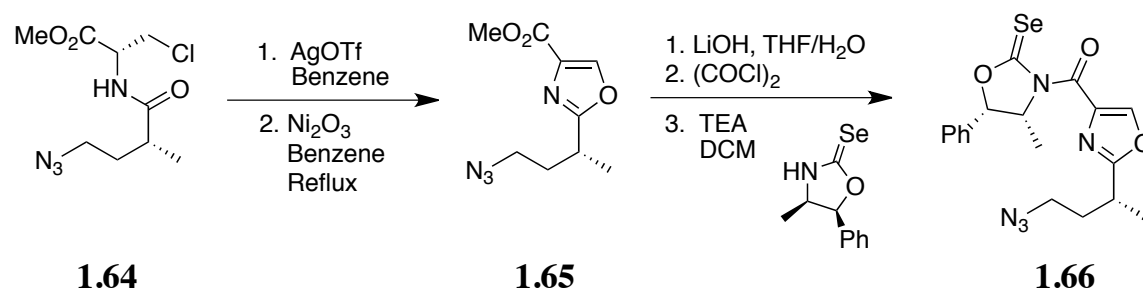


Figure 1.18. Additional chiral selenones that were used to enantioselectively differentiate **1.22** and **1.41**.

This analytical *ee* method was used by Smith and coworkers to assess the enantiomeric purity of synthetic intermediate **1.64**.⁶⁹ This species comprises the C(26)-C(32) fragment of the natural product calyculin A. The authors were interested in creating the ring segment through methodology published by Wipf,⁷⁰ and needed to assess the extent of epimerization that occurred throughout the reaction (**Scheme 1.7**). The previous protocol they used for analysis, namely the Anderson-Shapiro method,⁷¹ did not accurately measure the enantiomeric purity of the product. Thus, the authors applied chiral selenone **1.58** to assess the enantiomeric purity. They found that the ⁷⁷Se signals were fully resolved, with a difference in chemical shift of around 2.0 ppm. This approach allowed the authors to determine that less than 2% of epimerization was occurring, proving that the applied methodology was successful.



Scheme 1.7. Determination of epimerization for the conversion of **1.64** to **1.65** by way of selenone derivatization.

These reported examples represent some of the ways that NMR has been applied to enantioselective sensing of chiral carboxylic acids. The variety of substrates has necessitated the application of several different NMR active nuclei. There is some overlap between the nuclei, with differentiation on a single molecule achieved using multiple methods. While these techniques are reasonably straightforward, they are still somewhat limited in their abilities. The majority of the methods described are based around derivatization of the analyte, which is an undesirable extra step in the analysis process. Further, NMR analysis is not yet fully amenable to high-throughput analysis. Only a single sample may be analyzed at one time, limiting the amount of samples that can be analyzed in a single day. These limitations have continued to push enantioselective sensing toward finding and applying new methods based on non-chromatographic methods.

1.3. OPTICAL SPECTROSCOPY

Significant research effort has been directed toward creating enantioselective sensing assays based on chromogenic receptors.⁷² One of the major advantages of this analysis method is the decrease in time required to perform the analysis, as discussed above. Many optical spectrometers hold the capability of being equipped with multiwell

plate readers, compounding the ease and increasing the speed of this analysis. In addition to the speed of analysis, the spectrometers required for optical analysis are typically less expensive than other instruments, such as an NMR spectrometer. They are also much more common pieces of laboratory equipment, increasing their exposure within the scientific community. The typical approach that has been applied to creating an optical sensor is based on obtaining a host molecule that contains both a chromogenic unit, as well as a binding site for the guest of interest.^{73,74} Thus, binding of the guest causes a change in the spectrum of the indicator to signal its presence. When the host molecule contains chiral functionalities, the guest is able to elicit an enantioselective response from chiral compounds. This section will cover examples of the most common forms of optical spectroscopy that have been applied to the *ee* determination of chiral carboxylic acids, namely fluorescence, and UV/vis spectroscopies.

1.3.1. Fluorescence Spectroscopy

Fluorescence spectroscopy allows for the potential of creating an assay to provide real-time analysis of important properties of a reaction, such as *ee* determination. Much of the pioneering work in enantioselective sensing of chiral carboxylic acids based on fluorescence comes from the Pu group. The scaffold that they have applied most often is BINOL. This molecule has repeatedly seen utility in asymmetric synthesis, and has been shown to lead to outstanding chiral induction in a variety of processes.⁷⁵ In addition to asymmetric synthesis, this scaffold had been demonstrated to serve as a sensor for the recognition of some saccharides.⁷⁶

Based on these reports, Pu synthesized a variety of bis-BINOL molecules.⁷² This set of molecules, **1.67-1.69**, was comprised in a linear fashion (**Figure 1.19**). It was envisioned that the phenol and amine functionalities would serve as hydrogen bonding

sites, and this interaction would “turn on” the fluorescence. The fluorescence of the BINOL is effectively quenched in the absence of the guest by photo-induced electron transfer (PET)^{77,78} from the lone pair on the nearby amine nitrogen atom. When the guest is bound to the complex the carboxylic acid proton will be transferred to the amine, and thus the lone pair is no longer free to quench the fluorescence through PET. The chirality of the BINOL moiety was expected to enantioselectively influence formation of complexes with different enantiomers of α -hydroxy carboxylic acids, such as mandelic acid **1.31**. These guests were of particular interest, as this structural unit is found in a variety of natural products and drug molecules.⁷⁹

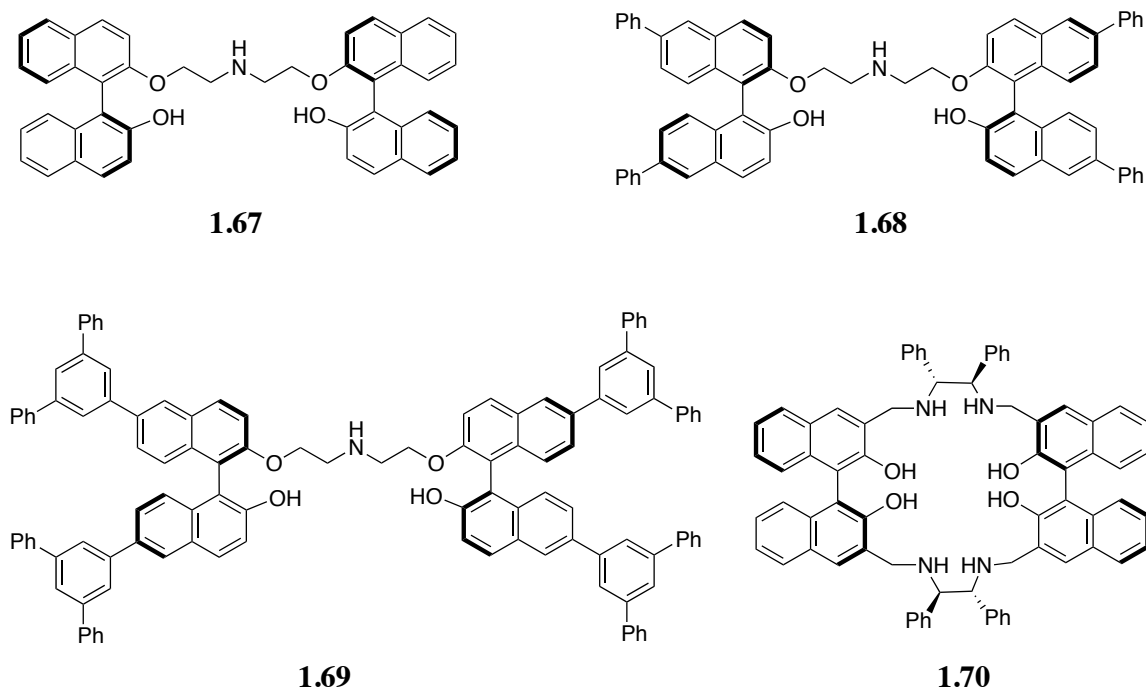


Figure 1.19. Chemical structures of bis-BINOL complexes **1.67-1.70** applied as enantioselective sensors of mandelic acid **1.31**.

The Pu group began by studying the fluorescence properties of compound (*S*)-**1.66** upon titration with either the (*R*)- or (*S*)-enantiomer of **1.31**. The fluorescence increased substantially for both enantiomers, as the PET quenching was arrested upon protonation of the amine nitrogen by the carboxylic acid. It was observed that this increasing fluorescence signal was very enantioselective, with the enhancement upon titration of (*S*)-**1.31** a factor of 1.75 times greater than that seen for (*R*)-**1.31**. The stoichiometry of binding was determined to be 4:1, for guest **1.31** relative to host **1.67**. In order to confirm that the enhancement was a result of the enantioselectivity of the host, the opposite enantiomer (*R*)-**1.67** was synthesized and titrated with each enantiomer of **1.31**. Mirror image fluorescence profiles were observed for these enantiomers of **1.67**, confirming that this receptor is cross-reactive and the fluorescence enhancement is a direct result of the enantioselectivity of the host.

In order to achieve enhancement, and thus improve enantioselective recognition, the authors synthesized dendritic derivatives of host **1.67**. These hosts were synthesized beginning with (*R*)-BINOL, and additional aromatic rings were added to improve the observed fluorescence signal. This signal was indeed enhanced, with the fluorescence emission of both hosts **1.68** and **1.69** significantly larger than **1.67**. When (*R*)-**1.31** was added to both of these hosts **1.68** and **1.69**, the fluorescence was enhanced by 14 and 22 times, respectively. Titration of both of these hosts with the other enantiomers of **1.31** allowed the enantioselective fluorescence enhancement to be calculated as 2.05 for **1.68** and 1.49 **1.69**. Even though the overall fluorescent enhancement is larger for **1.69**, this enhancement is less enantioselective than host **1.68**.

The next enhancement Pu made to this enantioselective fluorescence sensor was constraining the bis-BINOL moieties in a macrocycle.⁸⁰ This new macrocycle, **1.70**, has eight hydroxyl and amine groups directed toward the inner cavity of the macrocycle to

aid in hydrogen bonding with the α -hydroxycarboxylic acid guest. Treatment of receptor (-)-**1.70**, the enantiomer pictured in **Figure 1.19**, with (*S*)-**1.31** led to a significantly enhanced fluorescence spectrum. In contrast, little change was observed for addition of (*R*)-**1.31**. The enantioselective fluorescence enhancement from addition of (*S*)-**1.31** for this titration was calculated to be 12. Cross-reactivity was again observed for these guests, as found by synthesizing and testing (+)-**1.70**. In addition, both enantiomers of the new guest hexahydromandelic acid **1.71** (**Figure 1.20**) were studied with (-)-**1.70**. The enantiomer which gave the biggest enhancement was (*S*)-**1.71**, but the preference for this enantiomer of the guest was much smaller than for **1.31**.

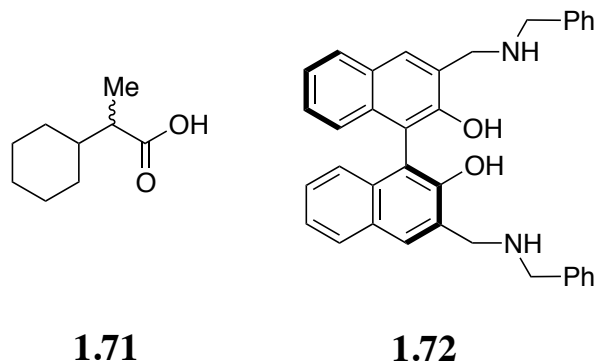


Figure 1.20. Chemical structures of new guest **1.71**, and monomeric BINOL host **1.72**.

The next study the Pu group conducted toward enantioselective fluorescence recognition was to analyze the monomeric BINOL derivative **1.72**.⁸¹ The synthesis of this monomeric species is much easier than the bis-BINOL derivatives, making these targets more attractive. A fluorescence enhancement of approximately one order of magnitude higher than any bis-BINOL sensors was observed when monomeric (*S*)-**1.72**, the enantiomer shown in **Figure 1.20**, was treated with (*R*)-**1.31**. The enantiomeric

fluorescence ratio was found to 4.2 for this host, much better than the previously reported bis-BINOL sensors. Through iterations to the original structure of the receptors, the Pu group has created a broad set of mono- and bis-BINOL receptors for the enantioselective fluorescence recognition of chiral α -hydroxy carboxylic acids. These sensors have been proven cross-reactive, showing that the selective fluorescence enhancement are an artifact of the chirality of the host structure.

The James group created boronic acid-containing host **1.73** for enantioselective fluorescence sensing of chiral α -hydroxy carboxylic acids (**Figure 1.21**).⁸² This molecule is based on the fluorescence of an appended anthracene, whose signal is quenched in solution. Binding of the guest species to the boronic acid causes the lone pair on the nitrogen atom to be unavailable to participate in PET quenching, and thus elicits a “turn on” response of the fluorescence signal. Titration of (*S*)-**1.73**, pictured in **Figure 1.21**, with both enantiomers of **1.31** produced enantioselective fluorescence enhancement. It was observed that the fluorescence was further enhanced for the (*R*)-**1.31** than it was for (*S*)-**1.31**. The binding constants were calculated for each enantiomer, giving values of K as $5.04 \times 10^3 \text{ M}^{-1}$ for (*R*)-**1.31** and $2.77 \times 10^3 \text{ M}^{-1}$ for (*S*)-**1.31**. A further titration of each enantiomer of guest **1.31** into the opposite enantiomer of the host, namely (*R*)-**1.73**, gave rise to mirror image fluorescence spectra. This experiment confirmed that these hosts were cross-reactive.

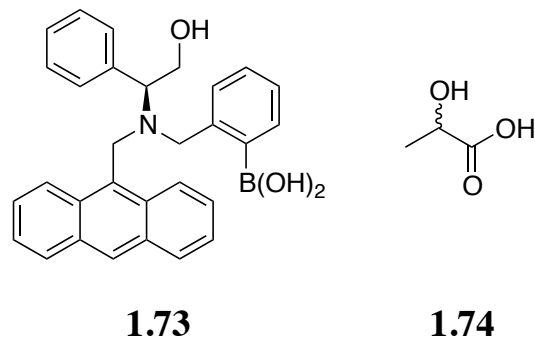
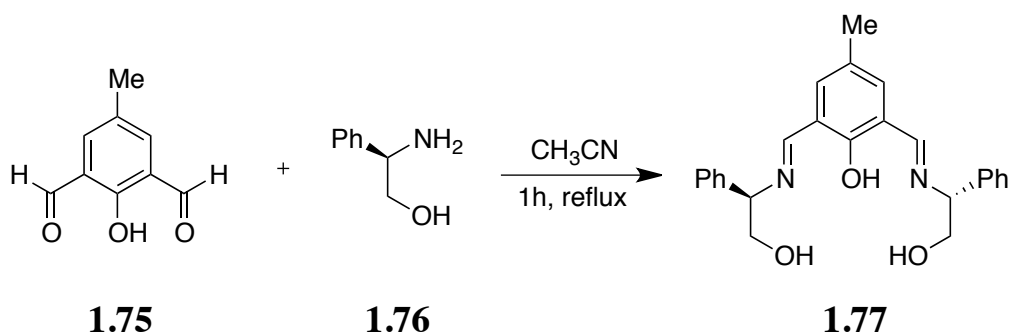


Figure 1.21. Boronic acid-based sensor **1.73**, and newly applied chiral α -hydroxy carboxylic acid analyte **1.74**.

The authors next turned their attention toward applying this host to recognition of lactic acid **1.74**. This α -hydroxy carboxylic acid suffers less steric hinderance from its methyl group rather than a larger group such as phenyl, and thus it is a more challenging target for enantioselective sensing. Nonetheless, sensor **1.73** showed an enantioselective fluorescence enhancement profile when titrated with each enantiomer of **1.74**. Greater enhancement was observed when the (*S*)-**1.73** host was titrated with (*R*)-**1.74**, and the converse was true for (*R*)-**1.73**. The enantioselective fluorescence enhancement for this host was smaller, estimated to be 1.2. This example represents the first time that a mono boronic acid has been applied to enantioselectively sense α -hydroxy carboxylic acids.

Banerjee and coworkers developed a chiral Schiff-base fluorescence sensor for mandelic acid **1.31**.⁸³ The sensor **1.77** can be made in one easy synthetic step, as demonstrated in **Scheme 1.8**, and requires no chromatographic purifications. The fluorescence of the (*R,R*)-**1.77** sensor was significantly enhanced upon addition of each enantiomer of **1.31**, with an enhancement of 122 times found for (*S*)-**1.41** and only 42 times for (*R*)-**1.31**. Hence, the fluorescence was enhanced by a factor of 2.9 for (*S*)-**1.31**. The opposite trends were observed for the (*S,S*)-**1.77** sensor, indicating that the receptor

is cross reactive towards guest addition. The authors wanted to probe the physical basis of the enantioselectivity of receptor *(R,R)*-**1.77**, and chose ¹H NMR as an analysis tool. The methine proton (*S*)-**1.31** shifted significantly upfield, while the methine proton in (*R*)-**1.31** showed very little difference in chemical shift when added to (*R,R*)-**1.77**. This likely means that the sensor is located deeper within the cavity of this receptor, resulting in a greater fluorescence enhancement upon binding.



Scheme 1.8. One-step synthesis of receptor **1.77** from commercially available starting materials.

In a slightly different approach, Cheng and Zhu created chiral salen-based enantioselective polymer sensors for the detection of α -hydroxy carboxylic acids.⁸⁴ This is one of the first examples where enantioselective fluorescence recognition was carried out with a macromolecule, rather than a small molecule of defined structure. To achieve this task, polymer sensors **1.78** and **1.79** were synthesized (**Figure 1.22**). The piperidine groups were added to help improve the chiral environment into which guest **1.31** was anticipated to bind. Subsequent studies on the polymers indicated that they both have moderate molecular weights, with high thermal stability. Enantioselective enhancement was observed when polymer **1.78** was titrated with each enantiomer of **1.31**, with a greater enhancement occurring for addition of (*R*)-**1.31**. The enhancement of

fluorescence ratio was calculated to be 8.41, indicating that enantioselective recognition occurs in a highly selective fashion. The fluorescence is enhanced by protonation of the imine nitrogen atom, ending the PET quenching mechanism.

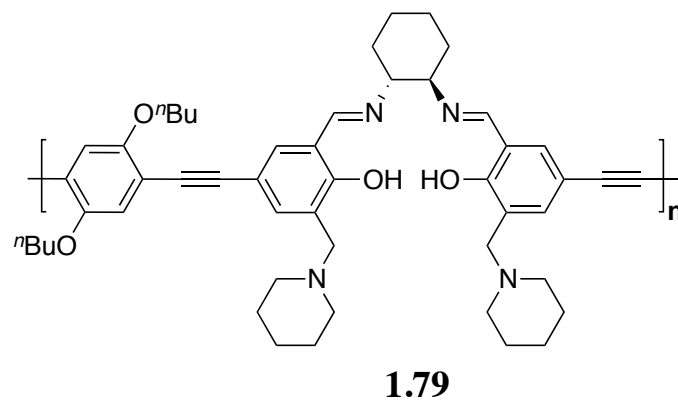
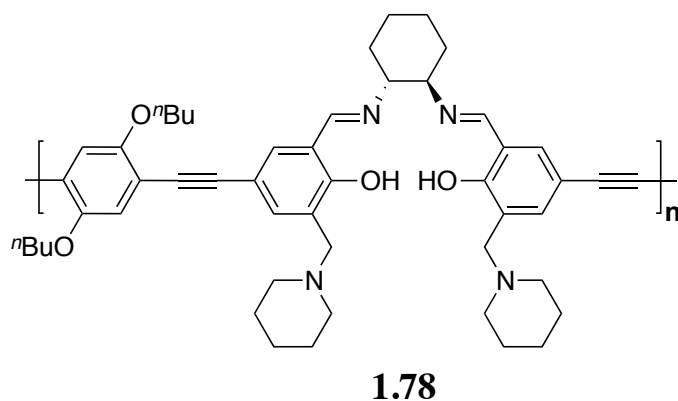


Figure 1.22. Chiral salen-based enantioselective polymer sensors **1.78** and **1.79**.

In contrast, titration of either enantiomer of **1.31** to sensor **1.79** led to quenching of the fluorescence of the salen-based polymer. The fluorescence was further quenched for (*S*)-**1.31** than for its (*R*)-enantiomer. This observation is attributed to the flexible and twisted structure of the polymer backbone. In this structure, the hydrogen bonds are thought to be disordered. When the guest binds a channel is created to allow the excited

state to decay through relaxation. The initial excitation migrates along the isoenergetic sites on the conjugated system, activating a nonradiative pathway of decay. Thus, binding of the guest to this receptor is unable to produce a fluorescent sensor capable of enantioselective recognition.

The previous examples present a variety of fluorescent sensors that are able to enantioselectively sense chiral α -hydroxy carboxylic acids. In each case, preferential binding was observed for one of the enantiomers. This binding caused an enhancement of the characteristic fluorescence signal, and the enantioselective fluorescence enhancement was calculated. These systems, however, lack general application across all carboxylic acids. The presence of the hydroxide group on the stereocenter served to strengthen the interaction with the receptor, since these receptors have been designed to maximize hydrogen bonding. Several of these groups did control studies and determined that the hydroxide group in the α -position was necessary, since reaction at this position to create an ether led to either an enhancement of fluorescence that was not enantioselective or a diminished fluorescence enhancement. Within the class of α -hydroxy carboxylic acids, the majority of the studies were geared towards mandelic acid **1.31**. Only a few of the studies attempted enantioselective recognition with additional guests, such as hexahydromandelic acid **1.71** and lactic acid **1.74**, whose fluorescence enhancement was markedly less than **1.31**. There have been a few reports of receptors that are able to branch further than α -hydroxy carboxylic acids, and those reports will now be presented.

The Wolf group published the first report of enantioselective fluorescence sensing of chiral carboxylic acids without a hydroxide at the α -position.⁸⁵ To accomplish this goal, a highly congested 1,8-diacridylnaphthalene receptor **1.80** was synthesized (**Figure 1.23**). This atropisomeric receptor possesses C_2 -symmetry, and no racemization of this species is observed even at high temperatures. The enantiomers can be resolved by

HPLC, and possess a reasonable fluorescence quantum yield of 0.17. When (+)-**1.80** was titrated with each enantiomer of camphanic acid **1.81**, the fluorescence emission at 550 nm decreased in an enantioselective fashion. The signal is quenched further for (*R*)-**1.81** than for the (*S*)- enantiomer, leading to an enantioselectivity of 4.5 for this guest. Analysis was performed to determine the binding stoichiometry, and it was found to vary based on the structure of the guest. For example, guest **1.81** required two equivalents to saturate the fluorescence signal, but 2-chloropropionic acid **1.82** required only one equivalent of guest.

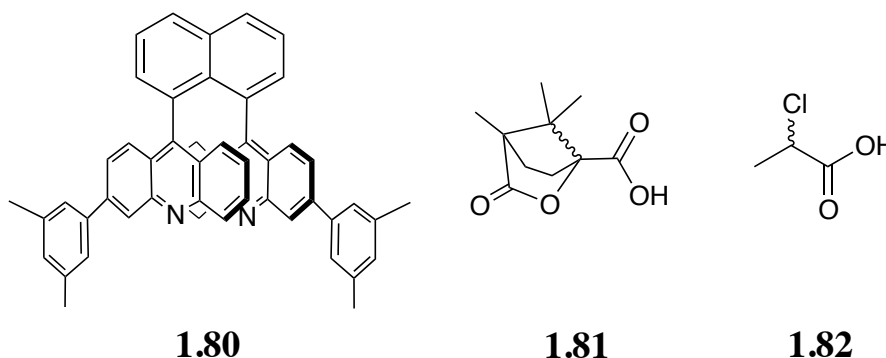


Figure 1.23. 1,8-Diacridylnaphthalene sensor **1.80** used for enantioselective fluorescence sensing of guests such as **1.81** and **1.82**.

The authors believe that the fluorescence quenching observed upon addition of the carboxylic acid guests is caused by static quenching. This static quenching is a result of nonradiative relaxation of the diastereomeric species. The binding of the guests to the sensor is likely a result of a proton being shared between the carboxylate and the acridinium nitrogen, however the authors weren't certain the exact position of this proton. In order to test the accuracy of this method, a set of samples with varying *ee* values were prepared and evaluated. The samples varied in *ee* from 70% (*S*), to 92.5% (*R*), and the

fluorescence of the unknowns were related to the *ee* through calibration curves. Three replicates were tested, and the unknown samples were determined within $\pm 3\%$ of the actual *ee* values.

The Wolf group further refined the structure of the 1,8-diacridylnaphthalene, replacing the 3,5-dimethylphenyl group with a *tert*-butyl (**Figure 1.24A**).⁸⁶ The newly synthesized host **1.83** is expected to show the same rigid structure with steric hinderance, that does have a large amount of flexibility in a single dimension. The flexibility of this molecule is a rocking motion between the two acridyl groups attached to the naphthalene segment, leading to enantiomers shown in **Figure 1.24B**. The same enantioselective fluorescence quenching seen for **1.79** was observed for this receptor, with (+)-**1.83** being further quenched with the (*R*)-enantiomer of the guests.

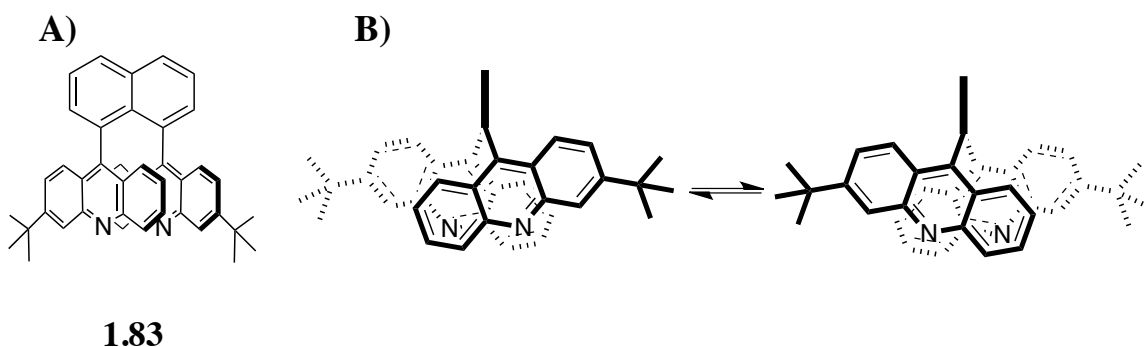


Figure 1.24. A) Chemical structure of new 1,8-diacridylnaphthalene host **1.83**. B) One-dimensional flexibility that is possessed by this host.

The main difference with this second contribution was the focus that was given to determining the concentration of the guest, as well as the *ee* of the sample. In order to measure the concentration, host (\pm)-**1.83** was applied. The quenching of the fluorescence in this system is a function of guest concentration, as no enantioselectivity should be

observed for the racemate. Thus, a calibration curve can be created to relate the fluorescence of this racemate to the guest concentration. Analysis was undertaken for guest **1.82**, and the concentration was determined within $\pm 3\%$ error. The *ee* analysis was performed in the same fashion as with sensor (+)-**1.83**, and this value was also determined within $\pm 3\%$ error. This work has shown that concentration and *ee* can be determined with high accuracy for samples covering a range of concentrations and *ee* values. This system is, however, a “turn off” system. This type of response is less sensitive, since it is easier to see a small change in the absence of fluorescence, than a small change amongst a very large signal.

The Tanaka group reported the calixarene-like salen macrocycle **1.40** as a ¹H NMR chiral shift reagent to determine the *ee* and absolute configuration of a variety of carboxylic acid derivatives.⁴⁸ This reagent was tested for enantioselective fluorescence recognition of guest **1.31**, but unfortunately did not work as a luminescence sensor. In order to promote conjugation, and thus enhance the fluorescence signal, new salen macrocycles **1.84-1.87** were synthesized (**Figure 1.25**).⁸⁷ Titration of host **1.84** with either enantiomer of **1.31** led to an enantioselective fluorescence enhancement, with the indicated enantiomer of host **1.84** enhanced twice as much by (*S*)-**1.31** than the enhancement seen for (*R*)-**1.31**. The largest enantioselective enhancement was observed with this host, likely due both to its electronic properties and the increased steric bulk. This strategy was applied to additional simple carboxylic acids, and an enantioselective enhancement was observed. The extent of the enantioselectivity for additional guests was significantly diminished, but the process was enantioselective nonetheless.

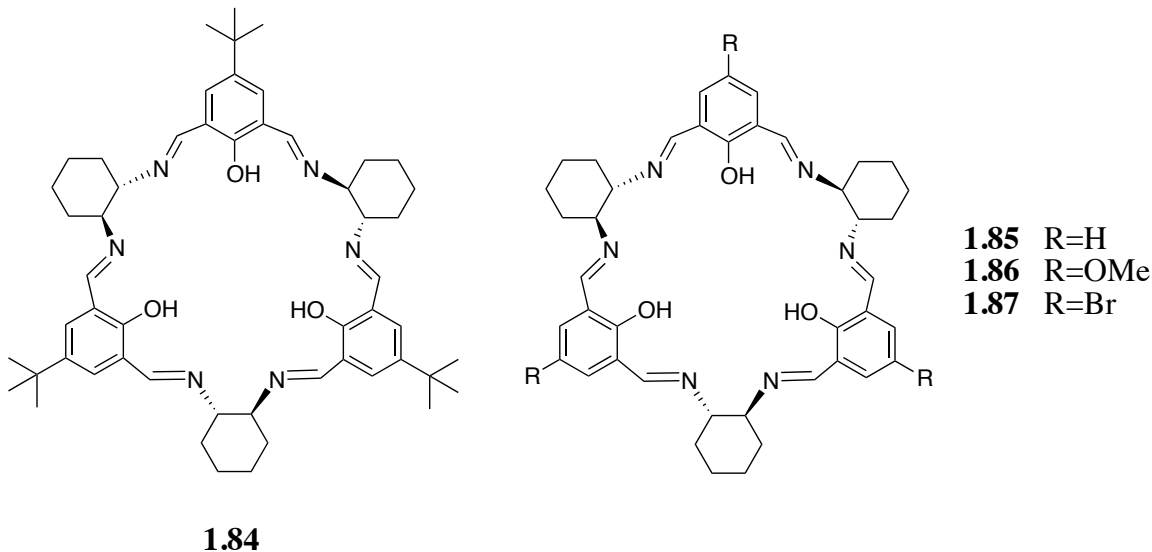


Figure 1.25. Chemical structures of macrocyclic structures **1.84-1.87**.

In a disparate approach to create enantioselective fluorescence sensors for chiral carboxylic acids, Zheng *et al* explored the use of aggregation-induced emission.⁸⁸ While most fluorophores are quenched in the solid state, the class of molecules known as aggregation-induced emission fluorophores form highly fluorescent solid precipitates or suspensions that show intense signals in the emission spectrum.⁸⁹ One such fluorophore is based on a chiral α -aromatic cinnamyl nitrile derivative, denoted as **1.88** in **Figure 1.26**. The (*R,R*)-host by itself showed no fluorescence behavior, but was observed to form a highly emissive solid complex that formed when (*S*)-**1.41** was added. In contrast, no change in the solution appearance or fluorescence emission was found when (*R*)-**1.41** was introduced to the sensor. The fluorescence enhancement found for (*S*)-**1.41** was 16,865 times greater than the enhancement of (*R*)-**1.41**. This trend was generally observed for a variety of both mono- and dicarboxylic acids. The sensor was even able to discriminate **1.61**, with the stereocenter located several bonds away from the carboxylic acid portion. Equal and opposite trends were observed when the (*S,S*)- enantiomer of the

was used, proving cross-reactivity of the host. Thus, the difference in the fluorescence enhancement was determined to be a result of the chirality of the sensor.

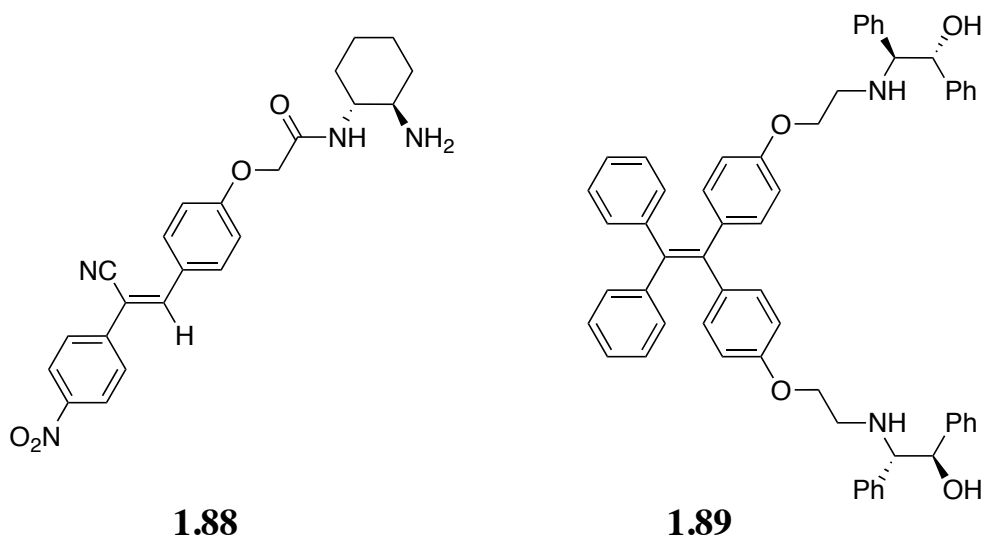


Figure 1.26. Aggregation-induced emission hosts **1.88** and **1.89** that form highly fluorescent precipitates or suspensions with a single enantiomer of a chiral carboxylic acid guest.

The authors next set out to understand the selectivity of (*R,R*)-**1.88** that was observed for (*S*)-**1.31**. To this end, FE-SEM images were taken of the solutions containing the host with each enantiomer of the guest. The precipitates collected for (*S*)-**1.31** were determined to be nanofibers, while addition of (*R*)-**1.31** resulted no such formation. Additional 2D NOESY spectra were recorded for these interactions. Intermolecular signals observed between phenyl protons of the carboxylic acid and the phenoxy group of the host were strong, meaning these groups are close in proximity. This places the carboxylic acid group close to the amine group, with the position of the hydroxyl group determining the amount of hinderance. No NOE is observed for the methine proton of (*R*)-**1.31** with the phenyl protons of the receptor, while (*S*)-**1.31** shows

a strong NOE at this position. This is expected for enantiomeric complexes, but indicates that more steric hinderance is observed for the interaction found for (*R*)-**1.31**. These factors come together to create a host molecule that is capable of very sensitive enantioselective fluorescence enhancement.

1.3.2. Ultraviolet/Visible Spectroscopy

In addition to optical sensors based on fluorescence, several recent efforts have reported the use of ultraviolet or visible light for enantioselective recognition of chiral carboxylic acids. Using these colorimetric sensors has several advantages over their fluorescence counterparts. First of all, sensors that absorb in the visible portion of the electromagnetic spectrum can change colors to signal binding. The human eye is very sensitive to small changes in this portion of the spectrum, thus allowing easy naked eye detection. Further, there are several factors that complicate fluorescence analysis. A fluorophore can be negatively affected by quantum yield and fluorescence lifetime, rendering certain fluorescent molecules useless to analysis. Also, the commonly observed autofluorescence, light scattering, and interferences from electrical sources are avoided by using chromophores that absorb in the UV/vis portion of the spectrum. Some of the pioneering work in this area was reported by Kubo and coworkers.⁹⁰

In order to create a colorimetric detection system, the Kubo group designed and synthesized chiral calix[4]crown hosts **1.90** and **1.91**. These hosts contain two indophenol chromophores and an enantiopure (*S,S*)-BINOL moiety, and differ only in the length of the crown ether tethering unit (**Figure 1.27**). The host (**1.90**) by itself was dissolved in ethanol, and the red solution had an absorbance at 515 nm. When (*R*)-**1.92** was added to the host, a significant shift was seen in the visible portion of the spectrum. This change was visible to the naked eye, with the solution changing from a red color to a

much more purple hue. When the opposite (*R*)-**1.92** enantiomer was added to the host, there was virtually no change in the UV/vis spectrum, and the solution retained the same red color it previously had. This system is built on a conformational change resulting from a proton transfer upon recognition. This change causes the spectra of the two chromophores attached to the binding cavity to change. This report served as a base upon which further advances in colorimetric sensing could be built.

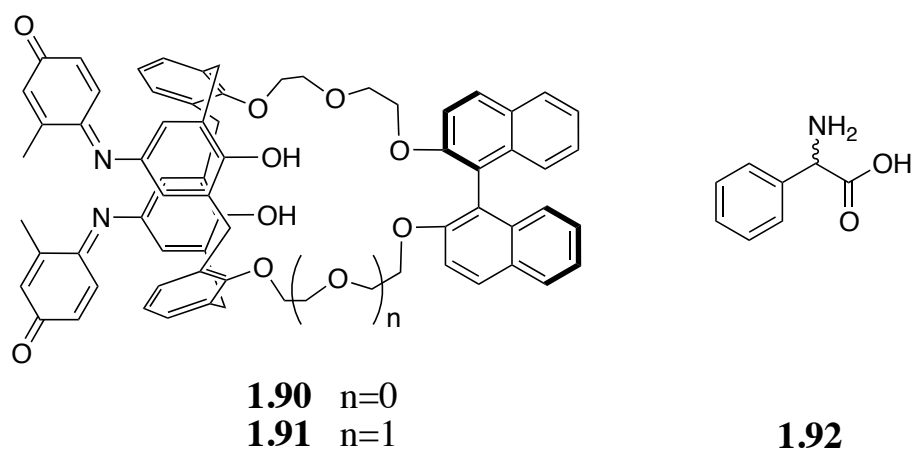


Figure 1.27. Chemical structures of calix[4]crown hosts **1.89** and **1.90**, used for colorimetric enantioselective recognition of phenylglycine species **1.91**.

He *et al* made some iterations to the calixarene receptor reported by Kubo, and applied it to the enantioselective sensing of both guests **1.92** and **1.31**.⁹¹ These hosts, shown in **Figure 1.28**, make use of thiourea moieties as binding sites. This group was chosen for binding because it is known to interact strongly with carboxylate anions.⁹² Closely located in space near these groups were two *para*-nitroanisole chromophores, and L-amino acid groups to impart chirality on the host. The host has an absorbance at 359 nm in the absence of exogenous guest, likely the result of intramolecular charge transfer. When (*S*)-**1.92** was added to the host, the absorbance at 359 nm gradually decreased and

shifted bathochromically. At the same time, a new peak at 481 nm grew in that represents the host:guest complex. Additionally, the clear solution became yellow upon this addition. Similar observations were made for (*S*)-**1.92** addition, but the new peak that grew in had a markedly greater absorbance than the same peak for (*R*)-**1.92**.

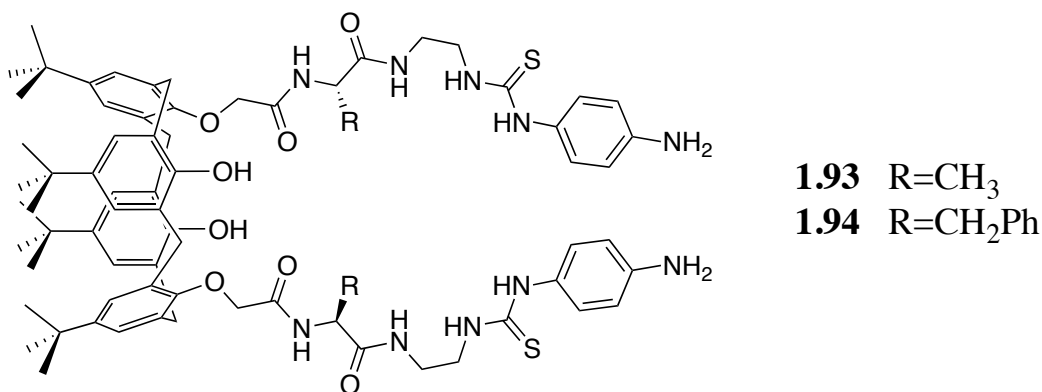
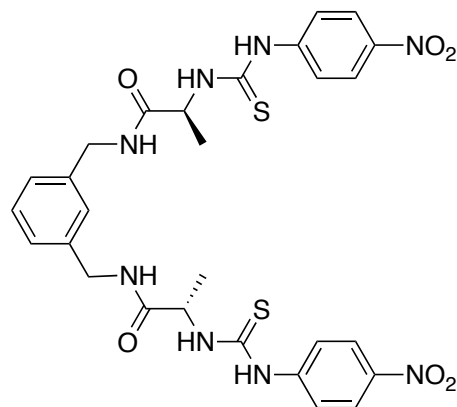


Figure 1.28. Chiral calixarene sensors **1.93** and **1.94**.

The new peak is characteristic of a charge transfer to the electron poor *para*-nitroaniline group from the electron rich thiourea fragment. The binding of the guests take place through hydrogen bonding, which is more favorable for (*S*)-**1.92**. The binding constants were calculated for **1.93** with each enantiomer of **1.92**, and the ratio of these constants was 2.84. The same trend was observed for this guest with the other host **1.94**, but the enantioselectivity was lower. This system was then expanded to guest **1.31**, with the homochiral (*S*)-**1.31** guest exhibiting a stronger binding constant. These binding constants were weaker than **1.92** by two orders of magnitude, but had comparable ratios for enantioselectivity.

Calixarenes have some limitations to their broad application as hosts for molecular recognition. The synthesis of these compounds can be rather challenging,

often producing a mixture of cyclic and linear forms. The distribution of these species can also be difficult to control, resulting in low yielding processes. Additionally, these species can be difficult to solubilize in aqueous solvents. This solubility issue can make these species hard to handle, and prone to higher observed errors. For these reasons, it is desirable to expand this colorimetric enantioselective sensing to a different scaffold. This was accomplished by the He group, who built a sensor **1.95** around a phenyl ring core.⁹³ This sensor had two arms containing the thiourea binding site, L-alanine for enantiodiscrimination, and a *para*-nitroaniline chromophore. The arms were appended to the phenyl ring in the *meta*- position, in order to orient these groups towards each other. The host alone shows a UV absorption maximum at 356 nm, a result of intramolecular charge transfer. This peak gradually decreased with formation of a peak a host:guest complex peak at 470 nm when (*R*)-**1.31** was added. Studies revealed that the formation of this complex proceeds in a 1:1 fashion. Additionally, the color of the solution changed from clear to an orange/red color with the addition. This is consistent with the wavelength of absorbance for the new peak.



1.95

Figure 1.29. Host structure used for colorimetric enantioselective discrimination of **1.31**.

Addition of (*S*)-**1.31** caused similar results, albeit to a lesser extent than for the opposite enantiomer. This solution began as colorless, and addition of the guest caused it to turn a golden yellow color. Association constants measured for this interaction were calculated by iterative data fitting of the change in absorbance at 470 nm in a non-linear fashion. Comparing the association constants for (*R*)-**1.31** and (*S*)-**1.31** gave to a ratio of 4.2. The difference in the UV/visible signals, in addition to the visible difference in solution color, help to further validate the use of this sensor for colorimetric *ee* determination of carboxylic acid guests.

Yoon and Hyun reported a colorimetric sensor **1.96**, consisting of thiourea binding sites, an azophenol chromophore, and chiral glycopyranosyl enantioselective recognition groups, that functions as a chiral carboxylate anion sensor.⁹⁴ This sensor, shown in **Figure 1.30**, was applied to three simple carboxylic acids: **1.43**, **1.44**, and **1.97**. Upon addition of carboxylates a large bathochromic shift of around 145 nm was observed, shifting the absorption from 370 nm to a new location of 515 nm. The host by

itself had a very faint yellow/orange color, and addition of the guest gave rise to a visible color change to create a deep red/pink solution. It is believed that the anions cause deprotonation of the phenolic proton, leading to a photoinduced charge transfer.⁹⁵ The binding was determined to occur with 1:1 stoichiometry. The complex formed between host **1.96** and (*S*)-enantiomer of each acid studied gave rise to a larger absorbance at 515 nm than the (*R*)-enantiomer, and subsequently larger binding constants. Enantioselective ratios were calculated for these acids, and averaged 2.04 across the board.

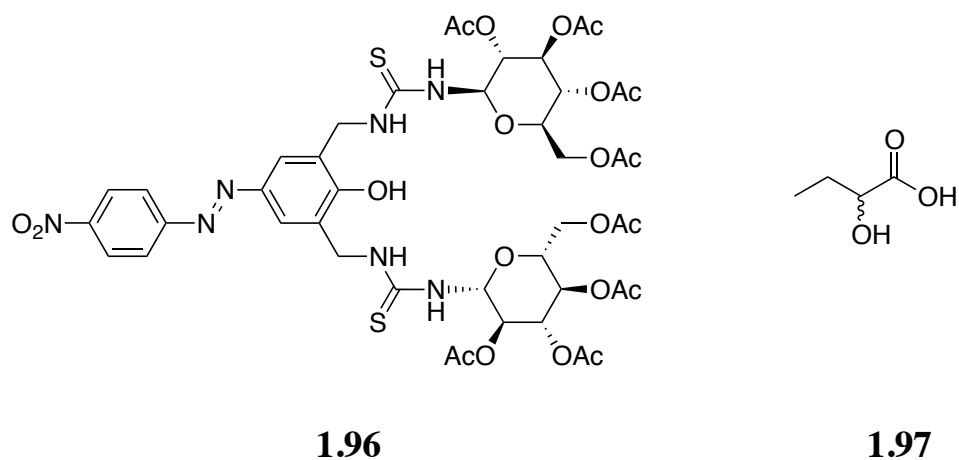


Figure 1.30. Colorimetric host **1.96**, used for enantioselective sensing of chiral carboxylic acids such as **1.97**.

Griesbeck *et al* recently developed a modular receptor-chromophore **1.97** to observe enantioselective recognition of chiral carboxylate anions.⁹⁶ This system is based on a conjugate of phthalimide-thiourea, the structure of which is shown in **Figure 1.31A**. The host is synthesized with (*S*)-methylbenzylamine, which is able to impart enantioselectivity to the assay. Addition of achiral acetate anion to the receptor caused the absorbance at 350 nm to increase, and shift to slightly longer wavelengths. This 20 nm shift in absorbance indicates that a change occurs for the ground state of the sensor,

though likely not full deprotonation of the thiourea. To confirm this prediction, protic solvents were added to the mix. The change that was seen reverted to the original spectrum, meaning that deprotonation of the receptor is highly unlikely. The proposed binding interaction is shown in **Figure 1.31B**. The change in absorbance of receptor **1.98** was found to be the greatest for (*S*)-**1.74**, increasing to a greater extent than the spectrum recorded for (*R*)-**1.74**. This difference was the largest when the smallest amount of guest had been added. When considering the ratio of equilibrium constants, (*S*)-**1.74** is preferred by a factor of 1.93.

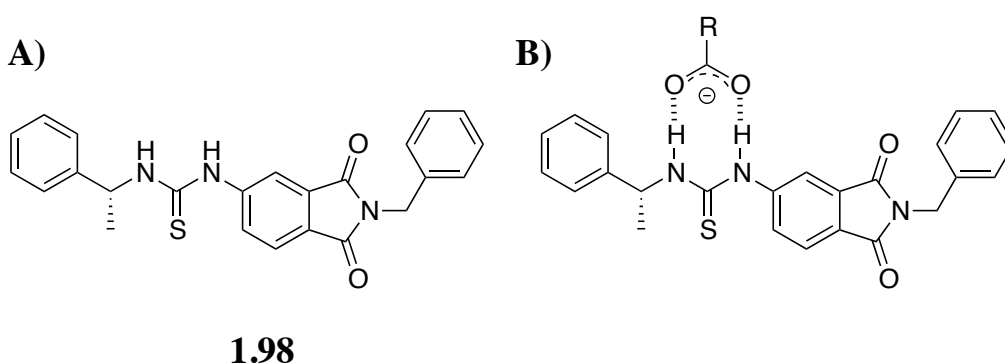


Figure 1.31. A) Chemical structure of chiral host **1.98**. B) Proposed binding mode for the carboxylate anion and the electron rich thiourea receptor.

1.4. CONCLUDING REMARKS

The task of creating assays for the determination of *ee* of chiral substrates is a very challenging endeavor. These species have the same chemical properties, and thus are indistinguishable in an achiral medium. The focus of the work presented above was creating chiral systems for the discrimination of carboxylic acid analytes, and then turning a molecular recognition event into an enantiospecific signal. The first part relied on the magnetic inequivalence of diastereomeric groups, spanning a range of different

nuclei. The examples presented showed the evolution of the process of enantioselective NMR spectrometry, honing the scaffolds and creating vastly different chemical shifts for the signals of the characteristic peaks. The next set of examples presented were based around optical spectroscopy. Fluorescence is an inherently sensitive luminescent technique, and has been applied to the differentiation of a variety of carboxylic acids. Much of the groundwork has been focused on assays for α -hydroxy carboxylic acids, which limits the application of these systems to other carboxylic acids. This work, however, has paved the way for improvements that will accommodate a larger scope of guest tolerability. Many improvements in this area are envisioned in the future, with the ability to create real-time monitoring of enantiomeric composition. Few examples are available that detail UV/vis sensors for chiral carboxylic acids. This area is relatively new, but holds immense promise. The sensitivity of vision to even the slightest change in colors makes this a very attractive area of research. The synergy of these three alternate strategies will continue to push the envelope in enantioselective sensing, creating increasingly more accurate means to assess enantiomeric purity.

1.5. REFERENCES FOR CHAPTER 1

- (1) Lin, G.-Q.; You, Q.-D.; Cheng, J.-F. *Chiral drugs : chemistry and biological action*; Wiley: Hoboken, N.J., 2011.
- (2) Erb, S. *Pharmaceut. Technol.* **2006**, *30*, 14.
- (3) FDA Address. *Chirality* **1992**, *4*, 338.
- (4) a) Blaschke, G.; Kraft, H. P.; Fickentscher, K.; Kohler, F. *Arzneimittel-Forsch* **1979**, *29-2*, 1640. b) Teo, S. K.; Colburn, W. A.; Tracewell, W. G.; Kook, K. A.; Stirling, D. I.; Jaworsky, M. S.; Scheffler, M. A.; Thomas, S. D.; Laskin, O. L. *Clin. Pharmacokinet.* **2004**, *43*, 311.

- (5) Lin, G.-Q.; Li, Y.-M.; Chan, A. S.-C. *Principles and applications of asymmetric synthesis*; John Wiley & Sons: New York, 2001.
- (6) Christmann, M.; Bräse, S. *Asymmetric synthesis : the essentials*; Wiley-VCH: Weinheim, 2007.
- (7) de Vries, J. G.; Lefort, L. *Chemistry – A European Journal* **2006**, *12*, 4722.
- (8) Lohray, B. B. *Curr. Sci.* **2001**, *81*, 1519.
- (9) Traverse, J. F.; Snapper, M. L. *Drug Discov Today* **2002**, *7*, 1002.
- (10) Shimizu, K. D.; Snapper, M. L.; Hoveyda, A. H. *Chem-Eur J* **1998**, *4*, 1885.
- (11) Reetz, M. T. *Angew Chem Int Edit* **2001**, *40*, 284.
- (12) Pescarmona, P. P.; van der Waal, J. C.; Maxwell, I. E.; Maschmeyer, T. *Catal Lett* **1999**, *63*, 1.
- (13) Kuntz, K. W.; Snapper, M. L.; Hoveyda, A. H. *Curr Opin Chem Biol* **1999**, *3*, 313.
- (14) Terrett, N. K.; Gardner, M.; Gordon, D. W.; Kobylecki, R. J.; Steele, J. *Tetrahedron* **1995**, *51*, 8135.
- (15) Nicolaou, K. C.; Sorensen, E. J. *Classics in total synthesis : targets, strategies, methods*; VCH: Weinheim ; New York, 1996.
- (16) Nicolaou, K. C.; Snyder, A. *Classics in Total Synthesis II: Targets, Strategies, Methods*; John Wiley & Sons, 2003.
- (17) Maruoka, K.; Ooi, T. *Chem Rev* **2003**, *103*, 3013.
- (18) Groger, H. *Chem Rev* **2003**, *103*, 2795.
- (19) Gubitz, G. *Chromatographia* **1990**, *30*, 555.
- (20) Subramanian, G. *Chiral separation techniques : a practical approach*; 2nd completely rev. and updated ed.; Wiley-VCH: Weinheim ; New York, 2001.
- (21) Schurig, V. *J Chromatogr A* **2001**, *906*, 275.
- (22) Bressolle, F.; Audran, M.; Pham, T. N.; Vallon, J. J. *J Chromatogr B Biomed Appl* **1996**, *687*, 303.
- (23) Ward, T. J.; Farris, A. B., 3rd *J Chromatogr A* **2001**, *906*, 73.
- (24) Yashima, E. *J Chromatogr A* **2001**, *906*, 105.

- (25) Sogah, G. D. Y.; Cram, D. J. *J Am Chem Soc* **1979**, *101*, 3035.
- (26) Haginaka, J. *Journal of Chromatography A* **2001**, *906*, 253.
- (27) Gübitz, G.; Schmid, M. G. *Chiral separations : methods and protocols*; Humana Press: Totowa, N.J., 2004.
- (28) Sajonz, P.; Gong, X.; Leonard, W. R., Jr.; Biba, M.; Welch, C. J. *Chirality* **2006**, *18*, 803.
- (29) Sajonz, P.; Schafer, W.; Gong, X.; Shultz, S.; Rosner, T.; Welch, C. J. *J Chromatogr A* **2007**, *1145*, 149.
- (30) Mateos, J. L.; Cram, D. J. *J Am Chem Soc* **1959**, *81*, 2756.
- (31) Raban, M.; Mislow, K. *Tetrahedron Lett* **1965**, 4249.
- (32) Wenzel, T. J. *Discrimination of chiral compounds using NMR spectroscopy*; Wiley-Interscience: Hoboken, N.J., 2007.
- (33) Demunari, S.; Marazzi, G.; Forgione, A.; Longo, A.; Lombardi, P. *Tetrahedron Lett* **1980**, *21*, 2273.
- (34) Carballeira, N. M.; Colon, R. *Tetrahedron-Asymmetr* **1999**, *10*, 3785.
- (35) Carballeira, N. M.; Colon, R.; Emiliano, A. *J Nat Prod* **1998**, *61*, 675.
- (36) Yabuuchi, T.; Kusumi, T. *J Org Chem* **2000**, *65*, 397.
- (37) Nagai, Y.; Kusumi, T. *Tetrahedron Lett* **1995**, *36*, 1853.
- (38) Ferreiro, M. J.; Latypov, S. K.; Quinoa, E.; Riguera, R. *J Org Chem* **2000**, *65*, 2658.
- (39) Parker, D. *J Chem Soc Perk T 2* **1983**, 83.
- (40) Fulwood, R.; Parker, D. *Tetrahedron-Asymmetr* **1992**, *3*, 25.
- (41) Ma, F. N.; Ai, L.; Shen, X. M.; Zhang, C. *Org Lett* **2007**, *9*, 125.
- (42) Wang, W.; Ma, F.; Shen, X.; Zhang, C. *Tetrahedron: Asymmetry* **2007**, *18*, 832.
- (43) Ema, T.; Tanida, D.; Sakai, T. *Org Lett* **2006**, *8*, 3773.
- (44) Chang, S. K.; Vanengen, D.; Fan, E.; Hamilton, A. D. *J Am Chem Soc* **1991**, *113*, 7640.
- (45) Demirtas, H. N.; Bozkurt, S.; Durmaz, M.; Yilmaz, M.; Sirit, A. *Tetrahedron-Asymmetr* **2008**, *19*, 2020.

- (46) Ikeda, A.; Shinkai, S. *Chem Rev* **1997**, *97*, 1713.
- (47) Asfari, Z. *Calixarenes 2001*; Kluwer Academic Publishers: Dordrecht ; Boston, 2001.
- (48) Tanaka, K.; Fukuda, N. *Tetrahedron-Asymmetr* **2009**, *20*, 111.
- (49) Dolbier, W. R.; Editor *Guide to Fluorine NMR for Organic Chemists*; John Wiley & Sons, Inc., 2009.
- (50) Wang, Y.; Mosher, H. S. *Tetrahedron Lett* **1991**, *32*, 987.
- (51) Pirkle, W. H.; Hauske, J. R. *The Journal of Organic Chemistry* **1977**, *42*, 2436.
- (52) Brown, E.; Chevalier, C.; Huet, F. o.; Le Grumelec, C.; L $\sqrt{\text{C}}\text{Z}\sqrt{\text{C}}$, A.; Touet, J. I. *Tetrahedron: Asymmetry* **1994**, *5*, 1191.
- (53) Gorenstein, D. G. *Prog Nucl Mag Res Sp* **1983**, *16*, 1.
- (54) Dreher, S. D.; Katz, T. J.; Lam, K. C.; Rheingold, A. L. *J Org Chem* **2000**, *65*, 815.
- (55) Weix, D. J.; Dreher, S. D.; Katz, T. J. *J Am Chem Soc* **2000**, *122*, 10027.
- (56) Wang, D. Z. G.; Katz, T. J. *J Org Chem* **2005**, *70*, 8497.
- (57) Alexakis, A.; Chauvin, A. S. *Tetrahedron-Asymmetr* **2000**, *11*, 4245.
- (58) Seebach, D.; Beck, A. K. *Chimia* **1997**, *51*, 293.
- (59) Knobel, A. K. H.; Escher, I. H.; Pfaltz, A. *Synlett* **1997**, 1429.
- (60) Alexakis, A.; Chauvin, A. S. *Tetrahedron-Asymmetr* **2001**, *12*, 1411.
- (61) Klapötke, T. M.; Broschag, M. *Compilation of reported ^{77}Se NMR chemical shifts : up to the year 1994*; Wiley: Chichester ; New York, 1996.
- (62) Luthra, N. P.; Dunlap, R. B.; Odom, J. D. *J Magn Reson* **1982**, *46*, 152.
- (63) Poleschner, H.; Radeaglia, R.; Meyer, H. *Org Magn Resonance* **1984**, *22*, 480.
- (64) Rabenstein, D. L.; Tan, K. S. *Magn Reson Chem* **1988**, *26*, 1079.
- (65) Patai, S.; Rappoport, Z.; Editors *The Chemistry of Organic Selenium and Tellurium Compounds, Vol. 1*; John Wiley and Sons, 1986.
- (66) Silks, L. A.; Dunlap, R. B.; Odom, J. D. *J Am Chem Soc* **1990**, *112*, 4979.
- (67) Silks, L. A.; Peng, J.; Odom, J. D.; Dunlap, R. B. *J Chem Soc Perk T 1* **1991**, 2495.

- (68) Silks, L. A.; Peng, J.; Odom, J. D.; Dunlap, R. B. *J Org Chem* **1991**, *56*, 6733.
- (69) Salvatore, B. A.; Smith, A. B. *Tetrahedron Lett* **1994**, *35*, 1329.
- (70) Wipf, P.; Miller, C. P. *Tetrahedron Lett* **1992**, *33*, 907.
- (71) Anderson, R. C.; Shapiro, M. J. *J Org Chem* **1984**, *49*, 1304.
- (72) Pu, L. *Chem Rev* **2004**, *104*, 1687.
- (73) James, T. D.; Sandanayake, K. R. A. S.; Shinkai, S. *J Chem Soc Chem Comm* **1994**, 477.
- (74) James, T. D.; Sandanayake, K. R. A. S.; Shinkai, S. *Angewandte Chemie-International Edition in English* **1994**, *33*, 2207.
- (75) Pu, L. *Chem Rev* **1998**, *98*, 2405.
- (76) James, T. D.; Sandanayake, K. R. A. S.; Shinkai, S. *Nature* **1995**, *374*, 345.
- (77) Bissell, R. A.; De Silva, A. P.; Gunaratne, H. Q. N.; Lynch, P. L. M.; Maguire, G. E. M.; Sandanayake, K. R. A. S. *Chem Soc Rev* **1992**, *21*, 187.
- (78) Bissell, R. A.; De Silva, A. P.; Gunaratne, H. Q. N.; Lynch, P. L. M.; Mccoy, C. P.; Maguire, G. E. M.; Sandanayake, K. R. A. S. *Fluorescent Chemosensors for Ion and Molecule Recognition* **1993**, 538, 45.
- (79) Coppola, G. M.; Schuster, H. F. *[Alpha]-hydroxy acids in enantioselective syntheses*; VCH: Weinheim, 1997.
- (80) Lin, J.; Zhang, H. C.; Pu, L. *Org Lett* **2002**, *4*, 3297.
- (81) Lin, J.; Rajaram, A. R.; Pu, L. *Tetrahedron* **2004**, *60*, 11277.
- (82) Chi, L.; Zhao, J.; James, T. D. *The Journal of Organic Chemistry* **2008**, *73*, 4684.
- (83) Dhara, K.; Sarkar, K.; Roy, P.; Nandi, M.; Bhaumik, A.; Banerjee, P. *Tetrahedron* **2008**, *64*, 3153.
- (84) Song, F.; Wei, G.; Wang, L.; Jiao, J.; Cheng, Y.; Zhu, C. *The Journal of Organic Chemistry* **2012**, *77*, 4759.
- (85) Mei, X.; Wolf, C. *J Am Chem Soc* **2004**, *126*, 14736.
- (86) Wolf, C.; Liu, S. L.; Reinhardt, B. C. *Chem Commun* **2006**, 4242.
- (87) Tanaka, K.; Tsuchitani, T.; Fukuda, N.; Masumoto, A.; Arakawa, R. *Tetrahedron-Asymmetr* **2012**, *23*, 205.

- (88) Li, D. M.; Zheng, Y. S. *Chem Commun* **2011**, 47, 10139.
- (89) Hong, Y.; Lam, J. W.; Tang, B. Z. *Chem Commun* **2009**, 4332.
- (90) Kubo, Y.; Maeda, S. y.; Tokita, S.; Kubo, M. *Nature (London)* **1996**, 382, 522.
- (91) Qing, G. Y.; He, Y. B.; Zhao, Y.; Hu, C. G.; Liu, S. Y.; Yang, X. *Eur J Org Chem* **2006**, 1574.
- (92) Choi, K.; Hamilton, A. D. *Angew Chem Int Edit* **2001**, 40, 3912.
- (93) Chen, Z. H.; He, Y. B.; Hu, C. G.; Huang, X. H.; Hu, L. *Aust J Chem* **2008**, 61, 310.
- (94) Choi, M. K.; Kim, H. N.; Choi, H. J.; Yoon, J.; Hyun, M. H. *Tetrahedron Lett* **2008**, 49, 4522.
- (95) Lee, D. H.; Lee, K. H.; Hong, J. I. *Org Lett* **2001**, 3, 5.
- (96) Griesbeck, A. G.; Hanft, S.; Miara, Y. D. *Photoch Photobio Sci* **2010**, 9, 1385.

Chapter 2: A Simple Method for the Determination of Enantiomeric Excess and Identity of Chiral Carboxylic Acids

2.1. INTRODUCTION

High-throughput screening is increasingly used as a technique to direct the discovery and optimization of asymmetric syntheses.¹⁻⁴ According to this methodology, several reactions are carried out simultaneously so that a target reaction can be quickly optimized. One of the ways this method is applied is in the discovery of chiral catalysts to carry out synthetic transformations. Catalysts are created from small building blocks, and the libraries can number from a few to thousands of entries.⁵⁻¹⁰ This optimization is directed not only toward maximizing the product yield, but also the enantiomeric excess (*ee*) if a chiral product is created. As presented in Chapter 1, products are typically analyzed through chromatographic techniques such as high performance liquid chromatography (HPLC), or gas chromatography (GC).

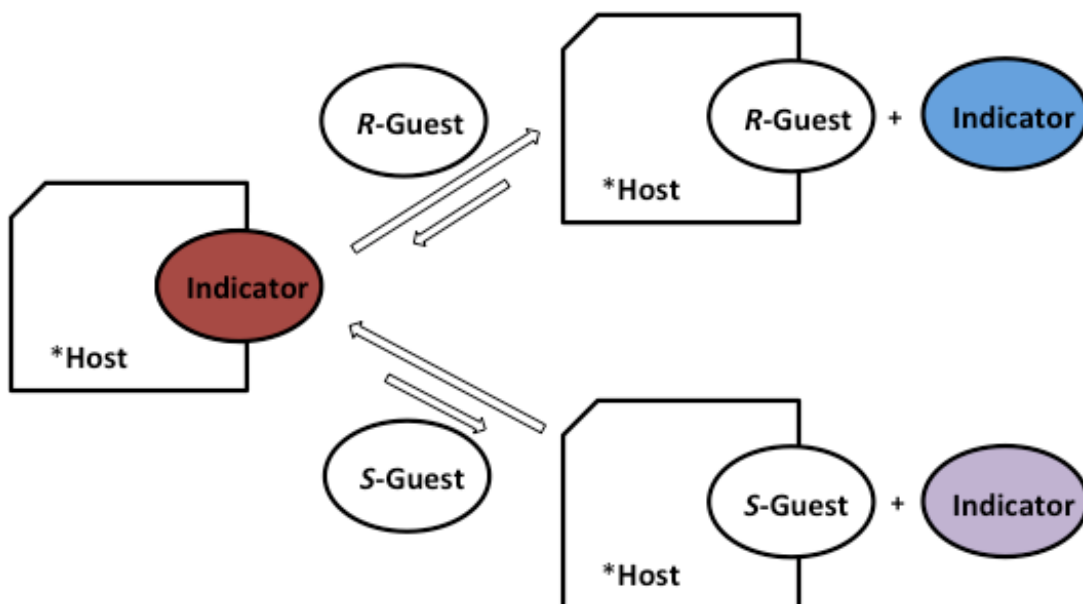
Both of these chromatographic methods are able to determine the *ee* of a chiral product very accurately, but high-throughput analysis of these chiral products using these techniques is time consuming and costly. Chromatography is inherently serial; HTS methods allow for the creation of thousands of samples very rapidly, but only one sample at a time can be analyzed using HPLC or GC. Further, sample analysis times are quite long. After conditions are optimized, it is possible to perform *ee* analysis in approximately ten minutes, meaning no more than 150 analyses can be run with a single instrument in a day.¹⁰ A bottleneck is sure to ensue if many more samples can be made in a day than can be analyzed.¹¹ Finally, this analysis method is costly in terms of solvents used and discarded, and hours spent on sample preparation. For these reasons, several research groups have turned toward optical sensing methods to rapidly assess *ee*.

Several groups have focused on developing assays to rapidly discern reaction success that rely on optical spectroscopy due to its speed of analysis. Optical spectroscopy, namely UV/Visible, fluorescence, or circular dichroism spectrometry, is attractive as an analysis method for several reasons: (1) it is a well-established technique that is operationally simple, (2) equipment is comparatively cheap, and (3) techniques can be interfaced with multi-well plate readers, allowing much more rapid parallel analysis to be achieved.

This chapter will detail efforts to create optical signaling protocols to enantioselectively sense chiral carboxylic acids. Chiral carboxylic acids, as mentioned in Chapter 1, are important substrates in both synthesis and drug discovery. The first approach applied to this problem, and discussed here, is enantioselective indicator displacement assay. Next, the transition from a UV/Visible assay to a circular dichroism approach will be detailed. Finally, the results obtained from this analysis will be outlined.

2.2. ENANTIOSELECTIVE INDICATOR DISPLACEMENT ASSAYS

The Anslyn group has pioneered the use of enantioselective indicator displacement assays (eIDAs) as a method of determining the *ee* of several types of chiral molecules.^{12,13} This competitive binding assay, shown in **Scheme 2.1**, is an extension of the indicator displacement assay (IDA) platform that the Anslyn group had used previously.¹⁴⁻¹⁷ The protocol relies on three main components: a chiral host molecule, an indicator, and an analyte. The host molecule interacts reversibly with the indicator, often a commercially available pH dye. The optical signal of the indicator must be different when it is free in solution than when it is bound to the host.

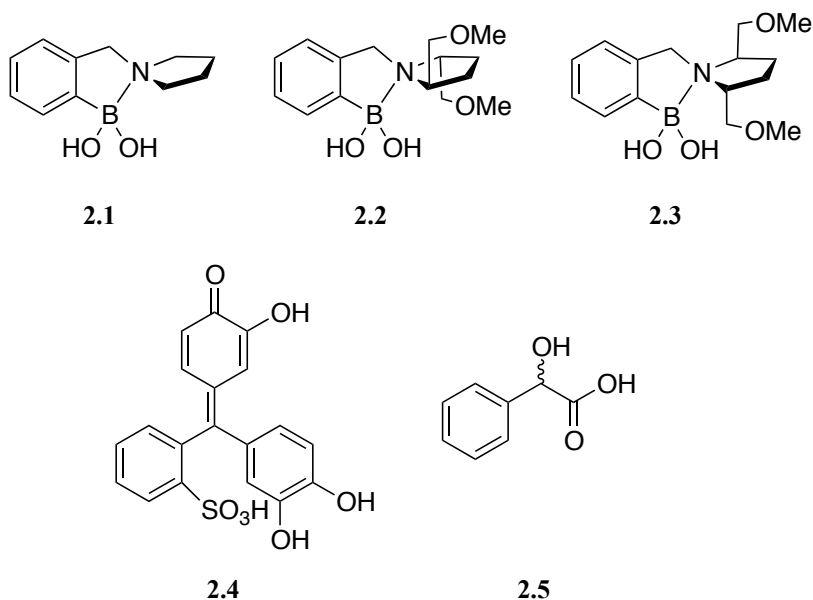


Scheme 2.1. Schematic representation of an eIDA between a chiral host and each enantiomer of a chiral guest. In this example, the preferred diastereomer is formed between the *R*-guest and the chiral host.

There are several advantages to using this equilibrium-based sensing ensemble. The traditional sensing approach relies on the synthesis of a host that contains both a binding site and a signaling mechanism. These syntheses are often not trivial, and require several steps and purifications, but it is not possible to predict the binding specificity or the signal modification before the host has been made. The use of an eIDA avoids these potential pitfalls; there is no requirement to synthetically attach the indicator to the host, since this portion is equilibrium controlled. Another benefit of using eIDAs is the ability to easily screen multiple indicators. The association between the indicator and the host is equilibrium based, avoiding the need to synthesize a new host containing the desired indicator. Finally, the analyses are performed in a solution of water and a miscible organic solvent. The binding of the host and guest can be tuned to a particular value by altering the composition of the solvent.

Introduction of a guest molecule causes competitive binding to occur; the guest competes with the indicator for binding to the host molecule. When the indicator is displaced, its optical signal will change, signaling the binding event between host and guest. When the chiral host associates with the chiral guest, the complexes that are formed are diastereomeric. These complexes have different energies and stabilities, and form to differing extents. This differential displacement will modulate the optical properties of the solution, thus allowing for the quantification of *ee*.

The first example of an eIDA made use of reversible covalent bond formation observed between boronic acids and α -hydroxycarboxylic acids or catechols in aqueous media.¹² The concentration of the desired guest was readily obtained using an IDA with achiral host **2.1** (**Scheme 2.2**). Pyrocatechol violet **2.4** was chosen as the indicator, as it contains a catechol moiety that is known to form reversible covalent bonds with boronic acid based receptors. The enantiomeric composition of the chiral substrate could be determined by incorporating chirality into the host structure, and thus chiral hosts **2.2** and **2.3** were synthesized. The complex that formed between either host **2.2** or **2.3** and indicator **2.4** was monitored by UV/Visible spectrometry, resulting in a new peak forming at λ_{max} at 520 nm. This peak was greatly shifted from absorbance of the pure indicator **2.4**, which had a λ_{max} at 425 nm.



Scheme 2.2. Chemical structures of components of the colorimetric eIDA to find the enantiomeric excess of phenylactic acid **2.5**.

The change in absorbance was monitored at 520 nm separately as a function of the amount of either D-**2.5** or L-**2.5** that had been added to the host:indicator complex. The absorbance value recorded was different for each enantiomer of the guest, with each exhibiting a unique UV absorbance. The indicator was more displaced from host **2.2** with the addition of L-**2.5** than it was when D-**2.5** was introduced. The difference in absorbance was observed to be as much as 0.27 absorbance units along the titration. The same experiment was performed with host **2.3**, and the indicator was more displaced with D-**2.5**. This displacement, while preferring binding with the opposite enantiomer, was of the same magnitude observed with enantiomeric host **2.2**. Thus, this receptor was deemed to be cross-reactive; the difference in absorbance is indeed a function of the chirality of the host. Equations were derived in order to relate the measured absorbances

to *ee* values, and were determined to be within $\pm 20\%$ error. This initial report helped to shape the use of eIDAs to determine *ee* values of unknown samples.

The previous example focused on reversible covalent bond formation between a boronic acid functionality and a vicinal diol moiety to create the complexes. This approach is one of many; other examples are based on coordination through electrostatic interactions¹⁸ or metal coordination.¹⁹⁻²³ Metal ions can readily form complexes with chiral ligands, subsequently forming a chiral host molecular assembly. Open coordination sites on the aforementioned metals can then interact reversibly with an indicator, allowing displacement of the indicator when a competitive guest is introduced. Numerous metal salts are commercially available, accessing a variety of oxidation states at the metal centers. This access allows for selection of a metal that possesses the desired properties for each individual assay. A few selected literature examples of eIDAs performed with metal-based hosts are detailed below.

2.2.1. eIDAs Performed With Metal-Based Hosts

The first example of an eIDA with a metal-based host was used to enantioselectively discriminate between hydrophobic α -amino acids in aqueous media.¹⁹ The host was designed around a Cu^{II} metal center. This metal is known to form five-membered ring complexes with amino acids,²⁴ making use of the facile exchange of ligands around the square planar metal center. Chirality was built into the host structure by complexation of a chiral ligand to the copper center. This ligand is based on a *trans*-diaminocyclohexane scaffold, where the diamine nitrogens were derivatized with bulky groups (**Figure 2.1a**). Binding of this complex to indicator **2.4** generated a blue complex, with a new peak in the visible spectrum occurring at a λ_{max} of 653 nm. Addition of an amino acid guest to the blue host:indicator complex caused displacement of the indicator

(**Figure 2.1b**), and regeneration of the yellow color characteristic of the indicator free in solution (λ_{max} of 502 nm).

Each enantiomer of valine caused a different degree of displacement, with (*S,S*)-**2.6** binding preferentially with D-amino acids. This difference was observed in the UV/Visible spectrum. Calibration curves were generated for three amino acids by recording the absorbance as a function of varying the *ee* for each enantiomer of the host complex (**Figure 2.1c**). The best-fit equation of the linear plot was then used to determine the *ee* values for a series of unknown samples, with an average error of $\pm 3\%$.

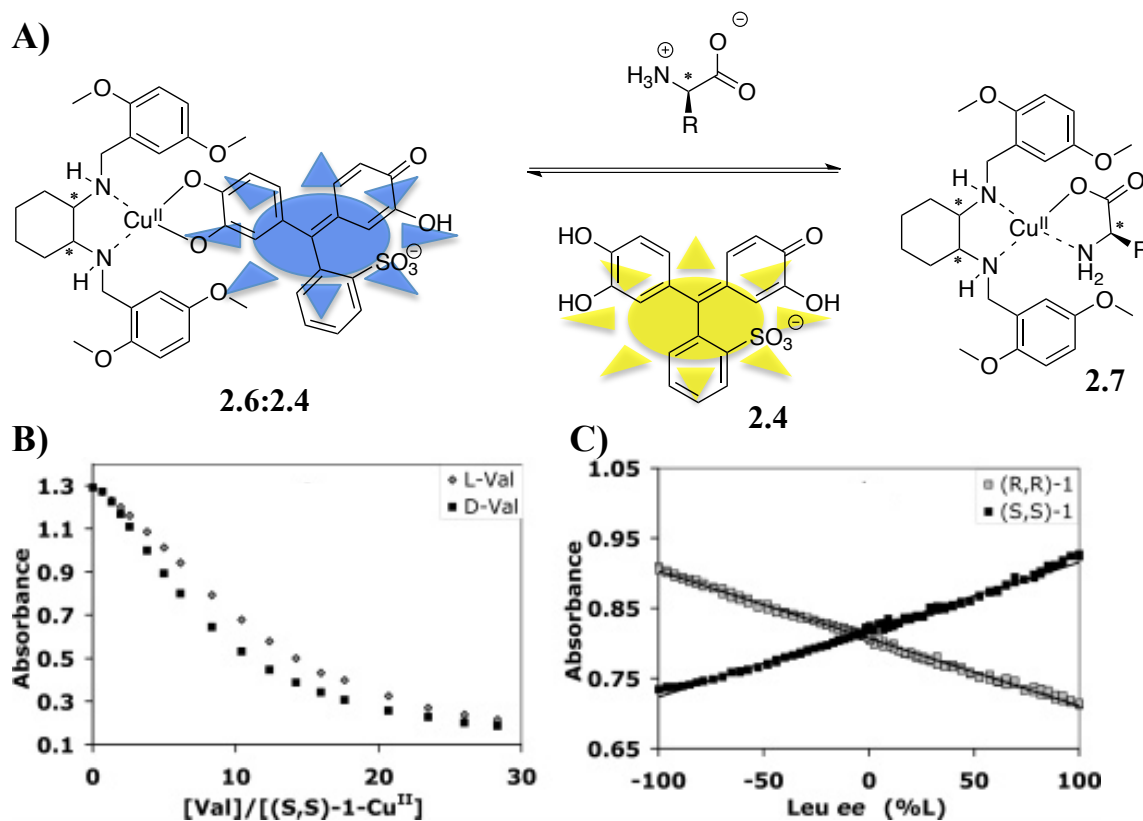
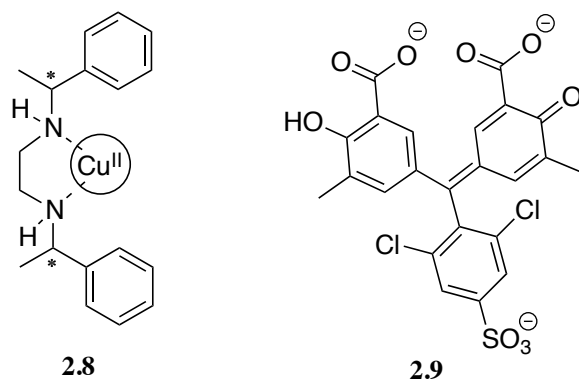


Figure 2.1. A) Displacement of indicator **2.4** from host complex **2.6** by addition of amino acid guests. B) Absorbance at 653 nm of complex **2.6** by addition of D- of L-valine. C) Absorbance as a function of *ee* for leucine with each enantiomer of the host.

Two different complexes formed from a diamine ligand and Cu^{II} center were used to expand the scope of the IDA to additional amino acid guests.²² The applied complexes were **2.6** from the previous study and the newly proposed **2.8** (**Scheme 2.3**). The indicator selected for this study was chrome azurol S **2.9**. This indicator in solution was yellow with a λ_{max} at 429 nm, while binding to the chiral metal complex gave rise to a new absorbance peak at λ_{max} at 602 nm. The drastic difference in absorption properties of this chiral scaffold allowed this complex to be applied as a chiral host for an eIDA. As in the previous eIDA, the (*R,R*)-enantiomer of the chiral hosts preferentially bound to the L-amino acid enantiomer.

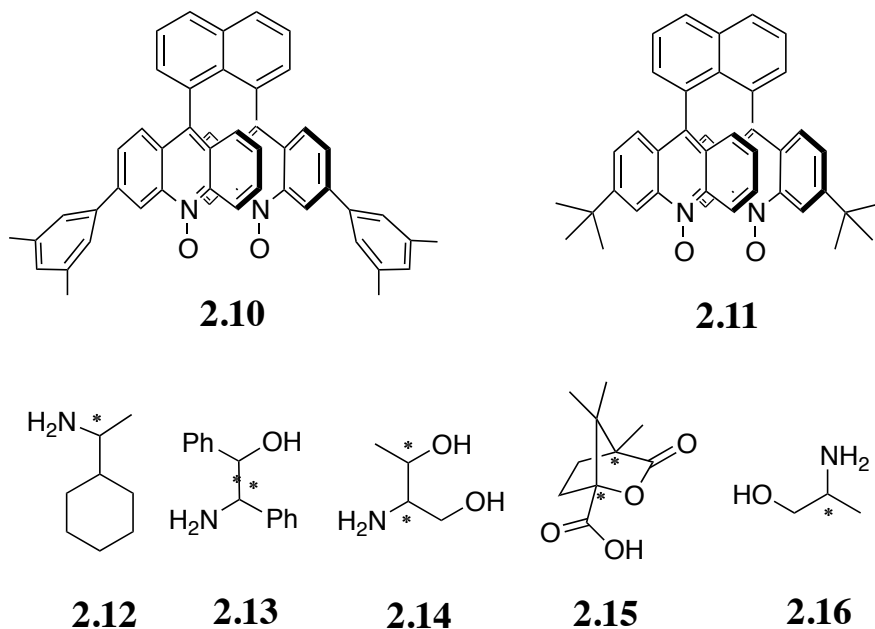


Scheme 2.3. Additional chiral host **2.8** and indicator chrome azurol S **2.9**; part of a second generation eIDA for *ee* of amino acid guests.

The complex between chiral host **2.6** and indicator **2.9** allowed enantioselective discrimination of nine of the 17 naturally occurring amino acids used in this study. Glycine was omitted because it has no stereocenter, and cysteine and tyrosine because of insolubility in the buffered solvent. Interestingly, three amino acids (asparagine, aspartic acid, and histidine) were found to give the opposite enantioselectivities from the others. This can be explained by coordination of the side chain functionalities to the Cu^{II} metal

center instead of the N-terminal amine. The remaining eight amino acids that were not enantioselectively discriminated using chiral host **2.6** were subjected to analysis with chiral receptor **2.8**. For this receptor, the (*R,R*)-enantiomer was selective toward binding the L-amino acids. This receptor was also cross-reactive, and facilitated discrimination of four of the remaining eight amino acids. This assay was successful in discriminating 13 out of the 17 amino acids that were studied.

In another report, the Wolf group developed a system that functions in a congruent fashion to the eIDA.²¹ This system facilitates enantiodifferentiation of amines, amino alcohols, amino acids, and carboxylic acids. This system does not utilize an indicator in the same manner as the other eIDAs, but instead utilizes two equivalents of a colorimetric N,N'-dioxide ligand **2.10** complexed to a Sc^{III} metal center (**Scheme 2.4**). Charge transfer leads to the presence of an absorption band at λ_{max} at 410 nm. When enantiomerically pure guests were added one of the chromogenic units was displaced from the Sc^{III} metal center. This displacement caused a decrease in the absorbance at 410 nm. It was found that the L-amino acids displaced the ligand from the complex to a greater extent than the D-amino acids, and thus the concentration of the guest could be determined using a racemic mixture of the ligand.



Scheme 2.4. Chemical structures for the hosts and guests used by the Wolf group in their eIDA.

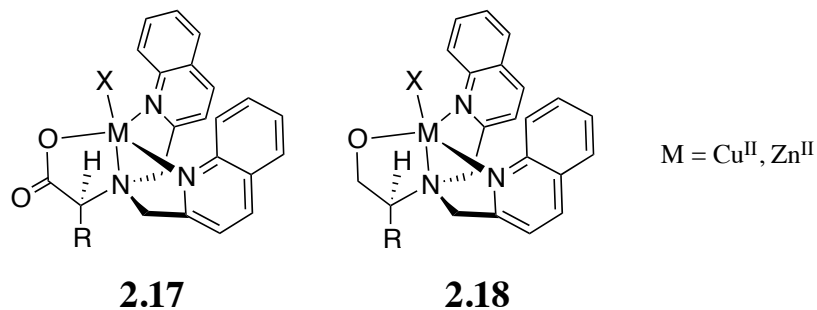
Calibration curves for guests **2.12-2.15** were created in order to test the validity of this system. The concentration was determined using the racemic host by studying a variety of different known guest concentrations. The chiral receptor was used to make the curve for the *ee* values. Samples of unknown concentration and *ee* were then tested, and the values input to the appropriate calibration curve. The calculated values for the unknowns matched well with actual values, validating the use of this method.

The Wolf group then extended this method to target α -amino alcohols **2.16** using the fluorescent Sc^{III} complex **2.11**.²³ This complex excited at 420 nm and had an emission at 588 nm, that was quenched upon the addition of the chiral amino alcohols. For the most part, the quenching was greater for the (*S*)-amino alcohol. As in the previous study, the concentration of the analyte was determined with the racemic ligand complex, while the enantiopure host allowed for *ee* determination. Unknowns were

analyzed using the same procedure as previously reported, and again gave good agreement with actual values.

2.3 EIDA DESIGN CRITERIA

In order to apply an eIDA utilizing metal complexes to determine the *ee* of chiral carboxylic acids, a chiral host with a complimentary binding site for an indicator and carboxylic acid was desired. The target interaction that was chosen was the coordination of carboxylate anions with a copper center, since it has been demonstrated to be a strong interaction.²⁵ The Canary group reported chiral metal complexes based on derivatized chiral molecules such as amino acids or amino alcohols (**Scheme 2.5**).²⁶⁻²⁸ Two equivalents of a quinolone chromophore were attached to the N-terminal amine, and the resultant chiral ligand was then complexed to either a Cu^{II} or Zn^{II} metal center. The complex exhibited a helical chirality that was indicated by exciton-coupled circular dichroism (ECCD), a technique that will be discussed more thoroughly later. The direction of this helicity was indicative of the stereocenter of the derivitized guest, and the magnitude of the signal was linearly related to *ee*.



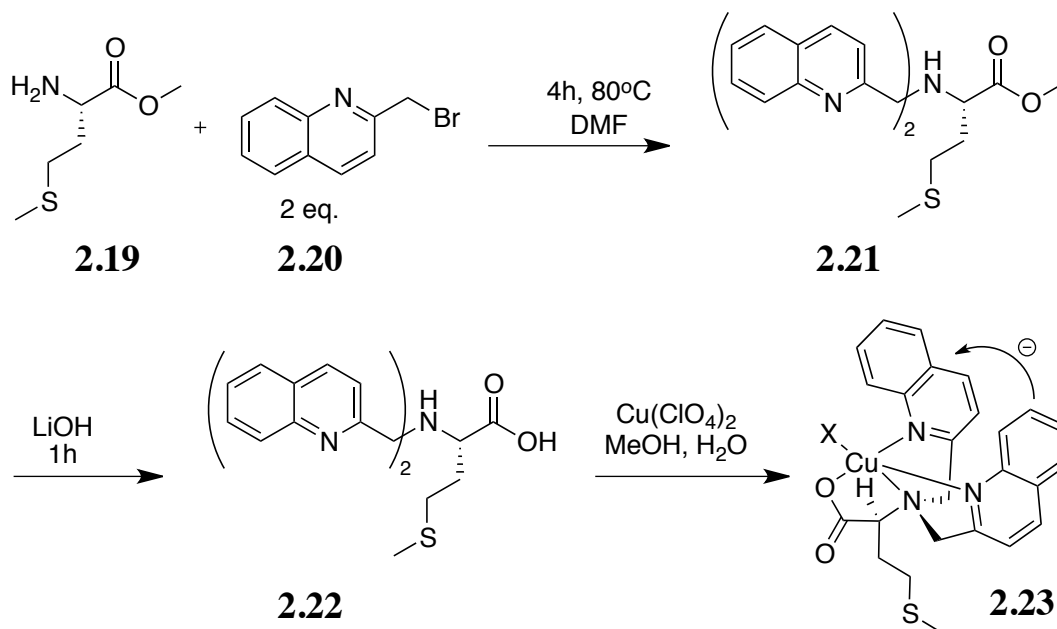
Scheme 2.5. Helically chiral guests formed by derivatizing either amino acids (**2.17**) or amino alcohols (**2.18**).

In this application, the five-coordinate metals Cu^{II} and Zn^{II} adopted a trigonal bipyramidal geometry upon complex formation. The tetradentate tripodal ligand occupied four of these coordination sites, while the fifth was occupied by an exogenous ligand such as a molecule of solvent. This empty coordination site was envisioned to serve as a docking site for a carboxylate ion (both for carboxylate containing indicators and guests). The derivatized amino acid that the Canary group found to give the largest CD signal was derived from methionine. This complex had the greatest degree of helical chirality, and hence the metal complex formed by derivitizing L-methionine was selected to serve as the chiral host. Choice of a suitable indicator was necessary to complete the components of the eIDA, requiring a similar mode of coordination to the metal center that the guest would have. For this reason, indicators containing a carboxylic acid moiety were chosen for application as indicators.

2.3.1. Host Synthesis and Properties

As mentioned previously, L-methionine was selected as the amino acid to be derivatized to construct the host structure. The synthesis of this host complex was published by the Canary group,²⁷ and can be completed in a few steps from commercially available starting materials (**Scheme 2.6**). The methyl ester of L-methionine **2.19** was derivatized with two equivalents of bromomethylquinoline **2.20** by S_N2 displacement of the bromide with the amine to give intermediate **2.21**. Bromomethylquinoline **2.20** was obtained in a single step from the chloride adduct by literature procedure,²⁹ since the reaction with the chloride proceeded slowly with a poor yield. Subsequent saponification of intermediate **2.20** was performed with aqueous potassium hydroxide to give the derivatized amino acid product **2.22**. Once the ligand had been synthesized,

metallation with copper(II) perchlorate gave the helically chiral copper complex **2.23** in good yield.



Scheme 2.6. Synthesis of chiral derivatized amino acid complex **2.23**.

Because the amino acid that was derivatized was L- α -methionine, the stereocenter is directly attached to the carbonyl. It is possible that treatment of this species with hydroxide base could lead to epimerization at this stereocenter. This racemization would be a major problem for this analysis, since the helical chirality imparted by the amino acid stereocenter is expected to give rise to enantiodiscrimination. To ensure that epimerization had not occurred, a circular dichroism (CD) spectrum was recorded for complex **2.23**. This spectrum, shown in **Figure 2.2**, shows a negative couplet. The maximum signal occurred at λ_{max} at 239 nm with a magnitude of 161 millidegrees, both

values that correspond well with literature values.²⁷ With the helical chirality of the complex confirmed attention was turned toward indicator binding.

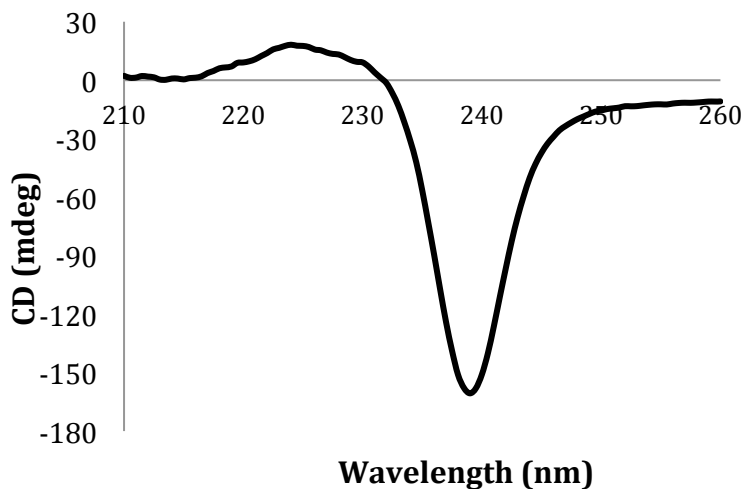


Figure 2.2. CD spectrum recorded for complex **2.23** (0.3mM) in CH₃CN.

2.3.2. Indicator Selection

Several pH indicators containing carboxylic acid functional groups are commercially available, and a variety of these compounds (**2.24-2.31**) were screened for application in this assay (**Scheme 2.7**). The ideal indicator would undergo a visible color change when a solution of a Cu^{II} metal ion was added to the free indicator in solution. To this end, separate solutions were made for of each indicator as well as the indicators with equimolar Cu(ClO₄)₂. According to this protocol, indicators chromoxane cyanine R **2.26**, chrome azurol S **2.29**, and methyl red **2.30** were selected in order to initiate further studies.

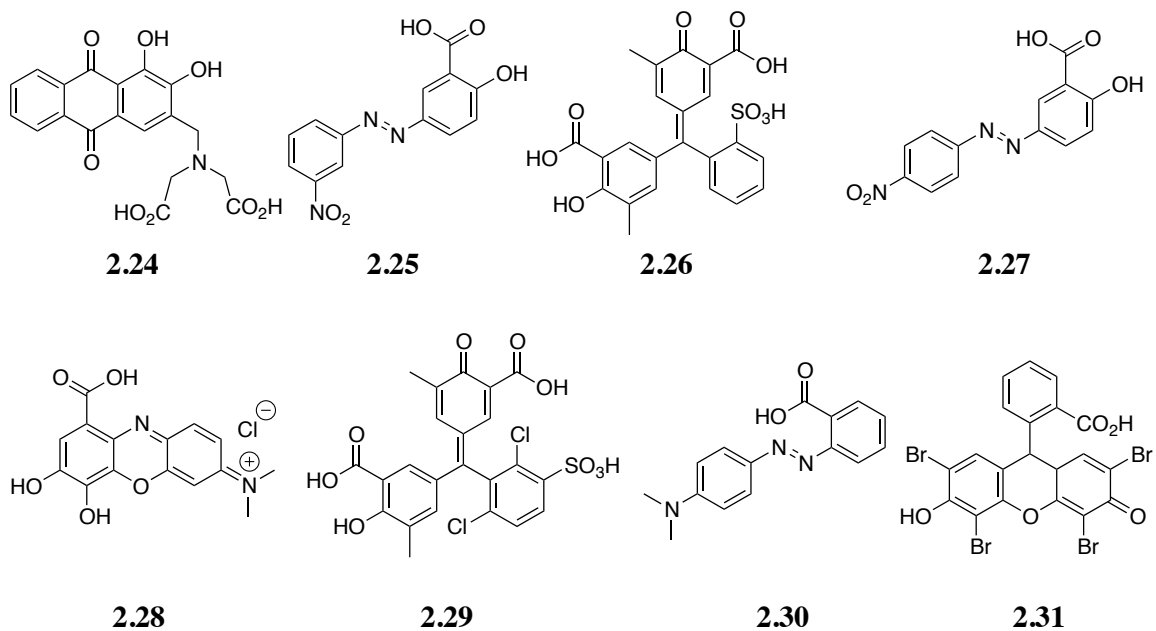


Figure 2.3. Indicators screened for color change upon binding copper(II).

2.3.3. Binding Studies

Titration experiments were performed with each of the three indicators. The indicator was used in the maximum concentration possible that kept the absorbance of the dye in accordance with Beer's law, roughly an absorbance value of one. The titrations of both chromoxane cyanine R **2.26** and methyl red **2.30** gave UV spectra that did not readily saturate. In each case, an excess of at least 20 equivalents of the indicator was required in order for the newly formed absorbing species to begin leveling off. A different scenario was observed upon the addition of host **2.23** to the indicator chrome azurol S **2.29**. The indicator by itself showed an absorbance with a $\lambda_{\text{max}} = 450 \text{ nm}$ (**Figure 2.4A**). Addition of the host formed a host:indicator complex, represented by the new peak that appeared at λ_{max} at 602 nm.

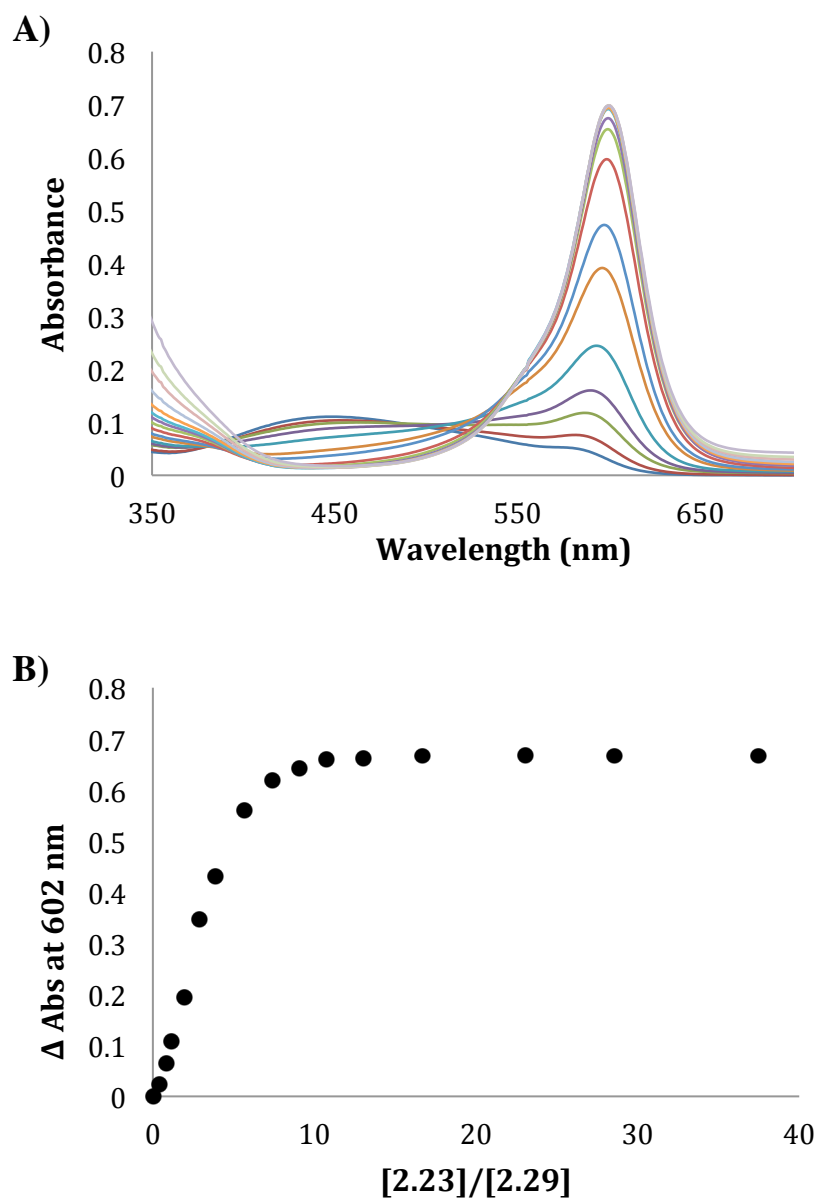


Figure 2.4. A) Titration of host **2.23** (0-165 μM) into indicator **2.29** (10 μM) in default buffer (75% MeCN, H_2O with 20 mM HEPES pH=7.416). B) Difference in absorbance of the host:indicator complex at 602 nm.

The formation of the complex is demonstrated by the isotherm shown in **Figure 2.4B**. The difference in absorption at 602 nm was plotted as a function of equivalents of host **2.23** that had been added relative to indicator **2.29**. In this plot, the saturation of the signal representing the host:indicator complex was observed to occur after approximately seven equivalents of the host had been added. The graph lacks an isosbestic point, indicating that more than two absorbing species are present during the titration. Thus, no binding constant was calculated for this association. The titration served as a way to find the point at which the indicator was 90% saturated with host, since precedent has established that this is the ideal ratio to perform the displacement.³⁰

2.3.4. Indicator Displacement

After establishing that the ideal ratio of host relative to indicator was 6.5:1, displacement of the indicator was performed by adding the (*R*)-enantiomer of the phenylbutyric acid guest **2.32**. Addition of the guest to the host:indicator complex led to a diminution of the peak at 602 nm, shown in **Figure 2.5A**, while concurrently leading to an increase in the free indicator peak at 450 nm. These trends were opposite from those found when the indicator bound to the host, indicating that the formation of the host:guest complex led to the indicator's displacement from the host, restoring the indicator to solution.

The analogous titration was performed for the opposite enantiomer, namely (*S*)-**2.32**, and a similar pattern was observed. Indeed, the free indicator absorbance at 450 nm increased concomitantly with decay of the host:indicator complex peak at 602 nm that represented the complex. The change in absorbance recorded at 602 nm for both of these guests was plotted against the equivalents of the indicated guest that had been added, as this value represents the displacement of the indicator from the host, and thus the

formation of the host:guest complex. The isotherms for these titrations are shown in graphical form in **Figure 2.5B**, and exhibit a virtually identical response to exogenous guest addition. The non-enantiospecific response of this receptor is generally observed, since differentiation was also unsuccessful for 2-bromopropionic acid guest **2.33**. The displacements occurred to varying degrees across the different guests, but showed no difference between enantiomers of either guest. Though the host retains helical chirality, as proven by the CD spectrum shown in **Figure 2.2**, this host does not lead to enantioselective differentiation for the guests.

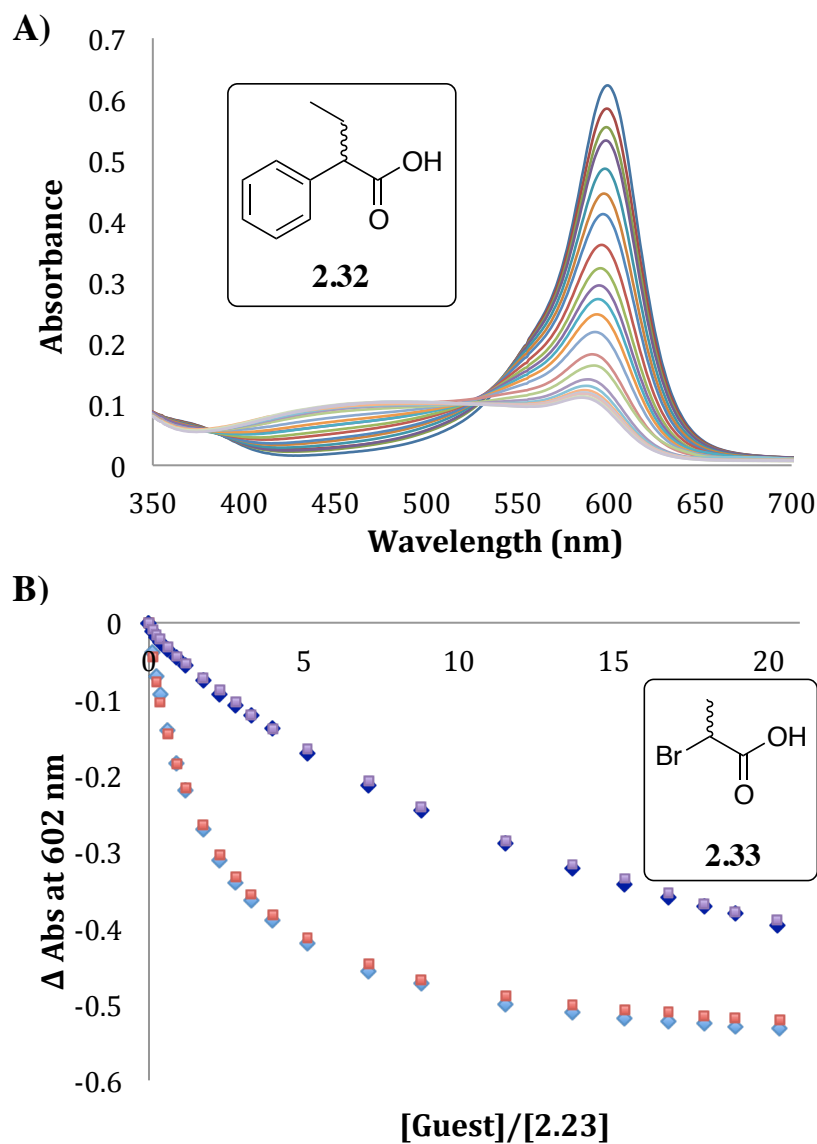


Figure 2.5. A) Titration of (R) -**2.32** (0-1.3 mM) into host **2.23** (65.1 μM) and indicator **2.29** (10 μM) in the default buffer. B) Change in absorbance at 602 nm upon addition of either (R) -**2.32** (\blacklozenge), (S) -**2.32** (\blacklozenge), (R) -**2.33** (\blacklozenge), or (S) -**2.33** (\blacklozenge).

Unfortunately, this approach to creating a colorimetric assay to differentiate chiral carboxylic acids proved fruitless. The focus of this project was diverted away from UV/visible assays and directed toward circular dichroism (CD).

2.4. EXCITON-COUPLED CIRCULAR DICHROISM

The use of circular dichroism as a means to decipher absolute configuration as well as *ee* of chiral compounds has seen increasing utility in the scientific literature. The Anslyn group in particular has been interested in creating CD assays to rapidly assess the *ee* of chiral analytes.³¹⁻³⁶ When light is passed through a chiral sample, one can envision that right and left circularly polarized light interact with the sample in a different fashion.³⁷ In addition to traveling at different speeds through the sample, they are also absorbed to different extents. This differential absorption arises from the difference in molar absorptivity coefficients (ϵ_L and ϵ_R) for left and right circularly polarized light. The difference in these absorptivity values is known as circular dichroism.

It is possible to observe exciton-coupled circular dichroism (ECCD) for chiral species that have two or more chromophores held in close proximity. This method is built around the interaction between the electronic transition dipoles of these chromophores. The chromophores need not be identical, nor attached to the same molecule. They only need to be held in close proximity in space in order for the excited states to couple. The chromophoric interaction breaks the degeneracy of these excited states, and leads to states with two different energy levels. This scenario, depicted in **Figure 2.6A**, is expected to have ramifications in optical spectroscopy. First, consider the case of a UV/Visible spectrum. This chromophoric coupling gives rise to two intrinsic spectra with the same sign. As a result these spectra are generally additive, appearing as a single absorption with twice the magnitude (**Figure 2.6B**). However, two peaks can be obtained if there is sufficient difference in energy between the two states.

This additivity of spectra is not generally observed in the CD spectrum. The different states manifest as bisignate curves displaying opposite Cotton effects (CEs). The CE refers to the change of the CD signal at wavelengths comparable to the

absorption of the chromophore of interest, with the first CE designated as the signal appearing at the longest wavelength. For example, the top spectrum in **Figure 2.6B** shows a positive first CE. If the chromophores are arranged in a clockwise fashion, the resulting complex will display a positive first CE. This scenario is represented pictorially by the positive couplet shown in **Figure 2.6C**. The distance between maxima of the spectra recorded for the two different states is known as Davydov splitting.³⁸ One useful feature of this type of CD spectrum is that several methods exist for the theoretical calculation of the bisignate curve.³⁹ Another hallmark of ECCD is that the maximum absorption in the UV/Vis spectrum corresponds to the zero-point null between the two CEs, illustrated in **Figure 2.6B**.

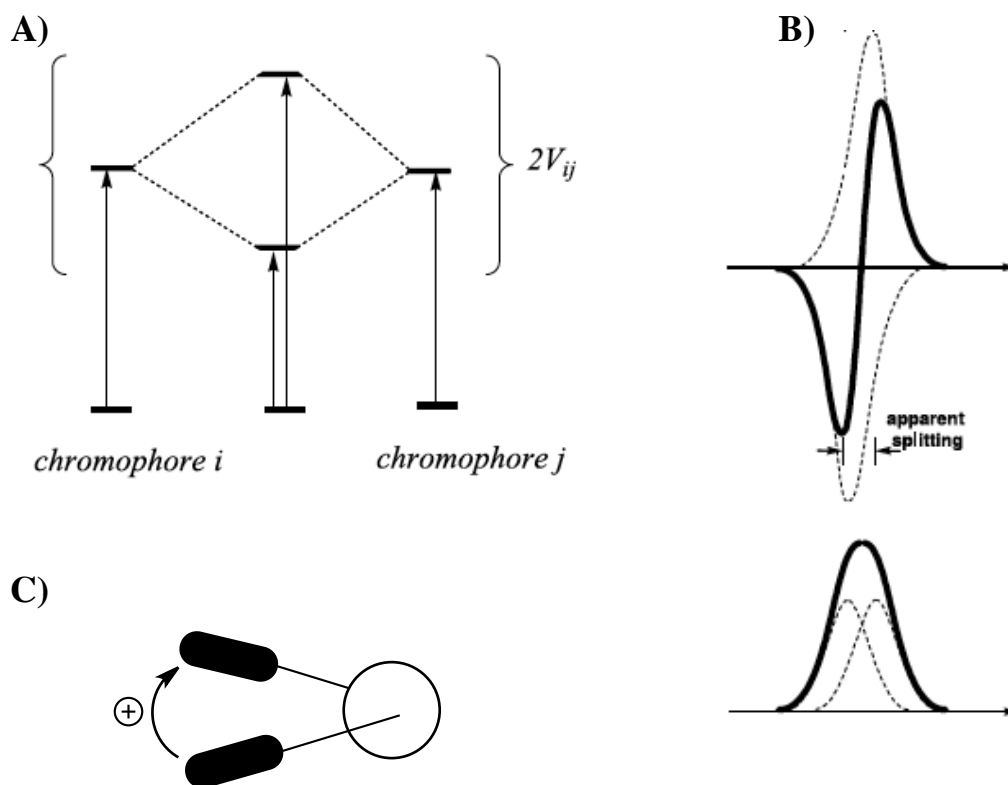
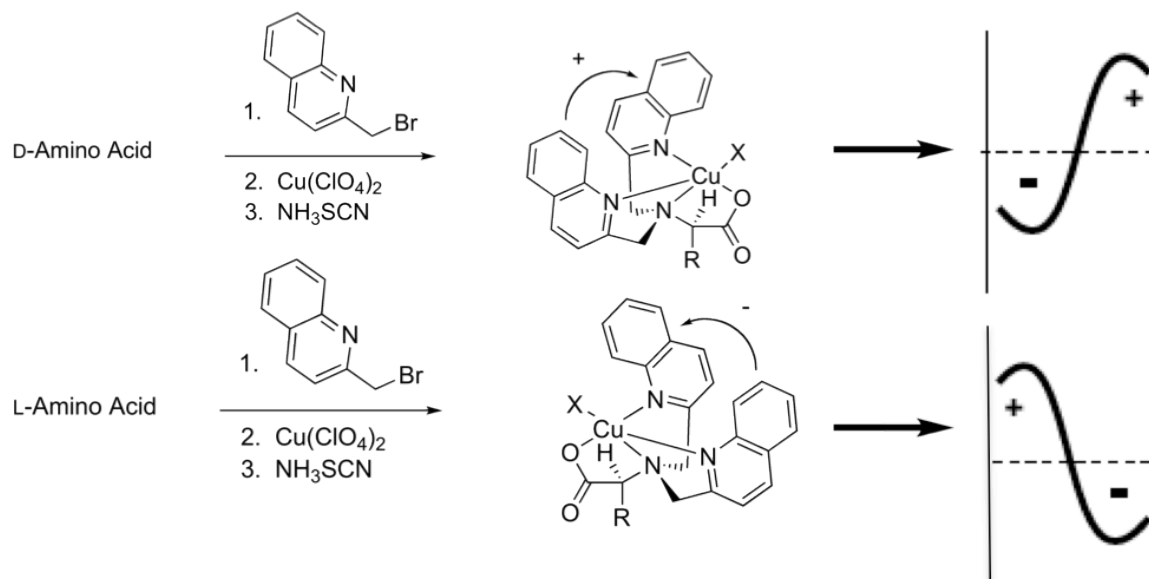


Figure 2.6. A) The splitting observed when the excited states of two chromophores, *i* and *j*, are coupled. B) The CD spectrum (top) and the UV/Vis spectrum (bottom) that result from the summation of these states. C) The spatial orientation of two chromophores in a clockwise direction, leading to a positive first CE.

2.4.1. Optical Sensor Based on ECCD

Many optical sensors based on the principle of ECCD have been published, by the Canary group,^{26-28,40,41} and others.⁴²⁻⁴⁷ The characteristic couplets seen in these analyses have allowed researchers to determine the absolute configuration and *ee* values for chiral analytes with a broad range of functional groups: α -amino acids, β -amino alcohols, and primary amines.

The Canary group typically begins by derivatizing the analyte of interest with quinoline chromophores to create a chiral ligand. This ligand is then complexed to a metal center, often Cu^{II} or Zn^{II} . The complex formation accentuates the helical twist of the compound, and brings the chromophores into close proximity, allowing ECCD to take place. The analyte stereocenter is responsible for the formed helicity, and enantiospecific CD spectra are obtained. To illustrate this approach, the example of absolute configuration determination for α -amino acids by the Canary group is presented in **Scheme 2.7**.²⁷ The D-enantiomer of the amino acid induces a left-handed helix with a clockwise arrangement of the chromophores, leading to the formation of a positive ECCD couplet. The opposite is true for the L-enantiomer of the amino acid guest.

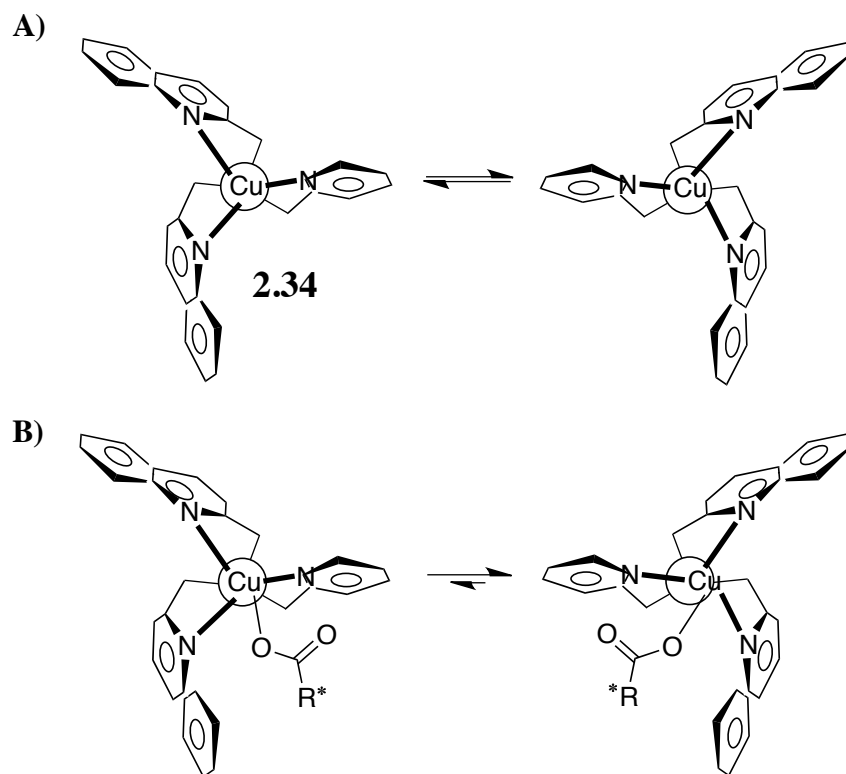


Scheme 2.7. Derivatization protocol of the Canary group for absolute configuration assignment for chiral amino acids.

This method reported by the Canary group was rather effective in its ability to rapidly assess the absolute configuration of the amino acid guest under study. Calibration curves were constructed that showed a linear correlation between the magnitude of the CD signal and the *ee* value of the guest. Determination of *ee* of truly unknown samples was not studied, but it can be inferred that this could have been achieved. One severely limiting drawback is that the analyte must be derivatized in order for the analysis to be performed. This requirement adds an additional step to the analysis, and irreversibly alters the structure of the guest. This may not be a detriment to analysis of naturally occurring amino acids, but one could imagine this is undesirable for a more synthetically challenging analyte.

2.4.2. Design Criteria

The new approach, in collaboration with the Canary group, involves complexation of an achiral [(BQPA)Cu^{II}(ClO₄)₂] host **2.34** with chiral carboxylic acid guests. The host is formally achiral, however it is expected to rapidly interconvert between the two different helices at room temperature, as shown in **Scheme 2.8A**. The chirality of the guest is expected to be transferred to the host complex upon binding, a phenomenon noted by Pfeiffer while resolving chiral coordination complexes.⁴⁸ In the infancy of coordination chemistry, he observed that chiral properties were adopted by racemic transition metal complexes when chiral additives were incorporated. The equilibrium interconverting the enantiomeric metal complexes will be perturbed, leading to preferential formation of particular diastereomers. Hence, it is possible to resolve the metal complexes in this fashion. This scenario is expected when a chiral carboxylic acid guest binds to the metal center of the host, with a particular guest stereocenter biasing one of the helicities (**Scheme 2.8B**).



Scheme 2.8. (A) Rapid interconversion between two helical structures. (B) The equilibrium is towards one of the diastereomers by addition of a chiral carboxylate guest.

There are two important reasons why host **2.34** was selected for these studies. First, it is easily and readily synthesized. The host is available in two easy steps from commercially available materials, minimizing required preparation time. Second, the carboxylate guest is expected to be accommodated by the empty coordination site on the trigonal bipyramidal Cu^{II} metal center. The open coordination site is available because the tripodal tetradentate BQPA ligand occupies four of the five available coordination sites on the metal center. The remaining site was postulated to contain a molecule of

solvent to complete the coordination sphere, which could be displaced upon introduction of a carboxylate guest.

Upon introduction of the chiral analyte to host **2.34**, the binding event was postulated to occur with distortion of the complex geometry. The direction of the helical distortion should be indicative of the absolute configuration of the chiral analyte. This should allow the analysis to be performed directly on a substrate without further modification. Further, binding between the host and guest is expected to occur upon mixing of these entities. This should allow the CD spectra to be obtained quickly and easily, and allow for the incorporation of a commercially available interfaced liquid controlling robot for automation.

2.4.3. X-ray Analysis

Initial experiments sought to determine the geometry about the metal center in the host complex through x-ray crystallography. X-ray quality crystals were grown, and the structure for the complex was determined. The structure is shown in **Figure 2.7**, and confirms the hypothesis that the ligand occupies four of the five coordination sites about the metal center. A molecule of water occupies the vacant coordination site, and is expected to be displaced by the carboxylate guest. The metal center in this structure appears to be a square pyramidal geometry, but it is distorted toward trigonal bipyramidal. The water oxygen and three of the nitrogen atoms occupy the basal plane, while one quinoline atom is coordinated in the apical position. The geometry in this crystal is consistent with a similar complex reported by Karlin⁴⁹ for an analogous chloride complex. Regardless, either of these geometries are capable of giving a conformation with twisted chromophores and hence give rise to an ECCD spectrum.⁵⁰

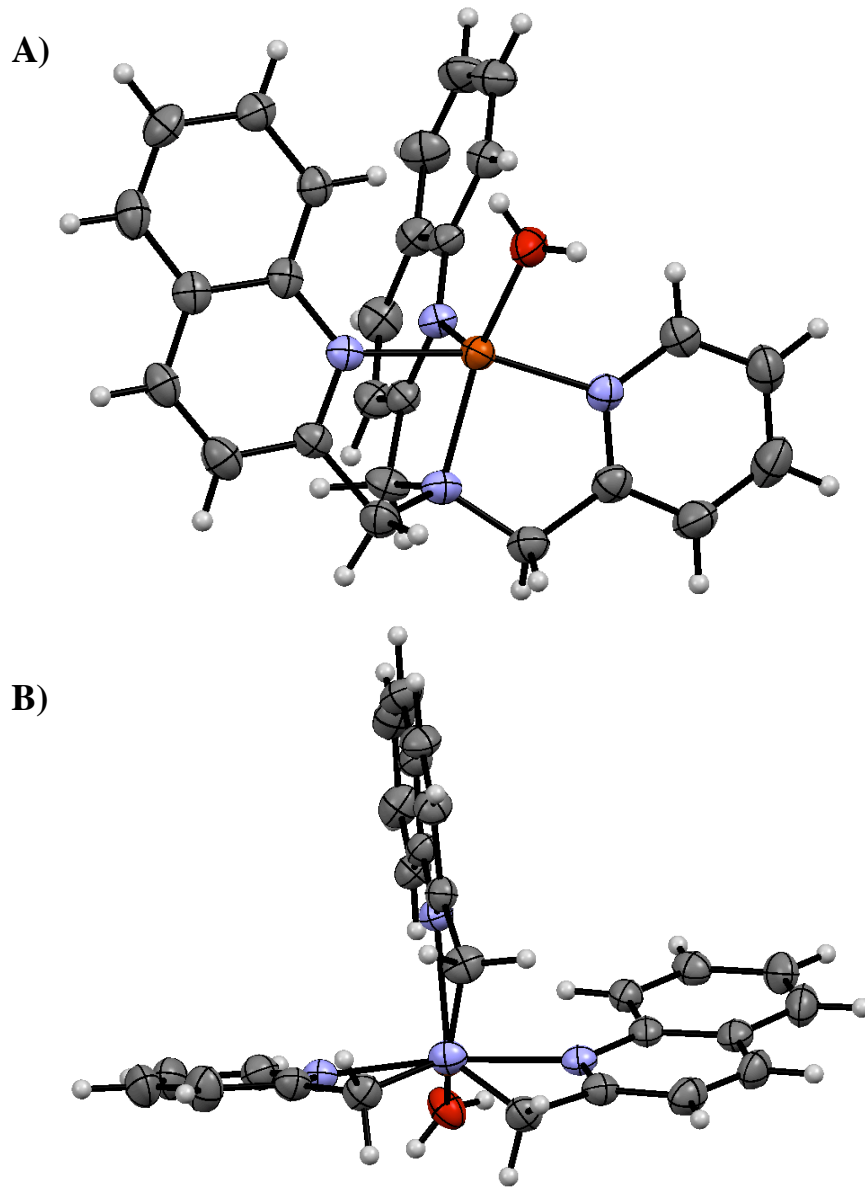


Figure 2.7. Two different views of copper complex **2.34**. Displacement ellipsoids are scaled to 50% probability, and counterions are omitted for clarity.

The two views provided show that the chromophores are tilted. The solid state structures switch between the two different helical structures in an achiral $C2/c$ space group. It is expected that complexation of host **2.34** to a chiral guest will cause a

preponderance of one of the twists. Hence, a signal in the CD spectrum is expected to arise from this interaction.

2.4.4. CD Analysis

In the absence of an external guest, achiral host **2.34** does not give a signal in the CD spectrum (**Figure 2.8A**). The carboxylate guests that were chosen for this study were also CD-silent at wavelengths greater than 230 nm (**Figure 2.8B**). Additionally, no CD signals were observed when the guests were added to a solution of $\text{Cu}(\text{ClO}_4)_2$ in the desired buffer solution. Therefore, any signal that is observed above 230 nm is a result of a complex formed between host **2.34** and a chiral carboxylate guest. To this end, the association between host **2.34** and carboxylic acid **2.32** was studied to determine if complex formation imparted a helical twist on the complex. The CD spectra were recorded for each enantiomer of the guest with a two-fold excess relative to the host in a solution containing HEPES buffer (75% acetonitrile, 25% water) at pH 7.4. At this pH the dominant guest species is the carboxylate.

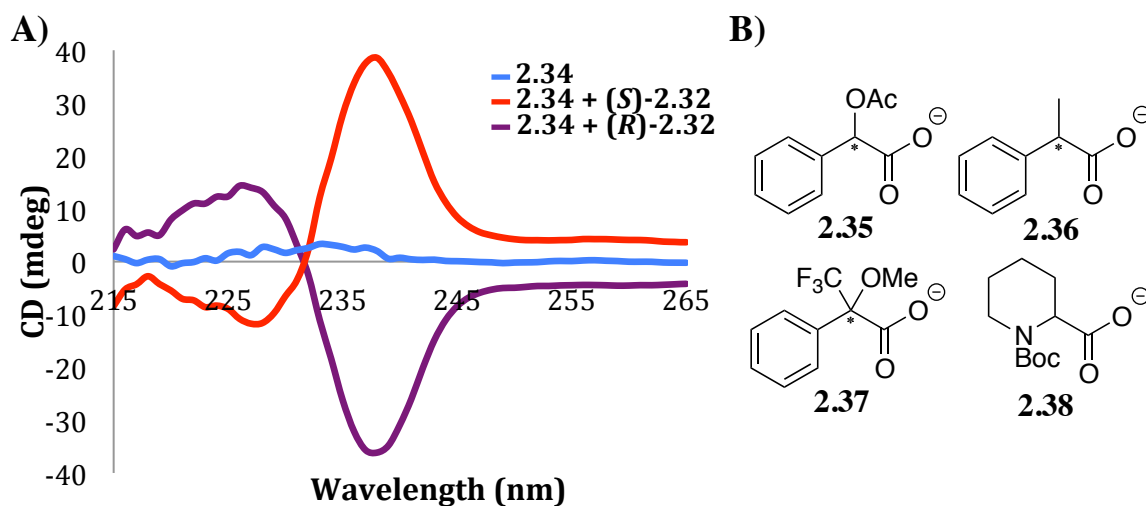


Figure 2.8. (A) Addition of each enantiomer of **2.32** (1.0mM) to a solution containing **2.34** (0.5mM) in buffer. (B) Chemical structures for chiral carboxylate guests **2.35-2.39**.

Analyte incorporation gave rise to a CD couplet that is indicative of ECCD, with a first Cotton effect (CE) occurring at a λ_{max} of 238 nm and a second CE at 227 nm. The corresponding λ_{max} in the isotropic deep UV spectrum is observed at 233 nm, aligning with the null in the CD spectrum. This observation is consistent with the classification of an ECCD couplet. Owing to its larger magnitude, the first CE will be used to represent the output signal. As demonstrated in **Figure 2.8A**, the (*R*)-enantiomer of **2.32** gives rise to a negative CD couplet, while its (*S*)-counterpart gave a positive CD couplet of equal and opposite magnitude. These signals are indicative of P- and M-type helices, respectively.⁵¹ As mentioned previously, the assignment of exciton chirality involves the orientation of the transition dipoles for both chromophores. An arc vector is drawn from the chromophore closest to the reader to the chromophore that is furthest away. This corresponds to a positive couplet in the ECCD spectrum. Hence, an M-propeller gives rise to a positive ECCD couplet. As a result of these analyses, the enantiomeric nature of the complexes formed from the binding of enantiomeric guests was confirmed. The

direction of the twist in the two quinoline substituents on host **2.34** is determined by the orientation of the guests attached to the stereocenter of the carboxylate guest.

Titration experiments were performed independently with both enantiomers of guest **2.32**, and showed a saturation of the CD signal when exogenous guest addition had reached one equivalent (Figure 2.9). Several attempts were made to quantify this binding process, but none proved successful. The required dilution of the solutions diminished the CD signals to the point where noise was too large to maintain an accurate signal. It was postulated that the size of the groups on the stereocenter would affect the magnitude of the observed signal. To this end, CD spectra were recorded for complexes formed between host **2.34** and each enantiomer of all guests used in this study.

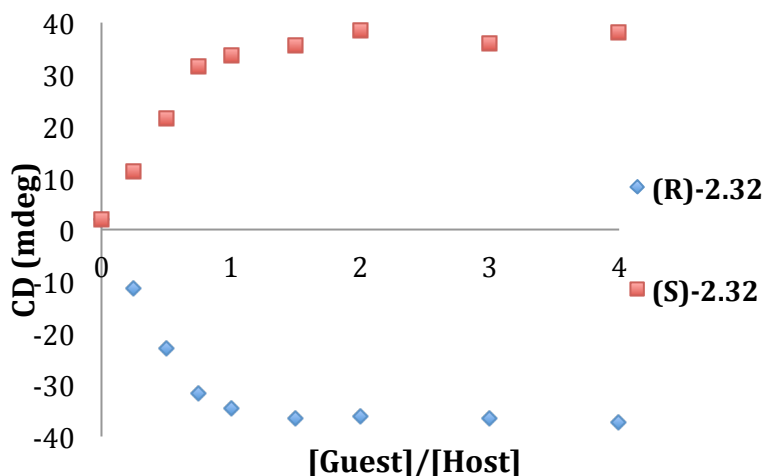


Figure 2.9. Change in CD signal at 238 nm with addition of indicated enantiomer of **2.32**.

The spectra recorded for the guests all showed the same saturation of the CD signal at one equivalent of added guest, meaning that the signal was concentration-dependent below this threshold. Hence, all analyses were performed with two

equivalents of the guest relative to the host to obviate this concentration dependence. As expected, the CD spectra recorded for each guest was unique in its magnitude and shape. The same positive first CE was observed for all of the homochiral (*S*)-carboxylate guests (**Figure 2.10**), while a negative first CE was observed for the (*R*)-enantiomers. Two main differences were observed for these CD spectra: the magnitude of the peaks was different, as were the shapes of the curves that were recorded. Additionally, each enantiomer of the same guest rendered a mirror image CD spectrum. Based on the sign of the first CE, it is possible to assign the absolute configuration of the guest stereocenter. It was postulated that this differing magnitude and shape of the CD signal could lead to identity determination of the carboxylate guests using pattern recognition protocols.

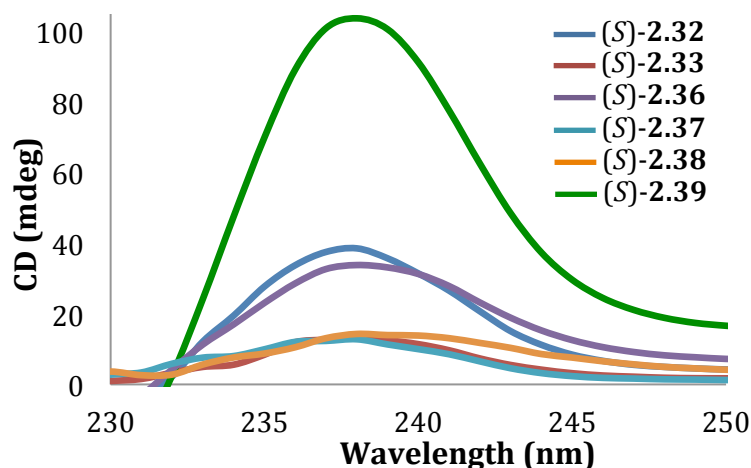


Figure 2.10. CD spectra for (*S*)-enantiomer of indicated guest (1.0 mM) and host **2.34** (0.5 mM) in buffer.

2.4.5. Analysis of the CD Data

In order to determine the chiral carboxylate identity, a technique called linear discriminant analysis (LDA) was used.^{52,53} This statistical analysis method aims to

minimize the separation between points within an analyte class, while maximizing the distance between the different classes of analytes. To achieve this goal, the program creates linear algebraic functions with the data that has been input. This technique is referred to as “supervised,” since the classification of each data point is known prior to analysis. For this analysis, five different samples were made and analyzed for each enantiomer of each guest. These samples contained two equivalents of the guest relative to the host, and made up a sample set of 70 different members. The input data were the CD signals observed between 235 and 265 nm, and were broken down into 1 nm increments. These wavelengths were selected as they represent the portion of the spectrum that has the greatest change upon guest addition. Shorter wavelengths were omitted since they overlapped to a small extent with some of the carboxylate guests used in this study.

The LDA plot recorded for this data set is shown in **Figure 2.11**, and generally shows good discrimination of the carboxylate guests studied. The only exception was some overlap between guests **2.33** and **2.36**. The greatest amount of differentiation in the dataset occurs along the F1 axis, and represents the absolute configuration of the stereocenter of the guest. The homochiral (*S*)-enantiomers show up on the positive side of the plot, while the corresponding (*R*)-enantiomers are on the negative side. The distance from the axis along F1 signifies the magnitude of the CD spectra, with the largest magnitude species falling the furthest from the origin. Reflection through the origin of one enantiomer of a guest gives the other enantiomer. The F2 axis represents the second largest axis of variation, though much smaller than the variance represented by the F1 axis. The separation along this axis has been postulated to be the shape of the spectra, since there are regions where some of the spectra cross.

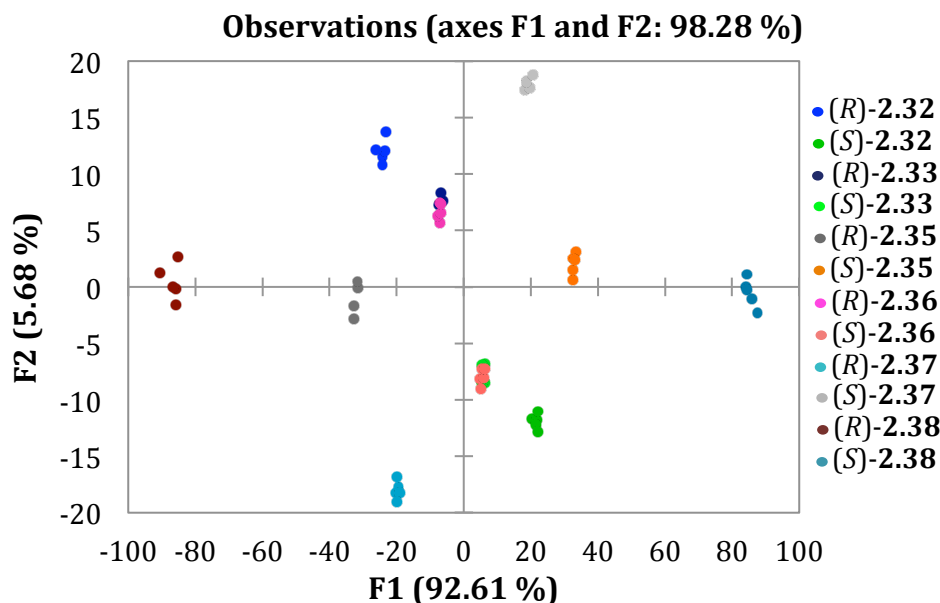


Figure 2.11. Two-dimensional LDA plot showing the response of each carboxylate guest.

The predictive power of this plot can be assessed using a jack-knife analysis. This leave-one-out analysis technique operates by omitting a single data point among the dataset. In the absence of this point a new set of functions is created, and then the omitted point is assigned to a group based on these new functions. This analysis is repeated for each data point, and the percent of correctly assigned points is calculated. The validity of the plot is determined by the correct assignment of each data point. This cross-validation technique helps to remove any bias that may be associated with the supervision of the data. The LDA plot depicted in **Figure 2.11** had a jack-knife analysis of 98.25%, demonstrating a very successful identity assignment amongst the carboxylate guests.

In order to understand the helicity and magnitude of the CD spectrum, a model was created for the host:guest complex. A greater twist between the quinoline

chromophores gives rise to a larger observed signal. A Newman-style projection was created for the complex formed with guest **2.32**, looking down the copper to tertiary nitrogen bond (**Figure 2.12**). This situation is the reverse of the picture that is shown in the crystal structure in **Figure 2.7B**. Representing the complex in this fashion allows for visualization of the propeller twist easily. In the front of the projection are the substituent groups attached to the stereocenter of the carboxylate guest that is bound to the copper metal center.

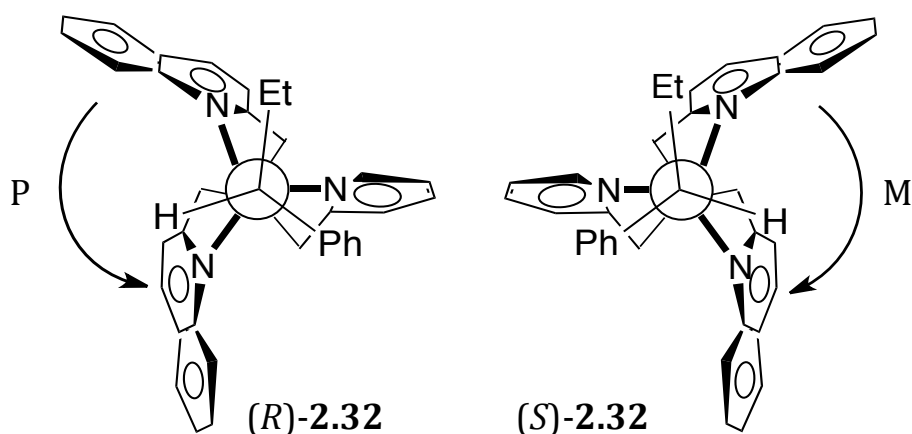


Figure 2.12. Newman-type projections for host **2.34** with each enantiomer of **2.32** guest, with the M-propeller giving a (+) chirality for the orientation of the electronic dipole moments of the quinoline chromophores.

A rationalization of the CD spectra using the Newman-style models was constructed as follows. Without the addition of a chiral guest, the complex exists as two propeller-like conformations that are enantiomers of each other. The propeller of note is formed by the planes of the heterocyclic quinoline and pyridine groups. Formation of the complex causes steric strain between these same heterocycles and the added carboxylate guest. In order to avoid this strain, the smallest group on the stereocenter is directed

between the quinoline groups. The medium and large groups are directed toward the chromophoric species, and bias the formation of a specific propeller conformation. The direction of the twist is dictated by the orientation of the groups on the stereocenter. Thus, the (*S*)-enantiomer of the twist promotes the M-type propeller and the (*R*)-enantiomer of the guest leads to formation of the P-type propeller. Like all models created for molecular interactions, there are certain caveats that one must consider. This model conveys a static picture of an interaction that is undoubtedly dynamic. It is likely that there are several conformations of the molecule that lead to the output CD signal. These conformations average out to the spectra that are observed for each of the enantiomers of this substrate. This model is unfortunately lacking sufficient solid state evidence, as all attempts to grow x-ray suitable crystals proved fruitless. Nevertheless, this model accurately predicts the preferential twist formed by the homochiral carboxylate guests. It is likely that the intensity of the CD spectrum is determined by several competing factors, though the dominant role is likely played by the steric interaction between the quinoline chromophores and the groups attached to the stereocenter.

The scope of the analysis was expanded to new guests in order to test the effect that the steric size of the substituents on the stereocenter has on the sign and magnitude of the signal. Thus, carboxylic acids **2.39** and **2.40** were obtained and applied to this assay (**Figure 2.13A**). Carboxylic acid **2.39** was particularly attractive owing to its similarity to guest **2.33**, differing only by the size of the alkyl group on the stereocenter. The homochiral enantiomers of these species are assigned the same stereochemical descriptors for their molecular orientation in space, as denoted by the Cahn-Ingold-Prelog (CIP) rules.⁵⁴ Excluding the carboxylate substituent on the stereocenter that is bound to the metal, the bromine substituent gets the highest priority in numbering. The bromine is

followed in priority by the alkyl group, and the hydrogen substituent has the lowest priority. For carboxylate guest **2.33** the group steric size follows these CIP rules. When considering the newly studied guest **2.39**, group size does not match up with the CIP rules. In this case, the isopropyl substituent is expected to be larger than the bromine substituent, though the bromine retains the priority in numbering. Indeed, the CD spectrum recorded for (*R*)-**2.39** shows a positive first CE (**Figure 2.13B**). The same trend was observed for guest **2.40**, as the (*R*)-enantiomer also gave rise to a positive CD couplet. This is opposite the signal recorded for the homochiral (*R*)-**2.32** guest. These observations provide evidence for the steric model that has been proposed here. The focus of this work then shifted to the magnitude of the signals that arise from this complex formation.

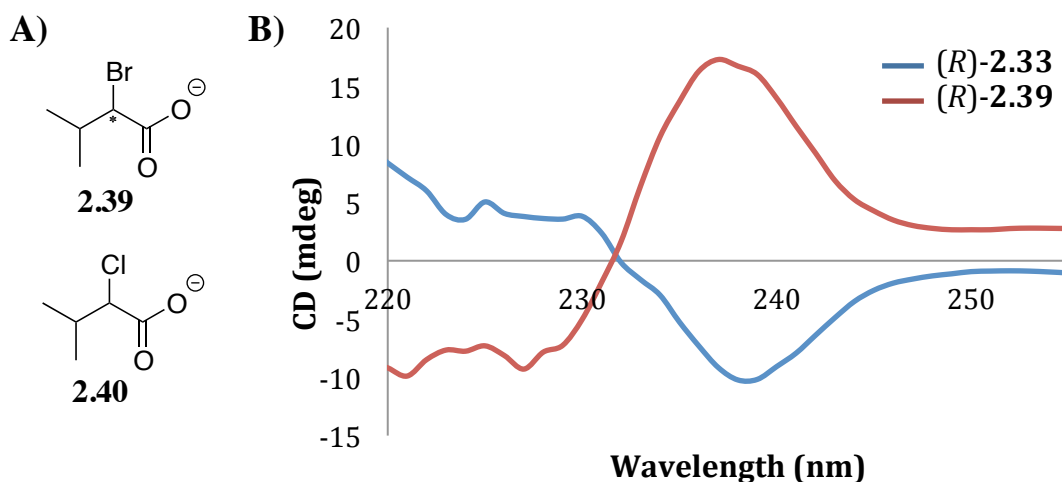


Figure 2.13. (A) Chemical structures for additional guests applied to this study. (B) CD spectra recorded for the indicated guests (1.0 mM) and the host (0.5 mM) in buffer.

Taft steric parameters have been applied in order to understand the effect that group steric size has on the observed CD signals. In his work, Taft attempted to quantify

the size of substituent groups using a linear free energy relationship.⁵⁵ The reference reaction that he chose was the acid-catalyzed hydrolysis of a methyl ester to its parent carboxylic acid. Comparing the rate of hydrolysis observed for the substrate of interest to that of a reference reaction with a hydrogen substituent allowed for designation of the steric size of a group (**Figure 2.14**). This parameter was defined by Taft as E_S . Taft chose the acid-catalyzed pathway in order to selectively study the steric effects in the absence of overwhelming electronic contributions. He believed the acid-catalyzed pathway to be freer of electronic considerations because of the similar charge state of the species. In other words, the rate-determining step of nucleophilic addition to the carbonyl proceeds without affecting the charge state of the molecule being studied. The extra size of the proton is assumed to be negligible, since it is present in both structures. The base-catalyzed pathway forms a molecule with a negative charge from a neutral starting material. This pathway is expected to be much more susceptible to these aforementioned competing electronic effects.

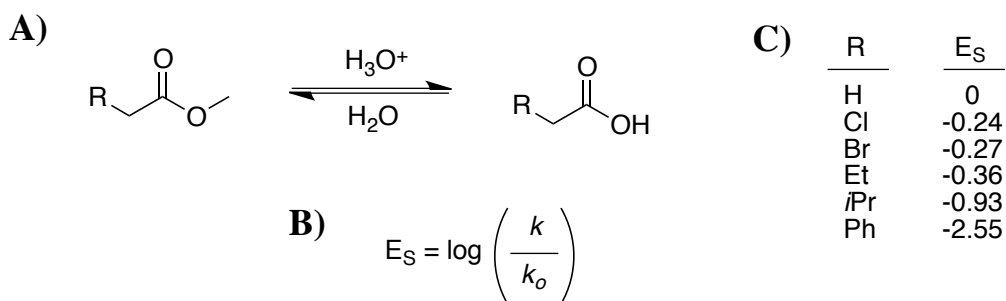


Figure 2.14. A) Acid-catalyzed ester hydrolysis used by Taft to quantify steric size. B) Equation used to calculate Taft parameter E_S . C) Taft parameters for selected substituent groups.

The relative sizes of the substituent groups were used to understand the magnitude of the observed signal, since steric factors were found to play an important role. It is

expected that the largest group on the stereocenter, without considering the carboxylate, will be directed toward the pyridine ring. This orientation will help to relieve steric strain, and a less pronounced effect will arise from this group. In the proposed model, the twist will be primarily dictated by the small and medium groups attached to the stereocenter. These groups are expected to have more interaction with the quinoline chromophores as a result of this placement.

Only a subset of the guests that were analyzed with host **2.34** were selected to be analyzed with the Taft parameters. These guests, **2.32**, **2.33**, **2.36**, **2.39**, and **2.40**, were chosen because the E_s values for relevant substituents on the stereocenter had been previously reported. The difference between the E_s values for the medium and small groups was computed and subsequently plotted against the magnitude of the observed CD signal for the (*S*)-enantiomer of the guests. This plot is shown in **Figure 2.15**. Of note, the difference in E_s values was expressed as a negative value for guests **2.39** and **2.40**, since the orientation of these groups is opposite of the others. The resultant plot shows a linear correlation between observed CD signal and *ee* value, validating the hypothesis that the magnitude of the signal is related directly to the steric size of the substituent groups on the stereocenter. Another noteworthy feature of this graph is the overlap observed between **2.32**, and **2.36**. These two carboxylates gave similar CD signal magnitudes and shapes, and were not fully differentiated previously by the LDA analysis. This explanation of the overlap of these two guests provided evidence that this model is an accurate representation of the complex that was formed.

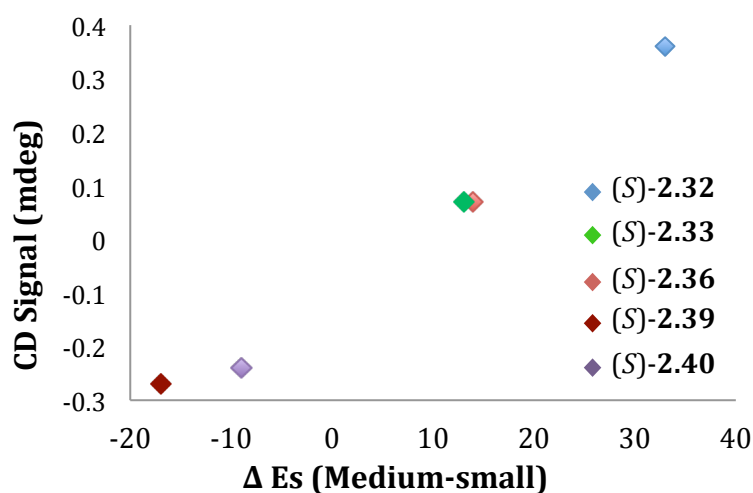


Figure 2.15. Graph of the CD signal for the (*S*)-enantiomer of indicated guest as a function of the difference in the E_s values of the medium and small groups.

2.4.6. Determination of Unknown ee Values

Following differentiation of carboxylate guest identity and understanding of the size and magnitude of the observed CD signals, the focus of the study turned to determination of the *ee* values for truly unknown samples. In order to realize this goal, calibration curves were created for three carboxylate guests selected for study. These three guests, **2.32**, **2.36**, and **2.38**, were selected because their CD signals cover a broad range of amplitudes. The calibration curve values for *ee* vary between 100% and -100%, and were calculated using $[(R)-[S])/([R]+[S])] \times 100$. Hence, an *ee* value of 100% corresponds to a sample containing only the (*R*)-enantiomer. In order to maintain concentration independence for a saturated signal, two equivalents of the carboxylate guest were again added with respect to the host.

A representative example of a calibration curve, which was generated for guest **2.32**, is shown in **Figure 2.16**. A linear regression was carried out, in order to find a best-fit line for the data. The equation for this line correlates the observed CD signal

with the ee value of the sample, and the plot displayed an $R^2 = 0.99$. Eight solutions of unknown ee values were prepared for each carboxylate, independent of the samples that had been applied to the calibration curves.

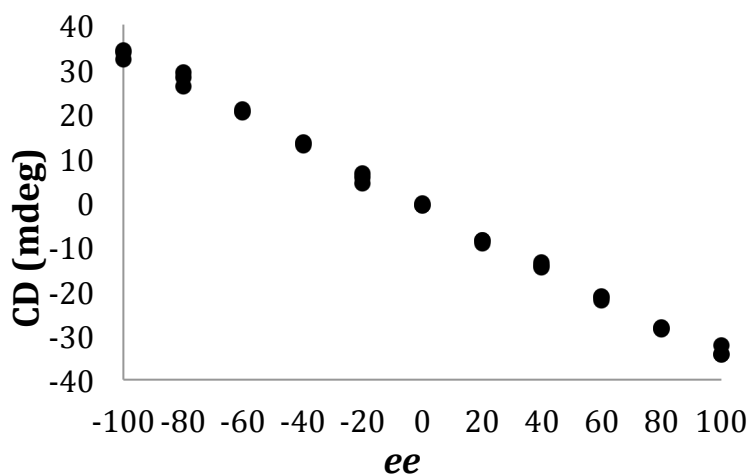


Figure 2.16. CD signal at 238 nm for a solution containing **2.32** (1.0 mM) and host **2.34** (0.5 mM) in buffer as a function of ee .

The CD signal for each sample was measured, and the signal at 238 nm was used to determine the ee by applying the equation found by the linear regression. The summary of the average values obtained for each guest are illustrated in **Table 2.1**. The average absolute error is herein defined as the difference between the actual and calculated values. The observed error indeed varies according to the difference in amplitude between the guest enantiomers, with the largest magnitude guest giving the lowest error. However, in reality there was no significant difference between the guests with the largest magnitude and those with the smallest. The average error across the entire suite of guest samples was calculated to be $\pm 3.0\%$. This error value is well within the range of acceptable errors for HTS.⁵⁶

Guest	Average Error (%)	ΔCD_{238} (mdeg)
2.32	3.2	68.8
2.36	4.1	25.3
2.38	1.8	200.8

Table 2.1. Errors for the *ee* calculations of unknown guests related to the difference in their CD signal magnitude.

2.5. CONCLUDING REMARKS

The method described in this chapter utilizes the principles of ECCD in order to rapidly assess the absolute configuration of chiral carboxylates. Mirror image spectra were observed for each enantiomeric carboxylate, indicating that their complexes with **2.34** were enantiomers of each other. Both the magnitude and the shape of the measured CD signal allowed the identities of each of the carboxylate guests to be uncovered by the pattern recognition protocol known as LDA. Further, calibration curves were generated for a suite of guests by varying the *ee* values for known samples. The curve for each guest was then applied to a series of unknown samples of that particular guest, and the best-fit line equation was used to relate this signal to an *ee* value. An average error for this assignment was calculated to be 3.0%. The host applied to this analysis can be easily synthesized from commercially available starting materials, and no further treatment of analytes is required. Based on the success of this system, its application to other types of systems will be presented in further detail in the next chapter.

2.6. EXPERIMENTAL

2.6.1. Materials and Methods

All reagents and solvents were purchased from commercial sources and used as received. Amino acid **2.19**, $\text{Cu}(\text{ClO}_4)_2$, indicators **2.24-2.31**, and guests **2.32**, **2.33**, and

2.35-2.40 were purchased from Sigma Aldrich. Bromomethyl quinoline **2.20**, and guests **2.35**, and **2.36** were purchased from TCI. Circular dichroism measurements were performed at 25°C on a JASCO J-815 spectropolarimeter, using a Starna Type 21 1-cm quartz cuvette. The program used to carry out linear discriminant analysis (LDA) was XLSTAT 2011.

2.6.2. Host Synthesis

BQPA was prepared according to literature procedure⁵⁷ and dissolved (0.196g, 0.5 mmol) in 10 mL dry MeOH. To this stirred solution, Cu(ClO₄)₂ (0.185g, 0.5 mmol) dissolved in 5 mL dry MeOH was added dropwise. This green solution was stirred for 10 mins. A light blue precipitate formed upon addition of Et₂O (45 mL). This suspension was stirred for 1 hour, and the precipitate was subsequently collected by vacuum filtration. A total of 0.234 g product were collected, for an isolated yield of 71.9%. ESI MS: m/z 453.33 (Cu⁺BQPA); calculated 453.11.

2.6.3. X-ray Structure of 2.34

2.6.3.1. Experimental Details

Crystals grew as large, blue needles by slow evaporation from methanol. The data crystal was cut from a larger crystal and had the approximate dimensions: 0.22 x 0.20 x 0.18 mm. The data were collected on a Nonius Kappa CCD diffractometer using a graphite monochromator with MoK α radiation ($\lambda = 0.71073\text{\AA}$). A total of 581 frames of data were collected using ω -scans with a scan range of 1° and a counting time of 97 seconds per frame. The data were collected at 153 K using an Oxford Cryostream low temperature device. Details of crystal data, data collection and structure refinement are listed in Table 1. Data reduction were performed using DENZO-SMN.⁵⁸ The structure was solved by direct methods using SIR97⁵⁹ and refined by full-matrix least-squares on

F^2 with anisotropic displacement parameters for the non-H atoms using SHELXL-97. The hydrogen atoms on carbon were calculated in ideal positions with isotropic displacement parameters set to 1.2xUeq of the attached atom (1.5xUeq for methyl hydrogen atoms). The hydrogen atoms on the full occupancy water molecules were located in a ΔF map. Their bond lengths were idealized and their positions were refined riding on the oxygen atom.

One of the perchlorate anions was disordered. The disorder resulted from a rotation about one of the O-Cl bonds and involved three of the four oxygen atoms of the group. The disorder was modeled by assigning the variable x to the site occupancy of one group of atoms, O6, O7 and O8, and $(1-x)$ to the site occupancy of the alternate group of atoms, O6a, O7a and O8a. A common isotropic displacement parameter was refined for these atoms while refining x . The geometry of the perchlorate ions was restrained to be equivalent throughout the refinement process. In this way the site occupancy factor for the major component of the disorder refined to 52(1)% for atoms O6a, O7a and O8a.

In addition to the disordered perchlorate ion, a molecule of water, O3w, was disordered across a crystallographic two-fold rotation axis at $1/2, y, 1/4$. The hydrogen atoms on this molecule were not included in the refinement model.

The function, $\sum w(|F_o|^2 - |F_c|^2)^2$, was minimized, where $w = 1/[(\sigma(F_o))^2 + (0.0639*P)^2 + (4.0351*P)]$ and $P = (|F_o|^2 + 2|F_c|^2)/3$. $R_w(F^2)$ refined to 0.123, with $R(F)$ equal to 0.0559 and a goodness of fit, S , = 1.37. Definitions used for calculating $R(F)$, $R_w(F^2)$ and the goodness of fit, S , are given below. The data were checked for secondary extinction but no correction was necessary. Neutral atom scattering factors and values used to calculate the linear absorption coefficient are from the International Tables for X-ray Crystallography (1992). All figures were generated using

SHELXTL/PC. Tables of positional and thermal parameters, bond lengths and angles, torsion angles and figures are found elsewhere.

2.6.3.2. Crystal Parameters

The following tables detail many important characteristics of the solved crystal structure.

Table 2.2. Crystal data and refinement for **2.34**.

Empirical formula	C ₂₆ H ₂₇ Cl ₂ Cu N ₄ O _{10.50}	
Formula weight	697.96	
Temperature	153(2) K	
Wavelength	0.71069 Å	
Crystal system	Monoclinic	
Space group	C2/c	
Unit cell dimensions	a = 27.5602(15) Å	a = 90°.
	b = 15.0350(9) Å	b = 116.196(3)°.
	c = 15.2552(10) Å	g = 90°.
Volume	5672.0(6) Å ³	
Z	8	
Density (calculated)	1.635 Mg/m ³	
Absorption coefficient	1.026 mm ⁻¹	
F(000)	2864	
Crystal size	0.22 x 0.20 x 0.18 mm	
Theta range for data collection	2.98 to 27.49°.	
Index ranges	-35<=h<=35, -19<=k<=19, -19<=l<=19	
Reflections collected	12477	
Independent reflections	6475 [R(int) = 0.0499]	
Completeness to theta = 27.49°	99.4 %	
Absorption correction	Semi-empirical from equivalents	
Max. and min. transmission	1.00 and 0.780	

Refinement method	Full-matrix least-squares on F^2
Data / restraints / parameters	6475 / 268 / 426
Goodness-of-fit on F^2	1.256
Final R indices [$I > 2\sigma(I)$]	R1 = 0.0559, wR2 = 0.1234
R indices (all data)	R1 = 0.1044, wR2 = 0.1488
Largest diff. peak and hole	0.614 and -0.498 e. \AA^{-3}

Table 2.3. Atomic coordinates ($\times 10^4$) and equivalent isotropic displacement parameters ($\text{\AA}^2 \times 10^3$) for 1. $U(\text{eq})$ is defined as one third of the trace of the orthogonalized U^{ij} tensor.

	x	y	z	$U(\text{eq})$
Cu1	6470(1)	7709(1)	1957(1)	27(1)
N1	5669(1)	8286(2)	1599(2)	27(1)
N2	6054(1)	6527(2)	1686(2)	30(1)
N3	6624(1)	7397(2)	3337(2)	26(1)
N4	6307(1)	7629(2)	560(2)	29(1)
Cl1	7480(1)	5888(1)	1442(1)	35(1)
O1	7293(1)	6574(2)	1870(2)	40(1)
O2	7281(2)	6040(2)	429(2)	74(1)
O3	8056(1)	5851(2)	1912(2)	53(1)
O4	7277(1)	5041(2)	1592(2)	54(1)
Cl2	5681(1)	3744(1)	1097(1)	43(1)
O5	5678(1)	4064(2)	213(2)	63(1)
O6	5611(4)	4410(6)	1665(6)	88(4)
O7	5251(3)	3093(5)	831(7)	55(3)
O8	6179(3)	3263(6)	1639(5)	74(3)
O6A	5374(3)	4383(5)	1370(7)	95(4)
O7A	5447(4)	2908(4)	988(6)	61(3)
O8A	6225(2)	3790(6)	1835(5)	84(3)
O1W	7088(1)	8557(2)	2243(2)	37(1)
O2W	7809(1)	8655(3)	1543(2)	73(1)

O3W	4780(4)	5171(6)	2156(9)	111(4)
C1	5492(2)	9155(2)	1468(2)	27(1)
C2	5855(2)	9848(3)	1576(3)	32(1)
C3	5686(2)	10715(3)	1459(3)	38(1)
C4	5146(2)	10920(3)	1232(3)	44(1)
C5	4791(2)	10258(3)	1119(3)	41(1)
C6	4947(2)	9361(3)	1230(3)	32(1)
C7	4587(2)	8651(3)	1083(3)	37(1)
C8	4764(2)	7800(3)	1191(3)	33(1)
C9	5318(2)	7640(3)	1463(3)	28(1)
C10	5516(2)	6694(3)	1671(3)	33(1)
C11	6394(2)	5967(3)	2541(3)	33(1)
C12	6566(2)	6527(3)	3448(3)	29(1)
C13	6653(2)	6150(3)	4347(3)	38(1)
C14	6784(2)	6687(3)	5140(3)	36(1)
C15	6830(2)	7609(3)	5047(3)	31(1)
C16	6955(2)	8198(3)	5840(3)	40(1)
C17	6999(2)	9088(3)	5725(3)	39(1)
C18	6910(2)	9428(3)	4807(3)	33(1)
C19	6780(2)	8876(3)	4021(3)	29(1)
C20	6749(1)	7956(3)	4127(3)	28(1)
C21	6003(2)	6159(3)	744(3)	34(1)
C22	6056(2)	6874(3)	112(3)	33(1)
C23	5877(2)	6760(3)	-886(3)	44(1)
C24	5964(2)	7416(3)	-1423(3)	48(1)
C25	6230(2)	8185(3)	-964(3)	42(1)
C26	6388(2)	8272(3)	23(3)	34(1)

Table 2.4. Bond lengths [\AA] and angles [$^\circ$] for **2.34**.

Cu1-N4	1.978(3)	C23-H23	0.95	C7-C6-C1	118.0(4)
Cu1-N3	2.011(3)	C24-C25	1.382(7)	C8-C7-C6	120.5(4)
Cu1-O1W	2.015(3)	C24-H24	0.95	C8-C7-H7	119.8

Cu1-N2	2.056(3)	C25-C26	1.377(5)	C6-C7-H7	119.8
Cu1-N1	2.205(3)	C25-H25	0.95	C7-C8-C9	118.8(4)
N1-C9	1.321(5)	C26-H26	0.95	C7-C8-H8	120.6
N1-C1	1.378(5)	N4-Cu1-N3	163.09(13)	C9-C8-H8	120.6
N2-C21	1.487(5)	N4-Cu1-O1W	92.29(12)	N1-C9-C8	122.8(4)
N2-C11	1.487(5)	N3-Cu1-O1W	98.79(11)	N1-C9-C10	119.3(3)
N2-C10	1.493(5)	N4-Cu1-N2	83.71(13)	C8-C9-C10	117.8(3)
N3-C12	1.338(5)	N3-Cu1-N2	81.38(12)	N2-C10-C9	115.3(3)
N3-C20	1.382(5)	O1W-Cu1-N2	159.03(12)	N2-C10-H10A	108.4
N4-C26	1.346(5)	N4-Cu1-N1	91.75(12)	C9-C10-H10A	108.4
N4-C22	1.348(5)	N3-Cu1-N1	94.36(11)	N2-C10-H10B	108.4
C11-O2	1.412(3)	O1W-Cu1-N1	117.57(11)	C9-C10-H10B	108.4
C11-O3	1.425(3)	N2-Cu1-N1	83.20(12)	H10A-C10- H10B	107.5
C11-O1	1.433(3)	C9-N1-C1	119.1(3)	N2-C11-C12	108.0(3)
C11-O4	1.448(3)	C9-N1-Cu1	109.5(2)	N2-C11-H11A	110.1
C12-O7A	1.389(5)	C1-N1-Cu1	131.3(2)	C12-C11- H11A	110.1
C12-O6	1.392(5)	C21-N2-C11	113.0(3)	N2-C11-H11B	110.1
C12-O8A	1.426(5)	C21-N2-C10	112.2(3)	C12-C11- H11B	110.1
C12-O5	1.428(3)	C11-N2-C10	110.3(3)	H11A-C11- H11B	108.4
C12-O8	1.446(5)	C21-N2-Cu1	108.8(2)	N3-C12-C13	122.7(4)
C12-O7	1.451(5)	C11-N2-Cu1	103.5(2)	N3-C12-C11	115.9(3)
C12-O6A	1.457(5)	C10-N2-Cu1	108.6(2)	C13-C12-C11	121.3(4)
O1W-H1WA	0.8	C12-N3-C20	118.8(3)	C14-C13-C12	119.5(4)
O1W-H1WB	0.8	C12-N3-Cu1	112.2(2)	C14-C13-H13	120.3
O2W-H2WA	0.8	C20-N3-Cu1	128.9(3)	C12-C13-H13	120.3
O2W-H2WB	0.8	C26-N4-C22	118.8(3)	C13-C14-C15	119.6(4)
O3W- O3W#1	1.20(2)	C26-N4-Cu1	126.3(3)	C13-C14-H14	120.2
C1-C2	1.404(5)	C22-N4-Cu1	114.8(3)	C15-C14-H14	120.2
C1-C6	1.415(5)	O2-C11-O3	111.5(2)	C14-C15-C16	122.0(4)
C2-C3	1.369(6)	O2-C11-O1	109.71(18)	C14-C15-C20	118.7(4)
C2-H2	0.95	O3-C11-O1	110.15(18)	C16-C15-C20	119.3(4)
C3-C4	1.405(6)	O2-C11-O4	108.9(2)	C17-C16-C15	120.5(4)
C3-H3	0.95	O3-C11-O4	107.97(19)	C17-C16-H16	119.8
C4-C5	1.353(6)	O1-C11-O4	108.60(17)	C15-C16-H16	119.8
C4-H4	0.95	O7A-C12-O8A	114.1(4)	C16-C17-C18	119.9(4)
C5-C6	1.404(6)	O7A-C12-O5	112.6(4)	C16-C17-H17	120
C5-H5	0.95	O6-C12-O5	113.7(4)	C18-C17-H17	120

C6-C7	1.407(6)	O8A-C12-O5	107.2(4)	C19-C18-C17	121.0(4)
C7-C8	1.352(6)	O6-C12-O8	111.1(4)	C19-C18-H18	119.5
C7-H7	0.95	O5-C12-O8	108.5(3)	C17-C18-H18	119.5
C8-C9	1.415(5)	O6-C12-O7	109.8(4)	C18-C19-C20	120.2(4)
C8-H8	0.95	O5-C12-O7	107.5(4)	C18-C19-H19	119.9
C9-C10	1.507(5)	O8-C12-O7	105.9(4)	C20-C19-H19	119.9
C10-H10A	0.99	O7A-C12-O6A	109.4(4)	N3-C20-C19	120.2(3)
C10-H10B	0.99	O8A-C12-O6A	106.5(4)	N3-C20-C15	120.6(4)
C11-C12	1.507(5)	O5-C12-O6A	106.6(4)	C19-C20-C15	119.1(3)
C11-H11A	0.99	Cu1-O1W-H1WA	122.2	N2-C21-C22	111.2(3)
C11-H11B	0.99	Cu1-O1W-H1WB	124.2	N2-C21-H21A	109.4
C12-C13	1.403(5)	H1WA-O1W- H1WB	111.5	C22-C21- H21A	109.4
C13-C14	1.364(6)	H2WA-O2W- H2WB	103	N2-C21-H21B	109.4
C13-H13	0.95	N1-C1-C2	119.9(3)	C22-C21- H21B	109.4
C14-C15	1.405(6)	N1-C1-C6	120.8(3)	H21A-C21- H21B	108
C14-H14	0.95	C2-C1-C6	119.3(3)	N4-C22-C23	121.0(4)
C15-C16	1.413(6)	C3-C2-C1	120.5(4)	N4-C22-C21	116.9(3)
C15-C20	1.419(5)	C3-C2-H2	119.8	C23-C22-C21	122.0(4)
C16-C17	1.362(6)	C1-C2-H2	119.8	C24-C23-C22	119.7(4)
C16-H16	0.95	C2-C3-C4	120.2(4)	C24-C23-H23	120.1
C17-C18	1.406(5)	C2-C3-H3	119.9	C22-C23-H23	120.1
C17-H17	0.95	C4-C3-H3	119.9	C23-C24-C25	119.5(4)
C18-C19	1.369(5)	C5-C4-C3	119.9(4)	C23-C24-H24	120.3
C18-H18	0.95	C5-C4-H4	120	C25-C24-H24	120.3
C19-C20	1.400(5)	C3-C4-H4	120	C26-C25-C24	118.4(4)
C19-H19	0.95	C4-C5-C6	121.7(4)	C26-C25-H25	120.8
C21-C22	1.495(6)	C4-C5-H5	119.2	C24-C25-H25	120.8
C21-H21A	0.99	C6-C5-H5	119.2	N4-C26-C25	122.6(4)
C21-H21B	0.99	C5-C6-C7	123.6(4)	N4-C26-H26	118.7
C22-C23	1.387(5)	C5-C6-C1	118.4(4)	C25-C26-H26	118.7
C23-C24	1.370(6)				

Table 2.5. Anisotropic displacement parameters ($\text{\AA}^2 \times 10^3$) for 1. The anisotropic displacement factor exponent takes the form: $-2\pi^2 [h^2 a^{*2} U^{11} + \dots + 2 h k a^* b^* U^{12}]$

	U ¹¹	U ²²	U ³³	U ²³	U ¹³	U ¹²
Cu1	27(1)	25(1)	27(1)	1(1)	11(1)	-1(1)
N1	25(2)	25(2)	28(2)	-2(1)	10(1)	0(1)
N2	31(2)	24(2)	35(2)	-2(1)	14(1)	0(1)
N3	21(2)	26(2)	30(2)	0(1)	10(1)	0(1)
N4	28(2)	29(2)	30(2)	1(1)	14(1)	4(1)
Cl1	36(1)	38(1)	30(1)	2(1)	13(1)	7(1)
O1	40(2)	35(2)	43(2)	-4(1)	14(1)	8(1)
O2	96(3)	91(3)	34(2)	15(2)	28(2)	41(2)
O3	34(2)	63(2)	59(2)	1(2)	17(2)	4(2)
O4	54(2)	34(2)	77(2)	-6(2)	30(2)	0(2)
Cl2	42(1)	41(1)	40(1)	-5(1)	14(1)	-7(1)
O5	84(3)	47(2)	57(2)	8(2)	30(2)	-14(2)
O6	76(8)	80(6)	149(8)	-69(6)	86(7)	-49(5)
O7	51(5)	38(5)	69(6)	5(4)	20(4)	-10(4)
O8	46(5)	131(9)	43(4)	5(5)	19(4)	17(5)
O6A	71(7)	72(6)	171(9)	-65(6)	80(6)	-40(5)
O7A	90(7)	28(4)	68(5)	0(4)	38(5)	-13(5)
O8A	58(5)	105(8)	52(5)	-14(5)	-9(4)	6(5)
O1W	38(2)	41(2)	38(2)	-9(1)	23(1)	-11(1)
O2W	46(2)	133(4)	47(2)	-6(2)	27(2)	-6(2)
O3W	142(11)	72(5)	178(13)	-26(6)	123(9)	-14(5)
C1	30(2)	24(2)	23(2)	-1(2)	8(2)	3(2)
C2	29(2)	31(2)	30(2)	1(2)	9(2)	0(2)
C3	41(2)	29(2)	37(2)	0(2)	10(2)	-3(2)
C4	56(3)	25(2)	42(3)	4(2)	15(2)	8(2)
C5	36(2)	36(2)	45(2)	4(2)	13(2)	10(2)
C6	31(2)	32(2)	28(2)	0(2)	10(2)	6(2)
C7	24(2)	45(3)	40(2)	-1(2)	12(2)	2(2)
C8	29(2)	34(2)	35(2)	0(2)	13(2)	-3(2)
C9	28(2)	28(2)	25(2)	-2(2)	11(2)	-2(2)
C10	29(2)	27(2)	41(2)	0(2)	13(2)	-6(2)
C11	39(2)	27(2)	36(2)	4(2)	19(2)	5(2)

C12	27(2)	27(2)	34(2)	2(2)	14(2)	2(2)
C13	38(2)	35(2)	40(2)	10(2)	17(2)	4(2)
C14	37(2)	38(2)	30(2)	11(2)	13(2)	3(2)
C15	23(2)	38(2)	31(2)	2(2)	11(2)	2(2)
C16	39(2)	53(3)	27(2)	6(2)	13(2)	0(2)
C17	38(2)	46(3)	28(2)	-8(2)	10(2)	-1(2)
C18	29(2)	34(2)	37(2)	-4(2)	16(2)	-2(2)
C19	27(2)	33(2)	30(2)	2(2)	14(2)	2(2)
C20	20(2)	35(2)	28(2)	0(2)	11(2)	0(2)
C21	37(2)	28(2)	36(2)	-2(2)	15(2)	1(2)
C22	34(2)	30(2)	34(2)	0(2)	15(2)	6(2)
C23	57(3)	34(3)	36(2)	-6(2)	17(2)	0(2)
C24	58(3)	55(3)	31(2)	-1(2)	20(2)	13(2)
C25	50(3)	45(3)	39(2)	9(2)	25(2)	6(2)
C26	32(2)	35(2)	36(2)	4(2)	15(2)	4(2)

Table 2.6. Hydrogen coordinates ($\times 10^4$) and isotropic displacement parameters ($\text{\AA}^2 \times 10^{-3}$) for **2.34**.

	x	y	z	U(eq)
H1WA	7286	8512	1987	55
H1WB	7213	8872	2708	55
H2WA	7845	8487	1081	109
H2WB	8107	8611	1979	109
H2	6221	9715	1731	38
H3	5935	11180	1531	46
H4	5031	11523	1158	52
H5	4426	10405	961	49
H7	4217	8769	907	45
H8	4521	7320	1087	40
H10A	5537	6519	2312	39
H10B	5246	6305	1170	39

H11A	6716	5751	2476	40
H11B	6186	5444	2580	40
H13	6621	5526	4402	45
H14	6843	6438	5752	43
H16	7009	7971	6458	48
H17	7089	9478	6263	47
H18	6940	10049	4731	40
H19	6712	9118	3402	35
H21A	5646	5866	397	41
H21B	6286	5705	875	41
H23	5694	6229	-1195	53
H24	5843	7343	-2106	58
H25	6303	8642	-1320	51
H26	6560	8807	338	41

Table 2.7. Torsion angles [°] for **2.34**.

N4-Cu1-N1-C9	88.4(2)	Cu1-N1-C1-C2	-0.9(5)	N3-C12-C13-C14	2.4(6)
N3-Cu1-N1-C9	-75.8(2)	C9-N1-C1-C6	2.6(5)	C11-C12-C13-C14	-177.0(4)
O1W-Cu1-N1-C9	-178.1(2)	Cu1-N1-C1-C6	179.4(2)	C12-C13-C14-C15	0.0(6)
N2-Cu1-N1-C9	4.9(2)	N1-C1-C2-C3	-179.2(3)	C13-C14-C15-C16	178.9(4)
N4-Cu1-N1-C1	-88.7(3)	C6-C1-C2-C3	0.5(5)	C13-C14-C15-C20	-1.2(6)
N3-Cu1-N1-C1	107.1(3)	C1-C2-C3-C4	0.2(6)	C14-C15-C16-C17	179.8(4)
O1W-Cu1-N1-C1	4.8(3)	C2-C3-C4-C5	-0.7(6)	C20-C15-C16-C17	-0.2(6)
N2-Cu1-N1-C1	-172.2(3)	C3-C4-C5-C6	0.5(6)	C15-C16-C17-C18	1.1(6)
N4-Cu1-N2-C21	15.3(2)	C4-C5-C6-C7	-177.5(4)	C16-C17-C18-C19	-0.2(6)
N3-Cu1-N2-C21	-156.7(2)	C4-C5-C6-C1	0.2(6)	C17-C18-C19-C20	-1.7(6)
O1W-Cu1-N2-C21	-64.6(4)	N1-C1-C6-C5	179.1(3)	C12-N3-C20-C19	-176.1(3)
N1-Cu1-N2-C21	107.8(2)	C2-C1-C6-C5	-0.6(5)	Cu1-N3-C20-C19	0.1(5)
N4-Cu1-N2-C11	135.7(2)	N1-C1-C6-C7	-3.1(5)	C12-N3-C20-C15	2.0(5)
N3-Cu1-N2-C11	-36.3(2)	C2-C1-C6-C7	177.2(3)	Cu1-N3-C20-C15	178.2(2)
O1W-Cu1-N2-C11	55.8(4)	C5-C6-C7-C8	179.2(4)	C18-C19-C20-N3	-179.3(3)
N1-Cu1-N2-C11	-131.8(2)	C1-C6-C7-C8	1.5(6)	C18-C19-C20-C15	2.6(5)
N4-Cu1-N2-C10	-107.1(2)	C6-C7-C8-C9	0.6(6)	C14-C15-C20-N3	0.3(5)
N3-Cu1-N2-C10	80.9(2)	C1-N1-C9-C8	-0.4(5)	C16-C15-C20-N3	-179.8(3)

O1W-Cu1-N2-C10	173.0(3)	Cu1-N1-C9-C8	-177.9(3)	C14-C15-C20-C19	178.4(4)
N1-Cu1-N2-C10	-14.6(2)	C1-N1-C9-C10	-175.9(3)	C16-C15-C20-C19	-1.7(5)
N4-Cu1-N3-C12	-6.8(5)	Cu1-N1-C9-C10	6.6(4)	C11-N2-C21-C22	-137.1(3)
O1W-Cu1-N3-C12	-137.1(2)	C7-C8-C9-N1	-1.2(6)	C10-N2-C21-C22	97.5(4)
N2-Cu1-N3-C12	21.7(2)	C7-C8-C9-C10	174.4(4)	Cu1-N2-C21-C22	-22.7(4)
N1-Cu1-N3-C12	104.1(3)	C21-N2-C10-C9	-97.9(4)	C26-N4-C22-C23	-0.8(5)
N4-Cu1-N3-C20	176.8(4)	C11-N2-C10-C9	135.2(3)	Cu1-N4-C22-C23	174.6(3)
O1W-Cu1-N3-C20	46.4(3)	Cu1-N2-C10-C9	22.4(4)	C26-N4-C22-C21	176.7(3)
N2-Cu1-N3-C20	-154.8(3)	N1-C9-C10-N2	-20.2(5)	Cu1-N4-C22-C21	-7.9(4)
N1-Cu1-N3-C20	-72.4(3)	C8-C9-C10-N2	164.1(3)	N2-C21-C22-N4	21.0(5)
N3-Cu1-N4-C26	-161.3(4)	C21-N2-C11-C12	161.9(3)	N2-C21-C22-C23	-161.5(4)
O1W-Cu1-N4-C26	-30.2(3)	C10-N2-C11-C12	-71.7(4)	N4-C22-C23-C24	1.3(6)
N2-Cu1-N4-C26	170.5(3)	Cu1-N2-C11-C12	44.4(3)	C21-C22-C23-C24	-176.2(4)
N1-Cu1-N4-C26	87.5(3)	C20-N3-C12-C13	-3.3(5)	C22-C23-C24-C25	0.0(7)
N3-Cu1-N4-C22	23.7(6)	Cu1-N3-C12-C13	179.8(3)	C23-C24-C25-C26	-1.5(7)
O1W-Cu1-N4-C22	154.8(3)	C20-N3-C12-C11	176.1(3)	C22-N4-C26-C25	-0.8(6)
N2-Cu1-N4-C22	-4.5(3)	Cu1-N3-C12-C11	-0.7(4)	Cu1-N4-C26-C25	-175.6(3)
N1-Cu1-N4-C22	-87.5(3)	N2-C11-C12-N3	-30.7(4)	C24-C25-C26-N4	2.0(6)
C9-N1-C1-C2	-177.7(3)	N2-C11-C12-C13	148.8(3)		

Table 2.8. Hydrogen bonds for 1 [\AA and $^\circ$].

D-H...A	d(D-H)	d(H...A)	d(D...A)	$\angle(\text{DHA})$
O1W-H1WA...O2W	0.80	1.86	2.641(4)	167
O2W-H2WA...O2#2	0.80	2.29	2.943(4)	140
O1W-H1WB...O4#3	0.80	2.21	2.908(4)	147
O2W-H2WB...O8A#3	0.80	1.95	2.727(6)	164
O2W-H2WB...O8#3	0.80	2.22	2.999(8)	165

Symmetry transformations used to generate equivalent atoms:

#1 $-x+1, y, -z+1/2$ #2 $-x+3/2, -y+3/2, -z$ #3 $-x+3/2, y+1/2, -z+1/2$

2.6.4. Buffer Solution

The default buffer solution was prepared by degassing acetonitrile and water via sonication for 1 hour. 4-(2-hydroxyethyl)-1-piperazineethanesulfonic acid (HEPES,

4.76g, 20 mmol) was dissolved in acetonitrile:water (3:1, 900 mL). The pH of the solution was adjusted to 7.4 by addition of NaOH (2M). The solution was filtered, and subsequently diluted to 1L with additional acetonitrile:water (3:1).

2.6.5. Binding of 2.32

A stock solution of the host was made by dissolving **2.34** (74.58 mg, 0.114 mmol) in 10 mL default buffer. To prepare the **2.32** stock solutions, the corresponding enantiomer (7.78 μL , 0.05 mmol) was dissolved to 10 mL with the default buffer. Each point on the titration was a separate solution, containing host **2.34** (43.78 μL , 0.5 mM) and the indicated amount of guest (0-2 mM) diluted to 1 mL. The titration was performed in this manner due to the small volume that the CD cuvette holds (400 μL), as well as the inability to stir the contents of the cuvette.

2.6.6. Binding of 2.33

Stock solutions of the guest were made by independently dissolving each enantiomer of **2.33** (4.52 μL , 0.05 mmol) in 10 mL of default buffer. Each point on the titration was a separate solution, containing host **2.34** (43.78 μL , 0.5 mM) and the indicated amount of guest (0-2 mM) diluted to 1 mL. The titration was performed in this manner due to the small volume that the CD cuvette holds (400 μL), as well as the inability to stir the contents of the cuvette.

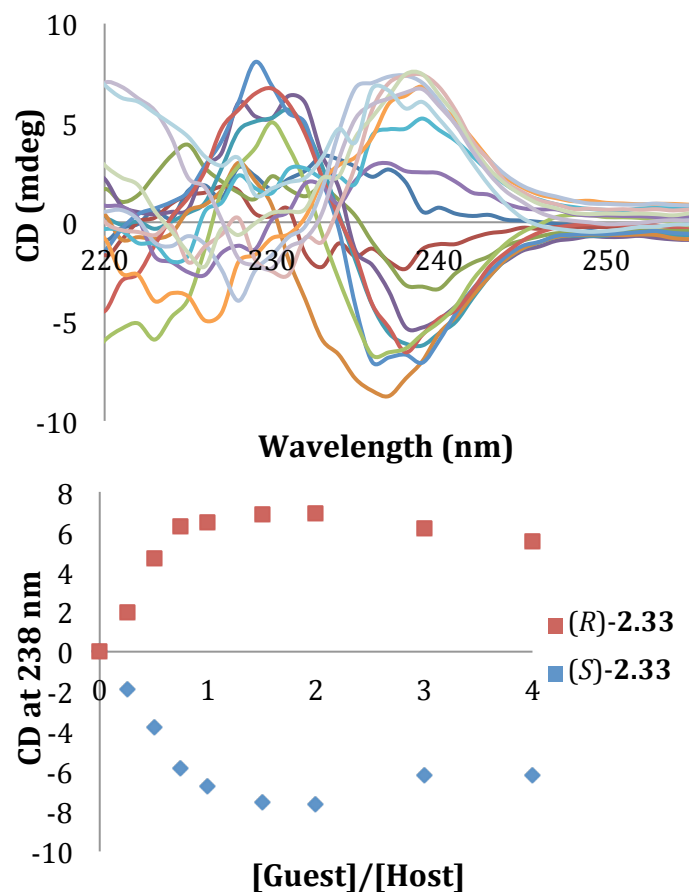


Figure 2.17. Top: CD spectra of host **2.34** (0.5 mM) upon addition of each enantiomer of **2.33** (0-2 mM) in buffer. Bottom: Change in CD signal at 238 nm recorded during this titration.

2.6.7. Binding of **2.36**

Stock solutions of the guest were made by independently dissolving each enantiomer of **2.33** (7.0 μL , 0.05 mmol) in 10 mL of default buffer. Each point on the titration was a separate solution, containing host **2.34** (43.78 μL , 0.5 mM) and the indicated amount of guest (0-2 mM) diluted to 1 mL. The titration was performed in this manner due to the small volume that the CD cuvette holds (400 μL), as well as the inability to stir the contents of the cuvette.

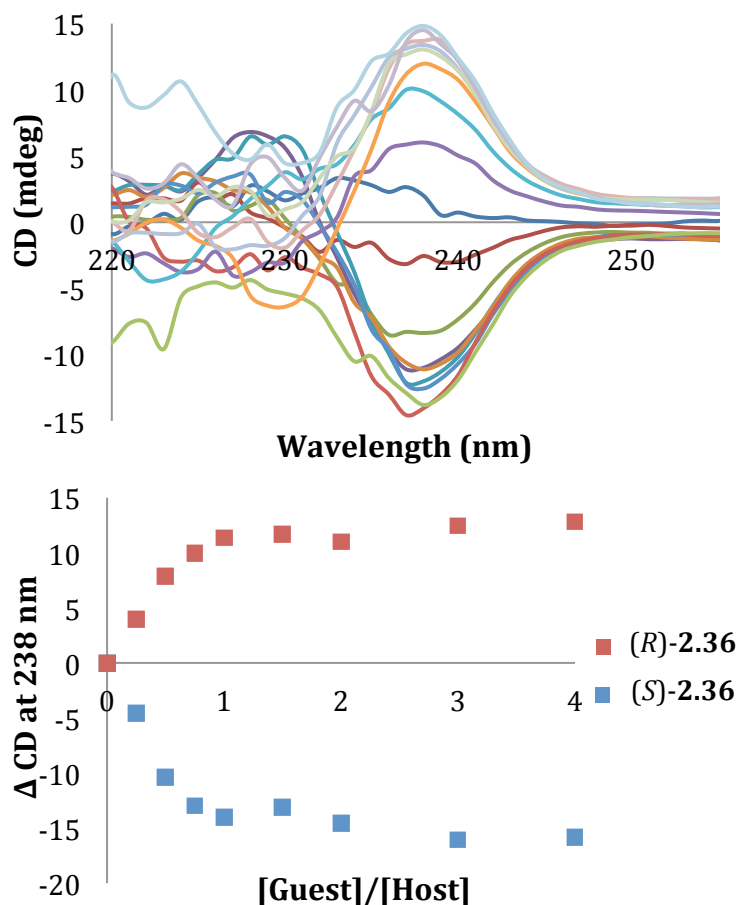


Figure 2.18. Top: CD spectra of host **2.34** (0.5 mM) upon addition of each enantiomer of **2.36** (0-2 mM) in buffer. Bottom: Change in CD signal at 238 nm recorded during this titration.

2.6.8. Binding of **2.38**

Stock solutions of the guest were made by independently dissolving either (*R*)-**2.38** (11.64 mg, 0.051 mmol) or (*S*)-**2.38** (11.27 mg, 0.049 mmol) in 10 mL of default buffer. Each point on the titration was a separate solution, containing host **2.34** (43.78 μ L, 0.5 mM) and the indicated amount of guest (0-2 mM) diluted to 1 mL. The titration was performed in this manner due to the small volume that the CD cuvette holds (400 μ L), as well as the inability to stir the contents of the cuvette.

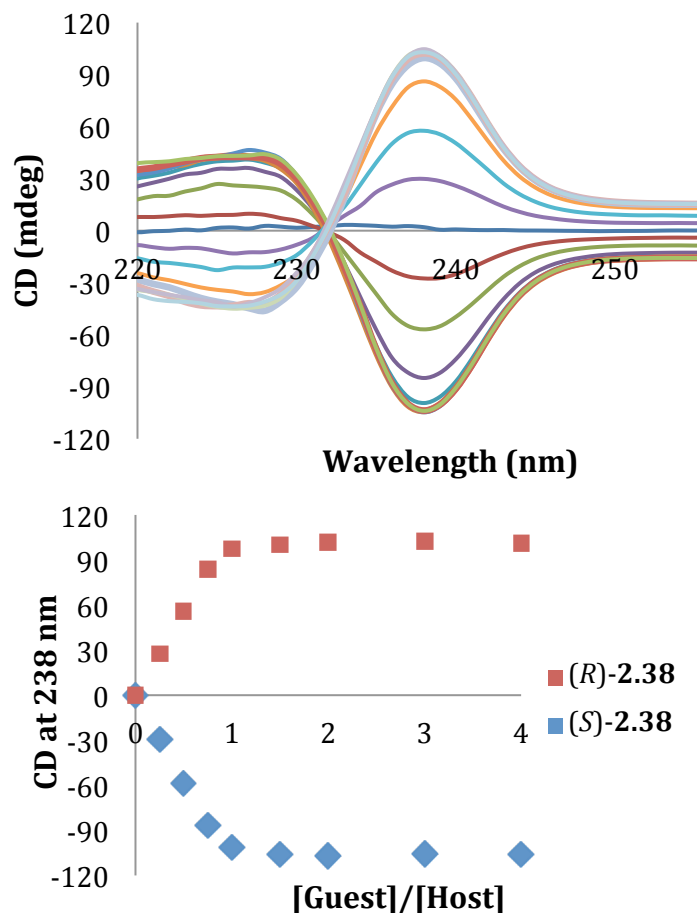


Figure 2.19. Top: CD spectra of host **2.34** (0.5 mM) upon addition of each enantiomer of **2.38** (0-2 mM) in buffer. Bottom: Change in CD signal at 238 nm recorded during this titration.

2.6.9. Binding of **2.40**

Stock solutions of the guest were made by independently dissolving each enantiomer of **2.33** (5.97 μL , 0.05 mmol) in 10 mL of default buffer. Each point on the titration was a separate solution, containing host **2.34** (43.78 μL , 0.5 mM) and the indicated amount of guest (0-2 mM) diluted to 1 mL. The titration was performed in this manner due to the small volume that the CD cuvette holds (400 μL), as well as the inability to stir the contents of the cuvette.

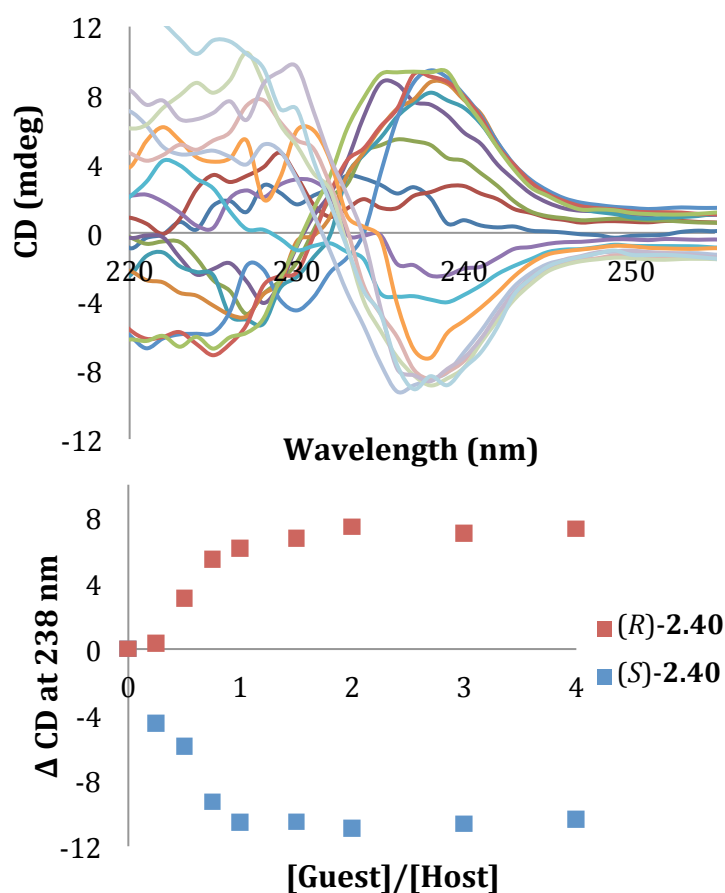


Figure 2.20. Top: CD spectra of host **2.34** (0.5 mM) upon addition of each enantiomer of **2.40** (0-2 mM) in buffer. Bottom: Change in CD signal at 238 nm recorded during this titration.

2.6.10. Guest Repetitions

A different sample was prepared for each enantiomer of all of the guests that were studied. The sample was comprised of host **2.34** (0.5 mM) and two equivalents of the desired guest (1.0 mM), dissolved in 1 mL of the default buffer. After the data had been collected, the CD values recorded between 235 and 265 nm for each sample were input into the LDA program to perform the pattern recognition analysis.

2.6.11. Analysis of Unknown 2.32 Samples

The CD signal at 238 nm was plotted against the known *ee* value for each sample, as determined by mixing different amounts of each enantiomer. Two total equivalents of the **2.32** guest (1.0 mM) were added relative to host **2.34** (0.5 mM). Three replicates were performed for each *ee* value to ensure reproducibility. A linear trendline was fit to the data, and the equation for this line, as well as correlation, are reported on the graph. The CD spectra for eight unknown samples were recorded at the same concentration of guest added as in the calibration curve. The *ee* values for the unknown samples were then determined by inputting the CD magnitude as the y-value in the best-fit trendline. The results are displayed in the accompanying table.

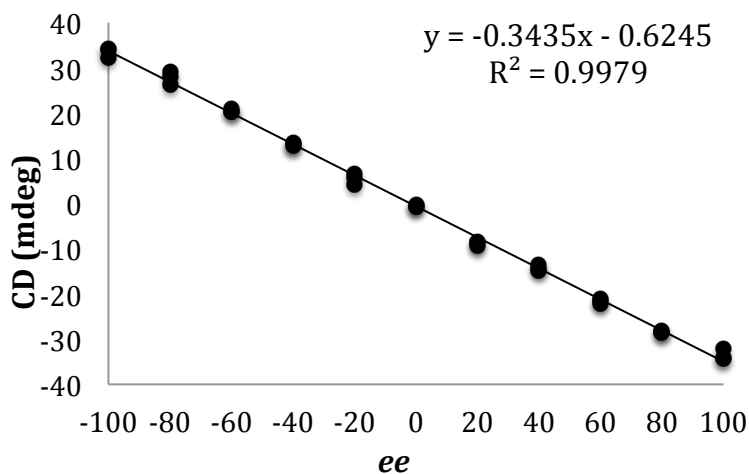


Figure 2.21. Graph relating the *ee* values of samples to the CD signals that were recorded. A value of 100% corresponds to 100% *R*, while -100% corresponds to 100% *S*.

Entry	CD at 238 nm (mdeg)	Calc. <i>ee</i>	Actual <i>ee</i>	Error
1	-2.78	6.3	7	0.7%
2	-16.9	47.3	43	4.3%
3	30.0	-89.1	-85	4.1%
4	6.3	-20.1	-18	2.1%
5	-32.4	92.5	97	4.5%
6	10.7	-33.0	-31	2.0%
7	20.8	-62.4	-59	3.4%
8	-27.5	78.3	74	4.3%

Table 2.9. Results of the analysis of the eight unknown samples. The average absolute error was determined to be 3.2% for these eight samples.

2.6.12. Analysis of Unknown 2.36 Samples

The CD signal at 238 nm was plotted against the known *ee* value for each sample, as determined by mixing different amounts of each enantiomer. Two total equivalents of the **2.36** guest (1.0 mM) were added relative to host **2.34** (0.5 mM). Three replicates were performed for each *ee* value to ensure reproducibility. A linear trendline was fit to the data, and the equation for this line, as well as correlation, are reported on the graph. The CD spectra for eight unknown samples were recorded at the same concentration of guest added as in the calibration curve. The *ee* values for the unknown samples were then determined by inputting the CD magnitude as the y-value in the best-fit trendline. The results are displayed in the accompanying table.

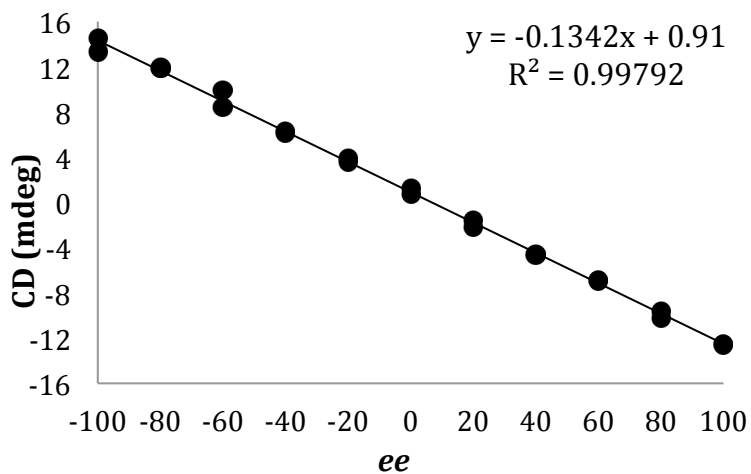


Figure 2.22. Graph relating the *ee* values of samples to the CD signals that were recorded. A value of 100% *ee* corresponds to 100% *R*, while -100% *ee* corresponds to 100% *S*.

Entry	CD at 238 nm (mdeg)	Calc. <i>ee</i>	Actual <i>ee</i>	Error
1	2.8	-14.2	-19	4.8%
2	12.6	-86.9	-90	3.1%
3	-7.8	65.1	59	6.1
4	-0.6	11.4	10	1.4%
5	10.4	-70.5	-71	0.5%
6	-10.3	83.3	84	0.7%
7	6.2	-39.1	-43	3.9%
8	-0.4	9.5	22	12.5%

Table 2.10. Results of the analysis of eight unknown samples. The average absolute error was determined to be 4.1% for these eight samples.

2.6.13. Analysis of Unknown 2.38 Samples

The CD signal at 238 nm was plotted against the known *ee* value for each sample, as determined by mixing different amounts of each enantiomer. Two total equivalents of the **2.38** guest (1.0 mM) were added relative to host **2.34** (0.5 mM). Three replicates were performed for each *ee* value to ensure reproducibility. A linear trendline was fit to the data, and the equation for this line, as well as correlation, are reported on the graph. The CD spectra for eight unknown samples were recorded at the same concentration of guest added as in the calibration curve. The *ee* values for the unknown samples were then determined by inputting the CD magnitude as the y-value in the best-fit trendline. The results are displayed in the accompanying table.

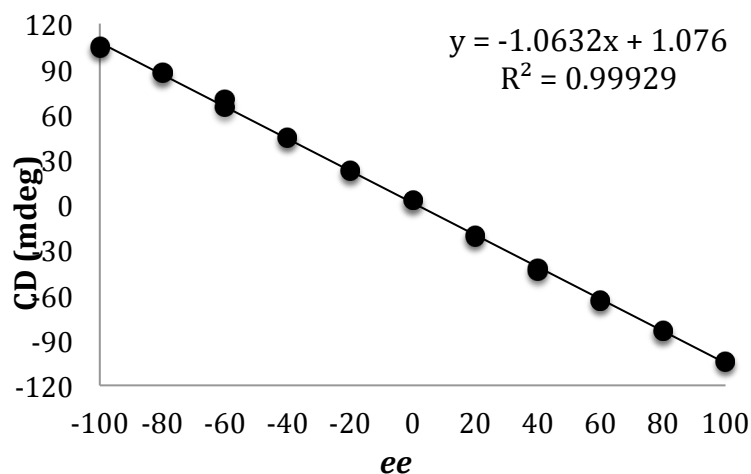


Figure 2.23. Graph relating the *ee* values of samples to the CD signals that were recorded. A value of 100% *ee* corresponds to 100% *R*, while -100% *ee* corresponds to 100% *S*.

Entry	CD at 238 nm (mdeg)	Calc. <i>ee</i>	Actual <i>ee</i>	Error
1	89.2	-82.9	-88	5.1%
2	-27.1	26.5	27	0.5%
3	34.5	-31.4	-31	0.4%
4	17.0	-15.0	-12	3.0%
5	-92.5	88.0	92.0	4.0%
6	-3.1	3.9	4	0.1%
7	-65.1	62.2	63.0	0.8%
8	52.8	-48.7	-49	0.3%

Table 2.11. Results of the analysis of eight unknown samples. The average absolute error was determined to be 4.1% for these eight samples.

2.7. REFERENCES FOR CHAPTER 2

- (1) Crabtree, R. H. *Chem Commun* **1999**, 1611.
- (2) Pescarmona, P. P.; van der Waal, J. C.; Maxwell, I. E.; Maschmeyer, T. *Catal Lett* **1999**, *63*, 1.
- (3) Wahler, D.; Reymond, J. L. *Curr Opin Biotech* **2001**, *12*, 535.
- (4) Lefort, L.; Boogers, J. A. F.; de Vries, A. H. M.; de Vries, J. G. *Top Catal* **2006**, *40*, 185.
- (5) Stambuli, J. P.; Hartwig, J. F. *Curr Opin Chem Biol* **2003**, *7*, 420.
- (6) Gennari, C.; Piarulli, U. *Chem Rev* **2003**, *103*, 3071.
- (7) de Vries, J. G.; Lefort, L. *Chem-Eur J* **2006**, *12*, 4722.
- (8) Jakel, C.; Paciello, R. *Chem Rev* **2006**, *106*, 2912.
- (9) Pamies, O.; Dieguez, M. *Chem-Eur J* **2008**, *14*, 944.

- (10) Traverse, J. F.; Snapper, M. L. *Drug Discov Today* **2002**, 7, 1002.
- (11) Tarasow, T. M.; Tarasow, S. L.; Eaton, B. E. *Nature* **1997**, 389, 54.
- (12) Zhu, L.; Anslyn, E. V. *J Am Chem Soc* **2004**, 126, 3676.
- (13) Zhu, L.; Zhong, Z. L.; Anslyn, E. V. *J Am Chem Soc* **2005**, 127, 4260.
- (14) Lavigne, J. J.; Anslyn, E. V. *Angew Chem Int Edit* **1999**, 38, 3666.
- (15) Lavigne, J. J.; Anslyn, E. V. *Angew Chem Int Edit* **2001**, 40, 3119.
- (16) Wiskur, S. L.; Ait-Haddou, H.; Lavigne, J. J.; Anslyn, E. V. *Accounts Chem Res* **2001**, 34, 963.
- (17) Nguyen, B. T.; Anslyn, E. V. *Coordin Chem Rev* **2006**, 250, 3118.
- (18) Kacprzak, K.; Grajewski, J.; Gawronski, J. *Tetrahedron-Asymmetr* **2006**, 17, 1332.
- (19) Folmer-Andersen, J. F.; Lynch, V. M.; Anslyn, E. V. *J Am Chem Soc* **2005**, 127, 7986.
- (20) Folmer-Andersen, J. F.; Kitamura, M.; Anslyn, E. V. *J Am Chem Soc* **2006**, 128, 5652.
- (21) Mei, X.; Wolf, C. *Tetrahedron Lett* **2006**, 47, 7901.
- (22) Leung, D.; Folmer-Andersen, J. F.; Lynch, V. M.; Anslyn, E. V. *J Am Chem Soc* **2008**, 130, 12318.
- (23) Liu, S. L.; Pestano, J. P. C.; Wolf, C. *J Org Chem* **2008**, 73, 4267.
- (24) Amendola, V.; Fabbrizzi, L.; Mangano, C.; Pallavicini, P.; Poggi, A.; Taglietti, A. *Coordin Chem Rev* **2001**, 219, 821.
- (25) Carrell, C. J.; Carrell, H. L.; Erlebacher, J.; Glusker, J. P. *J Am Chem Soc* **1988**, 110, 8651.
- (26) Zahn, S.; Canary, J. W. *Org Lett* **1999**, 1, 861.
- (27) Holmes, A. E.; Zahn, S.; Canary, J. W. *Chirality* **2002**, 14, 471.
- (28) Zhang, J.; Holmes, A. E.; Sharma, A.; Brooks, N. R.; Rarig, R. S.; Zubieta, J.; Canary, J. W. *Chirality* **2003**, 15, 180.
- (29) Rukachaisirikul, V.; Koert, U.; Hoffmann, R. W. *Tetrahedron* **1992**, 48, 4533.

- (30) Fabbrizzi, L.; Marcotte, N.; Stomeo, F.; Taglietti, A. *Angew Chem Int Edit* **2002**, *41*, 3811.
- (31) Nieto, S.; Lynch, V. M.; Anslyn, E. V.; Kim, H.; Chin, J. *J Am Chem Soc* **2008**, *130*, 9232.
- (32) Nieto, S.; Lynch, V. M.; Anslyn, E. V.; Kim, H.; Chin, J. *Org Lett* **2008**, *10*, 5167.
- (33) Nieto, S.; Dragna, J. M.; Anslyn, E. V. *Chem-Eur J* **2010**, *16*, 227.
- (34) Leung, D.; Anslyn, E. V. *Org Lett* **2011**, *13*, 2298.
- (35) You, L.; Berman, J. S.; Anslyn, E. V. *Nat Chem* **2011**, *3*, 943.
- (36) Dragna, J. M.; Pescitelli, G.; Tran, L.; Lynch, V. M.; Anslyn, E. V.; Di Bari, L. *J Am Chem Soc* **2012**, *134*, 4398.
- (37) Berova, N.; Nakanishi, K. o.; Woody, R. *Circular dichroism : principles and applications*; 2nd ed.; Wiley-VCH: New York, 2000.
- (38) Davydov, A. S. *Theory of molecular excitons*; McGraw-Hill: New York,, 1962.
- (39) Harada, N.; Nakanishi, K. o. *Circular dichroic spectroscopy : exciton coupling in organic stereochemistry*; University Science Books: Mill Valley, CA, 1983.
- (40) Holmes, A. E.; Das, D.; Canary, J. W. *J Am Chem Soc* **2007**, *129*, 1506.
- (41) Canary, J. W.; Mortezaei, S.; Liang, J. A. *Coordin Chem Rev* **2010**, *254*, 2249.
- (42) Hor, K.; Gimple, O.; Schreier, P.; Humpf, H. U. *J Org Chem* **1998**, *63*, 322.
- (43) Matile, S.; Berova, N.; Nakanishi, K.; Novkova, S.; Philipova, I.; Blagoev, B. *J Am Chem Soc* **1995**, *117*, 7021.
- (44) Matile, S.; Berova, N.; Nakanishi, K.; Fleischhauer, J.; Woody, R. W. *J Am Chem Soc* **1996**, *118*, 5198.
- (45) Tabei, J.; Shiotsuki, M.; Sanda, F.; Masuda, T. *Macromolecules* **2005**, *38*, 9448.
- (46) Gawronski, J.; Grajewski, J.; Drabowicz, J.; Mikolajczyk, M. *J Org Chem* **2003**, *68*, 9821.
- (47) Dalisay, D. S.; Tsukamoto, S.; Molinski, T. F. *J Nat Prod* **2009**, *72*, 353.
- (48) Pfeiffer, P.; Quehl, K.; Tappermann, F. *Ber. Dtsch. Chem. Ges. B* **1930**, *63B*, 1301.

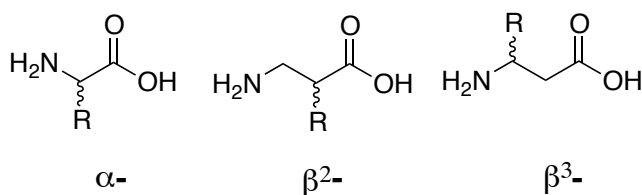
- (49) Wei, N.; Murthy, N. N.; Karlin, K. D. *Inorg Chem* **1994**, *33*, 6093.
- (50) Holmes, A. E.; Simpson, S. A.; Canary, J. W. *Monatsh Chem* **2005**, *136*, 461.
- (51) Castagnetto, J. M.; Xu, X.; Berova, N. D.; Canary, J. W. *Chirality* **1997**, *9*, 616.
- (52) Johnson, R. A. W., D. W. *Applied Multivariate Statistical Analysis*; Prentice-Hall: New Jersey, 1982.
- (53) Buryak, A.; Severin, K. *J Am Chem Soc* **2005**, *127*, 3700.
- (54) Cahn, R. S.; Ingold, C.; Prelog, V. *Angew. Chem., Int. Ed. Engl.* **1966**, *5*, 385.
- (55) Taft, R. W., Jr. *Steric effects in organic chemistry* **1956**, 556.
- (56) Lee, S. J.; Lin, W. B. *J Am Chem Soc* **2002**, *124*, 4554.
- (57) Karlin, K. D.; Wei, N.; Jung, B.; Kaderli, S.; Niklaus, P.; Zuberbuhler, A. D. *J Am Chem Soc* **1993**, *115*, 9506.
- (58) Otwinowski, Z.; Minor, W. *Macromolecular Crystallography, Pt A* **1997**, 276, 307.
- (59) Altomare, A.; Giacovazzo, C.; Guagliardi, A.; Moliterni, A. G. G.; Rizzi, R. *J Appl Crystallogr* **1999**, *32*, 963.

Chapter 3: Applications of The Copper(II)-Based Host to Amino Acid Differentiation and Synthetic Methodology Development

3.1. INTRODUCTION

The above research demonstrated the application of an achiral copper(II) containing complex to the *ee* determination of chiral carboxylic acids. Further, and perhaps more unexpected, this host served as a means to differentiate the identity of substrates through pattern recognition. This differentiation was achieved as a result of different shapes and magnitudes of the CD signals caused by the various groups attached to the stereocenter. After establishing this method for simple carboxylic acids, the focus of the research was shifted towards biologically relevant amino acids. The naturally occurring α -amino acids are the building blocks for peptides and proteins,¹ and serve as chiral starting materials for a variety of catalytic transformations and syntheses.² They are particularly interesting synthetic targets since only the L-enantiomer of the α -amino acids is commercially available. This means that the D-enantiomer of α -amino acids, and both enantiomers of β -amino acids must be prepared synthetically.^{3,4}

Addition of a single methylene unit between the carboxylate and amine termini of an α -amino acid gives rise to what is known as a β -amino acid. As can be imagined, the addition of the extra methylene gives two different carbon atoms that may serve as stereocenters. When the carbon closest to the carboxylic acid terminus is a stereocenter the amino acid is known as a β^2 -amino acid (**Scheme 3.1**). Alternatively, when the stereocenter is closest the amine terminus, this amino acid is known as a β^3 -amino acid.⁵ When the β^3 -amino acid has the same side chain as its α -amino acid counterpart it is known as a β -homoamino acid. To this end, β^3 -leucine will be herein referred to as β -homoleucine.



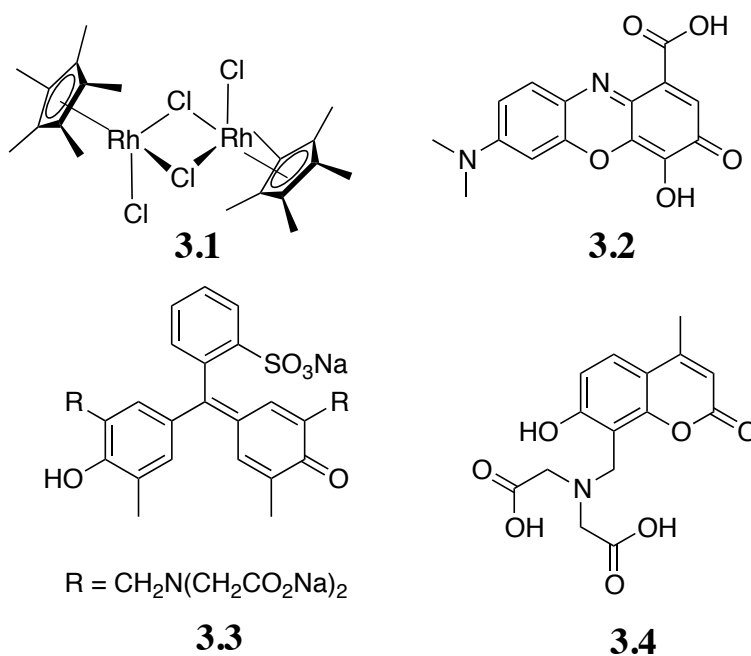
Scheme 3.1. Structures of α - and β -amino acids.

Historically, β -amino acids have received a very limited amount of research interest because they occur rarely in nature. But, much recent effort has been given to incorporating them into peptides. The resultant β -peptides and mixed α/β -peptides have shown very unique properties and structural features.⁶⁻¹⁰ Although significant effort has been directed toward differentiating α -amino acids, a literature search turned up no published reports for differentiating β -amino acids. It is therefore desirable to extend these methods so that they further encompass β -homoamino acids.

Several methods that have been reported to differentiate α -amino acids rely on indicator displacement assays (IDAs).¹¹⁻¹⁶ Recognition units known to interact with side chains of the amino acids are commonly included in order to enhance specificity of the receptor to the host structure. One such example differentiating hydrophobic amino acids was published by the Anslyn group.¹² The successful application of a copper(II)-based host allowed for each of the target guests to be well separated with excellent chemoselectivity.

A sensing system was constructed by Buryak and Severin from a variety of commercially available pH indicators and metal complexes (**Scheme 3.2**).¹⁴ Initially, the amino acid guests were classified into groups based on their affinity for a rhodium(III)-centered host. The guests within these groups were then subjected to a series of IDAs at different pH values and with different indicators. It was observed that the response seen in the UV spectrum was unique for each of the amino acid guests at differing pH values

of the host-indicator complexes. Application of the pattern recognition protocol linear discriminant analysis (LDA) gave good differentiation of each amino acid within each affinity group. In this study, good differentiation was observed between the amino acid guests considered in this study. The researchers, however, did not explore enantioselective discrimination.



Scheme 3.2. Components for differentiation of amino acids by an IDA: rhodium host **3.1**, indicators gallocyanine (**3.2**) xylenol orange (**3.3**), and calcein blue (**3.4**).

3.2. DESIGN CRITERIA FOR AMINO ACID RECOGNITION

The approach under discussion makes use of the same achiral copper(II)-containing host **2.34** that was used in the previous studies. This host has been identified as an ECCD sensor to rapidly assess the *ee* and identity of chiral carboxylic acids.¹⁷ Each enantiomer of guest gave rise to an ECCD couplet, and the spectra observed for a pair of enantiomers were equal and opposite. In specific, the (*R*)-enantiomer of the simple

carboxylic acids gave a negative couplet. This is indicative of a *P*-type or right-handed helix. The opposite trend was observed with the (*S*)-enantiomer, whose positive couplet indicated an *M*-type or left-handed helix. This strategy has been applied to a variety of assays to give enantiodiscrimination of a wide variety of guest structures.¹⁸⁻²³ As noted in Chapter 2, it is expected that **2.34** will rapidly interconvert between the *P* and *M* helices in solution. This trend has been observed for several other similar molecules.²⁴⁻²⁶

3.2.1. Boc-Protected α -Amino Acids

Initial studies undertaken were aimed at recording CD spectra for solutions containing various mixtures of host **2.34** and each enantiomer of the α -amino acid guest Boc-protected proline. These spectra are reported in **Figure 3.1**. As reported previously, the host showed no CD signals in the absence of chiral analytes. This observation confirms that the host rapidly interconverts between the two helices in solution, giving rise to a racemic mixture of these helices. Additionally, neither enantiomer of the guest gave CD signals above 230 nm. No signals were observed with the guests and Cu(ClO₄)₂, confirming that any observed signals are a result of chiral complex formation between host **2.34** and the Boc-protected proline guest. The CD spectra were taken for solutions containing host **2.34** and two equivalents of either enantiomer of the proline guest. To ensure that the carboxylate was the major species present in solution, the 75% acetonitrile and 25% water solvent was buffered to a pH of 7.4 with 20 mM 4-(2-hydroxyethyl)-1-piperazineethanesulfonic acid (HEPES). The deprotonated carboxylate anion is expected to have enhanced binding with the copper(II) metal center of the host species relative to the binding of a neutral carboxylic acid.

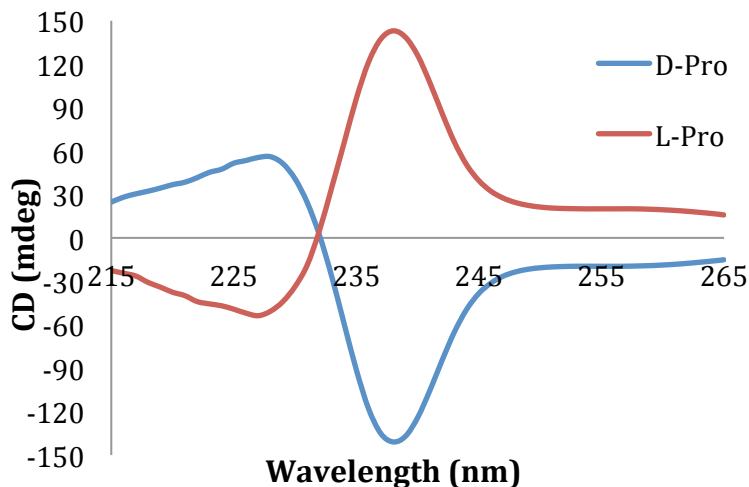


Figure 3.1. CD spectrum of host **2.34** (0.5 mM) with indicated enantiomer of Boc-proline (1.0 mM) in the default buffer (75% acetonitrile, 25% water with 20 mM HEPES buffer at pH 7.4).

As expected, an ECCD couplet arose when the complex formed, with a λ_{max} of 238 nm for the first Cotton effect (CE). This signal was the largest, as observed for the simple carboxylic acids, and will be used herein to denote the response of the amino acid guests. **Figure 3.1** shows that the D- and L-enantiomers of proline formed enantiomeric complexes, evidenced by the equal and opposite spectra. The negative couplet recorded for D-proline indicates formation of a *P*-type helix, while the positive couplet for L-proline is indicative of an *M*-type helix. The direction of the twist formed by these complexes is consistent with what was observed for homochiral species of the simple carboxylic acids.

A model was proposed for this interaction, differing slightly from the one put forth in Chapter 2. The Newman projection, looking down the copper to nitrogen bond axis, puts the substituent groups attached to the stereocenter with the largest substituent group directed at the pyridine ring (**Figure 3.2**). The chromophores of the molecule then twist away from steric interaction with the substituents, with the arrangement around the

stereocenter dictating the direction of the twist. This observation is again consistent with the picture found for the homochiral simple carboxylic acid guests, thus providing evidence that this system behaves in the same fashion as that reported in the previous chapter.

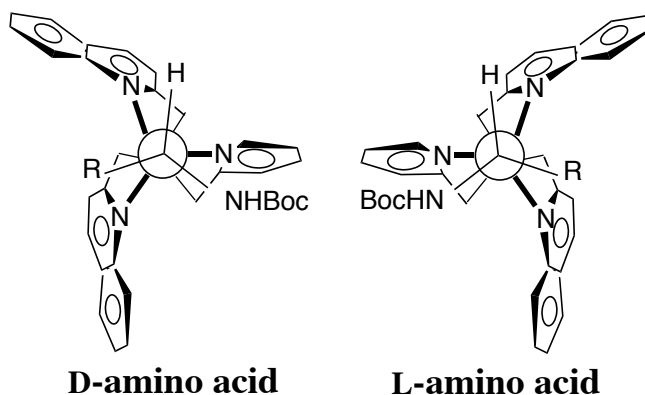


Figure 3.2. Model predicting the complex helicity with the guest bound, with the D-amino acid leading to a *P*-type helix and the L-amino acid preferring the *M*-type.

Titration were performed independently for each enantiomer of the Boc-protected proline guest into a solution containing host **2.34**. The signal saturated when one equivalent of guest had been added relative to the host, meaning that the observed CD signal above this point do not have any dependence on the concentration of guest (**Figure 3.3**). This point is important to future analyses, as it is desirable to have a CD signal that is concentration independent. As expected, the plot of the CD signal as a function of amount of Boc-protected proline guest added were equal and opposite for the two enantiomers. The magnitude of the CD signal was around 160 millidegrees at the longest wavelength CE.

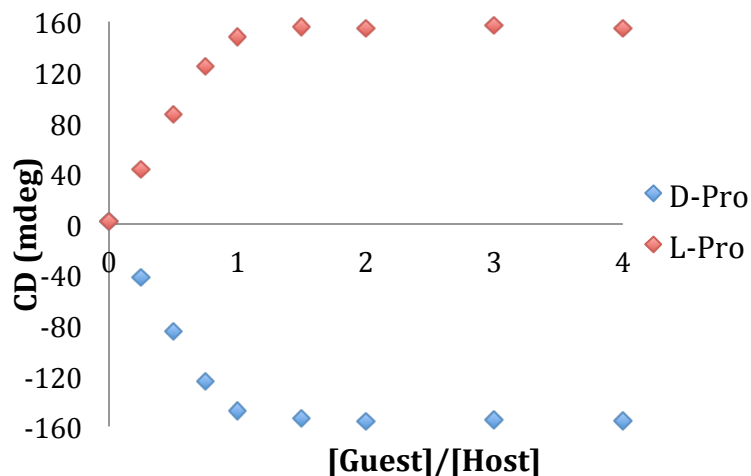


Figure 3.3. CD signal with addition of increasing amounts of indicated enantiomer of Boc-protected proline (0-2 mM) into host **2.34** (0.5 mM) in default buffer.

It was postulated that different side chains on the amino acids would give different signal magnitudes, since it had previously been proven that sterics play a large role in the size of the signal. In order to test this theory, CD spectra were recorded for each enantiomer of additional Boc-protected amino acids. Two equivalents of each enantiomer of the amino acid guest, namely leucine and serine, were separately added to a solution containing host **2.34**. As with previous studies, twofold excess of guest was applied in order to get rid of concentration dependence. It was observed that homochiral amino acid guests gave CD spectra that were of the same sign for each enantiomer, with all of the D-enantiomers giving a negative CD couplet and the L-enantiomers yielding a positive couplet. Additionally, each pair of guest enantiomers gave equal and opposite CD signals. As is demonstrated in **Figure 3.4**, each guest gave a signal that had a distinct magnitude and shape. These results indicate that the absolute configuration of the amino acid guest can be readily determined by the sign of the CD couplet produced.

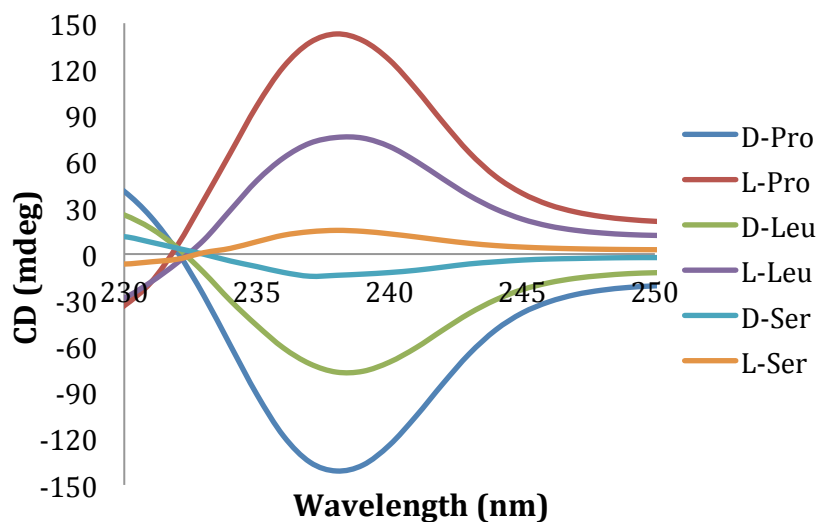


Figure 3.4. CD spectra of host **2.34** (0.5 mM) with indicated enantiomer of three different guests (1.0 mM) in the default buffer.

Once the general response of the receptor to the amino acids had been analyzed, the scope of the analysis was expanded to encompass several other amino acid guests. To this end, samples of all of the additional amino acid guests were prepared. The individual members of the guest set were selected to include representatives from several different classes of amino acids. Five duplicate samples were prepared for each enantiomer of each guest. The CD spectra of these samples were recorded for each enantiomer of the 10 guests, making up a total of 100 samples for analysis. The data from these spectra were recorded from 235 to 265 nm in 1 nm intervals, and then input in order to carry out the differentiation analysis. These wavelengths represent the greatest variance among the dataset without any spectral overlap from absorbances of the side chains of the amino acid guests. As with the simple carboxylic acids, linear discriminant analysis (LDA) was chosen to perform the pattern recognition analysis.

Successful differentiation of the chiral α -amino acids was achieved using host **2.34**, as is demonstrated by the LDA plot obtained from the replicate CD spectra of these

acids (**Figure 3.5**). The vast majority of the data points were well differentiated, with jack-knife analysis of 99%. A small extent of overlap was observed between phenylalanine and histidine. The planarity of the aromatic side chain likely leads to the similarity observed. The F1 axis corresponds to the size of the recorded CD signal, and represents the greatest amount of variance between groups in the dataset. All of the L-amino acids appear on the right or positive side, while their D-enantiomers appear on the left or negative side. The second axis, F2, represents a much smaller amount of variance. The differentiation along this axis can be attributed to the subtle difference in the shapes of the CD spectra. Enantiomers of the same guest are found reflected through the origin of the plot.

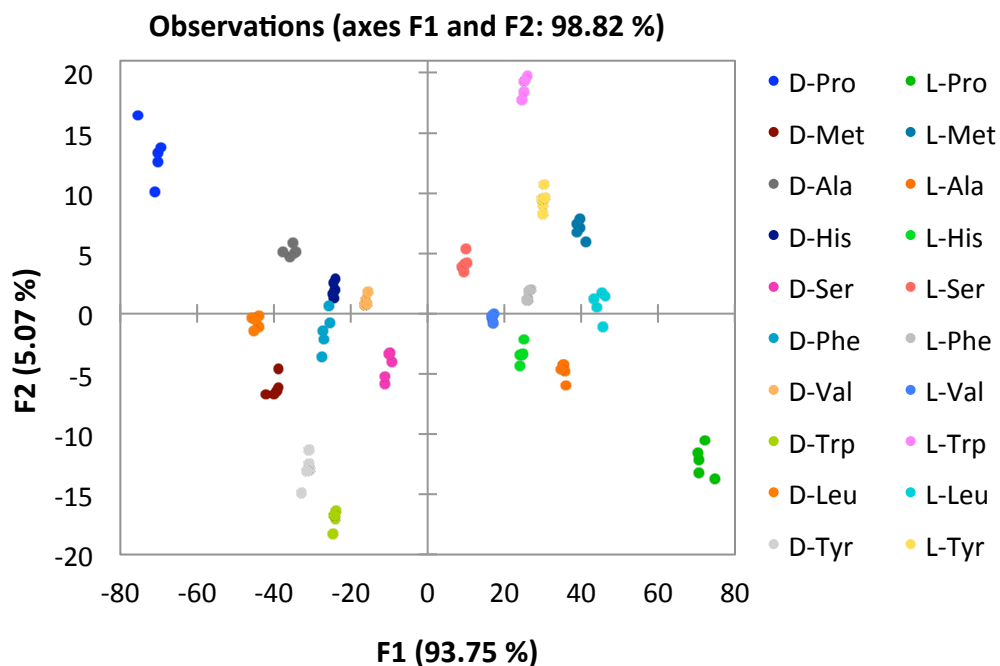


Figure 3.5. Two-dimensional LDA plot depicting the response of host **2.34** to each of the Boc-protected amino acid guests.

Several similar types of groups were classified together in this LDA plot. The only tertiary amine analyzed, Boc-protected proline, gave the largest signal. The cyclic structure provides a rigid scaffold, from which arose this substantial bias. This guest was found the furthest from the origin on the F1 axis. The next three Boc-protected amino acids that were encountered moving along the F1 axis toward the origin are alanine, leucine, and methionine. Each of these hydrophobic amino acids has a methylene carbon attached directly to the stereocenter, with two having longer alkyl chains. Since the magnitude of the signal is related to the steric size, it follows that they should be differentiated to similar extents along the F1 axis. They are still well differentiated along the F2 axis, with methionine being the most positive and alanine the most negative. The relative size of the substituent group, in molecular weight, increases in the same order as they appear on the F2 axis. This indicates that the shape of the signal also reflects the size of the groups.

The next group of Boc-protected α -amino acids that is encountered while continuing toward the origin is the phenylalanine, tryptophan, tyrosine, and histidine. It was previously mentioned that there was some overlap between phenylalanine and histidine, but it appears that every aromatic amino acid that was studied gave similar differentiation along the F1 axis. As with the previous group of hydrophobic amino acids, these groups were well differentiated along the F2 axis. The largest side chain, namely the indole ring of tryptophan, appears at the largest positive value. The histidine, the smallest of the aromatic side chains, appears furthest toward the negative side. The arrangement of these groups along the F2 axis is also consistent with the arrangement of group size that was reported for the previously presented group of hydrophobic amino acid guests.

The final two amino acids that are encountered are valine and serine. Valine has a methine attached to the stereocenter, and is expected to be more sterically encumbered than the other amino acids that have a methylene directly attached. The hydroxyl group in the serine guest may be much larger than anticipated in aqueous media, as a result of hydrogen binding. Thus, this amino acid will have a greater size than others with a similar methylene attached to the stereocenter. It is likely that the small observed CD signals for these more sterically bulky guests are a result of their similarity to the Boc-protected amine group. As the size of the largest and second largest groups, ignoring the carboxylate, on the stereocenter becomes similar the system is expected to have less of a bias to create one helix preferentially. After successfully differentiating the α -amino acid substrates, the focus of study was directed toward β -chiral analytes.

3.2.2. Boc-Protected β -Homoamino Acids

As was mentioned previously, β -homoamino acids contain the same side chains as their α -amino acid counterparts. The only difference between the two structures is the methylene homologation between the stereocenter geminal to the amine and the carboxylate terminus. The extra methylene addition was anticipated to give the molecule greater degrees of rotational freedom. The extra free rotation was postulated to diminish the magnitude of the observed CD signals, since the signal has a large steric component. The further removed the stereocenter was from the metal binding site the less interaction it was expected to have with the quinoline chromophores. In order to test the hypotheses that β -chiral species would give a CD signal and that said signal would have a smaller magnitude, Boc-protected β -homoleucine was studied as a guest.

Initial studies examined the CD spectra recorded for the addition of two equivalents of each enantiomer of β -homoleucine to host **2.34**. An ECCD couplet was

observed, analogous to that seen for α -leucine and other amino acids (**Figure 3.6**). The first CE had a λ_{max} of 238 nm, and the magnitude of the first CE was much larger than the second. Hence, the first peak will be used to represent the response of the receptor to the guest. The hypothesis of a diminished signal proved correct for β -homoleucine, as the signal was smaller than that of α -leucine by a factor of two. The signals observed for the enantiomers D- β -homoleucine and L- β -homoleucine were equal and opposite mirror images of each other, indicating the formation of enantiomeric complexes.

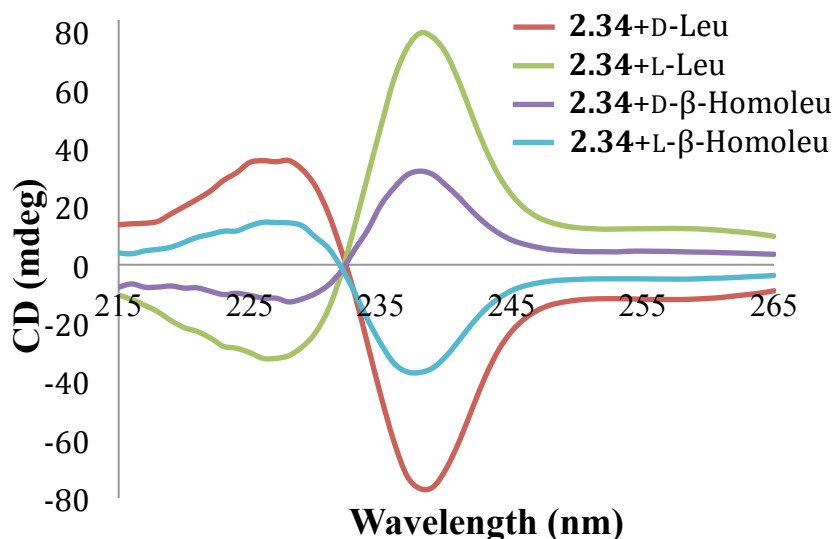


Figure 3.6. CD spectra of host **2.34** (0.5 mM) with indicated guest (1.0 mM) in the default buffer.

One major difference between the α -amino acids and the β -homoamino acids was the sign of the CD signal that was recorded. The homochiral α - and β -homo-amino acids gave opposite signs of the CD signal. The D-enantiomer of α -leucine gave a negative CD couplet indicative of a *P*-type propeller, whereas D-enantiomer of β -homoleucine gave a positive CD couplet indicating of an *M*-type propeller. Evidently, the extra methylene

both decreases the amount of twist and biases the system to reverse the direction of the propeller twist to avoid steric interactions. In order to confirm that this trend was general among all β -homoamino acids, CD spectra were recorded for both enantiomers of several additional substrates (**Figure 3.7**). These additional β -homoamino acids, namely β -homoalanine, β -homophenylalanine, and β -homovaline, were chosen because both of their enantiomers are commercially available. The recorded spectra were taken with two equivalents of guest relative to the amount of host **2.34**. The spectra were equal and opposite for the enantiomers of each guest, and this trend was general across the range of guests studied. The homochiral D- β -homoamino acids all gave a positive first CE, while the L- β -homoamino acids all showed a negative first CE. Thus, the opposite signs for the CD signals for the β -homoamino acids is generally observed across these guests. This general response allowed the absolute stereochemical configuration to be assigned based upon the sign of this response.

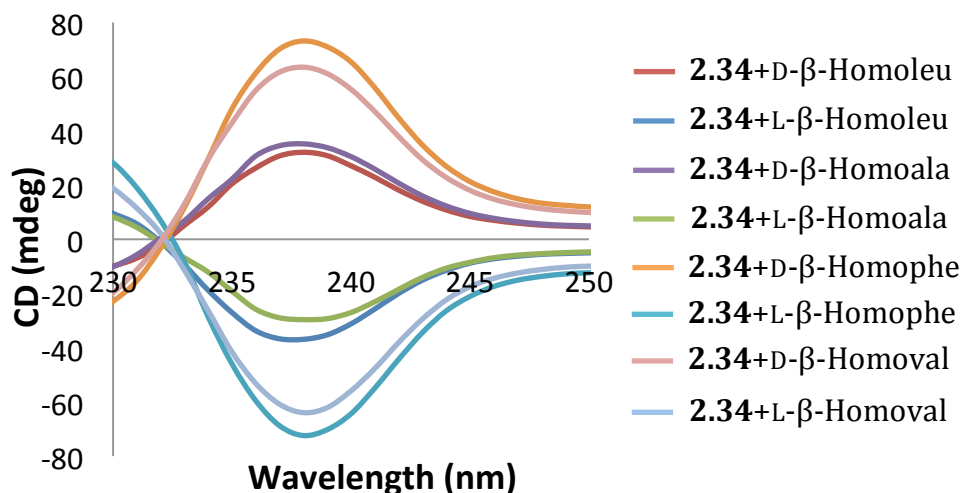


Figure 3.7. CD spectra for each enantiomer of each indicated guest (1.0 mM) and host **2.34** (0.5 mM) in default buffer.

As shown previously, it was necessary to confirm that two equivalents of guest that had been applied relative to host were sufficient for the system to be concentration independent. To this end, a titration was performed adding Boc-protected β -homoleucine to host **2.34** in buffer (**Figure 3.8**). As had been observed for the α -leucine counterpart, the CD signal for β -homoleucine saturated when one equivalent of guest had been added. This result showed that the data previously recorded was representative of the maximum magnitude of the CD signal, and established two equivalents of guest as the proportion that would be used in future studies. Once signal saturation had been confirmed, the focus was turned toward using pattern recognition protocols to find the identity of the β -homoamino acids. The variety of different magnitudes and shapes of the CD signals again pointed toward LDA as a viable means of analysis.

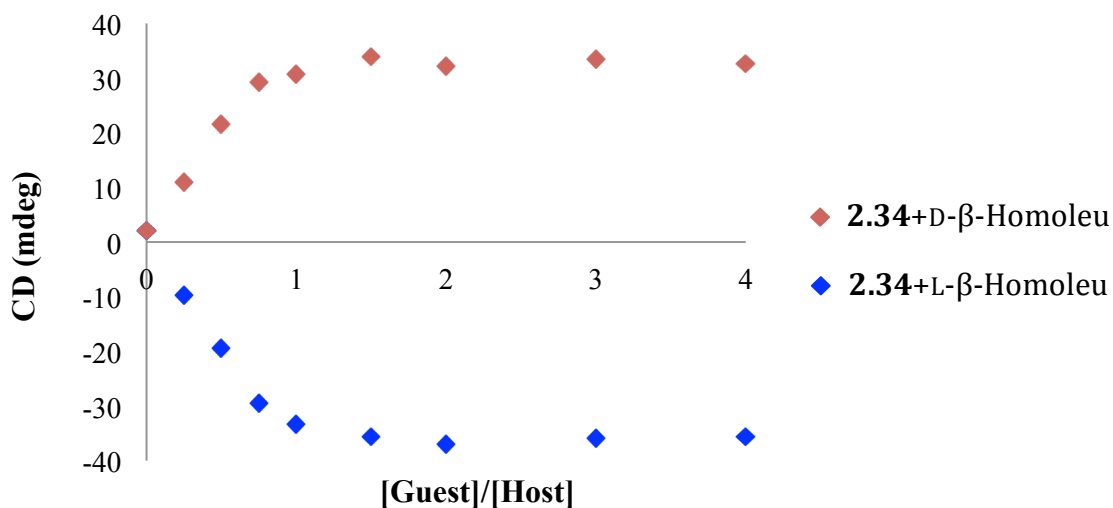


Figure 3.8. CD signal at 238 nm for titration of each enantiomer of β -homoleucine (0-2 mM) into a solution containing host **2.34** (0.5 mM) in default buffer.

Similarly to the α -amino acids, a set of five replicate samples was made for each enantiomer of each β -homoamino acid guest. The samples were assembled and the CD

spectra were recorded. A total of eight different analytes were tested, making up a set of 40 samples. The CD signals from 235 to 265 nm were input, as in the example for α -amino acids. The two-dimensional LDA plot obtained for this analysis, shown in **Figure 3.9**, shows good differentiation. All points were separated and the jack-knife analysis was calculated to be 100%. The F1 axis again represents the magnitude of the CD signals, with all of the D- β -homoamino acids on the left or negative side and the L- β -homoamino acids on the right or positive side. In this case, almost all of the variance in the dataset comes from the F1 axis. The second axis, F2, does not account for a significant difference between groups, relative to the CD amplitude. It is, however, greater than the scatter within the groups in the spectra. Three of the four β -homoamino acid guests are simple alkyl side chains, all appearing on the same side of the origin and opposite the phenylalanine guest possessing an aromatic side chain. This could be the system recognizing the difference in types of side chain of the guest, and manifesting in the shape of the signal. This is a very subtle difference, however. Once again, each pair of enantiomers are found reflected through the plot's origin.

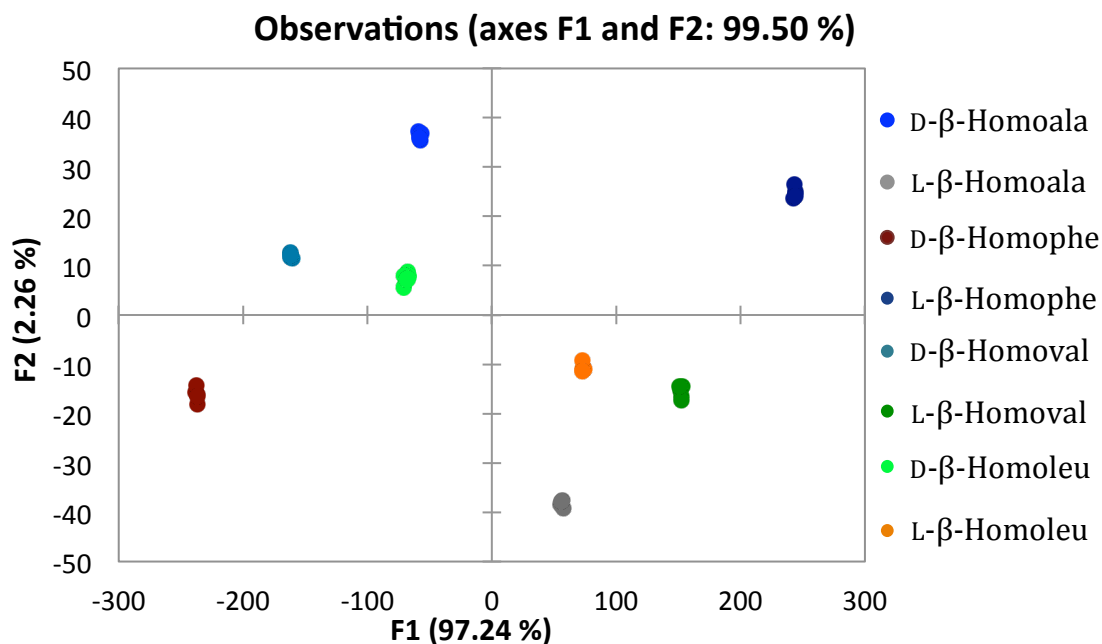


Figure 3.9. Two-dimensional LDA plot depicting the response of host **2.34** to each enantiomer of Boc-protected β -homoamino acid guest.

3.2.3. Combined Amino Acid Guests

After determining it was possible to individually differentiate both the α - and β -homo-amino acids, this pattern recognition protocol was applied to the two classes of amino acids together. The data for the α - and β -homo-amino acids were compiled, and the cumulative data were subjected to LDA analysis. For this specific analysis, the only α -amino acids that were considered were the ones whose β -homoamino acid counterparts were commercially available and had been analyzed previously. The data for the guests leucine, alanine, phenylalanine, and valine, were recorded in the two previous studies and combined across this dataset. The resulting plot is shown in **Figure 3.10**. The variation across the data set is almost entirely on the F1 axis, which again represents the sign and magnitude of the observed CD signal.

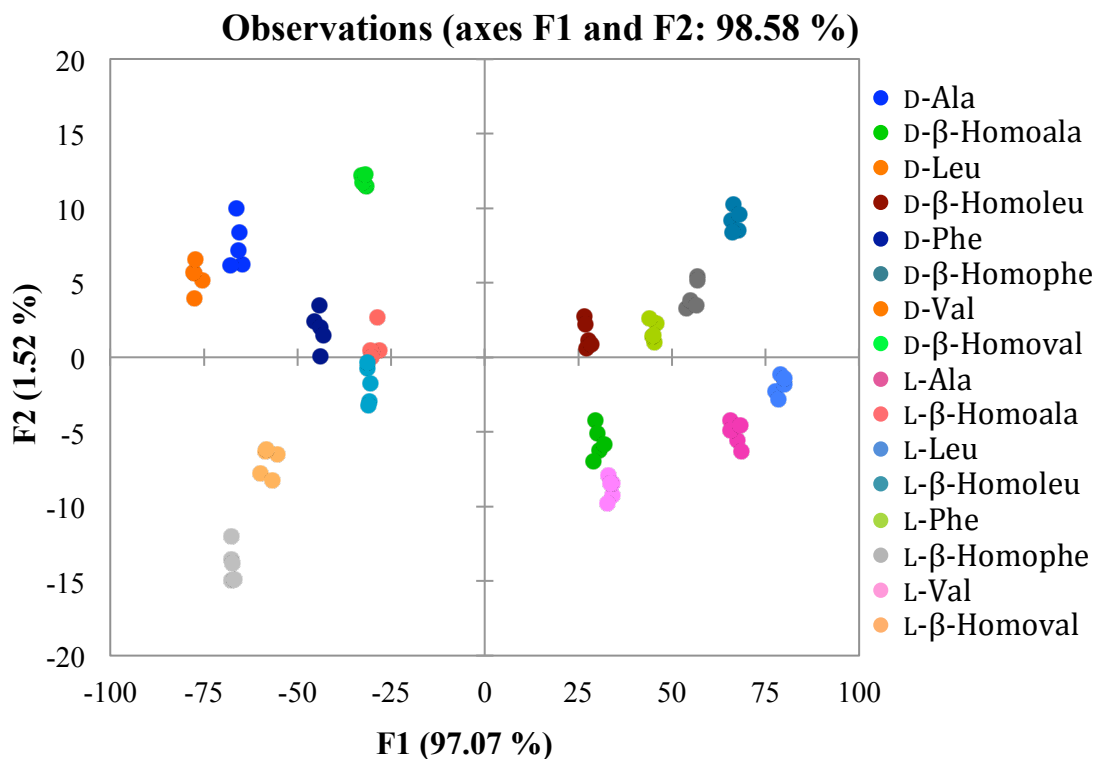


Figure 3.10. Two-dimensional LDA plot depicting the response of host **2.34** to each enantiomer of the α - and β -homoamino acid guests.

The variation that was observed along the secondary F2 axis is again attributed to the subtly different shapes of the resulting CD curves. Of note, the β -homoalanine and β -homoleucine guests are grouped much closer together than they were for the plot made from strictly β -homoamino acids. The obtained plot showed good separation of all of the data, with a jack-knife analysis of 100%. Also, the shape of the curve for the α -amino acids makes a more significant contribution to the values observed on the y-axis than does the shape of the β -homoamino acids. This is evidenced by how closely the β -homoamino acids are located in the combined plot.

Attempts were made to quantify both the enantio- and chemoselectivities for chiral species with stereocenters even further removed from the carboxylate functional

group. To this end, commercially available γ -amino acids were obtained. These guests, unfortunately, did not give rise to any observable CD signals. The stereocenter of the γ -amino acids must be too far removed from the chromophores to bias either helical twist preferentially.

3.3. APPLICATION TO SYNTHETIC METHODOLOGY DEVELOPEMENT

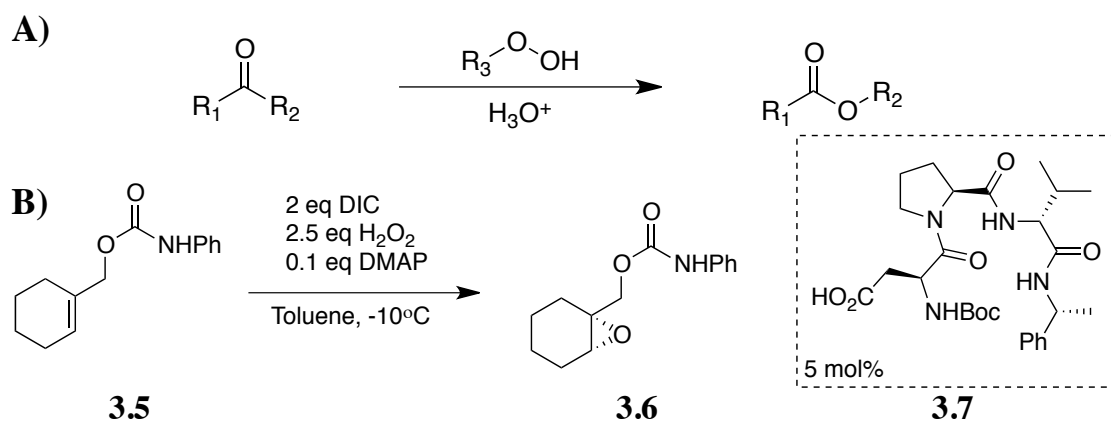
One of the main reasons for creating optical methods for *ee* analysis is to aid the synthetic methodology development community, both in reaction optimization and catalyst discovery. This particular assay, designed for carboxylic acids, was a good fit to transition to real synthetic examples that create compounds containing carboxylic acid functional groups. The extention of this work was envisioned to help bridge the gap between assay development and real use in a synthetic laboratory. In order to facilitate this transition, a collaboration was initiated with Professor Scott J. Miller at Yale University. Professor Miller's group has two on-going synthetic projects that were considered to fit well within the scope of this assay.

3.3.1. Asymmetric Baeyer-Villiger Oxidation

One focus of the Miller lab is the development of practical and efficient oxidation reactions. One such reaction is the Baeyer-Villiger reaction, a transformation known for over one hundred years.²⁷⁻²⁹ This reaction creates esters through oxidative conversion of either a ketone or aldehyde starting material, as shown in **Scheme 3.3A**. Despite its long presence in the literature, this reaction is limited by the scope in which it has been applied. Development of robust catalysts to promote this transformation has been limited by low catalyst turnover and thus low reaction efficiency. Further, few reports have appeared for asymmetric variants of this reaction. In order to obtain high enantiopurity of this reaction, chemists have turned to enzymatic catalysis.^{30,31} The enzymatic approach

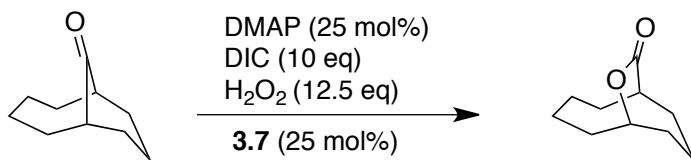
is limited by the scope of the substrate that can be tolerated, since enzymatic catalysis is an inherently specific process. Other variants that have been reported that promote enantioselectivity have been organometallic reagents,³²⁻³⁴ and systems based on flavin and organophosphoric acid moieties.³⁵ These methods are limited in that they have not been proven general, and no examples have achieved high catalyst turnover.

The Miller lab recently made advances in catalytic oxidation methodology by employing a peptide that helped create the transient peracid species.³⁶ This approach was applied to asymmetric epoxidation catalysis, a sample of which is shown in **Figure 3.3B**. This catalytic cycle relied on activation of the carbonyl by an aspartic acid residue on the peptide catalyst. The active ester surrogate was then trapped by hydrogen peroxide, and transfer of the oxygen atom to the olefin forms the product and regenerates the catalyst. This catalyst can reenter the catalytic cycle, leading to high turnover with as little as five mole percent catalyst. Additionally, the *ee* of the epoxide products was found to be as high as 92% for some substrates.



Scheme 3.3. A) Representation of the Baeyer-Villiger oxidation of a ketone to the corresponding ester. B) The Miller lab's development of a peptide-catalyzed asymmetric epoxidation reaction of alkenes.

The Miller lab recently demonstrated that this strategy can be effectively applied to the Baeyer-Villiger oxidation reaction.³⁷ This applicability is especially interesting because the Baeyer-Villiger reaction relies on a nucleophilic peracid moiety, while the epoxidation requires an electrophilic peracid. The oxygen atom is ultimately delivered from an intermediate of the Craiggie type.³⁸ Several catalyst turnovers have been achieved in this protocol, but the efficiency is largely dependent on the substrate. One promising aspect of the preliminary studies on these systems was the enantioselectivities that have been observed, up to 42% for the reaction shown in **Scheme 3.4**. This preliminary result helps to set the precedent for this reaction as a potential for optimization, however much work is necessary to expand this protocol. Very little information about the mechanism of this reaction is known, and thus optimization will be attempted in the absence of an understanding of the basis of asymmetric induction. Hence, this reaction is a good candidate for HTS.

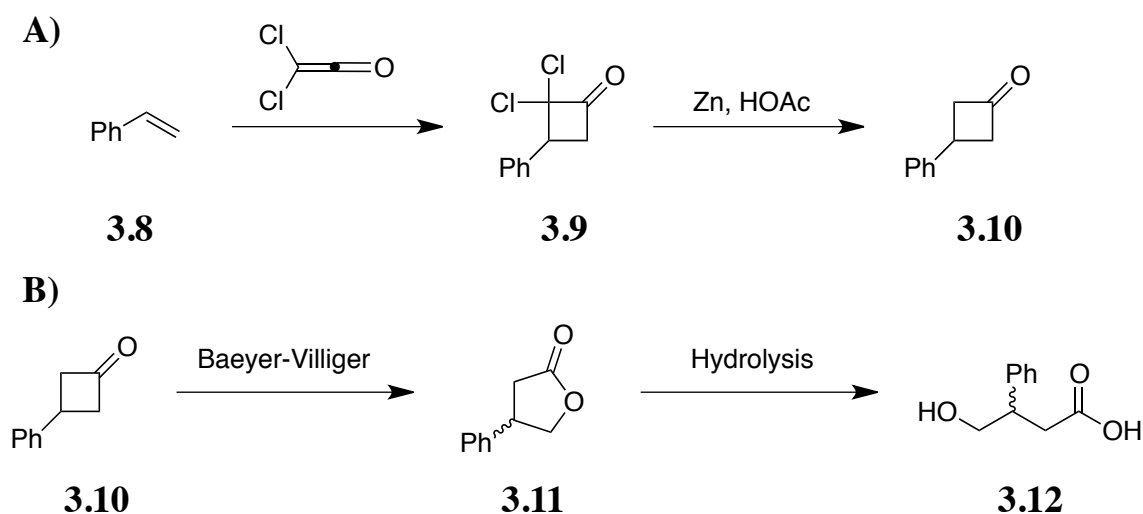


Scheme 3.4. Preliminary enantioselective Baeyer-Villiger oxidation reaction, catalyzed by a peptide catalyst.

3.3.1.1. Selection, Synthesis, and Initial Studies of Ketone Substrate

The creation of asymmetric esters through the Baeyer-Villiger oxidation does not immediately yield a carboxylic acid. Rather, it is envisioned that an alkaline workup will hydrolyze the ester and create a carboxylic acid. This carboxylic acid will be readily analyzed using the previously reported sensing methodology. Hydrolysis of the lactone substrate shown in **Scheme 3.4** will produce a β -chiral carboxylic acid. The location of

the stereocenter is further from the carboxylate binding site, with stereocenters further away than the β - position giving no observable CD signal. In order to obviate this problem, substituted cyclobutanone **3.10** was selected as a substrate (**Scheme 3.5**). Oxidation of this achiral substrate will produce a chiral γ -butyrolactone product, with a stereocenter that is β - to the carbonyl. The aromatic phenyl group was selected as it is envisioned to interact with the hydrophobic portions of the peptide catalysts that are used, and potentially benefit from secondary interactions leading to enantioselectivity. Hydrolysis of this substrate will thus produce β -chiral carboxylic acid **3.12**, an analyte amenable to the assay.



Scheme 3.5. Synthesis of 3-phenylcyclobutanone substrate for asymmetric Baeyer-Villiger reaction.

The substrate can be synthesized according to literature procedure,³⁹ beginning with commercially available styrene. The styrene is subjected to a [2+2] cycloaddition with a dichloroketene, to give 2,2-dichloro-3-phenyl cyclobutanone **3.9**. The dichloroketene was generated *in situ* from trichloroacetyl chloride, a zinc-copper couple,

and phosphorous oxychloride. The resultant 2,2-dichloro-3-phenyl cyclobutanone species can be further reduced to remove the chlorine atoms using zinc in glacial acetic acid. This route gives access to the desired cyclobutanone substrate **3.10** in good yield. One attractive approach to this substrate is that it can be synthesized in two easy steps from commercially available starting materials.

Before starting on the catalyst library selection and synthesis, it was necessary to ensure that a signal would be observed for these substrates. The 3-phenyl variant of the γ -butyrolactone product is not commercially available in either an enantioenriched or racemic form. Very few methods exist to create this substrate in a highly enantioselective fashion. Thus, the enantioenriched product needed to be synthesized through previously published methods.⁴⁰ This synthesis gave enantioenriched products, achieving *ee* values around 70%. Enantiopure substrates are typically required to create calibration curves and perform unknown analysis. Rather than run iterative analytical chiral HPLC separations to obtain a sufficient quantity of enantiopure sample, the decision was made to create calibration curves from these enriched samples. Since the CD signal of this system varies linearly with *ee*, it was postulated that a calibration curve made from non-enantiopure samples would be sufficient to establish the best-fit line.

The enriched samples of **3.12** were determined by chiral HPLC to have *ee* values of 67% for the (*R*)-enantiomer and 74% for the (*S*)-enantiomer. The CD spectra were individually recorded for two equivalents of either enantiomer of the guest with host **2.34**. The spectra are shown in **Figure 3.11**, and were of opposite sign for the enantiomeric samples. The first CE was again larger than the second, with the λ_{\max} observed at 240 nm. The (*R*)-enantiomer gave rise to a negative CD couplet, while a positive couplet was observed for the (*S*)-enantiomer. This trend is opposite of what was observed for the homochiral β -homoamino acids.

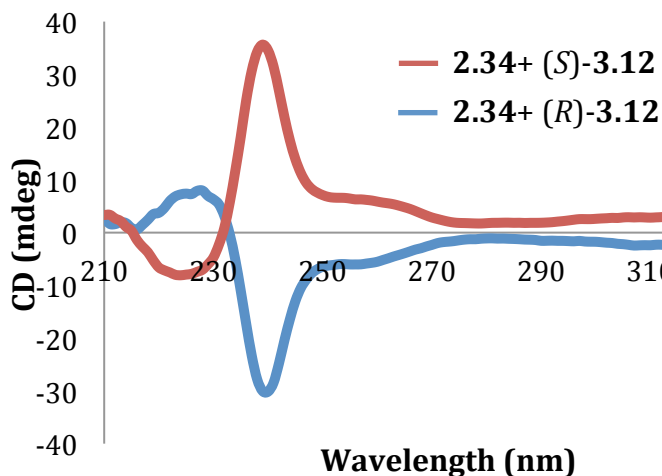


Figure 3.11. CD spectra for indicated enantiomer of guest (1.0 mM) and host **2.34** (0.5 mM) in default buffer.

This discrepancy in the sign of these signals is rationalized according to the difference between the steric size and Cahn-Ingold-Prelog (CIP) rules. Omitting the carboxylic acid group on the stereocenter, the phenyl substituent is the largest group. The phenyl is followed by the hydroxymethyl, and finally hydrogen. When looking down the bond of the stereocenter to the carbon α - to the carbonyl for the (*R*)-enantiomer, the group size priority goes in the clockwise direction (**Figure 3.12**). When considering the CIP rules, the priority is assigned based on the first point of difference between the groups. The substituent that first encounters a group with higher atomic number gets priority, irrespective of size. Thus, the oxygen atom of the hydroxymethyl dictates that this group gets the first priority. The hydroxymethyl is followed by the phenyl group, and finally the hydrogen. According to the CIP rules, the stereocenter is oriented in an anti-clockwise orientation. This contradiction is likely the root of the opposite sign observed for the CD signal.

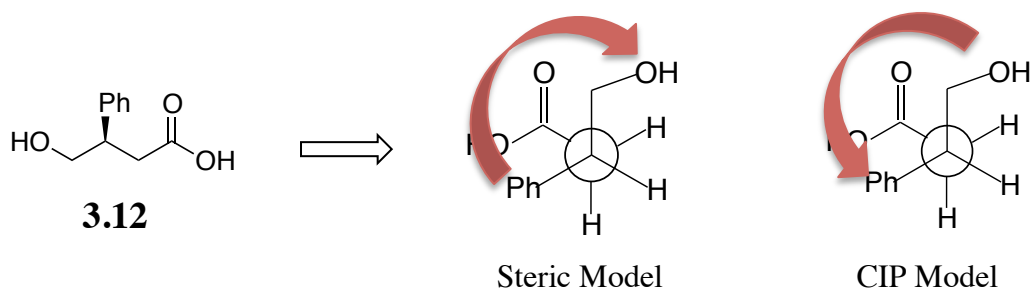


Figure 3.12. Newman projections explaining the discrepancy between orientation in the steric model and the CIP model.

Since the carboxylic acid guests are not enantioenriched to the same degree, the magnitude of their signals are also expected to be different. This behavior is indeed observed for these substrates. The less enantioenriched (*R*)-isomer, at 67% *ee*, gave a signal with a magnitude of -30.9 millidegrees. The CD signal of the 74% *ee* (*S*)-enantiomer was recorded 35.7 millidegrees. Since the CD spectrum is linearly dependent on *ee*, it is possible to extrapolate the signal to what would be theoretically seen for 100% *ee*. This extrapolation would yield signals of -46.1 for the (*R*)-enantiomer and 48.2 for the (*S*)-enantiomer. These signals are essentially equal and opposite, within experimental error that was incurred upon sample preparation.

These enantioenriched samples were used to create standard samples for a calibration curve. Using these samples, data were recorded for values that spanned a range of *ee*, having coverage between the extremes of +67% and -74% (**Figure 3.13**). The result of this plot was a straight line, and thus a linear regression was carried out in order to correlate the observed CD signal to the *ee* of the solution. The best-fit trendline fit the data very well, with a correlation of $R^2 = 0.999$. This calibration curve provided

evidence that this method could be applied to this substrate, and the focus was then turned toward creating a library of catalysts to promote this transformation.

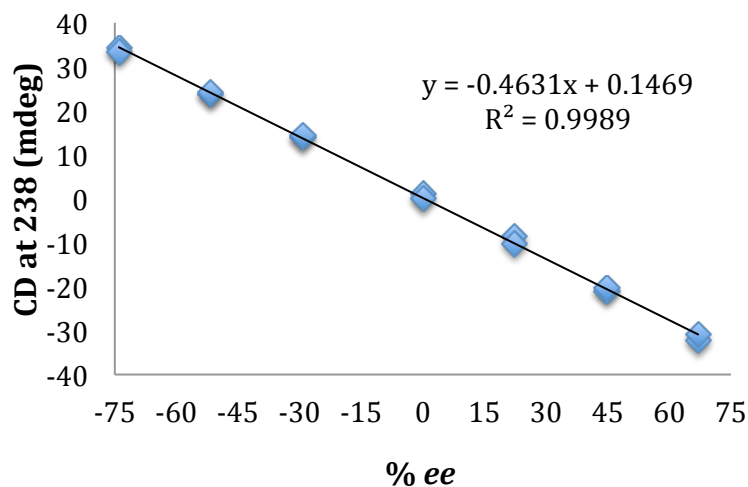


Figure 3.13. CD signal at 238 nm for a solution containing guest **3.12** (1.0 mM) and host **2.34** (0.5 mM) in default buffer as a function of *ee*.

3.3.1.2. Peptide Catalyst Library Synthesis

Small peptide sequences were selected to serve as catalysts for these transformations. The commercial availability of a litany of both enantiomers of amino acids makes this approach amenable to creating a large amount of diversity in structure rapidly. This strategy allows access to many different structures based on amino acids used, and can be very useful when little mechanistic information is understood for a particular transformation. Hence, this approach is a good fit for the particular attempts to optimize the asymmetric Baeyer-Villiger oxidation reaction.

Based on a prior protocol by the Miller group, a series of 48 tetrapeptide catalysts were designed and synthesized in parallel. Amine-terminated polyethyleneglycol polystyrene (PEG-PS) beads were selected as a solid support, since the nucleophilic and

robust amine linkage allowed for additional residues to be easily coupled without the fear or cleavage of the peptides from the resin. The amino acid residues were protected as fluorenylmethyloxycarbonyl (Fmoc) carbamates, easily cleaved under basic conditions to yield the free amine. The sequences were selected at random, though with a bias toward three residues that have given success in previous enantioselective reactions discovered by the Miller group. These residues, namely L-proline, D-valine, and L-phenylalanine, were incorporated to a higher extent than the other amino acids that were used. The terminal residue incorporated was glutamic acid, in hopes that it would serve as the acid-catalyst for the Baeyer-Villiger oxidation reaction.

A reaction block comprised of 48 wells was loaded with the amine-terminated PEG-PS beads. To this resin was added the solvent, coupling reagents, and the amino acid residues. The activating agents that were chosen were hydroxybenzotriazole (HOBt) and O-benzotriazole-N,N,N',N'-tetramethyluronium hexafluorophosphate (HBTU). These coupling reagents were selected since they have been known to promote peptide coupling reactions while avoiding racemization of the stereocenters of the coupled species.⁴¹ In this fashion, the 48 tetrapeptide sequences shown in **Figure 3.14** were synthesized. These residues cannot be cleaved from the resin, so the only form of characterization that could be performed was ninhydrin tests to check for the presence of free amine groups.⁴² Though there is a certain level of doubt with this method, this initial screen is aimed at elucidating any species that give good enantioselectivity. Assuming any hits are generated, these species would be synthesized and characterized in a more rigorous manner. This is often done in the Miller lab by synthesizing the peptide sequence in solution, rather than the resin, and its ability to facilitate enantioselective transformations is confirmed.⁴³ In order to test the reproducibility, several duplicate sequences were included in the 48 member library.

-F-V-P-E	-F-D-V-P-E	-F-D-V-D-P-E	-F-D-V-P-E	-F-D-V-P-E	-Y-D-V-P-E
-Y-D-V-P-E	-Y-D-V-P-E	-Y-V-P-E	-Y-V-P-E	-Y-V-P-E	-V-P-F-E
-F-P-V-E	-Y-D-V-P-E	-F-V-D-P-E	-F-D-V-D-P-E	-A-V-Y-E	-V-G-P-E
-D-V-G-P-E	-I-A-P-E	-I-A-V-E	-I-A-D-V-E	-A-V-Y-E	-A-D-V-Y-E
-A-D-V-Y-E	-A-D-V-Y-E	-P-L-A-E	-L-N-P-E	-L-I-P-E	-V-P-P-E
-V-D-P-P-E	-V-P-D-P-E	-V-V-P-E	-V-D-V-P-E	-V-D-V-P-E	-I-S-P-E
-I-L-L-E	-I-L-D-L-E	-S-Y-D-Q-E	-S-Y-D-Q-E	-S-Y-D-Q-E	-Y-D-V- ACPC-E
-Y-D-V- ACPC-E	-Y-D-V- ACPC-E	-S-A- ACPC-E	-A-A-P-E	-A-D-A-P-E	-D-A-A-P-E

Figure 3.14. Peptide library that was constructed for screening of Baeyer-Villiger oxidations.

3.3.1.3. Screening For Enantioselectivity

Each of the resins containing a single catalyst was loaded into one well of a 48 well plate. This plate was commercially available, and contained a frit filter at the bottom to remove the solution from the resin. The bottom was fitted with a cap, to prevent any unwanted spilling of the reaction solution. To this resin was added the cyclobutanone **3.10** dissolved in chloroform, followed by aqueous hydrogen peroxide. The peptide catalyst was applied in 25 mole percent, and the ratios of the other starting materials were in line with what the Miller lab had previously reported for this conversion.⁴⁴ After all starting materials were added to the plate, the top was sealed and the plate shaken overnight to allow the reaction to progress. It has been demonstrated that the yield of this reaction is relatively low, typically no more than ten percent

conversion. The exact turnover was not the goal of this study, but rather to identify possible hits that produce high enantioselectivity. To this end, the minimal conversion of five percent was envisioned. A higher rate of conversion will not have a detrimental effect to this analysis, since the signal saturates at one equivalent of guest added relative to host.

The contents of the reaction well were filtered into a second 48 well plate, this one without the frit. The solvent was removed in a Genevac evaporation system, and lactone hydrolyzed by introduction of lithium hydroxide in a water/tetrahydrofuran mixture. The plate was shaken for six hours to complete the hydrolysis, then the unreacted acid neutralized with perchloric acid. Following neutralization, the solvent was again removed in the Genevac evaporation system. The remaining residue was dissolved to the appropriate concentration in the buffer solution, again assuming a modest five percent conversion. The CD spectra for these samples were then recorded, and the results displayed in **Figure 3.15**. Though a large number of reactions were rapidly screened in parallel, none of the catalysts led to an enantioselective transformation. These results are consistent with unpublished results obtained by the Miller lab for Baeyer-Villiger reactions of cyclobutanone substrate **3.10**, which were subsequently analyzed by HPLC. Though no enantioselectivity was observed in this single iteration of a limited catalyst set, this work establishes the rapid screening technique as a viable approach.

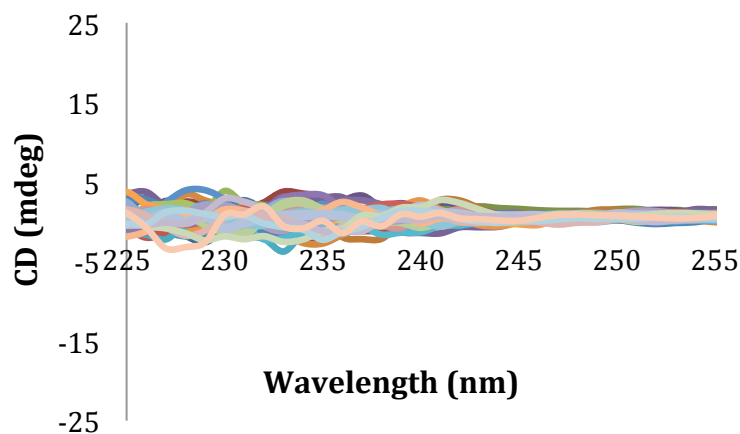


Figure 3.15. CD spectra recorded for host **2.34** (0.5 mM) and synthetic guests dissolved in buffer.

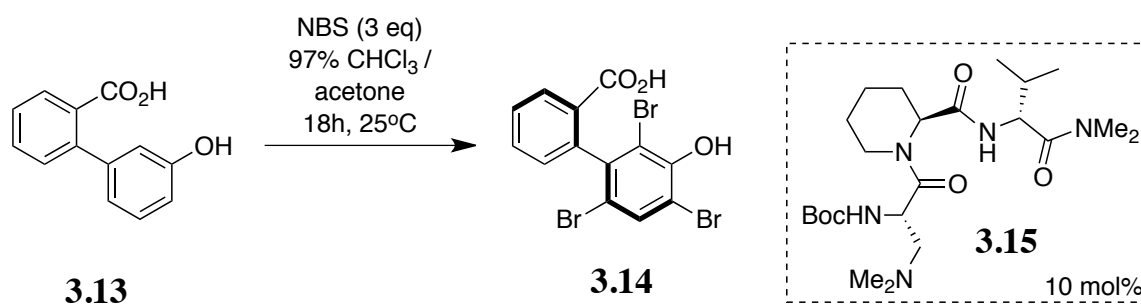
3.3.2. Resolution of Atropisomeric Biaryls Through Selective Bromination

An atropisomer is a type of stereoisomer that possesses no stereocenter, but rather has hindered rotation around a single bond. These types of isomers have been the source of interest to scientific research for most of the last century.^{45,46} Many atropisomers rely on a non-planarity of adjacent aromatic rings, leading to a helical axis of chirality. The bulky substituents on the aromatic rings restrict the rotation, creating barriers to rotation of greater than 25 kcal/mol. Were the barrier to rotation smaller, the free rotation would lead to eventual racemization of the atropisomeric species.⁴⁷

Atropisomeric compounds are often found as single isomers in nature, since substituents on the multi-aromatic rings raises the barrier to rotation sufficiently in order to prevent it. Additionally, rotation can be hindered by placement of these rings within multicyclic ring systems.^{48,49} It is certain that these considerations give rise to the interesting structure and function of single atropisomer containing biomolecules, such as the antibiotic vancomycin.⁵⁰ Additionally, chiral ligands based on 1,1'-binaphthyl species have received much attention in asymmetric synthesis⁵¹ and chiral sensing.⁵²

Despite the wide use of these classes of molecules, few literature reports have emerged of catalysts that promote the enantioselective synthesis of these species. High enantioselectivity has been achieved in forming a biaryl bond with metal-based catalysts, though this approach was very substrate dependent.⁵³⁻⁵⁷ In another approach, selective reaction was carried out with one atropisomer of a rapidly interconverting pair of biaryl species.⁵⁸⁻⁶⁰ This approach was quite intriguing, yet it required stoichiometric quantities of reactants.

The Miller group at Yale recently reported the dynamic resolution of biaryl atropisomers through a selective bromination reaction.⁶¹ This reaction is catalyzed by a small molecule catalyst, derived from a tripeptide motif. This molecule achieves resolution of a mixture of rapidly interconverting biaryl atropisomers through selective electrophilic aromatic substitution with simple brominating agents preferentially. This enantioselective synthesis, shown in **Scheme 3.6**, generates the resulting chiral tri-brominated biaryl species in both high chemical yield and high enantiomeric purity.



Scheme 3.6. Kinetic resolution of atropisomeric biaryl species through a peptide-catalyzed bromination reaction.

The enantioselectivity was rationalized through the potential conformation of the bound species shown in **Figure 3.16**. A key feature of this model is the substituted six

membered piperidine ring. The substituent is shown in the axial position, accessible in N-acyl derivatives to relieve allylic strain associated with diequatorial substituents.⁶² The substrate interacts with this catalyst according to the posited model. The proton of the carboxylic acid is transferred to the N,N-dimethylamino alanine residue at the N-terminus of the peptide. This transfer leads to salt bridge formation, and makes the initial contact for these molecules. Hydrogen bonding is expected to exist between the phenol and the interior amide and carbonyl of the catalyst, as demonstrated in the model. The bromine atom can then be transferred to the aromatic ring that is now directed toward the *O*-bromonium ion, giving the observed stereoisomer.

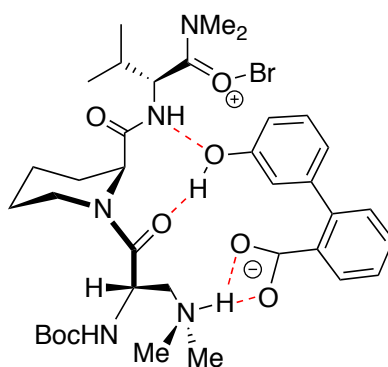


Figure 3.16. Possible docking model for the biaryl substrate to the peptide catalyst that explains the enantioselectivity of bromination.

Free rotation of partially brominated species is likely hindered by the hydrogen bonds formed by the phenolic proton and the peptide. It is also possible that the rotation occurs freely until the ortho-ortho' substituents have been installed. A complete mechanistic analysis is necessitated in order to fully understand the source of the enantioselectivity. This general approach allows rapid access to highly enantioenriched substrates, using simple NBS bromination reagents.

Assignment of the enantiomeric excess, however, is not as straightforward as it may seem. The product cannot be directly analyzed using chiral chromatography. The free acid does not behave well in the HPLC, and subsequent derivatization of the product to the methyl ester was required to obtain the *ee* values. While this modification leads to better analysis, the additional time and synthetic step are undesirable consequences. The newly created chiral biaryl species possesses a carboxylic acid moiety, and was a suitable candidate for application of the copper-based assay described previously. Though it contains no stereocenter, it was postulated that the steric hindrance of the biaryl would be sufficient to yield enantiospecific CD signals.

3.3.2.1. CD Analysis

In order to begin this project, an enantioenriched sample of the substrate was prepared by the Miller lab according to the previously noted protocol. This species was analyzed by chiral HPLC and was determined to have an *ee* of 92%. The prior analysis of Baeyer-Villiger products gave precedent to running analyses in the absence of enantiopure samples, provided the *ee* of the enriched sample is accurately known. This technique was further extended to encompass this analysis. Since host **2.34** had never been applied to an atropisomeric species before, initial experiments were directed toward determining if a signal would be produced. To this end, CD spectra were taken for the biaryl guest **3.14** (Figure 3.17). The first spectrum that was recorded was the chiral biaryl guest **3.14** by itself. This sample exhibited a broad peak in the CD spectrum, with a relatively small negative sign. This peak had a λ_{max} at around 237 nm with a smaller magnitude than that recorded when host **2.34** was added. The second peak had a positive magnitude and was sharper, exhibiting a λ_{max} at around 241 nm. The UV absorption for

this species occurred at a λ_{max} of 236 nm, corresponding to what may be seen as a null in the spectrum. Indeed, these observations are consistent with ECCD.

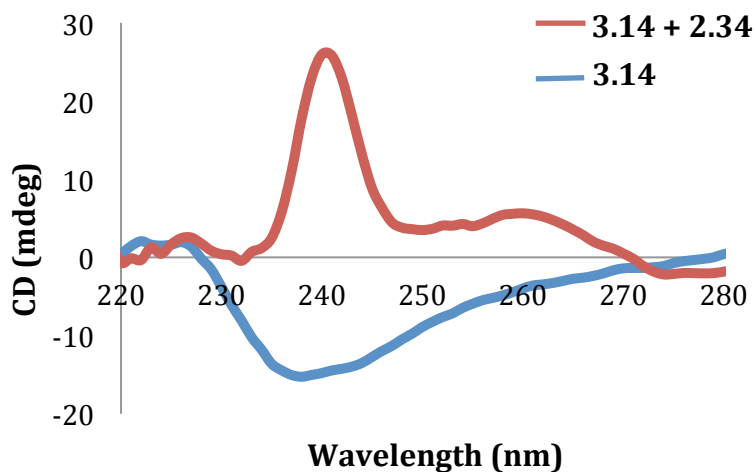


Figure 3.17. CD spectra recorded for biaryl guest **3.14** (1.0 mM) by itself, and with **2.34** (0.5 mM) in default buffer.

The guest by itself has a signal that occurs in the same region of the spectrum as the complex. While this may be seen as a detriment, it is not always the case that the guest being analyzed will have this type of conflicting absorbance.

The focus was turned toward determining if the signal created was linear as a function of *ee*. The Miller group provided an additional four samples that ranged in *ee* from 2%, all the way to 72%. The CD spectra recorded for these are shown in **Figure 3.18A**. The magnitude of the CD signal decreased directly while diminishing the *ee* of the substrate, with the sample of lowest *ee* giving a signal that was nearly baseline. The signal measured at 241 nm was plotted against the *ee* of the substrate, and a linear correlation was confirmed (**Figure 3.18B**). This linear relationship provided evidence that the utility of this sensor would encompass atropisomeric species lacking

stereocenters. The focus of this project then turned toward determining the *ee* value for unknown samples.

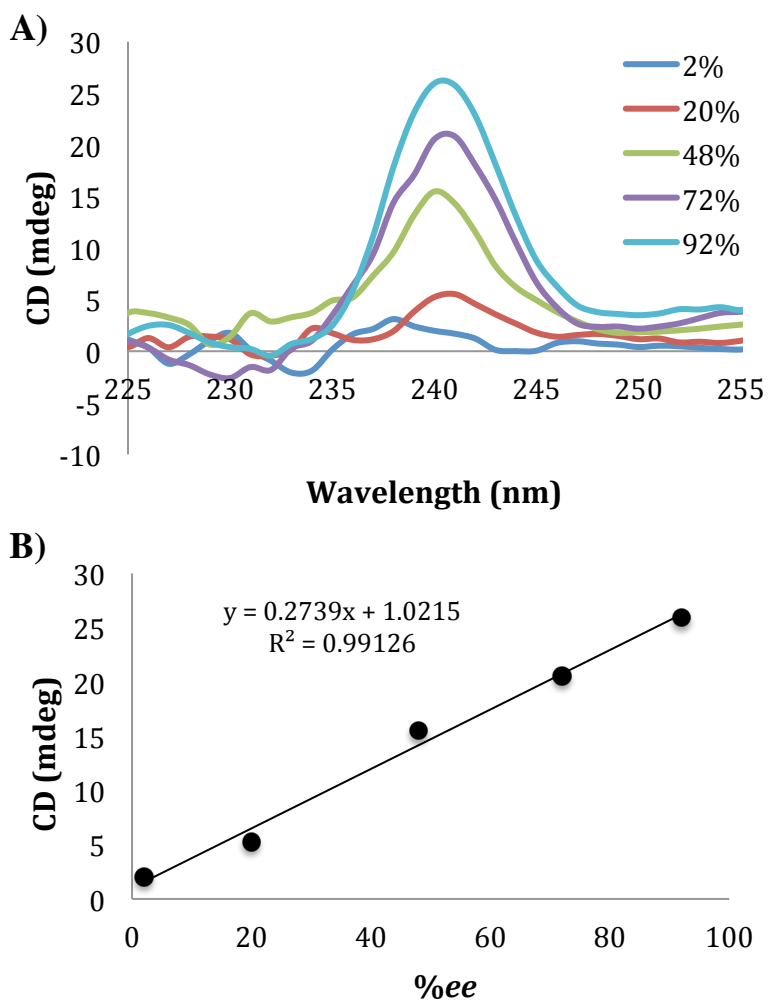


Figure 3.18. A) CD spectra for guest **3.14** (1.0 mM) and host **2.34** (0.5 mM) with indicated *ee* values. B) The CD spectrum at 241 nm plotted against *ee* of the solution.

3.3.2.2. Calculation of *ee* For Unknown Samples

Two different methods were undertaken in order to determine the *ee* value of four unknown samples provided by the Miller lab. The first method is based on creating a

calibration curve from the five known samples provided, as shown in **3.18B**. Performing a linear regression of the data yielded an equation to relate the CD spectrum to the *ee* value of the solution, and this equation was applied to determining the *ee* of the unknowns. The CD spectra were recorded for each of the four unknowns, and the CD signal at 241 nm obtained. These signals were used to determine *ee* values for the unknown samples, as shown in **Table 3.1**. The calculated unknown *ee* values matched up well with the known values, with an average error of 5.1%. This error is comparable to that observed previously for simple carboxylic acid samples, and for other types of analytes.

	CD (mdeg)	% <i>ee</i> (calc)	% <i>ee</i> (actual)	Error (%)
1	5.8	17.5	15.4	2.1
2	11.7	38.9	29.4	9.5
3	19.3	66.8	70.4	3.6
4	21.5	74.7	69.4	5.3

Table 3.1. CD signals recorded for each unknown, the % *ee* values calculated and actual, and the error that was found.

While the error for assigning the *ee* values for these chiral biaryl species was within an acceptable range for this analysis, it was still desirable to decrease the amount of time required to carry out this analysis. The major hurdle to HTS as a means for catalyst discovery is rapidly determining hits, and as such these researchers are less interested in determining the exact *ee* values with high accuracy. The present analysis still requires a calibration curve made from five samples, the *ee* values of each had been analyzed by chiral HPLC. It was hypothesized that this could be minimized to only a

single data point, whose *ee* was known accurately. The method used for chiral HPLC takes approximately 20 minutes per sample, and this improvement would save 80 minutes on the analysis by obviating chiral HPLC run on four of the known samples. This saving is in addition to the time saved by performing the CD analyses.

A line would be constructed from the CD spectrum of a single measured point, and pass through the origin. The origin was picked since no CD signal should be observed when a racemic mixture of the guest is analyzed. The point selected was 92% *ee*, since it was on the high range of the enantiomerically pure samples that had been synthesized. The resultant graph for this analysis is shown in **Figure 3.19**. The calculated best-fit line unsurprisingly shows perfect linear correlation, since it is made up of only two data points. The accuracy of this analysis was confirmed among the known samples before proceeding to the unknowns. The equation for this line was applied to the four additional samples used to make the previous calibration curve, namely those with 2, 20, 48, and 72% *ees*. Each was analyzed, and the overall error determined to be 3.5%. These results verified this approach, and the analyses turned again toward analyzing the four unknown samples.

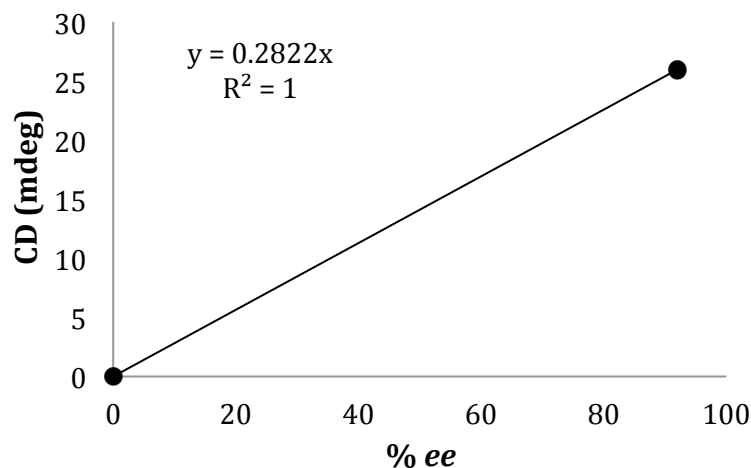


Figure 3.19. The CD spectrum at 241 nm plotted against *ee* of the solution the biaryl solution, with the trendline and equation included.

The same set of unknown samples that had been analyzed with the previous calibration curve were again targeted for analysis. The equation for the best-fit line obtained from these two points was used to translate the CD signals that had been recorded at 241 nm into *ee* values for the unknown samples. The results of this analysis are represented in **Table 3.2**. The average error recorded for these samples was found to be 6.5%. This corresponds to a slightly larger average error than for the calibration curve, but the error does not increase significantly with this analysis. It is quite remarkable that the previous necessity for enantiopure samples of each enantiomer in order to make a calibration curve to accurately determine *ee* has been reduced all the way down to a single sample of a known *ee* value. This approach represents a significant improvement towards minimizing the amount of time required to carry out *ee* analysis.

	CD (mdeg)	% ee (calc)	% ee (actual)	Error (%)
1	5.8	20.6	15.4	5.2
2	11.7	41.4	29.4	12.0
3	19.3	68.4	70.4	2.0
4	21.5	76.1	69.4	6.7

Table 3.2. CD signals recorded for each unknown, the % ee values calculated and actual, and the error that was found.

3.4. CONCLUDING REMARKS

The results presented in this chapter help to establish the generality of this sensing ensemble. In addition to simple carboxylic acids, the guest range has been extended to the α -amino acids containing a wide variety of side chain functional groups. The host proved general, and tolerated all of the side chains that were used. This approach was further expanded to encompass β -homoamino acids, where the stereocenter was one carbon further away from the carboxylate binding site. The more remote location of the stereocenter did not hinder the analysis, and it was shown that these species were able to be differentiated. Building upon the analysis of β -chiral species, the system was expanded to analyze the product of Baeyer-Villiger oxidation following appropriate hydrolysis. These β -chiral butyric acids gave CD signals that were linear in dependence on ee value, and the need for enantiopure samples was removed. A series of reactions that were catalyzed by resin-bound peptide catalysts was carried out and analyzed, though gave nothing but racemic substituted lactones. Finally, this sensing platform was further expanded to include atropisomers that lack a stereocenter. Unknown samples were analyzed with good accuracy, and this accuracy was not significantly affected by

performing an analysis from only a single known data point. The advances presented in this chapter represent significant improvements in accuracy and speed of analysis, and help to make optical methods for *ee* analysis more attractive for the HTS community.

3.5. EXPERIMENTAL

3.5.1. Materials and Methods

All reagents and solvents were purchased from commercial sources and used as received. All α -amino acids were purchased from Chem Imprex, while the β -homoamino acids were purchased from Peptech. Circular dichroism measurements were performed at 25°C on a JASCO J-815 spectropolarimeter, using Starna Type 21 1 cm quartz cuvette. The program used to carry out linear discriminant analysis (LDA) was XLSTAT 2011.

3.5.2. CD Titrations

3.5.2.1. N-Boc Proline Binding

Stock solutions of the guest were made by independently dissolving either N-Boc-D-proline (11.73 mg, 0.055 mmol), or N-Boc-L-proline (10.74 mg, 0.05 mmol) to 10 mL in default buffer. Each point on the titration was a separate solution, containing host **1** (43.02 μ L, 0.5 mM) and the indicated amount of guest (0-2 mM) diluted to 1 mL. The titration was performed in this manner due to the small volume that the CD cuvette holds (400 μ L), as well as the inability to stir the contents of the cuvette. Repetitions were made by adding two equivalents of either N-Boc-D-proline (1.0 mM, 183.49 μ L), or N-Boc-L-proline (1.0 mM, 200.42 μ L) to a solution containing the host (0.5 mM, 43.02 μ L), and recording the resulting CD spectra.

3.5.2.2. N-Boc Methionine Binding

Stock solutions of the guest were made by independently dissolving either N-Boc-D-methionine (13.02 mg, 0.052 mmol), or N-Boc-L-methionine (12.02 mg, 0.048 mmol) to 10 mL in default buffer. Each point on the titration was a separate solution, containing host **1** (43.02 μ L, 0.5 mM) and the indicated amount of guest (0-2 mM) diluted to 1 mL. The titration was performed in this manner due to the small volume that the CD cuvette holds (400 μ L), as well as the inability to stir the contents of the cuvette. Repetitions were made by adding two equivalents of either N-Boc-D-proline (1.0 mM, 183.49 μ L), or N-Boc-L-proline (1.0 mM, 200.42 μ L) to a solution containing the host (0.5 mM, 43.02 μ L), and recording the resulting CD spectra.

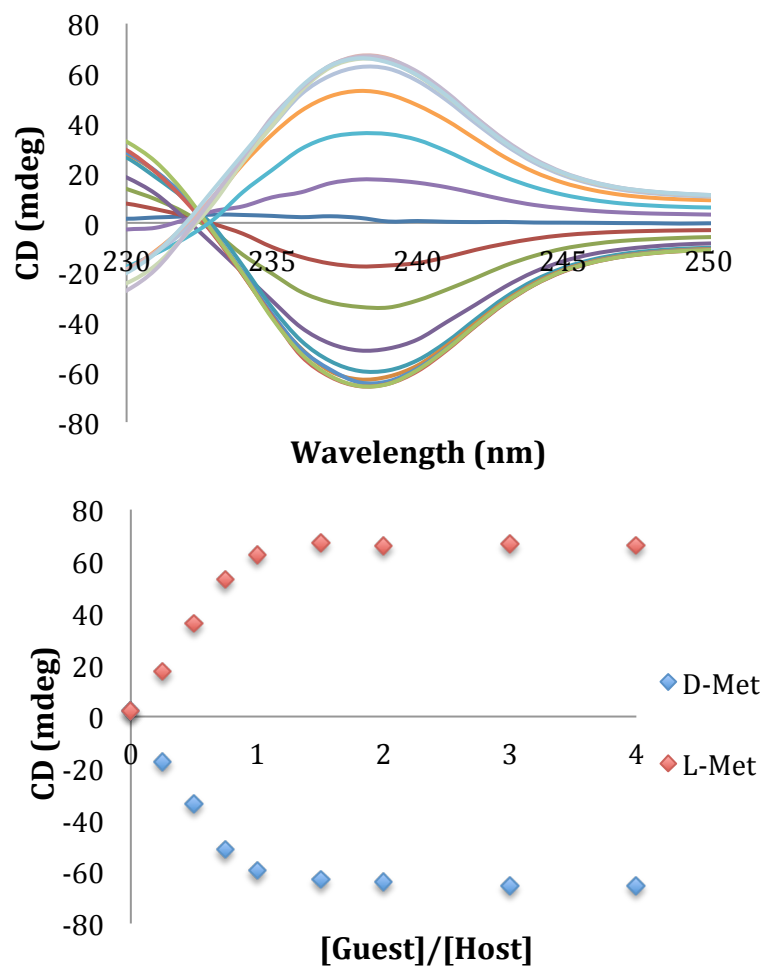


Figure 3.20. Top: CD spectra of host **1** (0.5 mM) upon addition of each enantiomer of N-Boc-Methionine (0-2 mM) in default buffer. Bottom: Change in CD signal at 238 nm recorded for this titration.

3.5.2.3. *N*-Boc Alanine Binding

Stock solutions of the guest were made by independently dissolving either N-Boc-D-alanine (10.96 mg, 0.058 mmol), or N-Boc-L-alanine (10.43 mg, 0.055 mmol) to 10 mL in default buffer. Each point on the titration was a separate solution, containing host **1** (43.02 μ L, 0.5 mM) and the indicated amount of guest (0-2 mM) diluted to 1 mL. The

titration was performed in this manner due to the small volume that the CD cuvette holds (400 μL), as well as the inability to stir the contents of the cuvette.

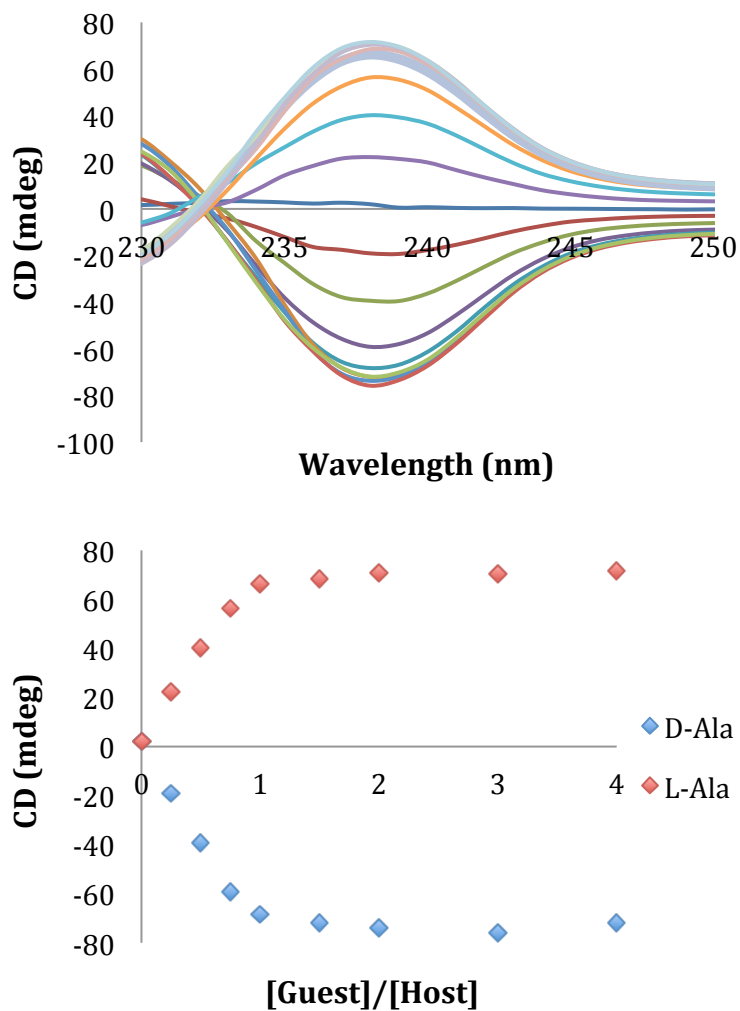


Figure 3.21. Top: CD spectra of host **1** (0.5 mM) upon addition of each enantiomer of N-Boc-Alanine (0-2 mM) in default buffer. Bottom: Change in CD signal at 238 nm recorded for this titration.

3.5.2.4. N-Boc Histidine Repetitions

Stock solutions of the guest were made by independently dissolving either N-Boc-D-Histidine (13.02 mg, 0.052 mmol) or N-Boc-L-Histidine (12.02mg, 0.048 mmol) in 10 mL of default buffer. Repetitions were made by adding two equivalents of either N-Boc-D-Histidine (1.0 mM, 190.11 μ L), or N-Boc-L-Histidine (1.0 mM, 185.19 μ L) to a solution containing the host (0.5 mM, 43.02 μ L) in the default buffer and recording the resulting CD spectra.

3.5.2.5. N-Boc Serine Repetitions

Stock solutions of the guest were made by independently dissolving either N-Boc-D-Serine (10.47 mg, 0.051 mmol) or N-Boc-L-Serine (12.11 mg, 0.059 mmol) in 10 mL of default buffer. Repetitions were made by adding two equivalents of either N-Boc-D-Serine (1.0 mM, 196.08 μ L), or N-Boc-L-Serine (1.0 mM, 169.49 μ L) to a solution containing the host (0.5 mM, 43.02 μ L) in the default buffer, and recording the resulting CD spectra.

3.5.2.6. N-Boc Phenylalanine Repetitions

Stock solutions of the guest were made by independently dissolving either N-Boc-D-Phenylalanine (12.92 mg, 0.049 mmol) or N-Boc-L-Phenylalanine (13.13 mg, 0.050 mmol) in 10 mL of default buffer. Repetitions were made by adding two equivalents of either N-Boc-D-Phenylalanine (1.0 mM, 205.34 μ L), or N-Boc-L-Phenylalanine (1.0 mM, 202.02 μ L) to a solution containing the host (0.5 mM, 43.02 μ L) in the default buffer, and recording the resulting CD spectra.

3.5.2.7. N-Boc Valine Repetitions

Stock solutions of the guest were made by independently dissolving either N-Boc-D-Valine (11.78 mg, 0.054 mmol) or N-Boc-L-Valine (11.06 mg, 0.051 mmol) in 10 mL

of default buffer. Repetitions were made by adding two equivalents of either N-Boc-D-Valine (1.0 mM, 184.50 μL), or N-Boc-L-Valine (1.0 mM, 196.46 μL) to a solution containing the host (0.5 mM, 43.02 μL) in the default buffer, and recording the resulting CD spectra.

3.5.2.8. N-Boc Tryptophan Repetitions

Stock solutions of the guest were made by independently dissolving either N-Boc-D-Tryptophan (16.56 mg, 0.054 mmol) or N-Boc-L-Tryptophan (16.19 mg, 0.053 mmol) in 10 mL of default buffer. Repetitions were made by adding two equivalents of either N-Boc-D-Tryptophan (1.0 mM, 183.82 μL), or N-Boc-L-Tryptophan (1.0 mM, 188.00 μL) to a solution containing the host (0.5 mM, 43.02 μL) in the default buffer, and recording the resulting CD spectra.

3.5.2.9. N-Boc Leucine Repetitions

Stock solutions of the guest were made by independently dissolving either N-Boc-D-Leucine (12.44 mg, 0.054 mmol) or N-Boc-L-Leucine (12.86 mg, 0.056 mmol) in 10 mL of default buffer. Repetitions were made by adding two equivalents of either N-Boc-D-Leucine (1.0 mM, 185.87 μL), or N-Boc-L-Leucine (1.0 mM, 179.86 μL) to a solution containing the host (0.5 mM, 43.02 μL) in the default buffer, and recording the resulting CD spectra.

3.6.2.10. N-Boc Tyrosine Repetitions

Stock solutions of the guest were made by independently dissolving either N-Boc-D-Tyrosine (14.66 mg, 0.052 mmol) or N-Boc-L-Tyrosine (14.12 mg, 0.050 mmol) in 10 mL of default buffer. Repetitions were made by adding two equivalents of either N-Boc-D-Tyrosine (1.0 mM, 191.94 μL), or N-Boc-L-Tyrosine (1.0 mM, 199.20 μL) to a

solution containing the host (0.5 mM, 43.02 μ L) in the default buffer, and recording the resulting CD spectra.

3.5.2.11. N-Boc Asparagine Repetitions

Stock solutions of the guest were made by independently dissolving either N-Boc-D-Asparagine (12.40 mg, 0.053 mmol) or N-Boc-L-Asparagine (12.01 mg, 0.052 mmol) in 10 mL of default buffer. Repetitions were made by adding two equivalents of either N-Boc-D-Asparagine (1.0 mM, 187.30 μ L), or N-Boc-L-Asparagine (1.0 mM, 193.40 μ L) to a solution containing the host (0.5 mM, 43.02 μ L) in the default buffer, and recording the resulting CD spectra.

3.5.2.12. N-Boc- β -Homoleucine Binding

Stock solutions of the guest were made by independently dissolving either N-Boc-D- β -Homoleucine (14.13 mg, 0.058 mmol), or N-Boc-L- β -Homoleucine (12.67 mg, 0.052 mmol) to 10 mL in default buffer. Each point on the titration was a separate solution, containing host **1** (43.02 μ L, 0.5 mM) and the indicated amount of guest (0-2 mM) diluted to 1 mL. The titration was performed in this manner due to the small volume that the CD cuvette holds (400 μ L), as well as the inability to stir the contents of the cuvette. Repetitions were made by adding two equivalents of either N-Boc-D- β -Homoleucine (1.0 mM, 173.60 μ L), or N-Boc-L- β -Homoleucine (1.0 mM, 193.60 μ L) to a solution containing the host (0.5 mM, 43.02 μ L), and recording the resulting CD spectra.

3.5.2.13. N-Boc- β -Homoalanine Binding

Stock solutions of the guest were made by independently dissolving either N-Boc-D- β -Homoalanine (11.34 mg, 0.056 mmol), or N-Boc-L- β -Homoalanine (12.64 mg,

0.062 mmol) to 10 mL in default buffer. Each point on the titration was a separate solution, containing host **1** (43.02 μL , 0.5 mM) and the indicated amount of guest (0-2 mM) diluted to 1 mL. The titration was performed in this manner due to the small volume that the CD cuvette holds (400 μL), as well as the inability to stir the contents of the cuvette. Repetitions were made by adding two equivalents of either N-Boc-D- β -Homoalanine (1.0 mM, 179.20 μL), or N-Boc-L- β -Homoalanine (1.0 mM, 160.80 μL) to a solution containing the host (0.5 mM, 43.02 μL), and recording the resulting CD spectra.

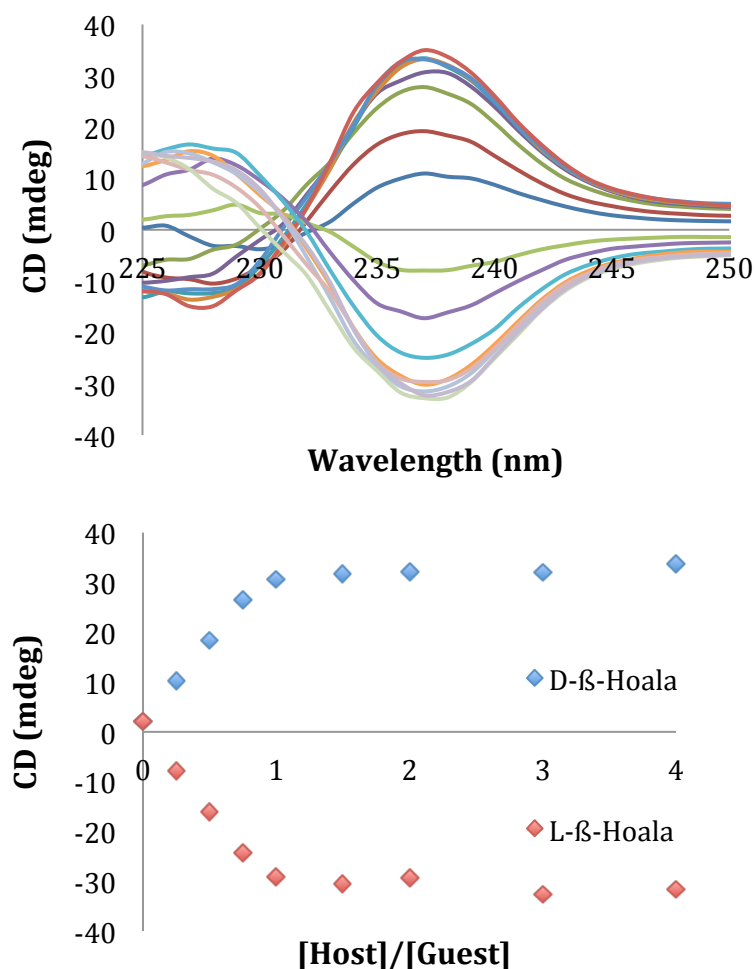


Figure 3.22. Top: CD spectra of host **1** (0.5 mM) upon addition of each enantiomer of N-Boc-β-Alanine (0-2 mM) in default buffer. Bottom: Change in CD signal at 238 nm recorded for this titration.

3.5.2.14. N-Boc-β-Homophenylalanine Repetitions

Stock solutions of the guest were made by independently dissolving either N-Boc-D-β-Homophenylalanine (14.97 mg, 0.054 mmol) or N-Boc-L-β-Homophenylalanine (14.55 mg, 0.052 mmol) in 10 mL of default buffer. Repetitions were made by adding two equivalents of either N-Boc-D-β-Homophenylalanine (1.0 mM, 186.60 μL), or N-

Boc-L- β -Homophenylalanine (1.0 mM, 191.90 μ L) to a solution containing the host (0.5 mM, 43.02 μ L) in the default buffer, and recording the resulting CD spectra.

3.5.2.15. *N*-Boc- β -Homovaline Repetitions

Stock solutions of the guest were made by independently dissolving either N-Boc-D- β -Homovaline (12.03 mg, 0.052 mmol) or N-Boc-L- β -Homovaline (13.65 mg, 0.059 mmol) in 10 mL of default buffer. Repetitions were made by adding two equivalents of either N-Boc-D- β -Homovaline (1.0 mM, 192.30 μ L), or N-Boc-L- β -Homovaline (1.0 mM, 169.50 μ L) to a solution containing the host (0.5 mM, 43.02 μ L) in the default buffer, and recording the resulting CD spectra.

3.5.3. Baeyer-Villiger Reactions

Each catalyst on resin (100 mg, .049 mmol) was loaded into one well of a 48 well plate. To this plate was added 3-phenylcyclobutanone (28.65 mg, .196 mmol) dissolved in 1 mL CHCl₃. Hydrogen peroxide (30% aqueous, 39.92 μ L, .392 mM) was added next, and the plate was sealed and shaken for 16 hours to complete the reaction. After 16 hours, the contents were filtered into a new plate. To this plate was added lithium hydroxide (5 eq relative to cyclobutanone substrate) dissolved in equivolume mixture of water and THF. This plate was sealed, and shaken for 6 hours to complete the hydrolysis. The product of oxidation and subsequent hydrolysis was confirmed by mass spectrometry, and the solvent was removed in each well by lyophilizing. The resultant product was dissolved to 1.0 mM in buffer solution, assuming a 5% overall conversion. These numbers are consistent with the yields confirmed through previous experiments. The host was added (0.5 mM), and the CD spectra taken. ESI MS: 179.20 ([M-H]⁻); calculated 179.08.

3.6. REFERENCES FOR CHAPTER 3

- (1) Voet, D.; Voet, J. G. *Biochemistry*; 4th ed.; John Wiley & Sons: Hoboken, NJ, 2011.
- (2) Seyden-Penne, J. *Chiral auxiliaries and ligands in asymmetric synthesis*; Wiley: New York, 1995.
- (3) Najera, C.; Sansano, J. M. *Chem Rev* **2007**, *107*, 4584.
- (4) Ma, J. A. *Angew Chem Int Ed Engl* **2003**, *42*, 4290.
- (5) Lelais, G.; Seebach, D. *Biopolymers* **2004**, *76*, 206.
- (6) Seebach, D.; Matthews, J. L. *Chem Commun* **1997**, 2015.
- (7) Seebach, D.; Gademann, K.; Schreiber, J. V.; Matthews, J. L.; Hintermann, T.; Jaun, B.; Oberer, L.; Hommel, U.; Widmer, H. *Helv Chim Acta* **1997**, *80*, 2033.
- (8) Hintermann, T.; Seebach, D. *Chimia* **1997**, *51*, 244.
- (9) Appella, D. H.; Christianson, L. A.; Klein, D. A.; Powell, D. R.; Huang, X. L.; Barchi, J. J.; Gellman, S. H. *Nature* **1997**, *387*, 381.
- (10) Krauthauser, S.; Christianson, L. A.; Powell, D. R.; Gellman, S. H. *J Am Chem Soc* **1997**, *119*, 11719.
- (11) Ait-Haddou, H.; Wiskur, S. L.; Lynch, V. M.; Anslyn, E. V. *J Am Chem Soc* **2001**, *123*, 11296.
- (12) Folmer-Andersen, J. F.; Lynch, V. M.; Anslyn, E. V. *Chem-Eur J* **2005**, *11*, 5319.
- (13) Folmer-Andersen, J. F.; Lynch, V. M.; Anslyn, E. V. *J Am Chem Soc* **2005**, *127*, 7986.
- (14) Buryak, A.; Severin, K. *J Am Chem Soc* **2005**, *127*, 3700.
- (15) Bonizzoni, M.; Fabbrizzi, L.; Piovani, G.; Taglietti, A. *Tetrahedron* **2004**, *60*, 11159.
- (16) Han, M. S.; Kim, D. H. *Tetrahedron* **2004**, *60*, 11251.
- (17) Berova, N.; Di Bari, L.; Pescitelli, G. *Chem Soc Rev* **2007**, *36*, 914.
- (18) Matile, S.; Berova, N.; Nakanishi, K.; Novkova, S.; Philipova, I.; Blagoev, B. *J Am Chem Soc* **1995**, *117*, 7021.

- (19) Matile, S.; Berova, N.; Nakanishi, K.; Fleischhauer, J.; Woody, R. W. *J Am Chem Soc* **1996**, *118*, 5198.
- (20) Zahn, S.; Canary, J. W. *Org Lett* **1999**, *1*, 861.
- (21) Holmes, A. E.; Zahn, S.; Canary, J. W. *Chirality* **2002**, *14*, 471.
- (22) Zhang, J.; Holmes, A. E.; Sharma, A.; Brooks, N. R.; Rarig, R. S.; Zubieta, J.; Canary, J. W. *Chirality* **2003**, *15*, 180.
- (23) Holmes, A. E.; Das, D.; Canary, J. W. *J Am Chem Soc* **2007**, *129*, 1506.
- (24) Misaki, H.; Miyake, H.; Shinoda, S.; Tsukube, H. *Inorg Chem* **2009**, *48*, 11921.
- (25) Winschel, C. A.; Kalidindi, A.; Zgani, I.; Magruder, J. L.; Sidorov, V. *J Am Chem Soc* **2005**, *127*, 14704.
- (26) Joyce, L. A.; Maynor, M. S.; Dragna, J. M.; da Cruz, G. M.; Lynch, V. M.; Canary, J. W.; Anslyn, E. V. *J Am Chem Soc* **2011**, *133*, 13746.
- (27) von Baeyer, A. V., V. *Berichte der Deutschen Chemischen Gesellschaft* **1899**, *32*, 3625.
- (28) Krow, G. R. In *Organic Reactions*; John Wiley & Sons, Inc.: 2004.
- (29) ten Brink, G. J.; Arends, I. W. C. E.; Sheldon, R. A. *Chem Rev* **2004**, *104*, 4105.
- (30) Katsuki, T. *Russian Chemical Bulletin* **2004**, *53*, 1859.
- (31) Mihovilovic, M. D. *Current Organic Chemistry* **2006**, *10*, 1265.
- (32) Colladon, M.; Scarso, A.; Strukul, G. *Synlett* **2006**, *2006*, 3515.
- (33) Frison, J.-C. d.; Palazzi, C.; Bolm, C. *Tetrahedron* **2006**, *62*, 6700.
- (34) Watanabe, A.; Uchida, T.; Irie, R.; Katsuki, T. *Proc Natl Acad Sci U S A* **2004**, *101*, 5737.
- (35) Murahashi, S.; Ono, S.; Imada, Y. *Angew Chem Int Ed Engl* **2002**, *41*, 2366.
- (36) Jakobsche, C. E.; Peris, G.; Miller, S. J. *Angew Chem Int Ed Engl* **2008**, *47*, 6707.
- (37) Peris, G.; Miller, S. J. *Org Lett* **2008**, *10*, 3049.
- (38) McCarpa, F.; Long, P. V. *Tetrahedron Letters* **1981**, *22*, 3009.
- (39) Malkov, A. V.; Friscourt, F.; Bell, M.; Swarbrick, M. E.; Kocovsky, P. *The Journal of Organic Chemistry* **2008**, *73*, 3996.
- (40) Hughes, G.; Kimura, M.; Buchwald, S. L. *J Am Chem Soc* **2003**, *125*, 11253.

- (41) Konig, W.; Geiger, R. *Chem Ber* **1970**, *103*, 788.
- (42) Kaiser, E.; Colescott, R. L.; Bossinger, C. D.; Cook, P. I. *Anal Biochem* **1970**, *34*, 595.
- (43) Lichtor, P. A.; Miller, S. J. *ACS Comb Sci* **2011**, *13*, 321.
- (44) Li, Y.; Miller, S. J. *The Journal of organic chemistry* **2011**, *76*, 9785.
- (45) Kenner, J.; Stubbings, W. V. *J. Chem. Soc., Trans.* **1921**, *119*, 593.
- (46) Adams, R.; Yuan, H. C. *Chem Rev* **1933**, *12*, 261.
- (47) Stoughton, R. W.; Adams, R. *J Am Chem Soc* **1932**, *54*, 4426.
- (48) Eliel, E. L.; Wilen, S. H.; Mander, L. N. *Stereochemistry of organic compounds*; Wiley: New York, 1994.
- (49) Seebach, D.; Jaeschke, G.; Gottwald, K.; Matsuda, K.; Formisano, R.; Chaplin, D. A.; Breuning, M.; Bringmann, G. *Tetrahedron* **1997**, *53*, 7539.
- (50) Clayden, J.; Moran, W. J.; Edwards, P. J.; LaPlante, S. R. *Angew Chem Int Ed Engl* **2009**, *48*, 6398.
- (51) Noyori, R.; Takaya, H. *Accounts Chem Res* **1990**, *23*, 345.
- (52) Pu, L. *Accounts Chem Res* **2011**, *45*, 150.
- (53) Bringmann, G.; Mortimer, A. J. P.; Keller, P. A.; Gresser, M. J.; Garner, J.; Breuning, M. *Angew Chem Int Edit* **2005**, *44*, 5384.
- (54) Shindo, M.; Koga, K.; Tomioka, K. *J Am Chem Soc* **1992**, *114*, 8732.
- (55) Li, X. L.; Hewgley, J. B.; Mulrooney, C. A.; Yang, J. M.; Kozlowski, M. C. *J Org Chem* **2003**, *68*, 5500.
- (56) Yin, J.; Buchwald, S. L. *J Am Chem Soc* **2000**, *122*, 12051.
- (57) Hayashi, T.; Hayashizaki, K.; Kiyoi, T.; Ito, Y. *J Am Chem Soc* **1988**, *110*, 8153.
- (58) Bringmann, G.; Menche, D. *Accounts Chem Res* **2001**, *34*, 615.
- (59) Clayden, J.; Fletcher, S. P.; McDouall, J. J. W.; Rowbottom, S. J. M. *J Am Chem Soc* **2009**, *131*, 5331.
- (60) Kakiuchi, F.; Le Gendre, P.; Yamada, A.; Ohtaki, H.; Murai, S. *Tetrahedron-Asymmetr* **2000**, *11*, 2647.
- (61) Gustafson, J. L.; Lim, D.; Miller, S. J. *Science* **2010**, *328*, 1251.

(62) Johnson, F. *Chem Rev* **1968**, 68, 375.

Chapter 4: Progress Toward the Creation of Self-Assembled Chiral Carboxylic Acid Receptors

4.1. INTRODUCTION

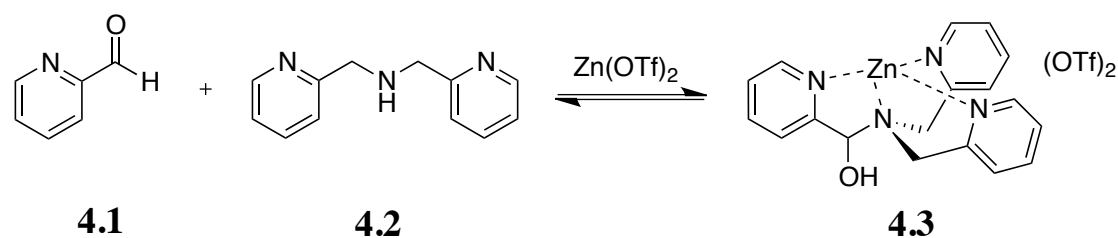
The previous two chapters have established that assays utilizing host **2.34** can rapidly and accurately determine the *ee* and identity of chiral carboxylic acids. While this method has proven quite general, it is not without its drawbacks. The CD signal occurs at short wavelength, deep in the UV portion of the spectrum. Several functional groups absorb in this region of the spectrum, and thus the signal of interest is susceptible to competitive absorption from these other species. Several chiral ligands that are used in synthesis absorb in this region of the spectrum, such as BINOL. These chiral entities have a signal that may interfere with analysis. For this reason it is desirable to extend the observed CD signal of the system to longer wavelengths. It is not possible to change the spectral properties of host **2.34** without synthesizing a new ligand with different chromophores. The structure of the ligand would likely be empirically chosen, with little predictive ability as to the spectral properties of the new iterations. In order to avoid this potential problem, the focus was turned towards a multi-component assembly strategy to create a host through reversible covalent bond formation.

4.1.1. Dynamic Multi-Component Assemblies

A significant amount of supramolecular chemistry research has been recently devoted to the study of systems that possess reversible covalent bonds. Systems of this type have been envisioned as sensors, molecular machines, and other complex architectures.¹⁻⁶ Along these lines, the dynamic properties of several types of these reversibly bonded systems have been explored. One such example is the addition of amine nucleophiles to carbonyls to create imine bonds.⁷⁻¹⁰ This approach was recently applied by the Anslyn group in the creation of a dynamic multicomponent assembly

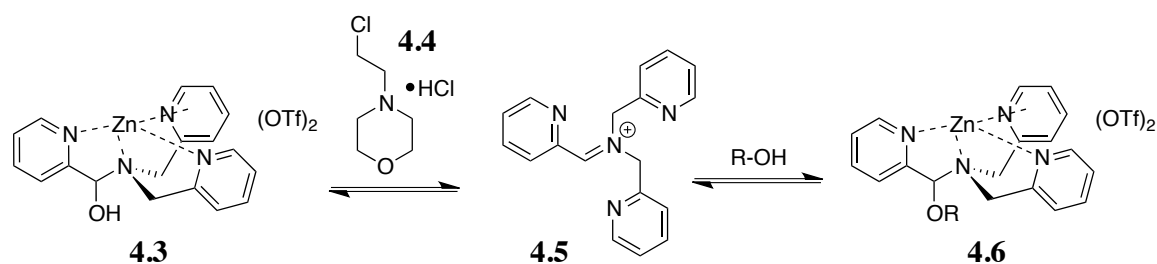
based around the formation of hemiaminal assemblies.¹¹ These assemblies were envisioned as a sensing system for determining the enantiomeric excess of chiral secondary alcohols.¹²

Assembly formation was carried out in acetonitrile by adding three components together: an aldehyde, a secondary amine, and a metal ion. An example of the assembly is shown in **Scheme 4.1**, where the three components applied are 2-pyridinecarboxaldehyde **4.1**, bis(2-pyridylmethyl)amine **4.2**, and a zinc metal salt (**Scheme 4.1**). Various salts of metal ions were studied, but complex formation was most favorable with zinc triflate. Additionally, the complex was found to form for a broad range of aromatic heterocyclic aldehydes. The zinc ion templates *in situ* formation of the metal complex, and complexes formed in this manner are remarkably similar to the class of tris-(2-pyridylmethyl)amine complexes that have received significant attention in the literature.¹³⁻¹⁷ The loss of water usually serves as the driving force for imine formation, but this process does not exist for this complex because the nucleophilic attack is from a secondary amine. Thus, the hemiaminal species has a much longer lifetime than typically observed.



Scheme 4.1. Three-component assembly formation of complex **4.3** from 2-pyridinecarboxaldehyde **4.1**, bis(2-pyridylmethyl)amine **4.2**, and zinc triflate.

The elimination of water from complex **4.3**, though, can be facilitated by the addition of a Brønsted acid. This acid activates the system toward water loss and subsequent formation of iminium ions such as **4.5** in **Scheme 4.2**. Several Brønsted acids were screened, with 4-(2-chloroethyl)morpholine hydrochloride **4.4** resulting in the greatest extent of complex formation. The newly formed iminium complex is a better electrophile than the carbonyl, and thus more susceptible to nucleophilic attack from the relatively poor alcohol nucleophile. Addition of chiral alcohols to the prochiral iminium ion leads to diastereomeric complexes and thus a difference in energy, causing one to form preferentially. The complexes that are formed have helical chirality, as seen with similar published systems.¹³⁻¹⁷ When an excess of one enantiomer of the alcohol is used, a CD signal is observed for the complex. The size of the CD signal can be related to the *ee* of the alcohol substrate through the creation of a calibration curve that allows for rapid assessment of enantiomeric composition.



Scheme 4.2. Brønsted acid-catalyzed dehydration of **4.3** to give iminium ion **4.5**, and subsequent nucleophilic addition of an alcohol to give complex **4.6**.

This report served as an inspiration for the creation of a self-assembled system that could enantioselectively sense chiral analytes. Owing largely to the structural similarity of the self-assembled complex to host **2.34**, the carboxylic acids seemed amenable to analysis with this type of self-assembled sensing system. The rest of this chapter will detail the efforts to create a self-assembled multi-component assembly sensor for carboxylates.

4.2. SELF-ASSEMBLED IMINE-METAL COMPLEX

The carboxylic acid sensor **2.34** presented earlier served as a good means to determine the *ee* and identity of a variety of α - and β -chiral carboxylic acids with both commercially available and synthetic substrates. As mentioned, several issues can be addressed to improve this system. This signal is at a low wavelength where it is susceptible to competitive absorption. This problem becomes more disconcerting when considering the goal of applying this sensor to synthetic samples that have more complex solution environments. Larger error would be expected for these types of samples, and the analysis would be less accurate than our fundamental studies.

For this reason, it is desirable to generate a signal in the visible portion of the electromagnetic spectrum. Fewer organic molecules absorb at these longer wavelengths,

and a signal here should be free of interference from other absorbing species. The location of the absorbance band is a property of the quinoline chromophores that make the sensor, and thus it is necessary to change these chromophores in order to change the location of the signal. Synthetic effort would have to be expended to create each newly envisioned sensor, without any promise of success. To avoid these pitfalls, a self-assembled sensor was envisioned. Rapid access may be afforded to complexes based on different chromophores, with the new absorbance values dictated by these structures. This system will now be presented in detail.

4.2.1. Design Criteria

The same core structure of host **2.34** was retained in the self-assembled system. Assembly was built up around a tertiary nitrogen atom. This tertiary nitrogen atom would have three arms, each having a terminal amine group to create a tetradentate ligand to coordinate a central metal ion. These arms would have two carbon atoms separating the tertiary nitrogen atom and the exterior nitrogens. The peripheral nitrogen atoms were envisioned to be imine nitrogens, formed by reaction of amines and an aldehyde. This is represented pictorially in **Figure 4.1**.

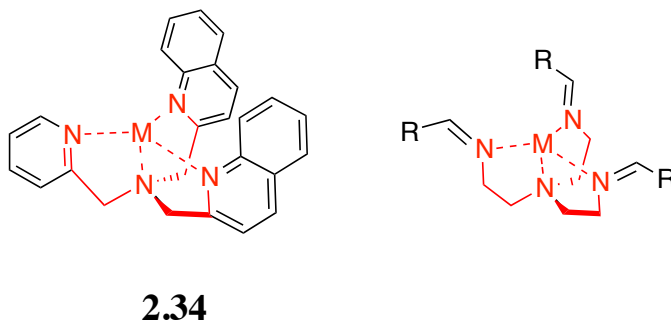
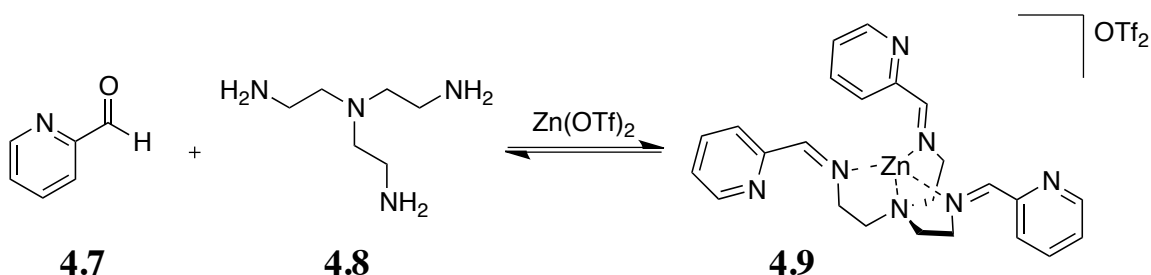


Figure 4.1. Structural similarity of carboxylic acid host **2.34** and the proposed structure of a self-assembled receptor.

4.2.2. Complex Formation

The tris-amine component tris(2-aminoethyl)amine **4.8** was selected for this study because it is commercially available and fits the criteria outlined on the previous page. The same aldehyde used in the alcohol sensor, namely 2-pyridinecarboxaldehyde **4.7**, was selected as the model aldehyde because its success had been demonstrated previously. The metal selected was zinc triflate, also selected based on prior results. The formation of the complex between these three components is shown in **Scheme 4.3**.



Scheme 4.3. Proposed structure of complex **4.9**, self-assembled from **4.7** and **4.8**.

In order to monitor complex formation, 1H NMR was chosen as an analysis tool. To this end, spectra were recorded for various permutations of these three components (**Figure 4.2**). Compound **4.7** shows a characteristic aldehyde peak around 10.0 ppm, that was monitored throughout complex formation. When three equivalents of **4.7** were added to the tris-amine ligand **4.8**, the aldehyde peak disappeared and a new peak grew in at 8.3 ppm. This singlet represents the imine proton, that replaces the aldehyde signal. The upfield shift of approximately 1.7 ppm is consistent with formation of an imine. This nucleus is more shielded in the imine than the aldehyde, since the imine nitrogen is less electron-withdrawing than the carbonyl oxygen. Finally, the imine proton of the complex formed upon addition of zinc triflate is shifted downfield to 8.6 ppm. This

downfield shift is consistent with formation of a bond between the imine nitrogen and the zinc metal center. This bond withdraws some electron density from the imine nitrogen, which in turn removes some electron density from this nitrogen, making it less shielded.

Another interesting feature of the spectrum of the metal complex is the methylene peaks that correspond to the hydrogens on the carbon atoms between the tertiary and amine nitrogen atoms. In the tris-imine species, the complex is free to rotate and these peaks average out into two clean triplets. When the metal binds to the tris-imine, these two peaks split into four peaks, one for each proton. The chemical non-equivalence of these protons can be attributed to the stereoisomers formed upon inversion between the two possible helices. If this inversion occurs rapidly in solution the protons become equivalent, reducing the number of peaks to two. Since four peaks are observed, the interconversion between the two helices is slow on the NMR timescale.

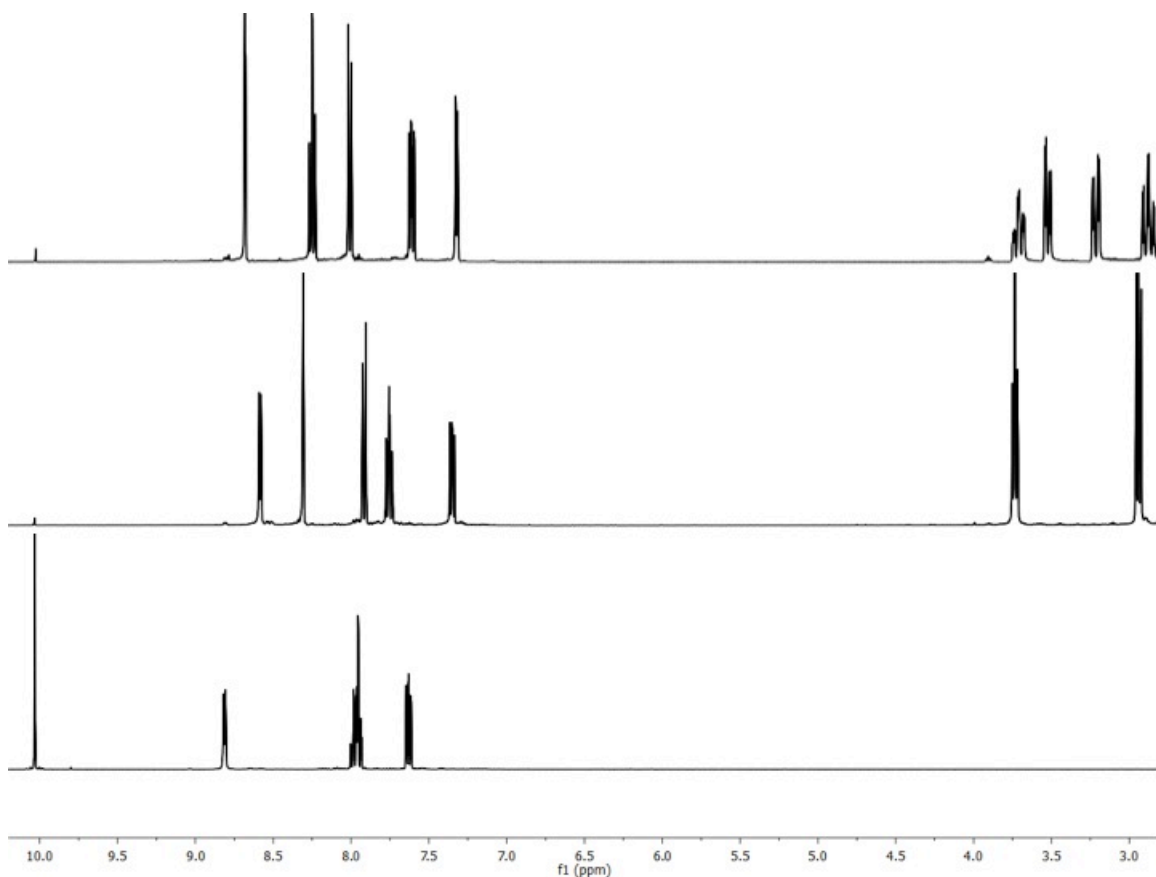


Figure 4.2. ^1H NMR spectra recorded (all in CD_3CN) for 2-pyridinecarboxaldehyde **4.7** alone, (bottom panel), the tris-imine formed between **4.7** and tris-amine **4.8** (middle panel), and these two components with $\text{Zn}(\text{OTf})_2$ (top panel).

The ^1H NMR provided evidence that the envisioned complex was forming when these components were mixed together in solution. Additional characterization was undertaken in order to further confirm the structure of the complex **4.9** in solution. The first additional characterization method applied was ^{13}C NMR. The spectrum showed the presence of eight unique signals corresponding to eight different types of carbon atoms in the product. The number of signals, along with their chemical shifts, corresponded to the spectrum envisioned for complex **4.9**. Additionally, mass spectrometry data were recorded for this sample. The peak seen in the mass spectrum corresponded to the

structure that was envisioned. The signal also contained the correct isotopic ratios for a compound with zinc metal, providing additional evidence that the *in situ*-generated complex has the proposed structure.

4.2.3. X-ray Analysis

In order to visualize the complex structure in the solid phase, an x-ray suitable crystal was grown by slow vapor diffusion of diethyl ether into a solution containing the complex in acetonitrile. It was anticipated that the zinc center would adopt a trigonal bipyramidal geometry, with the tris-imine acting as a tetradentate ligand through the three imine and tertiary amine nitrogen atoms. This structure would be analogous to that of the complexes such as **2.34** studied earlier. The structure obtained for this crystal is shown in **Figure 4.3**, and was markedly different than envisioned. Rather than forming a pentacoordinate trigonal bipyramidal geometry, the zinc metal center was a hexacoordinate distorted octahedral complex.

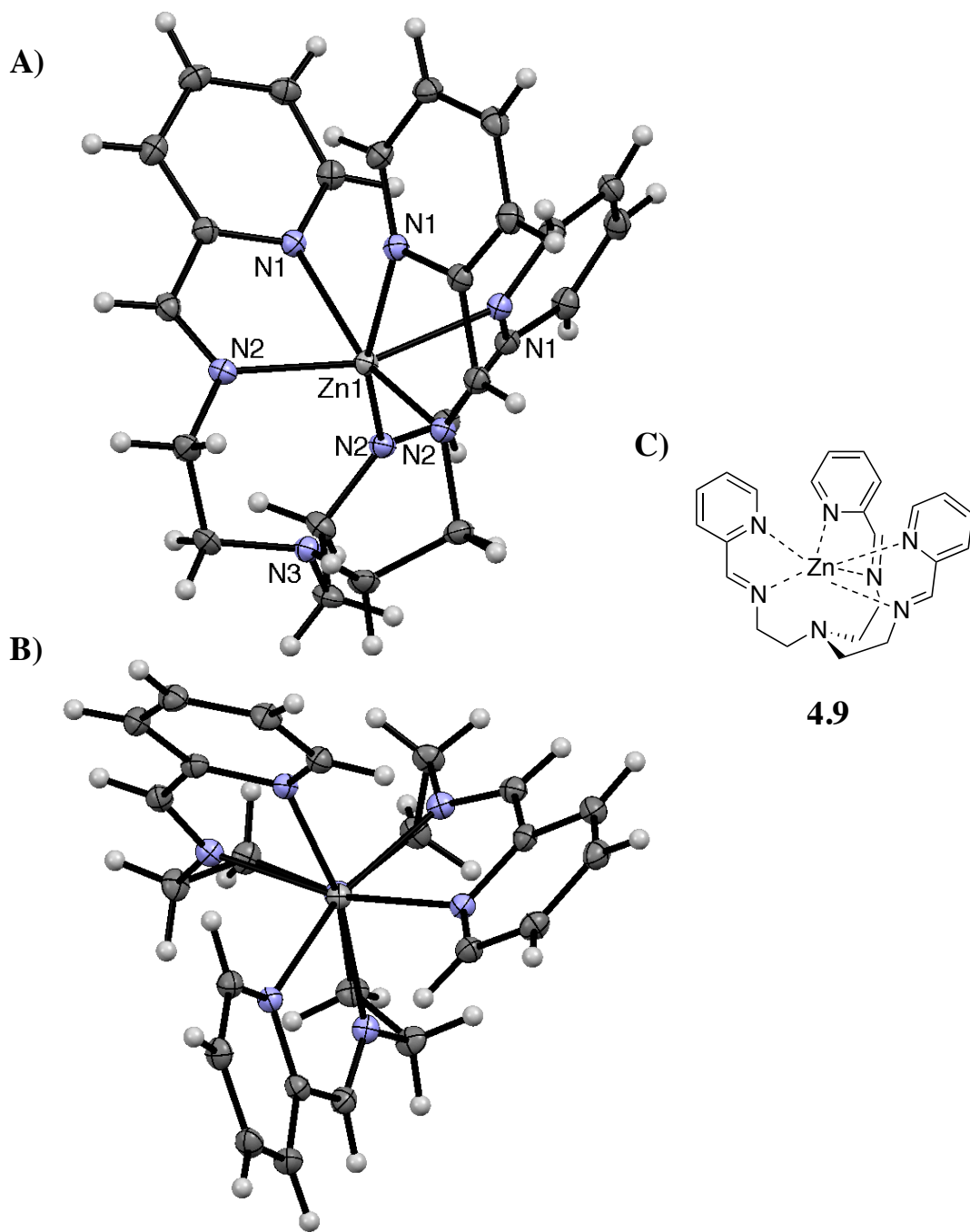


Figure 4.3. Crystal structure of complex **4.9**, viewed from the side (A) and the top (B). Displacement ellipsoids are scaled to 50%, and counterions removed for clarity. C) Structural representation of the complex.

In this crystal structure, no association was found between the tertiary nitrogen and the zinc metal, with the distance between these calculated to be 2.8Å. Instead of coordination to this tertiary nitrogen atom, the metal center is bound to the three pyridine nitrogen atoms. The three bonds between the zinc and imine nitrogen had an average length of 2.10Å, while the three between the metal and the pyridine nitrogens were found to be slightly longer, at an average of 2.29Å. These values are within the range of bond lengths typical of these complexes.^{18,19} It appears that the cooperative effect of the additional coordination available to the pyridine nitrogen atoms moves the zinc metal away from the tertiary amine segment. Additionally, the crystal structure shows three CH- π interactions between each proton in the 6-position of the aldehyde and the adjacent pyridine aromatic ring. This stabilizing force likely provides another driving force for the observed octahedral geometry.

Unfortunately, the six-coordinate complex cannot act as a self-assembled carboxylate sensor. No open coordination sites are available to accommodate the guest, and it is unlikely that a carboxylate analyte could replace coordination to one of the nitrogen atoms of the ligand. The structures that were formed from this self-assembly were unique, and studies were undertaken to explore the generality of this assembly. The first studies carried out focused on the effect of the aldehyde segment of the assembly.

4.2.4. Incorporation of Additional Aldehydes

The structure found in the three-component assembly reported in the last section has roots in the coordination of the pyridine nitrogen atoms from the aldehyde. Naturally, it was postulated that removing this atom could shift the preference of the system toward the five-coordinate trigonal bipyramidal geometry. The self-assembled ligand would take up four coordination sites on the metal, leaving one available to bind

the carboxylate guest. To this end, three equivalents of benzaldehyde **4.10** were added to the tris-amine **4.8** and $\text{Zn}(\text{OTf})_2$. The resultant complex was again monitored with ^1H NMR spectroscopy, with the analysis directed toward the aldehyde proton.

A spectrum was recorded for **4.10** alone, showing a peak corresponding to the aldehyde proton at 10.0 ppm (**Figure 4.4**). This peak disappeared when **4.8** was added, resulting in formation of the tris-imine species and the concurrent growth of a peak at 8.1 ppm. This peak corresponds to the newly formed imine proton, similar to the observation for aldehyde **4.7**. The next spectrum was recorded after addition of $\text{Zn}(\text{OTf})_2$ to the tris-imine complex. Rather than forming the metal complex as expected, the aldehyde peak of **4.10** was regenerated, with no remaining imine proton signal. Apparently, the metal causes hydrolysis of the imine bonds back to the amine and aldehyde. This is likely due to the missing pyridine nitrogen atoms that help form a stable octahedral complex.

To test whether this observed hydrolysis was a result of the electrophilicity of the aldehyde, two additional substituted benzaldehydes were tested for complex formation. Aldehyde **4.11** contained an electron-donating dimethylamino group to make the carbonyl less electrophilic, while **4.12** possessed an electron-withdrawing cyano to increase the electrophilic character of the carbonyl. The tris-imine was never detected for the complex using **4.11**, likely an artifact of the increased electronic character at the aldehyde carbon. In the case of aldehyde **4.12**, the same behavior was observed as for benzaldehyde **4.10**. The tris-imine was determined to form and then hydrolyze upon addition of the metal. Similar results were obtained for other metal salts, and imine hydrolysis was also seen when forming the complex over molecular sieves. Given the requirement of coordinating pyridine nitrogen in the aldehyde structure, the focus was shifted using differently substituted versions of 2-pyridinecarboxaldehyde.

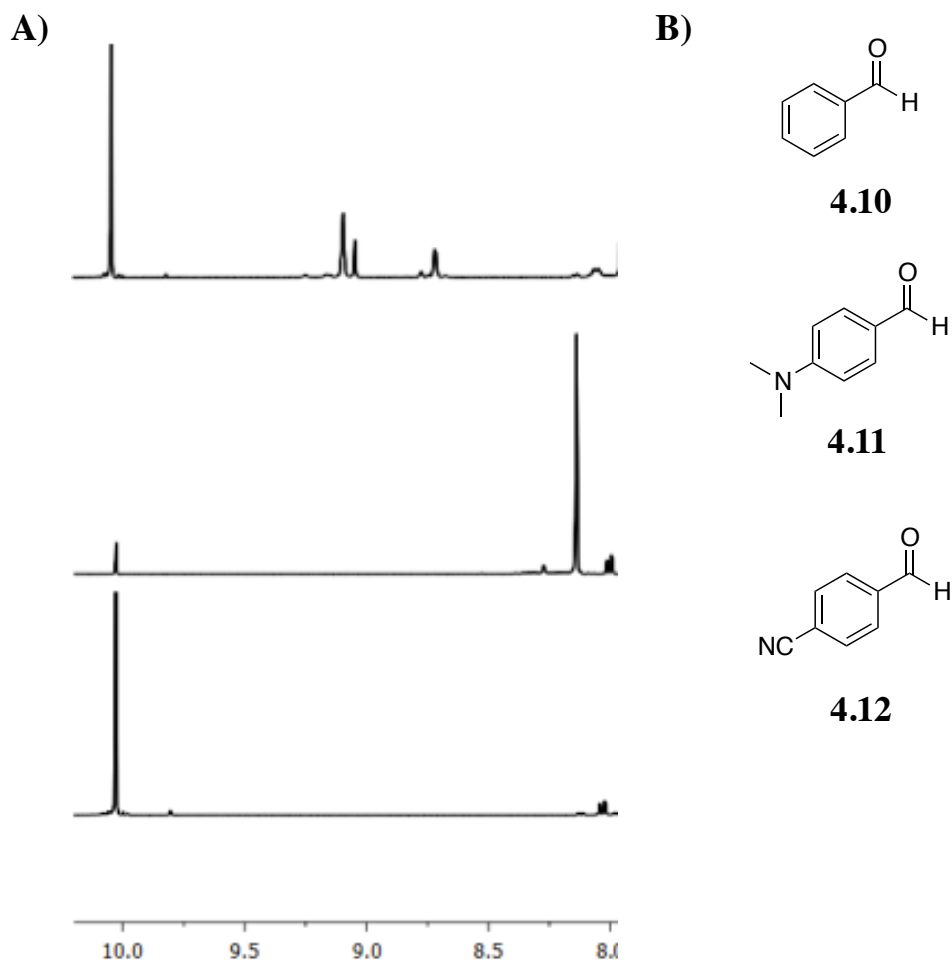


Figure 4.4. A) ¹H NMR spectra recorded for benzaldehyde **4.10** alone, (bottom panel), the tris-imine formed between **4.10** and tris-amine **4.8** (middle panel), and these two components with Zn(OTf)₂ (top panel) in CD₃CN. B) Chemical structures for aldehydes **4.10-4.12** used in this study.

There are four possible locations on the pyridine ring, aside from the 2-position with the aldehyde functional group, where it was possible to add substituents. Aldehydes with substituents at this position are shown in **Figure 4.5**. The aldehyde is numbered from the pyridine nitrogen, with the aldehyde located at the second position. Substitution at the remaining positions was studied in this *in situ* complexation, and x-ray

crystallography was chosen to visualize the complex formation. X-ray suitable crystals were grown as previously stated, by slow evaporation of diethyl ether into an acetonitrile solution of the complex.

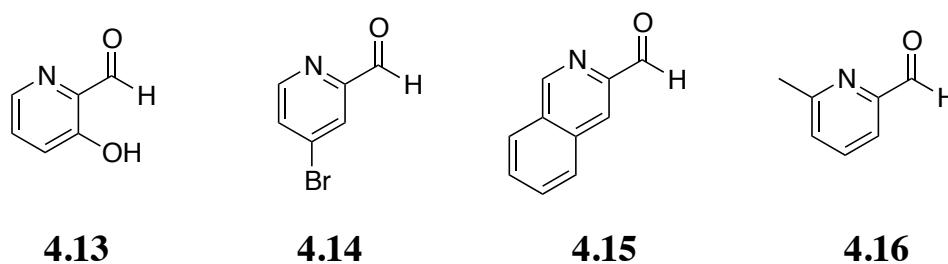


Figure 4.5. Chemical structure for substituted pyridines **4.13-4.16** used for complex formation.

The first aldehyde investigated was 3-hydroxypyridine-2-carboxaldehyde **4.13**. The structure of the complex **4.17** formed between aldehyde **4.13**, tris-amine **4.8**, and $\text{Zn}(\text{ClO}_4)_2$ is shown in **Figure 4.6**. The structure of this complex was similar to the structure of **4.9**, with the zinc metal adopting a hexacoordinate octahedral geometry. It was again observed that the tertiary nitrogen atom was not coordinated to the metal center. The bond distances between zinc and the pyridine nitrogen atoms are slightly shorter in this complex than for **4.9**, averaging 2.23 Å. These bonds are again longer than those between zinc and the imine nitrogen atoms, which average 2.14 Å. These values were slightly longer relative to the corresponding bonds in complex **4.9**. The zinc atom was further removed from the tertiary nitrogen atom in this complex, at a distance of 3.0 Å.

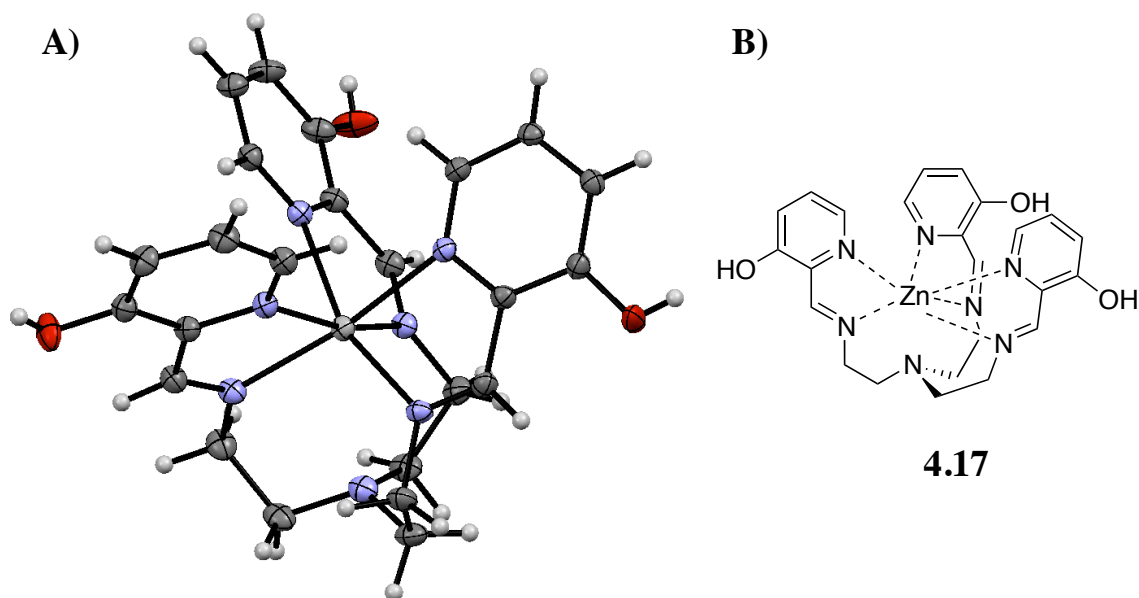


Figure 4.6. A) Crystal structure of complex **4.17**. Displacement ellipsoids are scaled to 50%, and counterions omitted for clarity. B) Structural representation of this complex.

The next aldehyde that was studied for complex formation was 4-bromopyridine-2-carboxaldehyde **4.14**. An x-ray quality crystal was grown of complex **4.18**, analogous to the previous example, and the crystal structure of this complex is shown in **Figure 4.7**. Many of the structural features of the previous complexes carried over to this structure, which had the same distorted octahedral arrangement of ligands around the zinc metal center. The bonds between the zinc and the imine nitrogens were of a similar length as the other assemblies, averaging 2.10 Å. Also similar to the other complexes, bonds between the zinc and pyridine nitrogen atoms averaged 2.29 Å. The distance between the tertiary nitrogen and the zinc metal center was calculated to be 2.95 Å, similar to the distances measured for the previous complex.

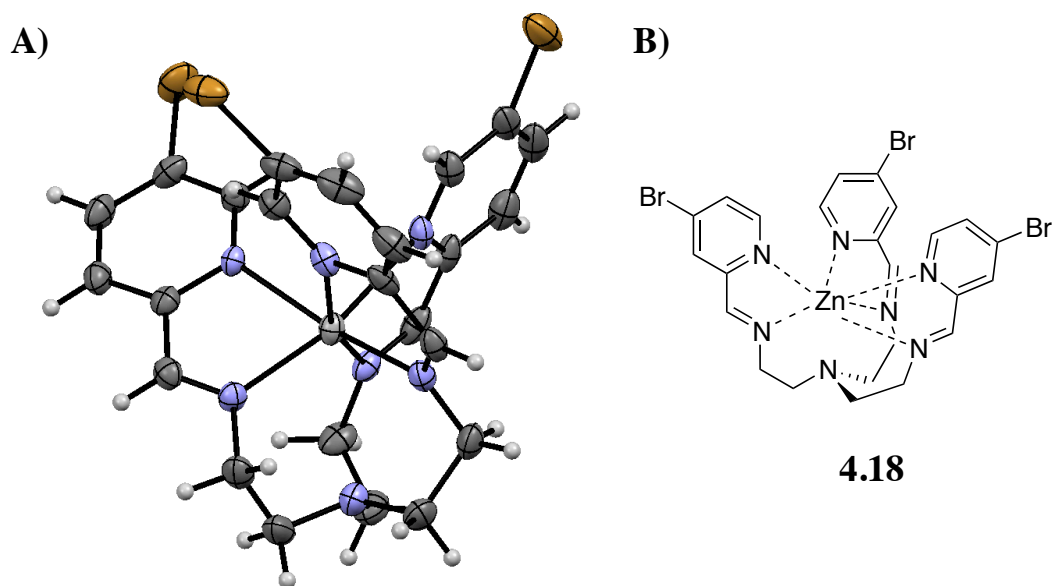


Figure 4.7. A) Crystal structure of complex **4.18**. Displacement ellipsoids are scaled to 50%, and counterions omitted for clarity. B) Structural representation of this complex.

The next aldehyde that was used was a more sterically encumbered species, namely isoquinoline-3-carbaldehyde **4.15**. This species is substituted at two positions, 4- and 5-, around the benzene ring, both positions. This aldehyde is particularly interesting, since the isoquinoline chromophore is similar to the quinoline used in the previously reported carboxylic acid sensor. A crystal of x-ray quality for complex **4.19** was grown in the same fashion as the previous few examples, and the structure was determined for this crystal. The complex was again observed to be a distorted octahedral geometry, with coordination of three imine nitrogen atoms and three quinoline nitrogens (**Figure 4.8**). Despite the increased steric bulk, the bond lengths were not significantly distorted from the crystals grown with pyridine-based aldehydes. The average bond length for the zinc to quinoline nitrogen was calculated to be 2.21 Å, while the bond to the imine nitrogen

averaged 2.13 Å. The metal was held even further from the tertiary nitrogen atom in this structure, with the distance calculated to be 3.14 Å.

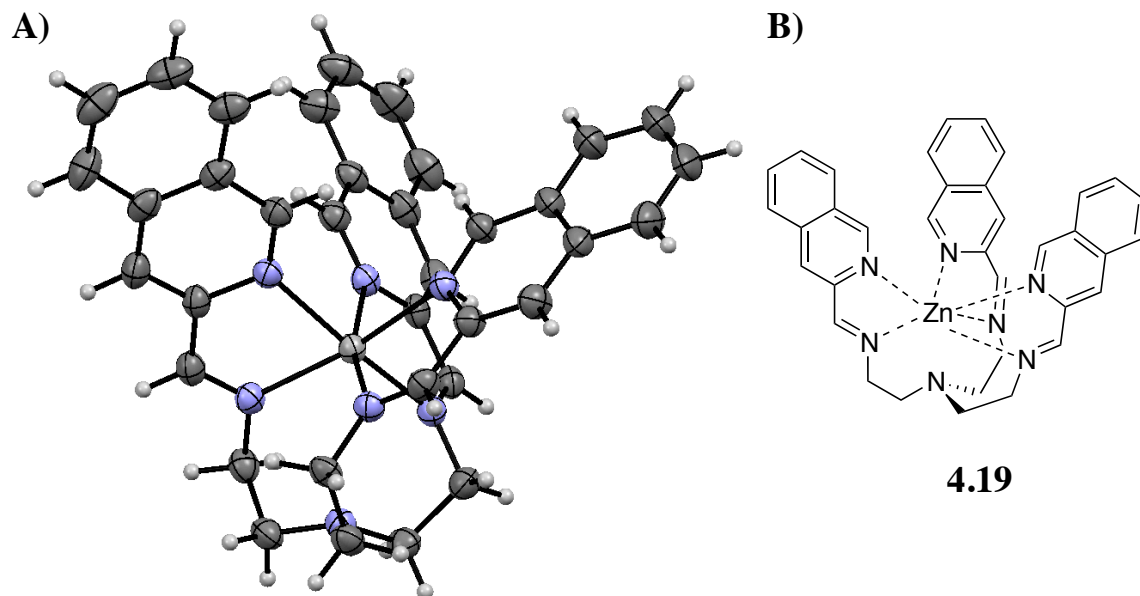


Figure 4.8. A) Crystal structure of complex **4.19**. Displacement ellipsoids are scaled to 50%, and counterions omitted for clarity. B) Structural representation of this complex.

The final location available for substitution on the pyridine ring was position 6-. The aldehyde with this substitution pattern that was used is 6-methylpyridine-2-carboxaldehyde **4.16**. All attempts to grow x-ray quality crystals for this complex failed, and subsequent NMR analysis revealed that complex formation did not occur. The reason this complex did not form was likely steric hindrance. The crystal structures reported for the assembled complexes using various pyridine structures all show three CH- π interactions between the proton in the 6- position of the pyridine ring and an adjacent pyridine ring. This is likely an extra stabilization afforded this molecule, and the distance is correct to accommodate this interaction. When bulkier substituents are placed

at this position it likely destabilizes the complex, preventing complex formation. After determining the range of pyridine-substituted aldehydes that was tolerated by this assembly, the focus of the study shifted toward assembling these components around additional transition metals.

4.2.5. Incorporation of Additional Transition Metals

The assemblies were initially envisioned to serve in a manner very similar to the synthesized complex **2.34**. For this reason, the first additional transition metal to be applied was copper(II). The tris-imine for aldehyde **4.7** and tris-amine **4.8** was formed, and $\text{Cu}(\text{ClO}_4)_2$ was subsequently added to create complex **4.20**. The copper(II) ion is a d^9 metal ion, and thus is paramagnetic. Its paramagnetism excludes it from NMR analysis, and thus x-ray crystallography was an alternative analysis method. To this end, x-ray quality crystals were obtained from vapor diffusion as described previously. The complex was found to form around the copper metal center, and the structure is shown in **Figure 4.9**. A structure similar to the analogous zinc complex was obtained, with a distorted octahedral metal center. This complex displays much greater Jahn-Teller distortion than the zinc analog.²⁰ One imine and one pyridine nitrogen were located at the apical positions, with lengthened bonds of 2.24 and 2.39 Å respectively. The other four bonds were averaged to 2.07 Å. This Jahn-Teller distortion is often observed for complexes of copper(II), as lengthening of these bonds breaks degeneracy and lowers orbital energy overall.²¹ The distorted apical bonds are shown in **Figure 4.9** in the z-axis of the molecule, straight up and down in the figure.

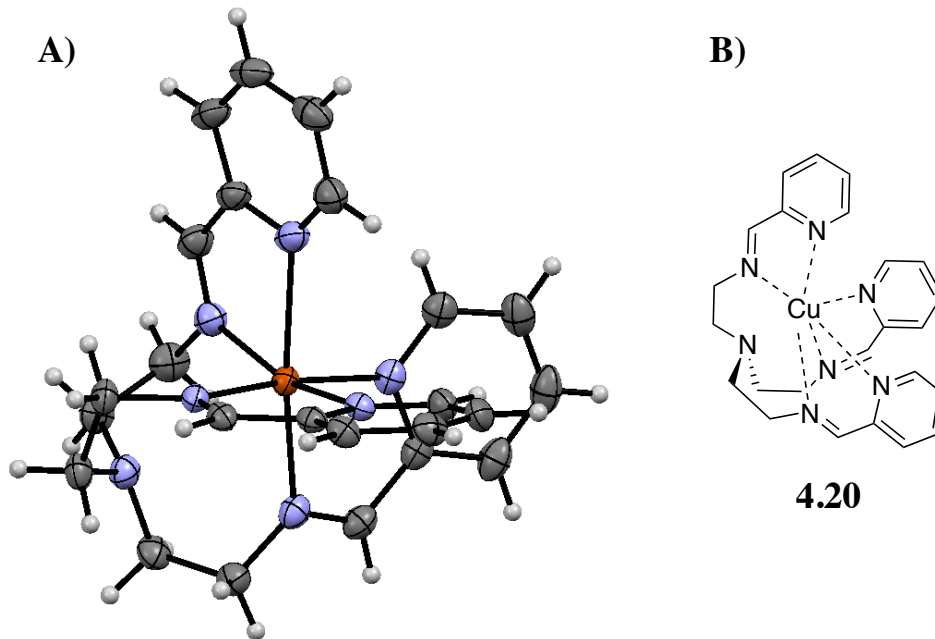


Figure 4.9. A) Crystal structure of complex **4.20**. Displacement ellipsoids are scaled to 50%, and counterions omitted for clarity. B) Structural representation of this complex.

Recently, the Anslyn group was able to successfully determine the *ee* of chiral primary amines through the use of an octahedral complex based around iron(II).²² Because of the recent success with complexes of this ion, this metal was selected for further study. Complex formation was initiated using components **4.7** and **4.8**, followed by addition of $\text{Fe}(\text{ClO}_4)_2$. The structure of this complex (**4.21**) was determined by analysis of an x-ray suitable crystal, and is shown in **Figure 4.10**. The geometry of this complex is almost fully octahedral, lacking the disparity in bond lengths found for the copper and zinc complexes. The average length of the iron to pyridine nitrogen bonds was 1.97 Å, and bonds were 1.95 Å between the iron and imine nitrogen atoms. The tertiary amine nitrogen was even further from the metal center, with the distance

calculated to be 3.49 Å. It seems that the further removed the metal is from the tertiary nitrogen the less distorted is the octahedral geometry of the complex.

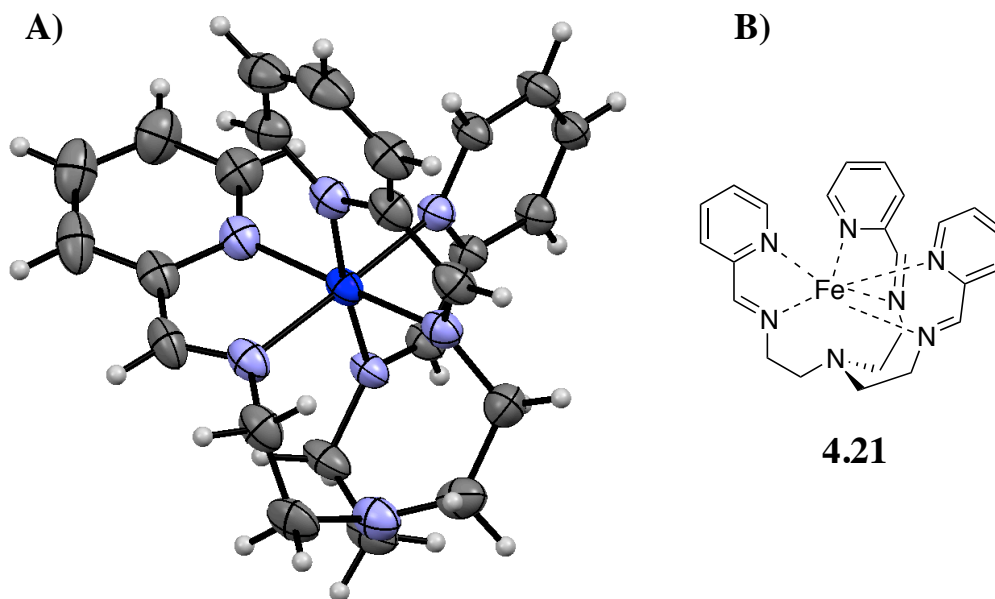


Figure 4.10. Crystal structure of the iron (II) complex with aldehyde **4.7**, viewed from the side. Displacement ellipsoids are scaled to 50%, and counterions omitted for clarity.

4.2.6. Incorporation of Additional Amines

In addition to tris(2-aminoethyl)amine **4.8**, another tris-amine species tris(3-aminopropyl)amine **4.22** is commercially available. This compound has an additional methylene group between the tertiary amine and the terminal amines. The increased size of the arms was postulated to move the tertiary nitrogen atom further from the zinc metal center, potentially creating a cavity that could incorporate an external guest. To this end, the tris-imine was formed between three equivalents of aldehyde **4.7** and tris-amine species **4.22**. $\text{Zn}(\text{OTf})_2$ was added to this tris-imine to form the metal complex, and an x-

ray suitable crystal of complex **4.23** was grown. The structure obtained from this crystal is shown in **Figure 4.11**. There is again a difference in bond lengths between the zinc and pyridine nitrogens, and zinc and imine nitrogens, leading to a distorted octahedral geometry. The average length was 2.2 Å between zinc and pyridine nitrogen atoms, and 2.14 Å between zinc and the imine nitrogens. The extra methylene did increase the size of the void located between the metal and the tertiary amine; this distance was calculated to be 3.44 Å.

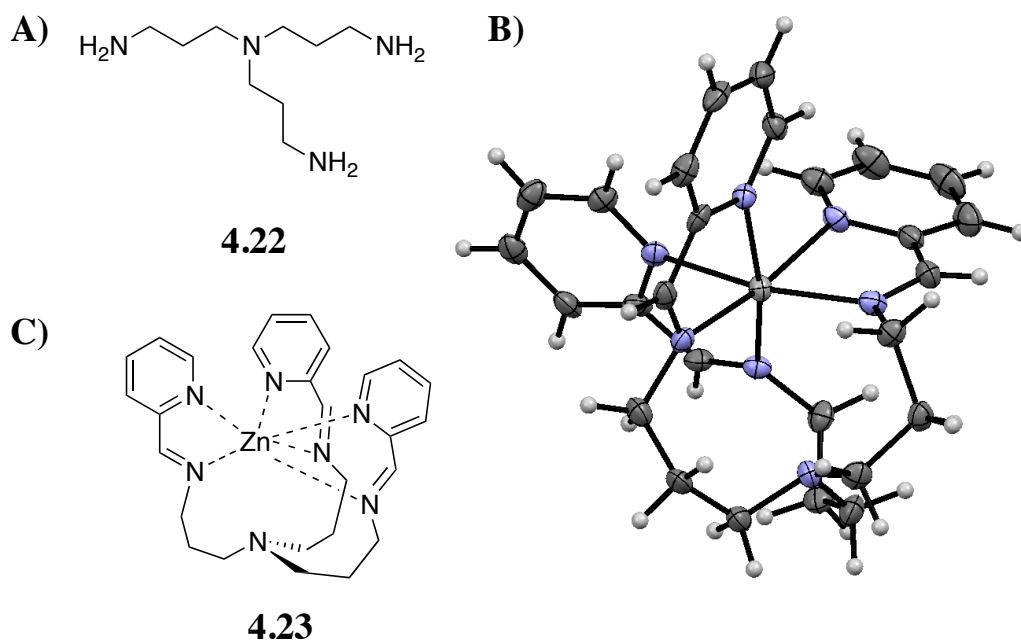
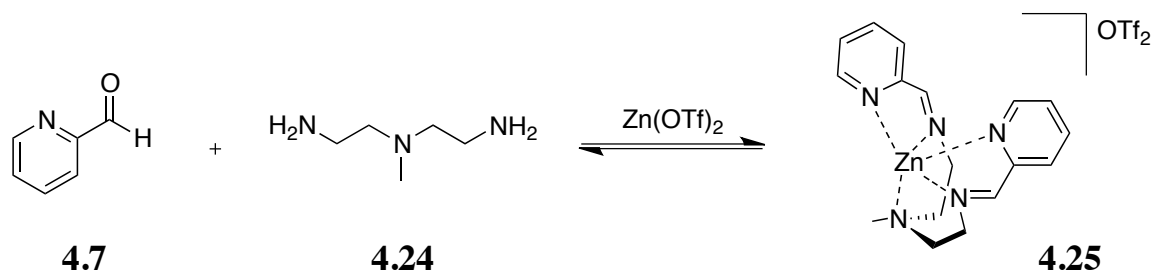


Figure 4.11. A) Structure of tris-amine **4.22**. B) Crystal structure of complex **4.23**. Displacement ellipsoids are scaled to 50%, and counterions omitted for clarity. C) Structural representation of the complex.

None of these species possessed structural features that made them amenable to sensing chiral carboxylic acids. The hexacoordinate metal centers were unable to accept further ligands. This complex formation allows for the creation of a large diversity in

the complex structure by selecting some of the many pyridine-carboxaldehydes, metals, and tris-amine species that have been demonstrated to work. It is still desirable to create a self-assembled sensing ensemble that can facilitate enantioselective recognition. Rather than select aldehydes without coordinating pyridine nitrogen atoms, which proved unsuccessful here, a new strategy was devised. Removing one of the amine arms would remove two coordinating nitrogens, one each from the imine and pyridine. This change was expected to bring about one of two possible changes. First, this complex might retain its octahedral geometry, with two open coordination sites. Alternatively, removing these two coordination sites could force coordination between the metal and the tertiary amine, and cause the geometry to become trigonal bipyramidal. Thus, commercially available bis-amine 2,2'-diamino-N-methyldiethylamine **4.24** was used as the imine-forming species (**Scheme 4.4**).



Scheme 4.4. Proposed formation of self-assembled receptor **4.25**, with an open coordination site to bind a carboxylate guest.

Again, ^1H NMR spectrometry was chosen to monitor complex formation. A spectrum was first recorded for the addition of two equivalents of aldehyde **4.7** to bis-amine complex **4.24**. The resultant bis-imine complex is shown in the middle panel of **Figure 4.12**. The aldehyde peak of **4.7**, located at 10.0 ppm, disappears when these components are mixed. A new peak corresponding to the proton attached to an imine

carbon appears at 8.5 ppm. This peak indicates that the bis-imine complex has formed to a large extent, leaving virtually no free aldehyde in solution. After confirming that the bis-imine complex formed nearly exclusively, $\text{Zn}(\text{OTf})_2$ was added to this solution. The result of this addition is shown in the top panel of **Figure 4.13**. This addition did not result in the hydrolysis of the imine back to the aldehyde, as the characteristic aldehyde peak remained very small. The rest of the spectrum went from clean and sharp peaks, to broader, messy peaks. Multiplicities became difficult to decipher, and methylene peaks appeared as broad singlets. This indicates that there are a variety of species present in solution, and that the peaks average out on the NMR timescale. Another interesting feature of this spectrum is the presence of two peaks around 6.0 ppm. Peaks of this magnitude and shape were determined to be hemiaminal peaks in the self-assembled hemiaminal complex for alcohol sensing.¹² This evidence would suggest that partial hydrolysis of the imine bonds is occurring to form hemiaminal species. A more detailed study of the multiple equilibria established upon addition of metal was necessary, to understand the interplay of these species.

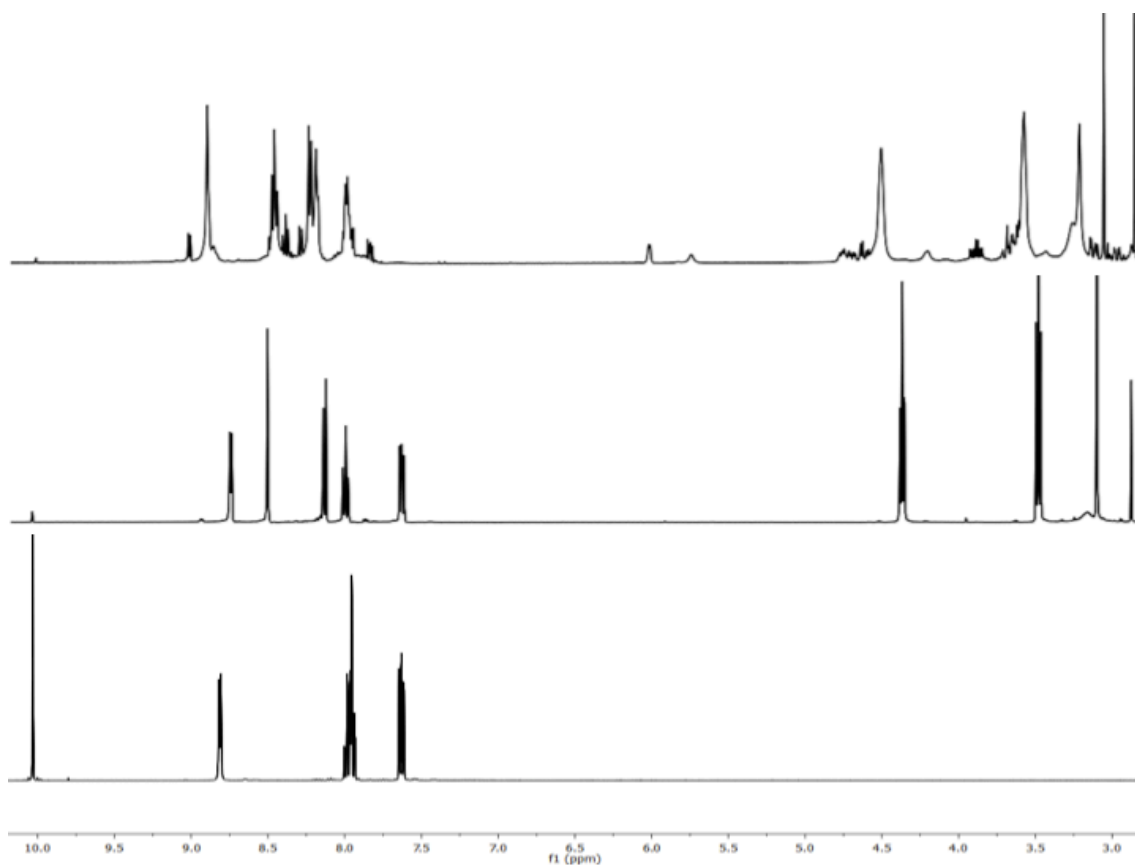


Figure 4.12. ^1H NMR spectra recorded for 2-pyridinecarboxaldehyde **4.7** alone, (bottom panel), the bis-imine formed between **4.7** and bis-amine **4.18** (middle panel), and these two components with $\text{Zn}(\text{OTf})_2$ (top panel) in CD_3CN .

4.2.7. Reversibility of the System

The presence of peaks in the ^1H NMR spectrum corresponding to hemiaminal species indicated that this system was potentially reversible. This reversibility has been proven for the dynamic hemiaminal assembly,¹¹ and could potentially allow greater freedom in the complex formation. This property of reversibility would allow for the possibility of a self-selection of the best aldehyde to bind, and ultimately form a complex. It is envisioned that secondary supramolecular interactions, such as hydrogen bonding, electrostatic attraction, or hydrophobicity, would lead to a preference for each guest to a

particular aldehyde or group of aldehydes. To study reversibility, the complex **4.9** was formed in solution by mixing the components. The aldehyde **4.13** was then added in excess, with the goal of replacing aldehyde **4.7** to form the complex as shown in **Scheme 4.5**.



Scheme 4.5. Envisioned reversibility of complex **4.9** through the addition of aldehyde **4.13**, forming **4.17**.

The imine proton peak in the ^1H NMR spectrum was used to monitor the extent of change to complex **4.9**. As shown previously, complex **4.9** displayed a singlet at 8.6 ppm. When aldehyde **4.13** was added to complex **4.9**, the spectrum was simply an addition of the spectra for **4.9** and **4.13**, indicating that no reaction was taking place. These spectra are shown in **Figure 4.13**. Attempts to form the desired complex by adding a larger excess of aldehyde **4.13** also proved unsuccessful. It was postulated that water was necessary to cause the exchange of aldehydes, since a hemiaminal was likely detected previously. Unfortunately, addition of water did not lead to exchange of the aldehydes either.

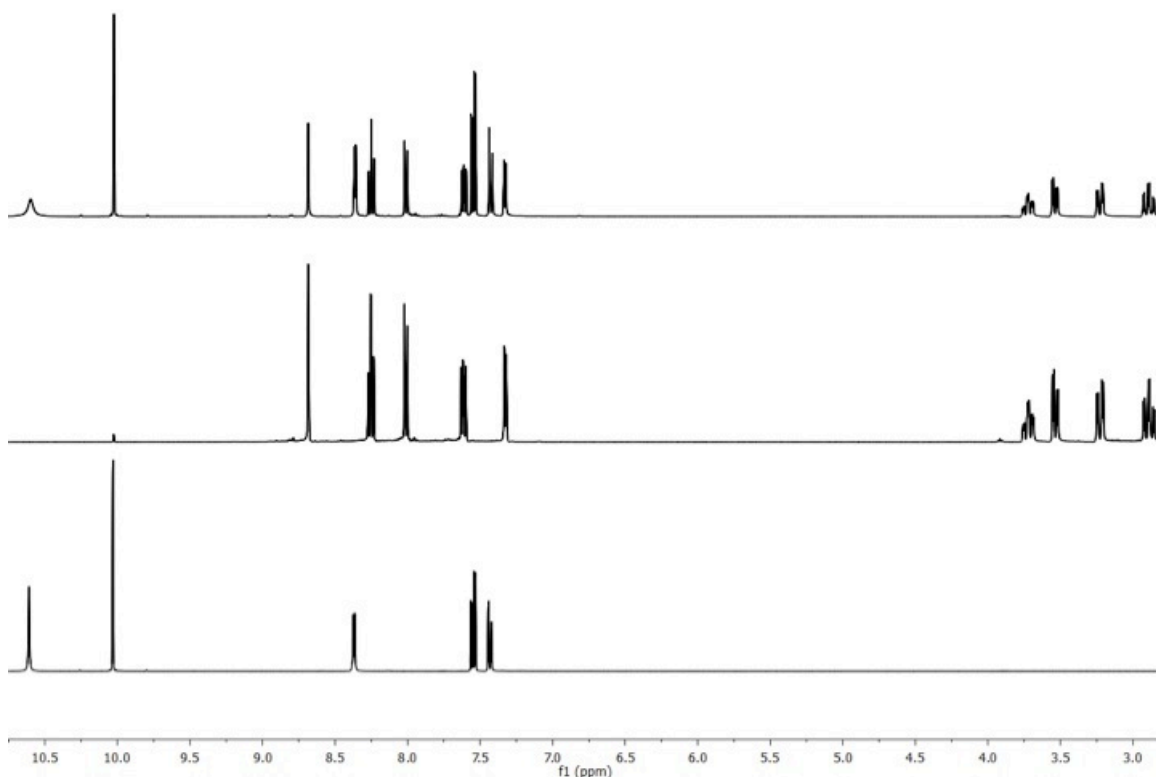
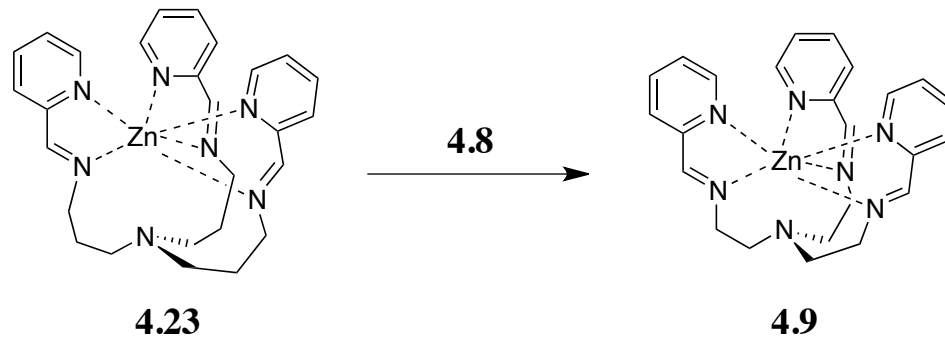


Figure 4.13. ^1H NMR spectra recorded for aldehyde **4.13** alone, (bottom panel), complex **4.9** (middle panel), and one equivalent of **4.13** added to **4.9** (top panel), in CD_3CN .

Reversibility has been achieved previously for dynamic assemblies based on imines. In pioneering work by Lehn and coworkers, the reversibility has been achieved by amine nucleophilicity, rather than adding additional aldehydes.²³ Thus, reversibility may be possible using alternate amine ligands. This theory was tested by initially forming complex **4.22** with the tris-amine ligand **4.17**. Once this complex had formed, one equivalent of the other tris-amine ligand **4.8** was added to the mixture. Any change to the resultant NMR spectrum would indicate that the system is reversible by addition of exogenous amine rather than aldehyde. This is represented pictorially in **Scheme 4.6**.



Scheme 4.6. Envisioned reversibility of complex **4.9** through the addition of tris-amine ligand **4.8**, forming complex **4.9**.

The NMR spectra taken for this experiment are shown in **Figure 4.14**. Addition of the other tris-amine affected the clean spectrum that had been recorded for complex **4.23**, resulting in the appearance of many new peaks. The new peaks do not directly correspond to complex **4.9**, nor are they an overlay of the spectra of complex **4.23** and tris-amine **4.8**. The peaks are quite broad, and correspond to several different types of protons in solution. The number of distinct amine groups in solution gives rise to a very complicated equilibrium mixture of many complexes, with various substitution between the two different tris-amine ligands. While these amines catalyze reversibility to some extent, it is clear from the NMR that no aldehyde is being released into solution. Thus, addition of the second tris-amine causes a shift toward a complicated equilibrium mixture of several components.

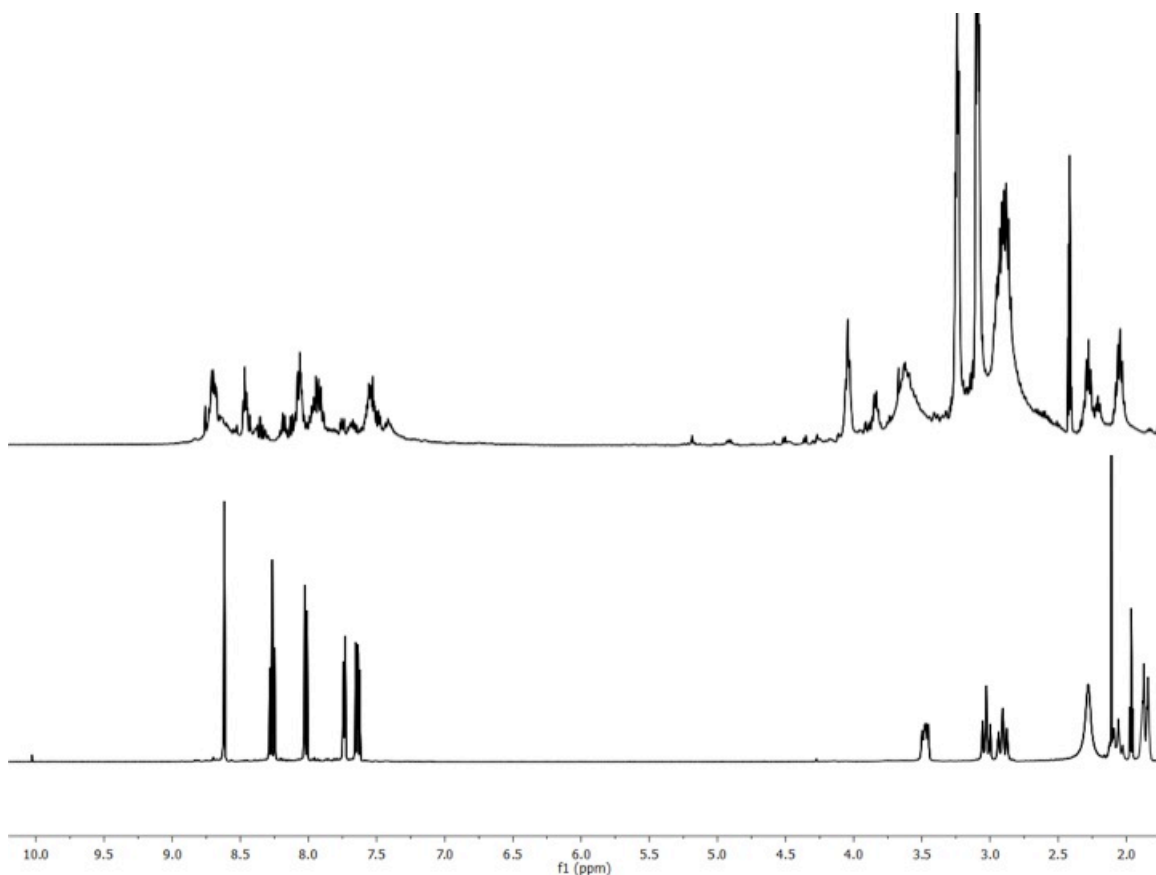


Figure 4.14. ^1H NMR spectra recorded for complex **4.22** alone, (bottom panel), and this complex with the addition of one equivalent of **4.8** (top panel), in CD_3CN .

4.3. CONCLUDING REMARKS

The research presented herein was directed toward creating a self-assembled complex that would serve as a chiral carboxylate sensor. It was found that three components assembled in solution to give the unforeseen complex **4.9**, where the three pyridine and three imine nitrogen atoms formed a hexacoordinate zinc metal complex. This octahedral complex lacked an open coordination site to accommodate an exogenous guest, and could ultimately not be applied as a sensor. Non-coordinating aldehydes were attempted to obviate this problem. However, addition of the metal salt caused hydrolysis of the imine back to the aldehyde. The effect of substitution on the pyridine was

determined, with substituents tolerated at any position on the ring except the 6-position. The 6-position was disfavored by steric repulsion between the methyl group and the pyridine ring toward which it was directed. Next, other transition metals were used in complex formation. Structures were determined for both iron(II) and copper(II). It was discovered that this system could be rendered dynamic by applying an additional amine rather than new aldehydes. Finally, preliminary studies into a coordinatively unsaturated complex **4.25** were undertaken.

4.4. FUTURE DIRECTIONS

Several directions are envisioned for the future of this self-assembly project. The first is built around the complex formed between bis-amine ligand **4.24** and aldehydes such as **4.7**. While the distribution of products is not entirely coherent, it is envisioned that the equilibrium could be shifted to allow application of this strategy to sensing carboxylic acids. It must be determined whether the hemiaminal species is indeed forming, as indicated by the peaks around 6.0 ppm in the ¹H NMR spectrum. If this species is forming, one of several approaches may be applied to mediate its creation. One is stringent removal of water, possibly beyond the use of molecular sieves. These sieves can remove the water that is created upon condensation, shifting the reaction away from the the hemiaminal species. Another technique would be to add an exogenous Brønsted acid, leading to elimination of water and formation of an imine species.

Another possible approach for this self-assembled complex would be to switch the structure of the tris-amine ligand. The tertiary nitrogen atom holding the three arms could be changed to a tertiary phosphorous atom like **4.26**. Phosphine structures of this nature are known in the literature,^{24,25} and could be paired with metals that have a high affinity for phosphines. This is expected to disfavor the hexacoordinate structure that

lacks an empty coordination site in favor of a pentacoordinate complex with binding between the metal and phosphine. Another way to change the amine-containing complex is to incorporate an expansive rigid template. One template that has received much attention is a cyclen.²⁶⁻²⁸ The four nitrogen atoms in cyclen **4.27**, as shown in **Figure 4.15**, can be loaded with amine containing arms that could form imine bonds with exogenous aldehydes. These amines could then complex a metal, such as a lanthanide, that can expand its structure past a hexacoordinate species. Of course these additional metals can be tried with tris-imines such as the product of **4.7** and **4.8**, since they can expand their coordination numbers.

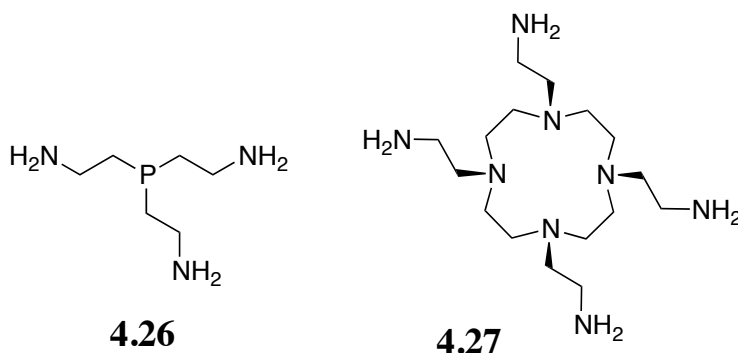


Figure 4.15. Chemical structures of tris- and tetra-amine templates that could possibly be applied to complex formation.

The final way that this system could be exploited is to make use of the cavity formed between the metal and the tertiary nitrogen atom. The crystal structure shows a nitrogen atom that is pyramidalized upward toward the metal center. The lone pair is directed toward the metal and is expected to act in a nucleophilic fashion. The metal is expected to be electropositive, due to its inherently low electronegativity and its oxidation state. This sort of arrangement may be amenable to a push-pull sort of

interaction, leading to the binding of a polarized guest molecule. Simple acids are envisioned to bind in this cavity, but it may be possible for a carboxylic acid to bind if the cavity size is tailored correctly. If this carboxylic acid were chiral, it would again be expected that the stereocenter would bias the system towards one of the helices preferentially. Thus, this strategy is envisioned as a chiral carboxylic acid sensor.

4.5. EXPERIMENTAL DATA

4.5.1. Materials and Methods

Reagents were purchased from reputable sources, and used as received unless otherwise indicated. ^1H and ^{13}C NMR were recorded in the University of Texas at Austin NMR facility. Mass spectra were obtained from the mass spectrometry facility at the University of Texas at Austin. X-ray data was obtained in the X-ray diffraction facility at the University of Texas at Austin.

4.5.2. Formation of Complex 4.9

The complex was prepared *in situ* without any further purification. The appropriate aldehyde (3 equiv, 180 mM) and tris-amine ligand (1 equiv, 60 mM) were dissolved to 1 mL in acetonitrile- d_3 . To this solution was added the $\text{Zn}(\text{OTf})_2$ (1 equiv, 60 mM), and the solution was shaken until the metal dissolved. In the case of the bis-amine ligand **4.24**, only two equivalents of the indicated aldehyde were used. These solutions were then transferred to NMR tubes, and the spectra recorded. For the reversibility studies, the second aldehyde or tris-amine component was added directly to this NMR tube, and the spectra again recorded. ^1H NMR (400 MHz, CDCl_3): 2.90 (dt, 1H), 3.22 (dd, 1H), 3.53 (dd, 1H), 3.75 (dt, 1H), 7.32 (dd, 1H), 7.62 (ddd, 1H), 8.01 (d, 1H), 8.25 (t, 1H). ^{13}C NMR (400 MHz, CDCl_3): 54.8, 56.5, 128.8, 129.6, 141.6, 147.0, 148.7. ESI MS: 626.33 ($[\text{M}(\text{OTf})]^+$); calculated 626.11.

4.5.3. Crystal Growth for X-ray Analysis

X-ray crystals were grown by the slow diffusion of diethyl ether into a solution containing the desired complex dissolved in acetonitrile- d_3 . The complex solution was prepared previously for NMR studies. The formed crystals were used without further treatment, and stored at room temperature before analysis.

4.5.4. X-ray Structural Parameters

4.5.4.1. Complex 4.9

Crystals grew as pale yellow prisms. The data crystal was cut from a larger crystal and had approximate dimensions; 0.44 x 0.22 x 0.20 mm. The data were collected on a Rigaku AFC12 diffractometer with a Saturn 724+ CCD using a graphite monochromator with MoK α radiation ($\lambda = 0.71073 \text{ \AA}$). A total of 1446 frames of data were collected using ω -scans with a scan range of 0.5° and a counting time of 20 seconds per frame. The data were collected at 100 K using a Rigaku XStream low temperature device. Details of crystal data, data collection and structure refinement are listed in Table 1. Data reduction were performed using the Rigaku Americas Corporation's Crystal Clear version 1.40. The structure was solved by direct methods using SIR97 and refined by full-matrix least-squares on F^2 with anisotropic displacement parameters for the non-H atoms using SHELXL-97. Structure analysis was aided by use of the programs PLATON98 and WinGX.

Table 4.1. Crystal data and structure refinement for complex 4.9.

Empirical formula	C ₂₄ H ₂₇ Cl ₂ N ₇ O ₈ Zn
Formula weight	677.80
Temperature	100(2) K
Wavelength	0.71075 Å

209

Crystal system	Trigonal	
Space group	P31c	
Unit cell dimensions	a = 9.7488(12) Å	a = 90°.
	b = 9.7488(12) Å	b = 90°.
	c = 16.566(2) Å	g = 120°.
Volume	1363.5(3) Å ³	
Z	2	
Density (calculated)	1.651 Mg/m ³	
Absorption coefficient	1.160 mm ⁻¹	
F(000)	696	
Crystal size	0.44 x 0.22 x 0.20 mm	
Theta range for data collection	2.41 to 27.48°.	
Index ranges	-12<=h<=12, -12<=k<=12, -21<=l<=21	
Reflections collected	19059	
Independent reflections	2086 [R(int) = 0.0263]	
Completeness to theta = 27.48°	100.0 %	
Max. and min. transmission	1.00 and 0.829	
Refinement method	Full-matrix least-squares on F ²	
Data / restraints / parameters	2086 / 1 / 164	
Goodness-of-fit on F ²	1.051	
Final R indices [I>2sigma(I)]	R1 = 0.0152, wR2 = 0.0400	
R indices (all data)	R1 = 0.0155, wR2 = 0.0402	
Absolute structure parameter	0.009(6)	

Largest diff. peak and hole 0.170 and -0.236 e.Å⁻³

Table 4.2. Atomic coordinates ($\times 10^4$) and equivalent isotropic displacement parameters ($\text{\AA}^2 \times 10^3$) for **4.9**. $U(\text{eq})$ is defined as one third of the trace of the orthogonalized U^{ij} tensor.

	x	y	z	U(eq)
Zn1	6667	3333	4710(1)	13(1)
N1	7552(1)	5420(1)	3830(1)	14(1)
N2	8842(1)	5088(1)	5189(1)	15(1)
N3	6667	3333	6401(1)	15(1)
C1	6964(1)	5513(2)	3118(1)	17(1)
C2	7864(2)	6620(1)	2535(1)	18(1)
C3	9431(2)	7699(1)	2699(1)	19(1)
C4	10044(1)	7659(1)	3448(1)	18(1)
C5	9072(1)	6496(1)	3990(1)	15(1)
C6	9675(2)	6320(2)	4775(1)	16(1)
C7	9426(2)	4901(2)	5972(1)	18(1)
C8	8211(2)	4663(2)	6617(1)	18(1)
Cl1	10000	10000	5631(1)	16(1)
O3	10000	10000	4775(1)	32(1)
O4	11473(1)	10199(2)	5926(1)	35(1)
Cl2	3333	6667	4119(1)	20(1)
O1	4548(1)	6368(1)	3830(1)	34(1)
O2	3333	6667	4984(1)	38(1)

Table 4.3. Bond lengths [\AA] and angles [$^\circ$] for **4.9**.

Zn1-N2#1	2.1035(11)	Cl2-O1#6	1.4360(11)	C4-C3-H3	123.4(10)
Zn1-N2	2.1035(11)	Cl2-O1	1.4360(10)	C5-C4-C3	118.38(12)
Zn1-N2#2	2.1035(11)	N2#1-Zn1-N2	106.66(3)	C5-C4-H4	119.8(9)
Zn1-N1#1	2.2928(10)	N2#1-Zn1-N2#2	106.66(3)	C3-C4-H4	121.7(10)
Zn1-N1#2	2.2928(10)	N2-Zn1-N2#2	106.66(3)	N1-C5-C4	123.14(12)
Zn1-N1	2.2928(10)	N2#1-Zn1-N1#1	74.88(4)	N1-C5-C6	115.56(11)
N1-C1	1.3341(16)	N2-Zn1-N1#1	92.83(4)	C4-C5-C6	121.24(11)

N1-C5	1.3460(16)	N2#2-Zn1-N1#1	158.68(4)	N2-C6-C5	119.11(11)
N2-C6	1.2641(17)	N2#1-Zn1-N1#2	92.83(4)	N2-C6-H6	124.7(11)
N2-C7	1.4642(15)	N2-Zn1-N1#2	158.68(4)	C5-C6-H6	116.1(11)
N3-C8#1	1.4573(14)	N2#2-Zn1-N1#2	74.88(4)	N2-C7-C8	108.57(10)
N3-C8	1.4573(14)	N1#1-Zn1-N1#2	83.82(4)	N2-C7-H7B	107.8(10)
N3-C8#2	1.4573(14)	N2#1-Zn1-N1	158.68(4)	C8-C7-H7B	112.4(9)
C1-C2	1.3853(17)	N2-Zn1-N1	74.88(4)	N2-C7-H7A	112.9(11)
C1-H1	0.961(16)	N2#2-Zn1-N1	92.83(4)	C8-C7-H7A	110.1(11)
C2-C3	1.3814(18)	N1#1-Zn1-N1	83.82(4)	H7B-C7-H7A	105.1(13)
C2-H2	0.915(19)	N1#2-Zn1-N1	83.82(4)	N3-C8-C7	110.04(11)
C3-C4	1.3858(19)	C1-N1-C5	117.67(10)	N3-C8-H8A	107.0(8)
C3-H3	0.916(16)	C1-N1-Zn1	129.71(8)	C7-C8-H8A	107.5(9)
C4-C5	1.3835(17)	C5-N1-Zn1	110.21(8)	N3-C8-H8B	112.3(11)
C4-H4	0.945(16)	C6-N2-C7	119.62(11)	C7-C8-H8B	109.6(11)
C5-C6	1.4720(17)	C6-N2-Zn1	118.38(9)	H8A-C8-H8B	110.3(14)
C6-H6	0.939(17)	C7-N2-Zn1	121.98(8)	O3-C11-O4#3	109.88(5)
C7-C8	1.5236(17)	C8#1-N3-C8	114.20(7)	O3-C11-O4#4	109.88(5)
C7-H7B	0.955(17)	C8#1-N3-C8#2	114.20(7)	O4#3-C11-O4#4	109.06(5)
C7-H7A	0.958(18)	C8-N3-C8#2	114.20(7)	O3-C11-O4	109.88(5)
C8-H8A	0.960(15)	N1-C1-C2	122.89(11)	O4#3-C11-O4	109.06(5)
C8-H8B	0.911(19)	N1-C1-H1	114.7(9)	O4#4-C11-O4	109.06(5)
C11-O3	1.4187(19)	C2-C1-H1	122.3(10)	O2-C12-O1#5	109.51(6)
C11-O4#3	1.4345(11)	C3-C2-C1	118.93(12)	O2-C12-O1#6	109.51(6)
C11-O4#4	1.4345(10)	C3-C2-H2	123.5(11)	O1#5-C12-O1#6	109.43(6)
C11-O4	1.4345(10)	C1-C2-H2	117.6(11)	O2-C12-O1	109.51(6)
C12-O2	1.432(2)	C2-C3-C4	118.93(12)	O1#5-C12-O1	109.43(6)
C12-O1#5	1.4360(10)	C2-C3-H3	117.7(10)	O1#6-C12-O1	109.43(6)

Symmetry transformations used to generate equivalent atoms:

#1 -x+y+1,-x+1,z #2 -y+1,x-y,z #3 -x+y+1,-x+2,z

#4 -y+2,x-y+1,z #5 -y+1,x-y+1,z #6 -x+y,-x+1,z

Table 4.4. Anisotropic displacement parameters ($\text{\AA}^2 \times 10^3$) for **4.9**. The anisotropic displacement factor exponent takes the form: $-2\pi^2 [h^2 a^{*2} U^{11} + \dots + 2 h k a^* b^* U^{12}]$

	U11	U22	U33	U23	U13	U12
Zn1	13(1)	13(1)	12(1)	0	0	6(1)
N1	14(1)	14(1)	15(1)	0(1)	0(1)	7(1)
N2	16(1)	17(1)	13(1)	-1(1)	0(1)	9(1)
N3	15(1)	15(1)	13(1)	0	0	8(1)
C1	16(1)	16(1)	18(1)	0(1)	-1(1)	9(1)
C2	21(1)	20(1)	15(1)	2(1)	-1(1)	12(1)
C3	20(1)	17(1)	20(1)	5(1)	5(1)	10(1)
C4	16(1)	16(1)	21(1)	1(1)	2(1)	7(1)
C5	17(1)	14(1)	15(1)	-1(1)	1(1)	8(1)
C6	15(1)	17(1)	16(1)	-3(1)	-1(1)	8(1)
C7	17(1)	21(1)	15(1)	1(1)	-3(1)	9(1)
C8	19(1)	21(1)	12(1)	-2(1)	-3(1)	9(1)
Cl1	19(1)	19(1)	12(1)	0	0	9(1)
O3	43(1)	43(1)	10(1)	0	0	22(1)
O4	27(1)	49(1)	34(1)	1(1)	-7(1)	23(1)
Cl2	18(1)	18(1)	25(1)	0	0	9(1)
O1	25(1)	30(1)	51(1)	3(1)	9(1)	17(1)
O2	45(1)	45(1)	26(1)	0	0	22(1)

Table 4.5. Hydrogen coordinates ($\times 10^4$) and isotropic displacement parameters ($\text{\AA}^2 \times 10^3$) for **4.9**.

	x	y	z	U(eq)
H1	5876(19)	4723(17)	3030(10)	14(3)
H2	7390(20)	6575(18)	2052(11)	25(4)
H3	10009(18)	8418(18)	2306(10)	14(3)
H4	11107(19)	8379(18)	3587(9)	12(3)
H6	10690(20)	7140(20)	4921(11)	14(4)

H7B	9596(17)	4020(19)	5934(10)	17(3)
H7A	10440(20)	5780(20)	6109(11)	27(4)
H8A	8109(16)	5592(17)	6621(9)	14(3)
H8B	8550(20)	4530(20)	7107(11)	27(4)

Table 4.6. Torsion angles [°] for **4.9**.

N2#1-Zn1-N1-C1	76.12(15)	C5-N1-C1-C2	2.55(17)
N2-Zn1-N1-C1	173.27(11)	Zn1-N1-C1-C2	-157.94(10)
N2#2-Zn1-N1-C1	-80.24(10)	N1-C1-C2-C3	-1.29(19)
N1#1-Zn1-N1-C1	78.64(8)	C1-C2-C3-C4	-1.25(18)
N1#2-Zn1-N1-C1	-5.79(10)	C2-C3-C4-C5	2.37(18)
N2#1-Zn1-N1-C5	-85.51(13)	C1-N1-C5-C4	-1.32(17)
N2-Zn1-N1-C5	11.64(8)	Zn1-N1-C5-C4	162.79(10)
N2#2-Zn1-N1-C5	118.14(8)	C1-N1-C5-C6	-178.58(10)
N1#1-Zn1-N1-C5	-82.99(9)	Zn1-N1-C5-C6	-14.47(12)
N1#2-Zn1-N1-C5	-167.41(8)	C3-C4-C5-N1	-1.12(18)
N2#1-Zn1-N2-C6	150.66(9)	C3-C4-C5-C6	175.98(11)
N2#2-Zn1-N2-C6	-95.65(11)	C7-N2-C6-C5	-179.77(10)
N1#1-Zn1-N2-C6	75.60(9)	Zn1-N2-C6-C5	1.84(15)
N1#2-Zn1-N2-C6	-4.63(17)	N1-C5-C6-N2	9.58(16)
N1-Zn1-N2-C6	-7.22(9)	C4-C5-C6-N2	-167.73(12)
N2#1-Zn1-N2-C7	-27.69(10)	C6-N2-C7-C8	123.08(12)
N2#2-Zn1-N2-C7	86.00(7)	Zn1-N2-C7-C8	-58.59(12)
N1#1-Zn1-N2-C7	-102.75(9)	C8#1-N3-C8-C7	82.48(18)
N1#2-Zn1-N2-C7	177.02(9)	C8#2-N3-C8-C7	-143.52(13)
N1-Zn1-N2-C7	174.42(10)	N2-C7-C8-N3	55.16(13)

Symmetry transformations used to generate equivalent atoms:

#1 -x+y+1,-x+1,z #2 -y+1,x-y,z #3 -x+y+1,-x+2,z

#4 -y+2,x-y+1,z #5 -y+1,x-y+1,z #6 -x+y,-x+1,z

4.5.4.2. Complex 4.17

Crystals grew as colorless prisms. The data crystal was cut from a larger crystal and had approximate dimensions; 0.34 x 0.18 x 0.16 mm. The data were collected on a

Rigaku AFC12 diffractometer with a Saturn 724+ CCD using a graphite monochromator with MoK α radiation ($\lambda = 0.71073\text{\AA}$). A total of 1200 frames of data were collected using ω -scans with a scan range of 0.5° and a counting time of 19 seconds per frame. The data were collected at 100 K using a Rigaku XStream low temperature device. Details of crystal data, data collection and structure refinement are listed in Table 1. Data reduction were performed using the Rigaku Americas Corporation's Crystal Clear version 1.40. The structure was solved by direct methods using SIR97 and refined by full-matrix least-squares on F^2 with anisotropic displacement parameters for the non-H atoms using SHELXL-97. Structure analysis was aided by use of the programs PLATON98 and WinGX.

Table 4.7. Crystal data and structure refinement for **4.17**.

Empirical formula	C ₂₄ H ₂₉ Cl ₂ N ₇ O ₁₂ Zn	
Formula weight	743.81	
Temperature	100(2) K	
Wavelength	0.71075 \AA	
Crystal system	Monoclinic	
Space group	P21/c	
Unit cell dimensions	a = 13.3636(12) \AA	$\alpha = 90^\circ$.
	b = 18.037(2) \AA	$\beta = 116.713(2)^\circ$.
	c = 14.2110(15) \AA	$\gamma = 90^\circ$.
Volume	3059.8(5) \AA^3	
Z	4	
Density (calculated)	1.615 Mg/m ³	
Absorption coefficient	1.051 mm ⁻¹	
F(000)	1528	
Crystal size	0.34 x 0.18 x 0.16 mm	
Theta range for data collection	3.04 to 27.48 $^\circ$.	

Index ranges	-17<=h<=17, -23<=k<=23, -18<=l<=18
Reflections collected	34314
Independent reflections	7009 [R(int) = 0.0269]
Completeness to theta = 27.48°	99.8 %
Absorption correction	Semi-empirical from equivalents
Max. and min. transmission	1.00 and 0.806
Refinement method	Full-matrix least-squares on F ²
Data / restraints / parameters	7009 / 151 / 473
Goodness-of-fit on F ²	1.022
Final R indices [I>2sigma(I)]	R1 = 0.0291, wR2 = 0.0767
R indices (all data)	R1 = 0.0311, wR2 = 0.0782
Largest diff. peak and hole	1.037 and -0.603 e.Å ⁻³

Table 4.8. Atomic coordinates (x 10⁴) and equivalent isotropic displacement parameters (Å²x 10³) for **4.17**. U(eq) is defined as one third of the trace of the orthogonalized U^{ij} tensor.

	x	y	z	U(eq)
Zn1	8079(1)	5887(1)	7149(1)	16(1)
Cl1	5288(1)	8515(1)	4945(1)	22(1)
Cl2	8970(1)	3351(1)	4771(1)	27(1)
O1	4848(1)	5603(1)	3293(1)	29(1)
O2	12298(1)	6740(1)	8544(1)	27(1)
O3	8123(2)	3589(1)	9473(1)	35(1)
O4	4933(2)	8921(1)	3973(1)	36(1)
O5	4351(1)	8484(1)	5205(1)	27(1)
O6	6198(1)	8892(1)	5775(2)	39(1)
O7	5605(2)	7781(1)	4830(2)	35(1)
O8	9524(4)	3923(2)	5525(3)	41(1)
O9	7930(4)	3636(3)	3983(4)	104(3)
O10	8711(4)	2764(2)	5285(3)	53(1)
O11	9742(6)	2902(4)	4513(6)	75(3)

O8A	9587(5)	3586(4)	5830(4)	52(2)
O9A	8743(5)	3923(3)	4080(4)	60(2)
O10A	8007(4)	2963(3)	4658(4)	46(1)
O11A	9544(7)	3055(6)	4269(8)	91(4)
O12	4057(1)	5249(1)	1272(1)	26(1)
N1	7597(1)	5772(1)	5476(1)	18(1)
N2	6319(1)	6127(1)	6412(1)	20(1)
N3	7363(2)	7112(1)	8117(1)	22(1)
N4	8926(1)	6900(1)	7327(1)	18(1)
N5	9881(1)	5555(1)	7571(1)	16(1)
N6	8428(1)	5724(1)	8754(1)	19(1)
N7	7793(1)	4686(1)	7242(1)	17(1)
C1	8254(2)	5587(1)	5038(2)	20(1)
C2	7814(2)	5399(1)	3976(2)	23(1)
C3	6675(2)	5396(1)	3363(2)	23(1)
C4	5974(2)	5595(1)	3816(2)	21(1)
C5	6475(2)	5787(1)	4881(2)	18(1)
C6	5819(2)	6016(1)	5428(2)	21(1)
C7	5694(2)	6395(1)	6966(2)	25(1)
C8	6157(2)	7150(1)	7452(2)	25(1)
C9	8006(2)	7737(1)	8036(2)	25(1)
C10	8357(2)	7615(1)	7163(2)	22(1)
C11	9975(2)	6879(1)	7629(2)	19(1)
C12	10545(2)	6156(1)	7836(2)	17(1)
C13	11709(2)	6105(1)	8292(2)	19(1)
C14	12200(2)	5403(1)	8469(2)	19(1)
C15	11508(2)	4791(1)	8180(2)	18(1)
C16	10354(2)	4886(1)	7730(2)	18(1)
C17	7705(2)	6841(1)	9182(2)	25(1)
C18	8716(2)	6325(1)	9523(2)	23(1)
C19	8331(2)	5065(1)	9015(2)	20(1)
C20	8000(2)	4474(1)	8222(2)	19(1)
C21	7920(2)	3740(1)	8476(2)	24(1)

C22	7638(2)	3202(1)	7688(2)	26(1)
C23	7440(2)	3428(1)	6691(2)	24(1)
C24	7520(2)	4173(1)	6494(2)	19(1)

Table 4.9. Bond lengths [\AA] and angles [$^\circ$] for **4.17**.

Zn1-N4	2.1042(17)	C22-C23	1.380(3)	N1-C5-C6	115.64(17)
Zn1-N6	2.1340(17)	C22-H22	0.95	C4-C5-C6	122.27(18)
Zn1-N2	2.1447(17)	C23-C24	1.388(3)	N2-C6-C5	118.98(18)
Zn1-N1	2.1755(17)	C23-H23	0.95	N2-C6-H6	120.5
Zn1-N7	2.2150(17)	C24-H24	0.95	C5-C6-H6	120.5
Zn1-N5	2.2841(16)	N4-Zn1-N6	98.31(7)	N2-C7-C8	108.90(18)
C11-O7	1.4212(18)	N4-Zn1-N2	107.21(7)	N2-C7-H7A	109.9
C11-O6	1.4295(18)	N6-Zn1-N2	102.37(7)	C8-C7-H7A	109.9
C11-O4	1.4417(17)	N4-Zn1-N1	95.34(6)	N2-C7-H7B	109.9
C11-O5	1.4582(16)	N6-Zn1-N1	165.99(7)	C8-C7-H7B	109.9
C12-O9A	1.361(4)	N2-Zn1-N1	76.39(6)	H7A-C7-H7B	108.3
C12-O11A	1.371(6)	N4-Zn1-N7	160.14(6)	N3-C8-C7	110.90(17)
C12-O10A	1.409(4)	N6-Zn1-N7	76.20(7)	N3-C8-H8A	109.5
C12-O10	1.415(3)	N2-Zn1-N7	92.63(6)	C7-C8-H8A	109.5
C12-O8A	1.416(4)	N1-Zn1-N7	89.87(6)	N3-C8-H8B	109.5
C12-O8	1.431(3)	N4-Zn1-N5	75.49(6)	C7-C8-H8B	109.5
C12-O9	1.432(4)	N6-Zn1-N5	89.14(6)	H8A-C8-H8B	108
C12-O11	1.483(4)	N2-Zn1-N5	167.48(6)	N3-C9-C10	111.18(17)
O1-C4	1.346(3)	N1-Zn1-N5	91.25(6)	N3-C9-H9A	109.4
O1-H10	0.75(4)	N7-Zn1-N5	85.28(6)	C10-C9-H9A	109.4
O2-C13	1.344(2)	O7-C11-O6	110.56(12)	N3-C9-H9B	109.4
O2-H20	0.76(4)	O7-C11-O4	110.42(11)	C10-C9-H9B	109.4
O3-C21	1.346(3)	O6-C11-O4	109.92(12)	H9A-C9-H9B	108
O3-H30	0.71(4)	O7-C11-O5	109.14(10)	N4-C10-C9	109.04(17)
O12-H12B	0.80(4)	O6-C11-O5	108.56(11)	N4-C10-H10A	109.9
O12-H12A	0.84(4)	O4-C11-O5	108.18(10)	C9-C10-H10A	109.9
N1-C1	1.328(3)	O9A-C12-O11A	85.1(6)	N4-C10-H10B	109.9
N1-C5	1.350(3)	O9A-C12-O10A	113.5(3)	C9-C10-H10B	109.9
N2-C6	1.266(3)	O11A-C12-O10A	116.4(5)	H10A-C10-H10B	108.3
N2-C7	1.464(3)	O9A-C12-O8A	112.0(4)	N4-C11-C12	119.26(18)
N3-C9	1.453(3)	O11A-C12-O8A	118.3(5)	N4-C11-H11	120.4

N3-C17	1.455(3)	O10A-C12-O8A	109.6(3)	C12-C11-H11	120.4
N3-C8	1.458(3)	O10-C12-O8	108.5(2)	N5-C12-C13	122.38(18)
N4-C11	1.269(3)	O10-C12-O9	107.2(3)	N5-C12-C11	116.19(17)
N4-C10	1.461(3)	O8-C12-O9	108.7(2)	C13-C12-C11	121.42(18)
N5-C16	1.334(3)	O9A-C12-O11	100.9(4)	O2-C13-C12	117.65(18)
N5-C12	1.343(3)	O10-C12-O11	94.5(3)	O2-C13-C14	123.68(18)
N6-C19	1.268(3)	O8-C12-O11	113.3(4)	C12-C13-C14	118.67(18)
N6-C18	1.463(3)	O9-C12-O11	122.8(4)	C15-C14-C13	118.40(18)
N7-C24	1.329(3)	C4-O1-H10	110(3)	C15-C14-H14	120.8
N7-C20	1.348(3)	C13-O2-H2O	109(3)	C13-C14-H14	120.8
C1-C2	1.393(3)	C21-O3-H3O	109(3)	C14-C15-C16	119.59(18)
C1-H1	0.95	H12B-O12-H12A	105(3)	C14-C15-H15	120.2
C2-C3	1.373(3)	C1-N1-C5	119.57(17)	C16-C15-H15	120.2
C2-H2	0.95	C1-N1-Zn1	127.08(14)	N5-C16-C15	122.33(18)
C3-C4	1.400(3)	C5-N1-Zn1	112.51(13)	N5-C16-H16	118.8
C3-H3	0.95	C6-N2-C7	120.02(18)	C15-C16-H16	118.8
C4-C5	1.395(3)	C6-N2-Zn1	115.22(14)	N3-C17-C18	110.77(17)
C5-C6	1.469(3)	C7-N2-Zn1	124.75(13)	N3-C17-H17A	109.5
C6-H6	0.95	C9-N3-C17	114.99(18)	C18-C17-H17A	109.5
C7-C8	1.527(3)	C9-N3-C8	115.72(17)	N3-C17-H17B	109.5
C7-H7A	0.99	C17-N3-C8	115.38(18)	C18-C17-H17B	109.5
C7-H7B	0.99	C11-N4-C10	119.87(18)	H17A-C17-H17B	108.1
C8-H8A	0.99	C11-N4-Zn1	117.84(14)	N6-C18-C17	108.40(17)
C8-H8B	0.99	C10-N4-Zn1	122.22(13)	N6-C18-H18A	110
C9-C10	1.526(3)	C16-N5-C12	118.61(17)	C17-C18-H18A	110
C9-H9A	0.99	C16-N5-Zn1	130.22(13)	N6-C18-H18B	110
C9-H9B	0.99	C12-N5-Zn1	110.37(13)	C17-C18-H18B	110
C10-H10A	0.99	C19-N6-C18	120.20(17)	H18A-C18-H18B	108.4
C10-H10B	0.99	C19-N6-Zn1	116.13(14)	N6-C19-C20	119.40(18)
C11-C12	1.471(3)	C18-N6-Zn1	123.62(13)	N6-C19-H19	120.3
C11-H11	0.95	C24-N7-C20	118.94(18)	C20-C19-H19	120.3
C12-C13	1.394(3)	C24-N7-Zn1	128.69(14)	N7-C20-C21	122.34(19)
C13-C14	1.395(3)	C20-N7-Zn1	112.25(13)	N7-C20-C19	115.99(18)
C14-C15	1.379(3)	N1-C1-C2	121.54(19)	C21-C20-C19	121.67(18)
C14-H14	0.95	N1-C1-H1	119.2	O3-C21-C20	117.6(2)
C15-C16	1.389(3)	C2-C1-H1	119.2	O3-C21-C22	123.9(2)

C15-H15	0.95	C3-C2-C1	119.70(19)	C20-C21-C22	118.49(19)
C16-H16	0.95	C3-C2-H2	120.2	C23-C22-C21	118.4(2)
C17-C18	1.529(3)	C1-C2-H2	120.2	C23-C22-H22	120.8
C17-H17A	0.99	C2-C3-C4	119.21(19)	C21-C22-H22	120.8
C17-H17B	0.99	C2-C3-H3	120.4	C22-C23-C24	119.7(2)
C18-H18A	0.99	C4-C3-H3	120.4	C22-C23-H23	120.1
C18-H18B	0.99	O1-C4-C5	117.98(18)	C24-C23-H23	120.1
C19-C20	1.469(3)	O1-C4-C3	124.13(19)	N7-C24-C23	122.06(19)
C19-H19	0.95	C5-C4-C3	117.88(19)	N7-C24-H24	119
C20-C21	1.389(3)	N1-C5-C4	122.09(18)	C23-C24-H24	119
C21-C22	1.399(3)				

Table 4.10. Anisotropic displacement parameters ($\text{\AA}^2 \times 10^3$) for **4.17**. The anisotropic displacement factor exponent takes the form: $-2\pi^2 [h^2 a^{*2} U^{11} + \dots + 2 h k a^* b^* U^{12}]$

	U ¹¹	U ²²	U ³³	U ²³	U ¹³	U ¹²
Zn1	18(1)	17(1)	14(1)	1(1)	7(1)	0(1)
Cl1	17(1)	25(1)	23(1)	4(1)	8(1)	1(1)
Cl2	32(1)	20(1)	25(1)	0(1)	9(1)	-3(1)
O1	21(1)	48(1)	16(1)	-8(1)	6(1)	1(1)
O2	17(1)	18(1)	35(1)	3(1)	3(1)	-3(1)
O3	66(1)	19(1)	28(1)	8(1)	29(1)	7(1)
O4	38(1)	41(1)	31(1)	15(1)	17(1)	7(1)
O5	20(1)	35(1)	29(1)	-1(1)	13(1)	-1(1)
O6	23(1)	46(1)	39(1)	-5(1)	6(1)	-11(1)
O7	39(1)	29(1)	44(1)	4(1)	25(1)	8(1)
O8	40(2)	23(2)	47(3)	-14(2)	9(2)	-7(2)
O9	68(3)	42(3)	108(4)	-22(3)	-45(3)	25(2)
O10	102(3)	30(2)	34(2)	-9(2)	38(2)	-26(2)
O11	43(3)	103(4)	57(4)	-49(3)	3(2)	29(3)
O8A	45(3)	68(4)	31(3)	-23(3)	6(2)	3(3)
O9A	90(4)	44(3)	47(3)	24(2)	30(3)	4(3)
O10A	58(3)	43(3)	53(3)	-19(2)	40(3)	-18(2)

O11A	50(5)	192(10)	50(5)	-65(5)	40(4)	-61(5)
O12	30(1)	30(1)	19(1)	-1(1)	12(1)	-1(1)
N1	20(1)	18(1)	15(1)	2(1)	8(1)	0(1)
N2	21(1)	22(1)	18(1)	0(1)	11(1)	2(1)
N3	27(1)	23(1)	18(1)	1(1)	11(1)	4(1)
N4	22(1)	15(1)	16(1)	2(1)	8(1)	3(1)
N5	18(1)	17(1)	15(1)	0(1)	7(1)	0(1)
N6	21(1)	20(1)	15(1)	0(1)	9(1)	2(1)
N7	17(1)	18(1)	18(1)	2(1)	9(1)	0(1)
C1	21(1)	22(1)	18(1)	2(1)	10(1)	1(1)
C2	26(1)	27(1)	21(1)	1(1)	15(1)	1(1)
C3	28(1)	28(1)	16(1)	-2(1)	11(1)	-1(1)
C4	22(1)	22(1)	17(1)	0(1)	8(1)	0(1)
C5	21(1)	18(1)	16(1)	1(1)	9(1)	1(1)
C6	19(1)	23(1)	19(1)	1(1)	8(1)	2(1)
C7	24(1)	33(1)	21(1)	-2(1)	13(1)	3(1)
C8	27(1)	30(1)	22(1)	0(1)	14(1)	8(1)
C9	34(1)	18(1)	25(1)	-2(1)	14(1)	5(1)
C10	26(1)	17(1)	24(1)	4(1)	11(1)	5(1)
C11	22(1)	16(1)	17(1)	2(1)	7(1)	-1(1)
C12	20(1)	16(1)	15(1)	2(1)	7(1)	0(1)
C13	19(1)	18(1)	17(1)	1(1)	6(1)	-2(1)
C14	18(1)	21(1)	17(1)	1(1)	7(1)	1(1)
C15	21(1)	16(1)	17(1)	-1(1)	9(1)	3(1)
C16	21(1)	16(1)	18(1)	-1(1)	9(1)	-1(1)
C17	33(1)	27(1)	18(1)	-2(1)	13(1)	4(1)
C18	29(1)	22(1)	15(1)	-1(1)	9(1)	1(1)
C19	24(1)	23(1)	16(1)	3(1)	11(1)	3(1)
C20	20(1)	20(1)	19(1)	2(1)	11(1)	3(1)
C21	31(1)	21(1)	24(1)	5(1)	17(1)	6(1)
C22	36(1)	16(1)	31(1)	4(1)	20(1)	4(1)
C23	29(1)	20(1)	25(1)	-2(1)	14(1)	2(1)
C24	19(1)	21(1)	18(1)	0(1)	9(1)	1(1)

Table 4.11. Hydrogen coordinates ($\times 10^4$) and isotropic displacement parameters ($\text{\AA}^2 \times 10^{-3}$) for **4.17**.

	x	y	z	U(eq)
H1	9043	5584	5458	24
H2	8300	5272	3677	28
H3	6366	5262	2641	28
H6	5030	6079	5049	25
H7A	5770	6039	7525	30
H7B	4889	6439	6467	30
H8A	5993	7518	6884	30
H8B	5782	7315	7879	30
H9A	8682	7805	8715	30
H9B	7549	8194	7887	30
H10A	7688	7621	6468	27
H10B	8865	8018	7175	27
H11	10388	7324	7720	23
H14	12991	5349	8781	22
H15	11819	4306	8288	22
H16	9886	4461	7528	22
H17A	7075	6571	9211	30
H17B	7900	7266	9673	30
H18A	9371	6603	9557	27
H18B	8912	6120	10231	27
H19	8470	4956	9718	24
H22	7585	2694	7835	31
H23	7249	3074	6142	28
H24	7376	4322	5803	23
H12B	4090(30)	5600(20)	940(30)	44(9)
H1O	4660(30)	5491(19)	2730(30)	43(9)
H3O	8140(30)	3200(20)	9540(30)	45(10)
H12A	4330(30)	4890(20)	1080(30)	46(9)

Table 4.12. Torsion angles [°] for **4.17**.

N4-Zn1-N1-C1	74.27(18)	C2-C3-C4-C5	-0.1(3)
N6-Zn1-N1-C1	-92.7(3)	C1-N1-C5-C4	1.5(3)
N2-Zn1-N1-C1	-179.28(18)	Zn1-N1-C5-C4	-168.67(16)
N7-Zn1-N1-C1	-86.54(17)	C1-N1-C5-C6	-178.51(18)
N5-Zn1-N1-C1	-1.27(18)	Zn1-N1-C5-C6	11.3(2)
N4-Zn1-N1-C5	-116.41(14)	O1-C4-C5-N1	177.92(19)
N6-Zn1-N1-C5	76.6(3)	C3-C4-C5-N1	-1.1(3)
N2-Zn1-N1-C5	-9.96(13)	O1-C4-C5-C6	-2.0(3)
N7-Zn1-N1-C5	82.78(14)	C3-C4-C5-C6	178.92(19)
N5-Zn1-N1-C5	168.05(14)	C7-N2-C6-C5	176.70(19)
N4-Zn1-N2-C6	98.87(16)	Zn1-N2-C6-C5	-3.9(3)
N6-Zn1-N2-C6	-158.25(16)	N1-C5-C6-N2	-5.3(3)
N1-Zn1-N2-C6	7.43(15)	C4-C5-C6-N2	174.7(2)
N7-Zn1-N2-C6	-81.80(16)	C6-N2-C7-C8	-118.0(2)
N5-Zn1-N2-C6	-1.8(4)	Zn1-N2-C7-C8	62.6(2)
N4-Zn1-N2-C7	-81.74(17)	C9-N3-C8-C7	138.98(18)
N6-Zn1-N2-C7	21.14(18)	C17-N3-C8-C7	-82.7(2)
N1-Zn1-N2-C7	-173.19(18)	N2-C7-C8-N3	-54.4(2)
N7-Zn1-N2-C7	97.58(17)	C17-N3-C9-C10	133.02(19)
N5-Zn1-N2-C7	177.6(3)	C8-N3-C9-C10	-88.5(2)
N6-Zn1-N4-C11	82.73(15)	C11-N4-C10-C9	-108.7(2)
N2-Zn1-N4-C11	-171.49(14)	Zn1-N4-C10-C9	68.3(2)
N1-Zn1-N4-C11	-94.11(15)	N3-C9-C10-N4	-53.0(2)
N7-Zn1-N4-C11	10.5(3)	C10-N4-C11-C12	177.27(17)
N5-Zn1-N4-C11	-4.20(14)	Zn1-N4-C11-C12	0.2(2)
N6-Zn1-N4-C10	-94.30(15)	C16-N5-C12-C13	-1.5(3)
N2-Zn1-N4-C10	11.49(16)	Zn1-N5-C12-C13	169.25(15)
N1-Zn1-N4-C10	88.87(15)	C16-N5-C12-C11	179.14(17)
N7-Zn1-N4-C10	-166.52(17)	Zn1-N5-C12-C11	-10.1(2)
N5-Zn1-N4-C10	178.77(16)	N4-C11-C12-N5	7.4(3)
N4-Zn1-N5-C16	177.10(18)	N4-C11-C12-C13	-171.96(19)
N6-Zn1-N5-C16	78.29(17)	N5-C12-C13-O2	-178.85(18)
N2-Zn1-N5-C16	-78.7(3)	C11-C12-C13-O2	0.4(3)
N1-Zn1-N5-C16	-87.71(17)	N5-C12-C13-C14	0.7(3)
N7-Zn1-N5-C16	2.06(17)	C11-C12-C13-C14	179.96(18)
N4-Zn1-N5-C12	7.70(12)	O2-C13-C14-C15	179.77(19)
N6-Zn1-N5-C12	-91.11(13)	C12-C13-C14-C15	0.3(3)
N2-Zn1-N5-C12	111.9(3)	C13-C14-C15-C16	-0.3(3)

N1-Zn1-N5-C12	102.89(13)	C12-N5-C16-C15	1.5(3)
N7-Zn1-N5-C12	-167.34(13)	Zn1-N5-C16-C15	-167.18(14)
N4-Zn1-N6-C19	-160.00(15)	C14-C15-C16-N5	-0.6(3)
N2-Zn1-N6-C19	90.23(16)	C9-N3-C17-C18	-81.7(2)
N1-Zn1-N6-C19	6.9(4)	C8-N3-C17-C18	139.62(19)
N7-Zn1-N6-C19	0.55(15)	C19-N6-C18-C17	-112.4(2)
N5-Zn1-N6-C19	-84.80(15)	Zn1-N6-C18-C17	64.9(2)
N4-Zn1-N6-C18	22.64(16)	N3-C17-C18-N6	-56.2(2)
N2-Zn1-N6-C18	-87.13(16)	C18-N6-C19-C20	177.78(18)
N1-Zn1-N6-C18	-170.5(2)	Zn1-N6-C19-C20	0.3(2)
N7-Zn1-N6-C18	-176.82(17)	C24-N7-C20-C21	-1.2(3)
N5-Zn1-N6-C18	97.84(16)	Zn1-N7-C20-C21	-177.38(16)
N4-Zn1-N7-C24	-101.1(2)	C24-N7-C20-C19	178.16(17)
N6-Zn1-N7-C24	-177.12(18)	Zn1-N7-C20-C19	1.9(2)
N2-Zn1-N7-C24	80.78(17)	N6-C19-C20-N7	-1.6(3)
N1-Zn1-N7-C24	4.41(17)	N6-C19-C20-C21	177.7(2)
N5-Zn1-N7-C24	-86.85(17)	N7-C20-C21-O3	-178.71(19)
N4-Zn1-N7-C20	74.6(2)	C19-C20-C21-O3	2.0(3)
N6-Zn1-N7-C20	-1.36(13)	N7-C20-C21-C22	1.5(3)
N2-Zn1-N7-C20	-103.46(13)	C19-C20-C21-C22	-177.81(19)
N1-Zn1-N7-C20	-179.83(13)	O3-C21-C22-C23	179.4(2)
N5-Zn1-N7-C20	88.91(13)	C20-C21-C22-C23	-0.8(3)
C5-N1-C1-C2	-0.7(3)	C21-C22-C23-C24	-0.2(3)
Zn1-N1-C1-C2	167.97(16)	C20-N7-C24-C23	0.2(3)
N1-C1-C2-C3	-0.6(3)	Zn1-N7-C24-C23	175.67(15)
C1-C2-C3-C4	0.9(3)	C22-C23-C24-N7	0.5(3)
C2-C3-C4-O1	-179.1(2)		

Table 4.13. Hydrogen bonds for **4.17** [\AA and $^\circ$].

D-H...A	d(D-H)	d(H...A)	d(D...A)	\angle (DHA)
O1-H1O...O12	0.75(4)	1.91(4)	2.654(2)	175(4)
O12-H12B...O5#1	0.80(4)	2.07(4)	2.865(2)	174(3)
O3-H3O...O10#2	0.71(4)	1.99(4)	2.663(4)	156(4)
O3-H3O...O10A#2	0.71(4)	2.11(4)	2.823(5)	174(4)
O12-H12A...O4#3	0.84(4)	2.03(4)	2.847(3)	164(3)

O2-H2O...O5#4	0.76(4)	1.99(4)	2.728(2)	164(4)
---------------	---------	---------	----------	--------

Symmetry transformations used to generate equivalent atoms:

#1 $x, -y+3/2, z-1/2$ #2 $x, -y+1/2, z+1/2$ #3 $-x+1, y-1/2, -z+1/2$

#4 $x+1, -y+3/2, z+1/2$

4.5.4.3. Complex 4.18

Crystals grew as large, colorless prisms. The data crystal had approximate dimensions; 0.40 x 0.35 x 0.20 mm. The data were collected on a Rigaku SCX-Mini diffractometer with a Mercury CCD using a graphite monochromator with MoK α radiation ($\lambda = 0.71075\text{\AA}$). A total of 1080 frames of data were collected using ω -scans with a scan range of 0.5° and a counting time of 25 seconds per frame. The data were collected at 153 K using a Rigaku XStream low temperature device. Details of crystal data, data collection and structure refinement are listed in Table 1. Data reduction were performed using the Rigaku Americas Corporation's Crystal Clear version 1.40.¹ The structure was solved by direct methods using SIR97² and refined by full-matrix least-squares on F^2 with anisotropic displacement parameters for the non-H atoms using SHELXL-97.³ Structure analysis was aided by use of the programs PLATON98⁴ and WinGX.⁵

Table 4.14. Crystal data and structure refinement for **4.18**.

Empirical formula	C ₂₄ H ₂₄ Br ₃ Cl ₂ N ₇ O ₈ Zn
Formula weight	914.50
Temperature	153(2) K
Wavelength	0.71075 Å
Crystal system	Monoclinic
Space group	I2/a

Unit cell dimensions	a = 15.176(4) Å	$\alpha = 90^\circ$.
	b = 14.351(3) Å	$\beta = 95.649(4)^\circ$.
	c = 28.688(7) Å	$\gamma = 90^\circ$.
Volume	6218(3) Å ³	
Z	8	
Density (calculated)	1.954 Mg/m ³	
Absorption coefficient	4.877 mm ⁻¹	
F(000)	3600	
Crystal size	0.40 x 0.35 x 0.20 mm	
Theta range for data collection	3.07 to 27.48°.	
Index ranges	-19 ≤ h ≤ 19, -18 ≤ k ≤ 18, -36 ≤ l ≤ 37	
Reflections collected	32067	
Independent reflections	7132 [R(int) = 0.0662]	
Completeness to theta = 27.48°	99.8 %	
Absorption correction	Semi-empirical from equivalents	
Max. and min. transmission	1.00 and 0.641	
Refinement method	Full-matrix least-squares on F ²	
Data / restraints / parameters	7132 / 105 / 417	
Goodness-of-fit on F ²	1.228	
Final R indices [I > 2σ(I)]	R1 = 0.0488, wR2 = 0.1114	
R indices (all data)	R1 = 0.0754, wR2 = 0.1209	
Largest diff. peak and hole	1.481 and -1.193 e.Å ⁻³	

Table 4.15. Atomic coordinates ($\times 10^4$) and equivalent isotropic displacement parameters ($\text{Å}^2 \times 10^3$) for **4.18**. $U(\text{eq})$ is defined as one third of the trace of the orthogonalized U^{ij} tensor.

	x	y	z	$U(\text{eq})$
C1	3974(3)	3617(3)	356(2)	30(1)
C2	4194(3)	3960(3)	-72(2)	37(1)
C3	5020(4)	3803(4)	-216(2)	44(1)
C4	5619(3)	3307(3)	83(2)	40(1)
C5	5378(3)	2988(3)	505(2)	30(1)

C6	5995(3)	2491(3)	847(2)	31(1)
C7	6361(3)	1771(3)	1574(2)	36(1)
C8	6506(3)	2369(3)	2016(2)	39(1)
C9	5557(3)	3549(4)	2341(2)	42(1)
C10	5223(3)	4162(3)	1924(2)	37(1)
C11	3665(3)	4111(3)	1748(2)	30(1)
C12	2850(3)	3631(3)	1554(1)	26(1)
C13	2021(3)	3938(3)	1651(2)	32(1)
C14	1289(3)	3436(3)	1481(2)	36(1)
C15	1415(3)	2645(3)	1221(2)	33(1)
C16	2257(3)	2378(3)	1133(2)	29(1)
C17	5320(3)	1873(4)	2489(2)	43(1)
C18	4338(3)	1702(4)	2345(2)	37(1)
C19	4001(3)	652(3)	1721(2)	35(1)
C20	3909(3)	397(3)	1222(2)	31(1)
C21	3711(3)	-505(3)	1078(2)	38(1)
C22	3642(3)	-706(3)	602(2)	44(1)
C23	3773(3)	2(3)	295(2)	37(1)
C24	3959(3)	891(3)	463(2)	32(1)
N1	4555(2)	3135(2)	638(1)	27(1)
N2	5742(2)	2230(2)	1230(1)	28(1)
N3	5658(2)	2591(3)	2191(1)	34(1)
N4	4412(2)	3753(2)	1697(1)	26(1)
N5	2972(2)	2866(2)	1298(1)	23(1)
N6	4207(2)	1474(3)	1849(1)	28(1)
N7	4023(2)	1092(2)	918(1)	28(1)
O4	2522(2)	5986(3)	1291(1)	65(1)
O1	4056(2)	5959(3)	1219(2)	54(1)
O2	3377(3)	7282(3)	1487(2)	64(1)
O3	3103(3)	6876(3)	706(1)	59(1)
O1A	3331(15)	5701(10)	840(6)	57
O2A	4069(10)	6492(14)	1468(6)	57
O3A	3208(17)	7314(9)	885(7)	57

O5	2023(3)	1479(2)	2218(1)	54(1)
O6	2356(2)	-101(2)	2347(1)	47(1)
O7	908(2)	351(3)	2075(1)	53(1)
O8	2041(2)	453(2)	1576(1)	42(1)
Br1	3354(1)	4676(1)	-452(1)	46(1)
Br2	445(1)	1907(1)	991(1)	52(1)
Br3	3682(1)	-204(1)	-361(1)	55(1)
Zn1	4409(1)	2478(1)	1337(1)	25(1)
Cl1	3264(1)	6484(1)	1161(1)	42(1)
Cl2	1832(1)	548(1)	2054(1)	35(1)

Table 4.16. Bond lengths [\AA] and angles [$^\circ$] for **4.18**.

C1-N1	1.330(5)	O6-Cl2	1.439(3)	H18A-C18-H18B	108.2
C1-C2	1.394(6)	O7-Cl2	1.438(4)	N6-C19-C20	120.7(4)
C1-H1	0.95	O8-Cl2	1.442(3)	N6-C19-H19	119.6
C2-C3	1.377(7)	N1-C1-C2	121.2(4)	C20-C19-H19	119.6
C2-Br1	1.895(5)	N1-C1-H1	119.4	N7-C20-C21	122.5(5)
C3-C4	1.383(7)	C2-C1-H1	119.4	N7-C20-C19	116.1(4)
C3-H3	0.95	C3-C2-C1	120.6(5)	C21-C20-C19	121.3(4)
C4-C5	1.378(6)	C3-C2-Br1	119.8(4)	C20-C21-C22	118.7(5)
C4-H4	0.95	C1-C2-Br1	119.5(4)	C20-C21-H21	120.7
C5-N1	1.358(5)	C2-C3-C4	117.5(4)	C22-C21-H21	120.7
C5-C6	1.472(7)	C2-C3-H3	121.2	C23-C22-C21	118.5(4)
C6-N2	1.257(6)	C4-C3-H3	121.2	C23-C22-H22	120.7
C6-H6	0.95	C5-C4-C3	120.0(5)	C21-C22-H22	120.7
C7-N2	1.453(6)	C5-C4-H4	120	C22-C23-C24	119.7(5)
C7-C8	1.527(7)	C3-C4-H4	120	C22-C23-Br3	121.5(4)
C7-H7A	0.99	N1-C5-C4	121.8(5)	C24-C23-Br3	118.8(4)
C7-H7B	0.99	N1-C5-C6	115.5(4)	N7-C24-C23	122.3(4)
C8-N3	1.463(6)	C4-C5-C6	122.7(4)	N7-C24-H24	118.8
C8-H8A	0.99	N2-C6-C5	119.8(4)	C23-C24-H24	118.8
C8-H8B	0.99	N2-C6-H6	120.1	C1-N1-C5	118.8(4)
C9-N3	1.453(6)	C5-C6-H6	120.1	C1-N1-Zn1	130.1(3)
C9-C10	1.530(7)	N2-C7-C8	109.9(4)	C5-N1-Zn1	111.1(3)
C9-H9A	0.99	N2-C7-H7A	109.7	C6-N2-C7	119.8(4)

C9-H9B	0.99	C8-C7-H7A	109.7	C6-N2-Zn1	117.3(3)
C10-N4	1.459(5)	N2-C7-H7B	109.7	C7-N2-Zn1	123.0(3)
C10-H10A	0.99	C8-C7-H7B	109.7	C9-N3-C17	116.2(4)
C10-H10B	0.99	H7A-C7-H7B	108.2	C9-N3-C8	115.5(4)
C11-N4	1.267(5)	N3-C8-C7	110.4(4)	C17-N3-C8	114.7(4)
C11-C12	1.476(6)	N3-C8-H8A	109.6	C11-N4-C10	120.7(4)
C11-H11	0.95	C7-C8-H8A	109.6	C11-N4-Zn1	116.8(3)
C12-N5	1.344(5)	N3-C8-H8B	109.6	C10-N4-Zn1	122.1(3)
C12-C13	1.386(6)	C7-C8-H8B	109.6	C16-N5-C12	118.0(3)
C13-C14	1.373(6)	H8A-C8-H8B	108.1	C16-N5-Zn1	129.7(3)
C13-H13	0.95	N3-C9-C10	110.5(4)	C12-N5-Zn1	111.2(3)
C14-C15	1.382(7)	N3-C9-H9A	109.6	C19-N6-C18	119.9(4)
C14-H14	0.95	C10-C9-H9A	109.6	C19-N6-Zn1	119.0(3)
C15-C16	1.380(6)	N3-C9-H9B	109.6	C18-N6-Zn1	121.0(3)
C15-Br2	1.879(5)	C10-C9-H9B	109.6	C24-N7-C20	118.3(4)
C16-N5	1.339(5)	H9A-C9-H9B	108.1	C24-N7-Zn1	132.1(3)
C16-H16	0.95	N4-C10-C9	108.5(4)	C20-N7-Zn1	109.5(3)
C17-N3	1.462(6)	N4-C10-H10A	110	N4-Zn1-N6	104.28(14)
C17-C18	1.528(7)	C9-C10-H10A	110	N4-Zn1-N2	105.25(13)
C17-H17A	0.99	N4-C10-H10B	110	N6-Zn1-N2	101.21(14)
C17-H17B	0.99	C9-C10-H10B	110	N4-Zn1-N5	76.30(12)
C18-N6	1.456(6)	H10A-C10-H10B	108.4	N6-Zn1-N5	89.82(12)
C18-H18A	0.99	N4-C11-C12	119.6(4)	N2-Zn1-N5	167.95(14)
C18-H18B	0.99	N4-C11-H11	120.2	N4-Zn1-N1	94.45(13)
C19-N6	1.266(6)	C12-C11-H11	120.2	N6-Zn1-N1	161.05(14)
C19-C20	1.471(7)	N5-C12-C13	123.1(4)	N2-Zn1-N1	76.14(14)
C19-H19	0.95	N5-C12-C11	115.5(4)	N5-Zn1-N1	91.85(13)
C20-N7	1.347(5)	C13-C12-C11	121.3(4)	N4-Zn1-N7	165.87(12)
C20-C21	1.383(6)	C14-C13-C12	118.7(4)	N6-Zn1-N7	74.52(14)
C21-C22	1.389(7)	C14-C13-H13	120.6	N2-Zn1-N7	88.70(13)
C21-H21	0.95	C12-C13-H13	120.6	N5-Zn1-N7	89.59(12)
C22-C23	1.373(7)	C13-C14-C15	118.2(4)	N1-Zn1-N7	86.61(13)
C22-H22	0.95	C13-C14-H14	120.9	O4-C11-O1	112.9(2)
C23-C24	1.384(6)	C15-C14-H14	120.9	O4-C11-O3	111.9(3)
C23-Br3	1.895(5)	C16-C15-C14	120.4(4)	O1-C11-O3	112.7(2)
C24-N7	1.330(6)	C16-C15-Br2	119.2(4)	O4-C11-O3A	124.2(11)
C24-H24	0.95	C14-C15-Br2	120.5(3)	O4-C11-O2A	119.7(10)
N1-Zn1	2.246(3)	N5-C16-C15	121.6(4)	O3A-C11-O2A	109.6(7)
N2-Zn1	2.105(4)	N5-C16-H16	119.2	O4-C11-O1A	83.3(10)
N4-Zn1	2.100(3)	C15-C16-H16	119.2	O3A-C11-O1A	107.1(7)

N5-Zn1	2.243(3)	N3-C17-C18	110.2(4)	O2A-C11-O1A	106.5(7)
N6-Zn1	2.101(3)	N3-C17-H17A	109.6	O4-C11-O2	105.8(2)
N7-Zn1	2.368(3)	C18-C17-H17A	109.6	O1-C11-O2	107.2(3)
O4-C11	1.414(3)	N3-C17-H17B	109.6	O3-C11-O2	105.8(3)
O1-C11	1.414(3)	C18-C17-H17B	109.6	O5-C12-O7	109.6(2)
O2-C11	1.476(4)	H17A-C17-H17B	108.1	O5-C12-O6	109.2(2)
O3-C11	1.422(4)	N6-C18-C17	109.6(4)	O7-C12-O6	109.4(2)
O1A-C11	1.464(7)	N6-C18-H18A	109.7	O5-C12-O8	110.1(2)
O2A-C11	1.432(7)	C17-C18-H18A	109.7	O7-C12-O8	109.1(2)
O3A-C11	1.428(7)	N6-C18-H18B	109.7	O6-C12-O8	109.4(2)
O5-C12	1.436(4)	C17-C18-H18B	109.7		

Table 4.17. Anisotropic displacement parameters ($\text{\AA}^2 \times 10^3$) for **4.18**. The anisotropic displacement factor exponent takes the form: $-2\pi^2 [h^2 a^{*2} U^{11} + \dots + 2 h k a^* b^* U^{12}]$

	U ¹¹	U ²²	U ³³	U ²³	U ¹³	U ¹²
C1	32(2)	27(2)	32(2)	-1(2)	5(2)	-5(2)
C2	46(3)	36(3)	28(2)	-2(2)	0(2)	-15(2)
C3	55(3)	47(3)	30(3)	0(2)	12(2)	-24(3)
C4	47(3)	40(3)	36(3)	-12(2)	15(2)	-14(2)
C5	30(2)	30(2)	31(2)	-13(2)	8(2)	-11(2)
C6	26(2)	26(2)	40(3)	-9(2)	10(2)	-4(2)
C7	25(2)	31(3)	51(3)	-2(2)	4(2)	7(2)
C8	25(2)	43(3)	47(3)	-6(2)	-3(2)	3(2)
C9	29(2)	49(3)	46(3)	-21(2)	-4(2)	3(2)
C10	28(2)	33(3)	48(3)	-11(2)	2(2)	-4(2)
C11	35(3)	23(2)	30(2)	2(2)	4(2)	1(2)
C12	26(2)	30(2)	24(2)	4(2)	4(2)	3(2)
C13	33(2)	35(3)	29(2)	-2(2)	7(2)	8(2)
C14	25(2)	47(3)	37(3)	3(2)	9(2)	9(2)
C15	24(2)	34(3)	41(3)	10(2)	-2(2)	-2(2)
C16	30(2)	24(2)	33(2)	0(2)	3(2)	0(2)
C17	44(3)	50(3)	33(3)	4(2)	0(2)	11(2)

C18	34(3)	48(3)	28(2)	12(2)	5(2)	2(2)
C19	24(2)	31(3)	50(3)	17(2)	6(2)	3(2)
C20	19(2)	23(2)	50(3)	4(2)	8(2)	2(2)
C21	25(2)	26(2)	63(4)	6(2)	8(2)	-2(2)
C22	23(2)	28(3)	80(4)	-15(3)	1(3)	-4(2)
C23	17(2)	35(3)	57(3)	-17(2)	4(2)	-2(2)
C24	26(2)	25(2)	47(3)	-5(2)	9(2)	-3(2)
N1	33(2)	22(2)	29(2)	-1(2)	11(2)	-3(2)
N2	25(2)	26(2)	33(2)	-6(2)	6(2)	-1(2)
N3	29(2)	35(2)	37(2)	-3(2)	2(2)	6(2)
N4	21(2)	25(2)	32(2)	-1(2)	4(2)	-1(1)
N5	20(2)	22(2)	25(2)	2(1)	6(2)	3(1)
N6	23(2)	32(2)	29(2)	7(2)	6(2)	5(2)
N7	25(2)	18(2)	40(2)	-3(2)	7(2)	1(1)
O4	52(2)	58(3)	88(3)	8(2)	30(2)	-17(2)
O1	44(2)	52(3)	68(3)	21(2)	20(2)	16(2)
O2	49(3)	55(3)	88(4)	-9(3)	5(3)	-5(2)
O3	42(2)	95(4)	43(3)	25(2)	14(2)	17(3)
O5	73(3)	32(2)	57(2)	-8(2)	9(2)	-5(2)
O6	53(2)	41(2)	47(2)	7(2)	2(2)	6(2)
O7	36(2)	60(3)	67(3)	-6(2)	25(2)	-1(2)
O8	43(2)	44(2)	40(2)	1(2)	14(2)	-2(2)
Br1	63(1)	41(1)	32(1)	4(1)	-8(1)	-12(1)
Br2	28(1)	45(1)	80(1)	1(1)	-5(1)	-6(1)
Br3	40(1)	63(1)	64(1)	-35(1)	9(1)	-11(1)
Zn1	22(1)	22(1)	31(1)	2(1)	7(1)	1(1)
Cl1	30(1)	54(1)	44(1)	18(1)	8(1)	-1(1)
Cl2	37(1)	32(1)	38(1)	-1(1)	11(1)	-2(1)

Table 4.18. Hydrogen coordinates ($\times 10^4$) and isotropic displacement parameters ($\text{\AA}^2 \times 10^{-3}$) for **4.18**.

	x	y	z	U(eq)
H1	3399	3730	448	36
H3	5174	4028	-508	53
H4	6197	3186	-4	48
H6	6583	2368	778	37
H7A	6933	1674	1442	43
H7B	6125	1154	1653	43
H8A	6886	2029	2259	46
H8B	6813	2953	1944	46
H9A	6134	3788	2483	50
H9B	5132	3574	2581	50
H10A	5104	4800	2033	44
H10B	5677	4200	1700	44
H11	3629	4685	1910	36
H13	1961	4485	1832	39
H14	711	3627	1540	43
H16	2330	1835	951	35
H17A	5404	2075	2820	51
H17B	5655	1288	2459	51
H18A	4125	1182	2531	44
H18B	3993	2266	2408	44
H19	3904	195	1950	42
H21	3624	-979	1301	46
H22	3506	-1319	492	53
H24	4043	1375	246	39

Table 4.19. Torsion angles [$^\circ$] for **4.18**.

N1-C1-C2-C3	0.3(7)	C19-C20-N7-C24	179.0(4)
N1-C1-C2-Br1	-178.1(3)	C21-C20-N7-Zn1	-177.6(3)

C1-C2-C3-C4	-0.8(7)	C19-C20-N7-Zn1	2.9(4)
Br1-C2-C3-C4	177.6(3)	C11-N4-Zn1-N6	-82.8(3)
C2-C3-C4-C5	0.2(7)	C10-N4-Zn1-N6	90.5(3)
C3-C4-C5-N1	0.9(7)	C11-N4-Zn1-N2	171.1(3)
C3-C4-C5-C6	-177.3(4)	C10-N4-Zn1-N2	-15.6(4)
N1-C5-C6-N2	0.4(6)	C11-N4-Zn1-N5	3.4(3)
C4-C5-C6-N2	178.8(4)	C10-N4-Zn1-N5	176.8(3)
N2-C7-C8-N3	54.2(5)	C11-N4-Zn1-N1	94.2(3)
N3-C9-C10-N4	54.5(5)	C10-N4-Zn1-N1	-92.4(3)
N4-C11-C12-N5	-5.4(6)	C11-N4-Zn1-N7	0.5(7)
N4-C11-C12-C13	172.0(4)	C10-N4-Zn1-N7	173.8(5)
N5-C12-C13-C14	0.5(7)	C19-N6-Zn1-N4	166.3(3)
C11-C12-C13-C14	-176.7(4)	C18-N6-Zn1-N4	-16.4(3)
C12-C13-C14-C15	0.1(7)	C19-N6-Zn1-N2	-84.6(3)
C13-C14-C15-C16	-0.6(7)	C18-N6-Zn1-N2	92.7(3)
C13-C14-C15-Br2	178.3(3)	C19-N6-Zn1-N5	90.5(3)
C14-C15-C16-N5	0.6(7)	C18-N6-Zn1-N5	-92.2(3)
Br2-C15-C16-N5	-178.4(3)	C19-N6-Zn1-N1	-4.7(6)
N3-C17-C18-N6	55.0(5)	C18-N6-Zn1-N1	172.7(4)
N6-C19-C20-N7	-2.5(6)	C19-N6-Zn1-N7	0.9(3)
N6-C19-C20-C21	178.0(4)	C18-N6-Zn1-N7	178.2(3)
N7-C20-C21-C22	1.1(6)	C6-N2-Zn1-N4	-94.3(3)
C19-C20-C21-C22	-179.4(4)	C7-N2-Zn1-N4	86.2(3)
C20-C21-C22-C23	0.0(6)	C6-N2-Zn1-N6	157.4(3)
C21-C22-C23-C24	-0.8(6)	C7-N2-Zn1-N6	-22.1(3)
C21-C22-C23-Br3	-179.5(3)	C6-N2-Zn1-N5	1.5(8)
C22-C23-C24-N7	0.5(7)	C7-N2-Zn1-N5	-177.9(5)
Br3-C23-C24-N7	179.2(3)	C6-N2-Zn1-N1	-3.4(3)
C2-C1-N1-C5	0.8(6)	C7-N2-Zn1-N1	177.1(3)
C2-C1-N1-Zn1	-179.1(3)	C6-N2-Zn1-N7	83.4(3)
C4-C5-N1-C1	-1.4(6)	C7-N2-Zn1-N7	-96.0(3)
C6-C5-N1-C1	176.9(4)	C16-N5-Zn1-N4	-173.5(4)
C4-C5-N1-Zn1	178.5(3)	C12-N5-Zn1-N4	-6.0(3)
C6-C5-N1-Zn1	-3.2(4)	C16-N5-Zn1-N6	-68.8(4)
C5-C6-N2-C7	-177.6(4)	C12-N5-Zn1-N6	98.7(3)
C5-C6-N2-Zn1	2.9(5)	C16-N5-Zn1-N2	87.6(7)
C8-C7-N2-C6	116.0(4)	C12-N5-Zn1-N2	-105.0(6)
C8-C7-N2-Zn1	-64.5(5)	C16-N5-Zn1-N1	92.3(4)
C10-C9-N3-C17	-135.4(4)	C12-N5-Zn1-N1	-100.2(3)
C10-C9-N3-C8	86.0(5)	C16-N5-Zn1-N7	5.8(4)

C18-C17-N3-C9	86.7(5)	C12-N5-Zn1-N7	173.2(3)
C18-C17-N3-C8	-134.4(4)	C1-N1-Zn1-N4	-72.1(4)
C7-C8-N3-C9	-136.7(4)	C5-N1-Zn1-N4	108.1(3)
C7-C8-N3-C17	84.1(5)	C1-N1-Zn1-N6	99.1(5)
C12-C11-N4-C10	-173.8(4)	C5-N1-Zn1-N6	-80.7(5)
C12-C11-N4-Zn1	-0.4(5)	C1-N1-Zn1-N2	-176.7(4)
C9-C10-N4-C11	105.1(5)	C5-N1-Zn1-N2	3.4(3)
C9-C10-N4-Zn1	-68.0(4)	C1-N1-Zn1-N5	4.3(4)
C15-C16-N5-C12	0.0(6)	C5-N1-Zn1-N5	-175.5(3)
C15-C16-N5-Zn1	166.8(3)	C1-N1-Zn1-N7	93.8(4)
C13-C12-N5-C16	-0.5(6)	C5-N1-Zn1-N7	-86.1(3)
C11-C12-N5-C16	176.8(4)	C24-N7-Zn1-N4	95.5(6)
C13-C12-N5-Zn1	-169.7(3)	C20-N7-Zn1-N4	-89.1(6)
C11-C12-N5-Zn1	7.7(4)	C24-N7-Zn1-N6	-177.5(4)
C20-C19-N6-C18	-176.9(4)	C20-N7-Zn1-N6	-2.0(3)
C20-C19-N6-Zn1	0.4(5)	C24-N7-Zn1-N2	-75.5(4)
C17-C18-N6-C19	109.2(5)	C20-N7-Zn1-N2	100.0(3)
C17-C18-N6-Zn1	-68.2(4)	C24-N7-Zn1-N5	92.6(4)
C23-C24-N7-C20	0.6(6)	C20-N7-Zn1-N5	-92.0(3)
C23-C24-N7-Zn1	175.7(3)	C24-N7-Zn1-N1	0.7(4)
C21-C20-N7-C24	-1.4(6)	C20-N7-Zn1-N1	176.2(3)

4.5.4.4. Complex 4.19

Crystals grew as large, pale yellow prisms. The data crystal was cut from a larger crystal and had approximate dimensions; 0.32 x 0.22 x 0.13 mm. The data were collected on a Rigaku SCX-Mini diffractometer with a Mercury CCD using a graphite monochromator with MoK α radiation ($\lambda = 0.71075\text{\AA}$). A total of 930 frames of data were collected using ω -scans with a scan range of 0.5° and a counting time of 30 seconds per frame. The data were collected at 253 K using a Rigaku XStream low temperature device. Details of crystal data, data collection and structure refinement are listed in Table 1. Data reduction were performed using the Rigaku Americas Corporation's Crystal Clear version 1.40. The structure was solved by direct methods using SIR97 and refined

by full-matrix least-squares on F^2 with anisotropic displacement parameters for the non-H atoms using SHELXL-97. Structure analysis was aided by use of the programs PLATON98 and WinGX.

Table 4.20. Crystal data and structure refinement for **4.19**.

Empirical formula	C ₄₀ H ₄₃ Cl ₂ N ₇ O ₉ Zn
Formula weight	902.08
Temperature	153(2) K
Wavelength	0.71075 Å
Crystal system	Orthorhombic
Space group	Pbca
Unit cell dimensions	a = 11.675(3) Å $\alpha = 90^\circ$.
b = 21.626(6) Å	$\beta = 90^\circ$.
c = 32.521(10) Å	$\gamma = 90^\circ$.
Volume	8211(4) Å ³
Z	8
Density (calculated)	1.459 Mg/m ³
Absorption coefficient	0.792 mm ⁻¹
F(000)	3744
Crystal size	0.32 x 0.22 x 0.13 mm
Theta range for data collection	2.08 to 27.50°.
Index ranges	-15 ≤ h ≤ 15, -28 ≤ k ≤ 28, -42 ≤ l ≤ 42
Reflections collected	77197
Independent reflections	9396 [R(int) = 0.0830]
Completeness to theta = 27.50°	99.8 %
Absorption correction	Semi-empirical from equivalents
Max. and min. transmission	1.00 and 0.790
Refinement method	Full-matrix least-squares on F^2
Data / restraints / parameters	9396 / 0 / 535
Goodness-of-fit on F^2	1.215

Final R indices [$I > 2\sigma(I)$]	R1 = 0.0623, wR2 = 0.1352
R indices (all data)	R1 = 0.0834, wR2 = 0.1469
Extinction coefficient	0.00053(13)
Largest diff. peak and hole	0.512 and -0.647 e.Å ⁻³

Table 4.21. Atomic coordinates ($\times 10^4$) and equivalent isotropic displacement parameters (Å² $\times 10^3$) for **4.19**. U(eq) is defined as one third of the trace of the orthogonalized U^{ij} tensor.

	x	y	z	U(eq)
Zn1	3538(1)	5529(1)	6512(1)	29(1)
N1	2324(2)	4909(1)	6844(1)	31(1)
N2	4260(2)	5456(1)	7118(1)	33(1)
N3	4636(2)	6717(1)	6902(1)	34(1)
N4	2519(2)	6333(1)	6566(1)	32(1)
N5	2526(2)	5524(1)	5940(1)	31(1)
N6	5004(2)	5930(1)	6217(1)	32(1)
N7	4547(2)	4719(1)	6304(1)	31(1)
C1	2672(3)	4796(1)	7243(1)	33(1)
C2	2085(3)	4419(2)	7505(1)	38(1)
C3	1095(3)	4107(2)	7366(1)	38(1)
C4	466(3)	3684(2)	7611(1)	50(1)
C5	-471(3)	3392(2)	7453(1)	55(1)
C6	-833(3)	3501(2)	7049(1)	51(1)
C7	-255(3)	3909(2)	6804(1)	44(1)
C8	726(3)	4218(1)	6959(1)	35(1)
C9	1384(3)	4632(2)	6715(1)	35(1)
C10	3730(3)	5109(1)	7370(1)	33(1)
C11	5299(3)	5779(2)	7261(1)	39(1)
C12	5052(3)	6473(2)	7289(1)	38(1)
C13	3643(3)	7119(2)	6923(1)	39(1)
C14	2534(3)	6747(2)	6920(1)	37(1)

C15	1907(3)	6468(2)	6253(1)	35(1)
C16	1902(3)	6059(1)	5894(1)	32(1)
C17	1325(3)	6201(2)	5541(1)	40(1)
C18	1338(3)	5785(2)	5206(1)	38(1)
C19	757(3)	5891(2)	4832(1)	49(1)
C20	768(3)	5451(2)	4532(1)	54(1)
C21	1367(3)	4893(2)	4585(1)	50(1)
C22	1967(3)	4781(2)	4939(1)	44(1)
C23	1953(3)	5225(2)	5258(1)	36(1)
C24	2537(3)	5128(2)	5633(1)	34(1)
C25	5502(3)	6868(2)	6597(1)	39(1)
C26	5200(3)	6594(1)	6173(1)	36(1)
C27	5769(3)	5553(2)	6095(1)	35(1)
C28	5604(3)	4888(2)	6157(1)	33(1)
C29	6454(3)	4466(2)	6086(1)	41(1)
C30	6259(3)	3829(2)	6160(1)	39(1)
C31	7103(3)	3367(2)	6120(1)	52(1)
C32	6837(3)	2763(2)	6210(1)	56(1)
C33	5739(3)	2591(2)	6335(1)	54(1)
C34	4899(3)	3026(2)	6373(1)	47(1)
C35	5152(3)	3655(2)	6290(1)	36(1)
C36	4327(3)	4129(1)	6357(1)	35(1)
Cl1	8668(1)	5847(1)	6604(1)	43(1)
O1	8501(4)	5205(2)	6557(1)	114(2)
O2	8311(3)	6167(1)	6242(1)	59(1)
O3	8002(3)	6059(2)	6948(1)	84(1)
O4	9831(2)	5974(2)	6697(1)	73(1)
Cl2	3366(1)	8201(1)	5937(1)	51(1)
O5	2923(3)	7621(1)	5807(1)	68(1)
O6	2989(4)	8688(2)	5684(1)	108(2)
O7	2999(3)	8313(1)	6354(1)	59(1)
O8	4617(3)	8155(2)	5927(1)	89(1)
O9	3718(3)	3447(2)	4824(1)	67(1)

C37	1857(5)	3037(2)	4704(2)	77(1)
C38	3053(5)	2876(2)	4815(2)	77(1)
C39	4833(5)	3366(4)	4998(2)	111(3)
C40	5398(6)	3974(4)	5007(2)	138(3)

Table 4.22. Bond lengths [\AA] and angles [$^\circ$] for **4.19**.

Zn1-N4	2.114(3)	C39-C40	1.471(10)	C16-C17-H17	120
Zn1-N6	2.145(3)	C39-H39C	0.99	C18-C17-H17	120
Zn1-N2	2.151(3)	C39-H39D	0.99	C19-C18-C17	123.8(3)
Zn1-N5	2.202(3)	C40-H40D	0.98	C19-C18-C23	118.9(3)
Zn1-N7	2.217(3)	C40-H40E	0.98	C17-C18-C23	117.2(3)
Zn1-N1	2.231(3)	C40-H40F	0.98	C20-C19-C18	120.0(4)
N1-C9	1.318(4)	N4-Zn1-N6	98.83(10)	C20-C19-H19	120
N1-C1	1.380(4)	N4-Zn1-N2	101.83(10)	C18-C19-H19	120
N2-C10	1.271(4)	N6-Zn1-N2	97.33(10)	C19-C20-C21	121.0(4)
N2-C11	1.475(4)	N4-Zn1-N5	76.79(10)	C19-C20-H20	119.5
N3-C12	1.449(4)	N6-Zn1-N5	92.99(10)	C21-C20-H20	119.5
N3-C13	1.450(4)	N2-Zn1-N5	169.67(10)	C22-C21-C20	120.8(4)
N3-C25	1.453(4)	N4-Zn1-N7	166.95(10)	C22-C21-H21	119.6
N4-C15	1.277(4)	N6-Zn1-N7	76.08(10)	C20-C21-H21	119.6
N4-C14	1.460(4)	N2-Zn1-N7	90.81(10)	C21-C22-C23	119.2(4)
N5-C24	1.317(4)	N5-Zn1-N7	91.35(10)	C21-C22-H22	120.4
N5-C16	1.375(4)	N4-Zn1-N1	95.53(10)	C23-C22-H22	120.4
N6-C27	1.272(4)	N6-Zn1-N1	165.21(9)	C22-C23-C24	121.7(3)
N6-C26	1.460(4)	N2-Zn1-N1	76.14(10)	C22-C23-C18	120.0(3)
N7-C36	1.312(4)	N5-Zn1-N1	93.74(10)	C24-C23-C18	118.2(3)
N7-C28	1.373(4)	N7-Zn1-N1	90.60(9)	N5-C24-C23	123.6(3)
C1-C2	1.364(4)	C9-N1-C1	117.6(3)	N5-C24-H24	118.2
C1-C10	1.468(4)	C9-N1-Zn1	130.4(2)	C23-C24-H24	118.2
C2-C3	1.413(5)	C1-N1-Zn1	111.9(2)	N3-C25-C26	111.4(3)
C2-H2	0.95	C10-N2-C11	118.5(3)	N3-C25-H25A	109.3
C3-C8	1.412(5)	C10-N2-Zn1	116.4(2)	C26-C25-H25A	109.3
C3-C4	1.418(5)	C11-N2-Zn1	125.1(2)	N3-C25-H25B	109.3
C4-C5	1.363(6)	C12-N3-C13	116.5(3)	C26-C25-H25B	109.3
C4-H4	0.95	C12-N3-C25	116.2(3)	H25A-C25-H25B	108
C5-C6	1.400(6)	C13-N3-C25	117.0(3)	N6-C26-C25	109.2(3)

C5-H5	0.95	C15-N4-C14	119.7(3)	N6-C26-H26A	109.8
C6-C7	1.368(5)	C15-N4-Zn1	115.9(2)	C25-C26-H26A	109.8
C6-H6	0.95	C14-N4-Zn1	124.3(2)	N6-C26-H26B	109.8
C7-C8	1.418(5)	C24-N5-C16	118.0(3)	C25-C26-H26B	109.8
C7-H7	0.95	C24-N5-Zn1	129.7(2)	H26A-C26-H26B	108.3
C8-C9	1.421(4)	C16-N5-Zn1	111.9(2)	N6-C27-C28	119.6(3)
C9-H9	0.95	C27-N6-C26	119.3(3)	N6-C27-H27	120.2
C10-H10	0.95	C27-N6-Zn1	116.1(2)	C28-C27-H27	120.2
C11-C12	1.531(5)	C26-N6-Zn1	124.5(2)	C29-C28-N7	122.2(3)
C11-H11A	0.99	C36-N7-C28	118.7(3)	C29-C28-C27	122.4(3)
C11-H11B	0.99	C36-N7-Zn1	128.6(2)	N7-C28-C27	115.3(3)
C12-H12A	0.99	C28-N7-Zn1	111.91(19)	C28-C29-C30	120.2(3)
C12-H12B	0.99	C2-C1-N1	122.9(3)	C28-C29-H29	119.9
C13-C14	1.524(5)	C2-C1-C10	121.4(3)	C30-C29-H29	119.9
C13-H13A	0.99	N1-C1-C10	115.6(3)	C31-C30-C35	118.6(3)
C13-H13B	0.99	C1-C2-C3	119.8(3)	C31-C30-C29	124.1(3)
C14-H14A	0.99	C1-C2-H2	120.1	C35-C30-C29	117.3(3)
C14-H14B	0.99	C3-C2-H2	120.1	C32-C31-C30	119.7(4)
C15-C16	1.464(4)	C8-C3-C2	117.8(3)	C32-C31-H31	120.1
C15-H15	0.95	C8-C3-C4	118.6(3)	C30-C31-H31	120.1
C16-C17	1.365(4)	C2-C3-C4	123.6(3)	C31-C32-C33	121.5(3)
C17-C18	1.413(5)	C5-C4-C3	120.2(4)	C31-C32-H32	119.2
C17-H17	0.95	C5-C4-H4	119.9	C33-C32-H32	119.2
C18-C19	1.411(5)	C3-C4-H4	119.9	C34-C33-C32	120.1(4)
C18-C23	1.417(5)	C4-C5-C6	121.2(3)	C34-C33-H33	119.9
C19-C20	1.365(5)	C4-C5-H5	119.4	C32-C33-H33	119.9
C19-H19	0.95	C6-C5-H5	119.4	C33-C34-C35	119.6(4)
C20-C21	1.404(6)	C7-C6-C5	120.5(4)	C33-C34-H34	120.2
C20-H20	0.95	C7-C6-H6	119.8	C35-C34-H34	120.2
C21-C22	1.369(5)	C5-C6-H6	119.8	C30-C35-C34	120.3(3)
C21-H21	0.95	C6-C7-C8	119.6(4)	C30-C35-C36	118.2(3)
C22-C23	1.414(5)	C6-C7-H7	120.2	C34-C35-C36	121.4(3)
C22-H22	0.95	C8-C7-H7	120.2	N7-C36-C35	123.2(3)
C23-C24	1.415(4)	C3-C8-C7	120.0(3)	N7-C36-H36	118.4
C24-H24	0.95	C3-C8-C9	117.7(3)	C35-C36-H36	118.4
C25-C26	1.541(5)	C7-C8-C9	122.3(3)	O1-C11-O4	110.2(2)
C25-H25A	0.99	N1-C9-C8	124.0(3)	O1-C11-O2	110.32(18)
C25-H25B	0.99	N1-C9-H9	118	O4-C11-O2	111.16(19)
C26-H26A	0.99	C8-C9-H9	118	O1-C11-O3	108.9(3)
C26-H26B	0.99	N2-C10-C1	119.9(3)	O4-C11-O3	107.0(2)

C27-C28	1.466(4)	N2-C10-H10	120	O2-C11-O3	109.19(19)
C27-H27	0.95	C1-C10-H10	120	O6-C12-O5	111.8(2)
C28-C29	1.368(4)	N2-C11-C12	109.2(3)	O6-C12-O7	109.3(2)
C29-C30	1.417(5)	N2-C11-H11A	109.8	O5-C12-O7	108.65(19)
C29-H29	0.95	C12-C11-H11A	109.8	O6-C12-O8	110.5(3)
C30-C31	1.409(5)	N2-C11-H11B	109.8	O5-C12-O8	107.2(2)
C30-C35	1.410(5)	C12-C11-H11B	109.8	O7-C12-O8	109.2(2)
C31-C32	1.374(6)	H11A-C11-H11B	108.3	C39-O9-C38	113.0(5)
C31-H31	0.95	N3-C12-C11	111.7(3)	C38-C37-H37D	109.5
C32-C33	1.396(6)	N3-C12-H12A	109.3	C38-C37-H37E	109.5
C32-H32	0.95	C11-C12-H12A	109.3	H37D-C37-H37E	109.5
C33-C34	1.364(5)	N3-C12-H12B	109.3	C38-C37-H37F	109.5
C33-H33	0.95	C11-C12-H12B	109.3	H37D-C37-H37F	109.5
C34-C35	1.416(5)	H12A-C12-H12B	108	H37E-C37-H37F	109.5
C34-H34	0.95	N3-C13-C14	111.4(3)	O9-C38-C37	107.9(4)
C35-C36	1.425(4)	N3-C13-H13A	109.4	O9-C38-H38C	110.1
C36-H36	0.95	C14-C13-H13A	109.4	C37-C38-H38C	110.1
C11-O1	1.409(3)	N3-C13-H13B	109.4	O9-C38-H38D	110.1
C11-O4	1.418(3)	C14-C13-H13B	109.4	C37-C38-H38D	110.1
C11-O2	1.430(3)	H13A-C13-H13B	108	H38C-C38-H38D	108.4
C11-O3	1.436(3)	N4-C14-C13	109.8(3)	O9-C39-C40	108.0(6)
C12-O6	1.405(3)	N4-C14-H14A	109.7	O9-C39-H39C	110.1
C12-O5	1.421(3)	C13-C14-H14A	109.7	C40-C39-H39C	110.1
C12-O7	1.441(3)	N4-C14-H14B	109.7	O9-C39-H39D	110.1
C12-O8	1.464(4)	C13-C14-H14B	109.7	C40-C39-H39D	110.1
O9-C39	1.430(6)	H14A-C14-H14B	108.2	H39C-C39-H39D	108.4
O9-C38	1.459(6)	N4-C15-C16	119.9(3)	C39-C40-H40D	109.5
C37-C38	1.483(7)	N4-C15-H15	120	C39-C40-H40E	109.5
C37-H37D	0.98	C16-C15-H15	120	H40D-C40-H40E	109.5
C37-H37E	0.98	C17-C16-N5	122.9(3)	C39-C40-H40F	109.5
C37-H37F	0.98	C17-C16-C15	122.4(3)	H40D-C40-H40F	109.5
C38-H38C	0.99	N5-C16-C15	114.7(3)	H40E-C40-H40F	109.5
C38-H38D	0.99	C16-C17-C18	120.0(3)		

Table 4.23. Anisotropic displacement parameters ($\text{\AA}^2 \times 10^3$) for **4.19**. The anisotropic displacement factor exponent takes the form: $-2\pi^2 [h^2 a^{*2} U^{11} + \dots + 2 h k a^* b^* U^{12}]$

	U11	U22	U33	U23	U13	U12
Zn1	28(1)	27(1)	32(1)	3(1)	1(1)	2(1)
N1	29(1)	29(1)	34(1)	2(1)	4(1)	2(1)
N2	34(1)	31(1)	34(1)	1(1)	-2(1)	4(1)
N3	35(1)	31(1)	37(1)	2(1)	-1(1)	0(1)
N4	28(1)	32(1)	36(1)	1(1)	3(1)	1(1)
N5	30(1)	29(1)	35(1)	3(1)	-1(1)	-2(1)
N6	31(1)	30(1)	35(1)	3(1)	1(1)	-2(1)
N7	29(1)	29(1)	36(1)	-1(1)	1(1)	2(1)
C1	30(2)	32(2)	36(2)	2(1)	3(1)	8(1)
C2	42(2)	39(2)	32(2)	7(1)	7(1)	7(1)
C3	35(2)	33(2)	47(2)	5(1)	13(1)	5(1)
C4	56(2)	43(2)	52(2)	10(2)	18(2)	3(2)
C5	49(2)	42(2)	73(3)	8(2)	23(2)	-7(2)
C6	43(2)	39(2)	72(3)	-12(2)	17(2)	-10(2)
C7	39(2)	43(2)	52(2)	-10(2)	11(2)	-5(2)
C8	33(2)	29(2)	44(2)	-2(1)	10(1)	2(1)
C9	34(2)	32(2)	37(2)	-3(1)	4(1)	3(1)
C10	36(2)	32(2)	32(2)	2(1)	-3(1)	7(1)
C11	35(2)	41(2)	39(2)	1(1)	-6(1)	-1(1)
C12	41(2)	39(2)	36(2)	-3(1)	-4(1)	-3(1)
C13	45(2)	29(2)	42(2)	-3(1)	0(1)	3(1)
C14	38(2)	36(2)	37(2)	-2(1)	2(1)	7(1)
C15	30(2)	34(2)	41(2)	5(1)	2(1)	4(1)
C16	27(2)	33(2)	36(2)	3(1)	1(1)	4(1)
C17	31(2)	44(2)	44(2)	7(2)	-3(1)	5(1)
C18	31(2)	47(2)	37(2)	7(2)	-2(1)	-7(1)
C19	39(2)	69(3)	38(2)	9(2)	-4(2)	6(2)
C20	42(2)	84(3)	35(2)	8(2)	-2(2)	-10(2)
C21	51(2)	62(3)	37(2)	-5(2)	1(2)	-19(2)
C22	44(2)	48(2)	40(2)	0(2)	3(2)	-13(2)
C23	33(2)	42(2)	33(2)	4(1)	1(1)	-7(1)
C24	35(2)	30(2)	38(2)	3(1)	0(1)	-1(1)

C25	39(2)	29(2)	50(2)	1(1)	2(1)	-4(1)
C26	40(2)	27(2)	42(2)	4(1)	4(1)	-4(1)
C27	28(2)	38(2)	40(2)	1(1)	4(1)	-4(1)
C28	29(2)	33(2)	38(2)	-4(1)	3(1)	1(1)
C29	32(2)	41(2)	49(2)	-5(2)	6(1)	1(1)
C30	39(2)	36(2)	42(2)	-8(1)	-6(1)	7(1)
C31	37(2)	49(2)	70(3)	-13(2)	-6(2)	10(2)
C32	51(2)	39(2)	78(3)	-13(2)	-15(2)	17(2)
C33	57(2)	29(2)	75(3)	-4(2)	-14(2)	9(2)
C34	47(2)	33(2)	62(2)	-2(2)	-6(2)	4(2)
C35	37(2)	30(2)	40(2)	-5(1)	-5(1)	5(1)
C36	36(2)	28(2)	40(2)	-1(1)	2(1)	2(1)
Cl1	45(1)	39(1)	44(1)	4(1)	-7(1)	-8(1)
O1	200(5)	39(2)	103(3)	11(2)	-78(3)	-23(2)
O2	84(2)	45(2)	49(2)	10(1)	-17(1)	-11(1)
O3	48(2)	146(3)	59(2)	8(2)	8(1)	25(2)
O4	33(2)	113(3)	73(2)	5(2)	-2(1)	-9(2)
Cl2	72(1)	35(1)	45(1)	5(1)	-3(1)	-2(1)
O5	97(2)	42(2)	65(2)	-5(1)	-15(2)	-9(2)
O6	202(5)	53(2)	68(2)	24(2)	-3(3)	37(3)
O7	68(2)	63(2)	47(2)	-4(1)	-2(1)	14(1)
O8	60(2)	103(3)	105(3)	-4(2)	21(2)	-10(2)
O9	66(2)	78(2)	57(2)	7(2)	8(1)	11(2)
C37	91(4)	74(3)	66(3)	-9(2)	12(3)	-22(3)
C38	115(4)	55(3)	60(3)	6(2)	21(3)	7(3)
C39	72(4)	202(8)	60(3)	28(4)	3(3)	39(4)
C40	89(5)	235(10)	90(5)	40(5)	-18(3)	-77(6)

Table 4.24. Hydrogen coordinates ($\times 10^4$) and isotropic displacement parameters ($\text{\AA}^2 \times 10^{-3}$) for **4.19**.

	x	y	z	U(eq)
H2	2341	4367	7780	45
H4	698	3604	7886	60
H5	-886	3110	7620	66
H6	-1485	3290	6944	61
H7	-508	3985	6531	53
H9	1131	4714	6443	42
H10	4018	5053	7641	40
H11A	5935	5704	7066	46
H11B	5530	5619	7534	46
H12A	4472	6547	7505	46
H12B	5761	6694	7368	46
H13A	3649	7405	6685	46
H13B	3681	7369	7177	46
H14A	2472	6503	7177	44
H14B	1870	7032	6906	44
H15	1456	6833	6253	42
H17	915	6579	5521	47
H19	358	6268	4790	59
H20	365	5522	4282	64
H21	1356	4591	4373	60
H22	2389	4408	4970	53
H24	2960	4756	5665	41
H25A	6252	6705	6688	47
H25B	5569	7323	6573	47
H26A	4503	6796	6064	44
H26B	5836	6668	5978	44
H27	6443	5702	5965	42
H29	7179	4600	5987	49
H31	7852	3473	6030	62
H32	7414	2456	6186	67
H33	5576	2170	6394	64
H34	4149	2908	6455	57

H36	3580	4013	6444	41
H37D	1537	3314	4914	116
H37E	1395	2659	4689	116
H37F	1848	3245	4437	116
H38C	3073	2673	5088	92
H38D	3376	2587	4609	92
H39C	5285	3074	4829	134
H39D	4771	3197	5279	134
H40D	5533	4116	4725	207
H40E	6131	3939	5152	207
H40F	4906	4271	5151	207

Table 4.25. Torsion angles [°] for **4.19**.

N4-Zn1-N1-C9	80.0(3)	C1-N1-C9-C8	-1.2(4)
N6-Zn1-N1-C9	-113.9(4)	Zn1-N1-C9-C8	176.3(2)
N2-Zn1-N1-C9	-179.1(3)	C3-C8-C9-N1	1.1(5)
N5-Zn1-N1-C9	3.0(3)	C7-C8-C9-N1	-177.3(3)
N7-Zn1-N1-C9	-88.4(3)	C11-N2-C10-C1	178.1(3)
N4-Zn1-N1-C1	-102.3(2)	Zn1-N2-C10-C1	-1.3(4)
N6-Zn1-N1-C1	63.7(5)	C2-C1-C10-N2	179.7(3)
N2-Zn1-N1-C1	-1.50(19)	N1-C1-C10-N2	-0.1(4)
N5-Zn1-N1-C1	-179.4(2)	C10-N2-C11-C12	-110.5(3)
N7-Zn1-N1-C1	89.2(2)	Zn1-N2-C11-C12	68.8(3)
N4-Zn1-N2-C10	94.3(2)	C13-N3-C12-C11	133.8(3)
N6-Zn1-N2-C10	-165.0(2)	C25-N3-C12-C11	-82.1(3)
N5-Zn1-N2-C10	13.2(7)	N2-C11-C12-N3	-55.6(4)
N7-Zn1-N2-C10	-88.9(2)	C12-N3-C13-C14	-85.6(3)
N1-Zn1-N2-C10	1.5(2)	C25-N3-C13-C14	130.6(3)
N4-Zn1-N2-C11	-85.0(2)	C15-N4-C14-C13	-103.6(3)
N6-Zn1-N2-C11	15.7(2)	Zn1-N4-C14-C13	72.4(3)
N5-Zn1-N2-C11	-166.2(5)	N3-C13-C14-N4	-53.7(4)
N7-Zn1-N2-C11	91.8(2)	C14-N4-C15-C16	179.1(3)
N1-Zn1-N2-C11	-177.8(3)	Zn1-N4-C15-C16	2.8(4)
N6-Zn1-N4-C15	85.5(2)	C24-N5-C16-C17	-1.8(5)
N2-Zn1-N4-C15	-175.1(2)	Zn1-N5-C16-C17	171.3(3)

N5-Zn1-N4-C15	-5.5(2)	C24-N5-C16-C15	178.4(3)
N7-Zn1-N4-C15	19.5(6)	Zn1-N5-C16-C15	-8.4(3)
N1-Zn1-N4-C15	-98.1(2)	N4-C15-C16-C17	-175.6(3)
N6-Zn1-N4-C14	-90.6(2)	N4-C15-C16-N5	4.2(4)
N2-Zn1-N4-C14	8.9(3)	N5-C16-C17-C18	1.1(5)
N5-Zn1-N4-C14	178.4(3)	C15-C16-C17-C18	-179.2(3)
N7-Zn1-N4-C14	-156.6(4)	C16-C17-C18-C19	179.3(3)
N1-Zn1-N4-C14	85.8(2)	C16-C17-C18-C23	0.8(5)
N4-Zn1-N5-C24	179.6(3)	C17-C18-C19-C20	-176.8(3)
N6-Zn1-N5-C24	81.3(3)	C23-C18-C19-C20	1.7(5)
N2-Zn1-N5-C24	-96.9(6)	C18-C19-C20-C21	-1.0(6)
N7-Zn1-N5-C24	5.1(3)	C19-C20-C21-C22	-0.8(6)
N1-Zn1-N5-C24	-85.6(3)	C20-C21-C22-C23	1.8(5)
N4-Zn1-N5-C16	7.5(2)	C21-C22-C23-C24	178.7(3)
N6-Zn1-N5-C16	-90.9(2)	C21-C22-C23-C18	-1.1(5)
N2-Zn1-N5-C16	91.0(6)	C19-C18-C23-C22	-0.7(5)
N7-Zn1-N5-C16	-167.0(2)	C17-C18-C23-C22	177.9(3)
N1-Zn1-N5-C16	102.3(2)	C19-C18-C23-C24	179.6(3)
N4-Zn1-N6-C27	-172.7(2)	C17-C18-C23-C24	-1.8(4)
N2-Zn1-N6-C27	84.0(2)	C16-N5-C24-C23	0.7(5)
N5-Zn1-N6-C27	-95.6(2)	Zn1-N5-C24-C23	-171.0(2)
N7-Zn1-N6-C27	-5.0(2)	C22-C23-C24-N5	-178.6(3)
N1-Zn1-N6-C27	21.3(5)	C18-C23-C24-N5	1.1(5)
N4-Zn1-N6-C26	11.3(3)	C12-N3-C25-C26	131.3(3)
N2-Zn1-N6-C26	-91.9(2)	C13-N3-C25-C26	-84.8(3)
N5-Zn1-N6-C26	88.4(2)	C27-N6-C26-C25	-104.4(3)
N7-Zn1-N6-C26	179.1(3)	Zn1-N6-C26-C25	71.4(3)
N1-Zn1-N6-C26	-154.6(3)	N3-C25-C26-N6	-54.1(4)
N4-Zn1-N7-C36	-113.4(5)	C26-N6-C27-C28	176.9(3)
N6-Zn1-N7-C36	178.2(3)	Zn1-N6-C27-C28	0.7(4)
N2-Zn1-N7-C36	80.9(3)	C36-N7-C28-C29	-3.8(5)
N5-Zn1-N7-C36	-89.0(3)	Zn1-N7-C28-C29	167.1(3)
N1-Zn1-N7-C36	4.7(3)	C36-N7-C28-C27	178.3(3)
N4-Zn1-N7-C28	76.9(5)	Zn1-N7-C28-C27	-10.9(3)
N6-Zn1-N7-C28	8.5(2)	N6-C27-C28-C29	-170.7(3)
N2-Zn1-N7-C28	-88.8(2)	N6-C27-C28-N7	7.3(4)
N5-Zn1-N7-C28	101.3(2)	N7-C28-C29-C30	0.7(5)
N1-Zn1-N7-C28	-165.0(2)	C27-C28-C29-C30	178.5(3)
C9-N1-C1-C2	-0.5(4)	C28-C29-C30-C31	-176.1(3)
Zn1-N1-C1-C2	-178.5(2)	C28-C29-C30-C35	2.6(5)

C9-N1-C1-C10	179.3(3)	C35-C30-C31-C32	-0.6(5)
Zn1-N1-C1-C10	1.4(3)	C29-C30-C31-C32	178.2(4)
N1-C1-C2-C3	2.3(5)	C30-C31-C32-C33	1.1(6)
C10-C1-C2-C3	-177.5(3)	C31-C32-C33-C34	-0.3(6)
C1-C2-C3-C8	-2.3(5)	C32-C33-C34-C35	-0.9(6)
C1-C2-C3-C4	176.9(3)	C31-C30-C35-C34	-0.7(5)
C8-C3-C4-C5	0.3(5)	C29-C30-C35-C34	-179.5(3)
C2-C3-C4-C5	-178.9(3)	C31-C30-C35-C36	176.0(3)
C3-C4-C5-C6	0.0(6)	C29-C30-C35-C36	-2.9(5)
C4-C5-C6-C7	-0.5(6)	C33-C34-C35-C30	1.4(5)
C5-C6-C7-C8	0.7(5)	C33-C34-C35-C36	-175.1(3)
C2-C3-C8-C7	179.2(3)	C28-N7-C36-C35	3.5(5)
C4-C3-C8-C7	0.0(5)	Zn1-N7-C36-C35	-165.6(2)
C2-C3-C8-C9	0.7(4)	C30-C35-C36-N7	-0.1(5)
C4-C3-C8-C9	-178.5(3)	C34-C35-C36-N7	176.4(3)
C6-C7-C8-C3	-0.4(5)	C39-O9-C38-C37	169.6(4)
C6-C7-C8-C9	178.0(3)	C38-O9-C39-C40	-177.5(4)

4.5.4.5. Complex 4.20

Crystals grew as large, green prisms. The data crystal was cut from a larger crystal and had approximate dimensions; 0.31 x 0.22 x 0.17 mm. The data were collected on a Rigaku SCX-Mini diffractometer with a Mercury CCD using a graphite monochromator with MoK α radiation ($\lambda = 0.71075\text{\AA}$). A total of 540 frames of data were collected using ω -scans with a scan range of 1 $^\circ$ and a counting time of 4 seconds per frame. The data were collected at 153 K using a Rigaku Tech50 low temperature device. Details of crystal data, data collection and structure refinement are listed in Table 1. Data reduction were performed using the Rigaku Americas Corporation's Crystal Clear version 1.40. The structure was solved by direct methods using SIR97 and refined by full-matrix least-squares on F^2 with anisotropic displacement parameters for the non-H atoms using SHELXL-97. Structure analysis was aided by use of the programs PLATON98 and WinGX.

Table 4.26. Crystal data and structure refinement for **4.20**.

Empirical formula	C ₂₄ H ₂₇ Cl ₂ Cu N ₇ O ₈
Formula weight	675.97
Temperature	153(2) K
Wavelength	0.71075 Å
Crystal system	Monoclinic
Space group	C2/c
Unit cell dimensions	a = 28.163(5) Å α = 90°.
b = 10.466(2) Å	β = 101.738(9)°.
c = 19.200(4) Å	γ = 90°.
Volume	5540.9(18) Å ³
Z	8
Density (calculated)	1.621 Mg/m ³
Absorption coefficient	1.043 mm ⁻¹
F(000)	2776
Crystal size	0.31 x 0.22 x 0.17 mm
Theta range for data collection	3.11 to 27.48°.
Index ranges	-36 ≤ h ≤ 36, -13 ≤ k ≤ 13, -24 ≤ l ≤ 24
Reflections collected	28766
Independent reflections	6355 [R(int) = 0.0323]
Completeness to theta = 27.48°	99.8 %
Absorption correction	Semi-empirical from equivalents
Max. and min. transmission	1.00 and 0.806
Refinement method	Full-matrix least-squares on F ²
Data / restraints / parameters	6355 / 0 / 379
Goodness-of-fit on F ²	1.237
Final R indices [I > 2σ(I)]	R1 = 0.0355, wR2 = 0.0906
R indices (all data)	R1 = 0.0409, wR2 = 0.0932
Largest diff. peak and hole	0.428 and -0.422 e.Å ⁻³

Table 4.27. Atomic coordinates ($\times 10^4$) and equivalent isotropic displacement parameters ($\text{\AA}^2 \times 10^3$) for **4.20**. $U(\text{eq})$ is defined as one third of the trace of the orthogonalized U^{ij} tensor.

	x	y	z	$U(\text{eq})$
Cu1	6362(1)	1576(1)	7322(1)	23(1)
Cl1	5263(1)	-2831(1)	6154(1)	29(1)
Cl2	7071(1)	4937(1)	9918(1)	32(1)
O1	5224(1)	-3311(2)	6843(1)	55(1)
O2	5736(1)	-2294(2)	6188(1)	52(1)
O3	4912(1)	-1833(2)	5968(1)	53(1)
O4	5176(1)	-3824(2)	5632(1)	56(1)
O5	6896(1)	4908(2)	9158(1)	47(1)
O6	6748(1)	4234(2)	10258(1)	62(1)
O7	7549(1)	4407(2)	10091(1)	55(1)
O8	7081(1)	6237(2)	10162(1)	55(1)
N1	6114(1)	2544(2)	8320(1)	33(1)
N2	6156(1)	3417(2)	6995(1)	31(1)
N3	5836(1)	1941(2)	5747(1)	29(1)
N4	5690(1)	797(2)	7034(1)	23(1)
N5	6458(1)	-148(2)	7929(1)	23(1)
N6	7077(1)	2003(2)	7659(1)	27(1)
N7	6698(1)	792(2)	6449(1)	29(1)
C1	6085(1)	2133(2)	8966(1)	37(1)
C2	5842(1)	2795(3)	9414(1)	41(1)
C3	5616(1)	3922(3)	9176(1)	41(1)
C4	5643(1)	4372(2)	8510(1)	37(1)
C5	5901(1)	3664(2)	8099(1)	31(1)
C6	5960(1)	4116(2)	7400(1)	35(1)
C7	6200(1)	3918(2)	6292(1)	38(1)
C8	5809(1)	3325(2)	5717(1)	36(1)
C9	5390(1)	1265(2)	5768(1)	31(1)
C10	5277(1)	1314(2)	6514(1)	29(1)
C11	5640(1)	-283(2)	7313(1)	24(1)

C12	6043(1)	-834(2)	7825(1)	23(1)
C13	5994(1)	-1950(2)	8188(1)	28(1)
C14	6386(1)	-2373(2)	8697(1)	32(1)
C15	6811(1)	-1669(2)	8813(1)	32(1)
C16	6834(1)	-568(2)	8416(1)	29(1)
C17	6157(1)	1347(2)	5339(1)	33(1)
C18	6455(1)	280(2)	5759(1)	33(1)
C19	7154(1)	904(2)	6592(1)	31(1)
C20	7384(1)	1496(2)	7275(1)	28(1)
C21	7881(1)	1524(2)	7514(1)	38(1)
C22	8071(1)	2086(2)	8163(2)	43(1)
C23	7759(1)	2603(2)	8552(1)	39(1)
C24	7264(1)	2551(2)	8283(1)	33(1)

Table 4.28. Bond lengths [Å] and angles [°] for **4.20**.

Cu1-N4	2.0316(17)	C23-C24	1.387(3)	C8-C7-H7A	109.7
Cu1-N6	2.0368(17)	C23-H23	0.95	N2-C7-H7B	109.7
Cu1-N2	2.0721(19)	C24-H24	0.95	C8-C7-H7B	109.7
Cu1-N5	2.1349(17)	N4-Cu1-N6	168.93(7)	H7A-C7-H7B	108.2
Cu1-N7	2.2420(18)	N4-Cu1-N2	95.92(7)	N3-C8-C7	110.75(19)
Cu1-N1	2.3936(19)	N6-Cu1-N2	95.12(7)	N3-C8-H8A	109.5
C11-O4	1.4299(18)	N4-Cu1-N5	79.47(6)	C7-C8-H8A	109.5
C11-O3	1.4321(19)	N6-Cu1-N5	90.27(7)	N3-C8-H8B	109.5
C11-O2	1.4342(17)	N2-Cu1-N5	161.41(7)	C7-C8-H8B	109.5
C11-O1	1.4396(19)	N4-Cu1-N7	99.32(7)	H8A-C8-H8B	108.1
C12-O6	1.427(2)	N6-Cu1-N7	77.12(7)	N3-C9-C10	110.80(18)
C12-O7	1.430(2)	N2-Cu1-N7	104.35(7)	N3-C9-H9A	109.5
C12-O8	1.437(2)	N5-Cu1-N7	94.19(6)	C10-C9-H9A	109.5
C12-O5	1.4427(18)	N4-Cu1-N1	88.85(6)	N3-C9-H9B	109.5
N1-C1	1.332(3)	N6-Cu1-N1	94.78(7)	C10-C9-H9B	109.5
N1-C5	1.346(3)	N2-Cu1-N1	74.94(7)	H9A-C9-H9B	108.1
N2-C6	1.273(3)	N5-Cu1-N1	86.90(7)	N4-C10-C9	109.80(17)
N2-C7	1.475(3)	N7-Cu1-N1	171.82(6)	N4-C10-H10A	109.7
N3-C9	1.449(3)	O4-C11-O3	110.17(13)	C9-C10-H10A	109.7
N3-C8	1.451(3)	O4-C11-O2	110.00(12)	N4-C10-H10B	109.7

N3-C17	1.451(3)	O3-C11-O2	108.27(13)	C9-C10-H10B	109.7
N4-C11	1.271(3)	O4-C11-O1	110.77(12)	H10A-C10-H10B	108.2
N4-C10	1.472(2)	O3-C11-O1	107.78(13)	N4-C11-C12	119.84(18)
N5-C16	1.337(3)	O2-C11-O1	109.80(12)	N4-C11-H11	120.1
N5-C12	1.350(3)	O6-C12-O7	110.49(13)	C12-C11-H11	120.1
N6-C24	1.335(3)	O6-C12-O8	108.02(14)	N5-C12-C13	123.23(18)
N6-C20	1.354(3)	O7-C12-O8	109.77(13)	N5-C12-C11	114.86(17)
N7-C19	1.263(3)	O6-C12-O5	109.42(12)	C13-C12-C11	121.88(18)
N7-C18	1.463(3)	O7-C12-O5	109.88(12)	C12-C13-C14	118.4(2)
C1-C2	1.388(3)	O8-C12-O5	109.22(12)	C12-C13-H13	120.8
C1-H1	0.95	C1-N1-C5	117.8(2)	C14-C13-H13	120.8
C2-C3	1.374(4)	C1-N1-Cu1	133.83(16)	C15-C14-C13	118.8(2)
C2-H2	0.95	C5-N1-Cu1	107.48(14)	C15-C14-H14	120.6
C3-C4	1.379(4)	C6-N2-C7	118.7(2)	C13-C14-H14	120.6
C3-H3	0.95	C6-N2-Cu1	118.60(16)	C14-C15-C16	119.2(2)
C4-C5	1.390(3)	C7-N2-Cu1	122.54(15)	C14-C15-H15	120.4
C4-H4	0.95	C9-N3-C8	116.83(18)	C16-C15-H15	120.4
C5-C6	1.465(3)	C9-N3-C17	116.36(18)	N5-C16-C15	122.5(2)
C6-H6	0.95	C8-N3-C17	116.04(18)	N5-C16-H16	118.8
C7-C8	1.523(3)	C11-N4-C10	118.30(17)	C15-C16-H16	118.8
C7-H7A	0.99	C11-N4-Cu1	114.72(13)	N3-C17-C18	111.39(18)
C7-H7B	0.99	C10-N4-Cu1	126.86(13)	N3-C17-H17A	109.3
C8-H8A	0.99	C16-N5-C12	117.85(18)	C18-C17-H17A	109.3
C8-H8B	0.99	C16-N5-Cu1	130.84(14)	N3-C17-H17B	109.3
C9-C10	1.529(3)	C12-N5-Cu1	111.02(13)	C18-C17-H17B	109.3
C9-H9A	0.99	C24-N6-C20	118.58(19)	H17A-C17-H17B	108
C9-H9B	0.99	C24-N6-Cu1	124.28(15)	N7-C18-C17	108.45(18)
C10-H10A	0.99	C20-N6-Cu1	116.14(14)	N7-C18-H18A	110
C10-H10B	0.99	C19-N7-C18	119.96(19)	C17-C18-H18A	110
C11-C12	1.460(3)	C19-N7-Cu1	111.63(15)	N7-C18-H18B	110
C11-H11	0.95	C18-N7-Cu1	128.28(14)	C17-C18-H18B	110
C12-C13	1.383(3)	N1-C1-C2	123.2(2)	H18A-C18-H18B	108.4
C13-C14	1.390(3)	N1-C1-H1	118.4	N7-C19-C20	118.4(2)
C13-H13	0.95	C2-C1-H1	118.4	N7-C19-H19	120.8
C14-C15	1.384(3)	C3-C2-C1	118.4(2)	C20-C19-H19	120.8
C14-H14	0.95	C3-C2-H2	120.8	N6-C20-C21	121.8(2)
C15-C16	1.391(3)	C1-C2-H2	120.8	N6-C20-C19	115.81(18)
C15-H15	0.95	C2-C3-C4	119.5(2)	C21-C20-C19	122.4(2)
C16-H16	0.95	C2-C3-H3	120.3	C20-C21-C22	119.2(2)
C17-C18	1.525(3)	C4-C3-H3	120.3	C20-C21-H21	120.4

C17-H17A	0.99	C3-C4-C5	118.6(2)	C22-C21-H21	120.4
C17-H17B	0.99	C3-C4-H4	120.7	C23-C22-C21	119.0(2)
C18-H18A	0.99	C5-C4-H4	120.7	C23-C22-H22	120.5
C18-H18B	0.99	N1-C5-C4	122.4(2)	C21-C22-H22	120.5
C19-C20	1.475(3)	N1-C5-C6	116.33(19)	C22-C23-C24	119.2(2)
C19-H19	0.95	C4-C5-C6	121.2(2)	C22-C23-H23	120.4
C20-C21	1.382(3)	N2-C6-C5	121.2(2)	C24-C23-H23	120.4
C21-C22	1.383(4)	N2-C6-H6	119.4	N6-C24-C23	122.3(2)
C21-H21	0.95	C5-C6-H6	119.4	N6-C24-H24	118.9
C22-C23	1.374(4)	N2-C7-C8	109.70(19)	C23-C24-H24	118.9
C22-H22	0.95	N2-C7-H7A	109.7		

Table 4.29. Anisotropic displacement parameters ($\text{\AA}^2 \times 10^3$) for **4.20**. The anisotropic displacement factor exponent takes the form: $-2\pi^2 [h^2 a^{*2} U^{11} + \dots + 2 h k a^* b^* U^{12}]$

	U ¹¹	U ²²	U ³³	U ²³	U ¹³	U ¹²
Cu1	20(1)	24(1)	24(1)	2(1)	5(1)	2(1)
Cl1	28(1)	32(1)	26(1)	0(1)	1(1)	-3(1)
Cl2	32(1)	33(1)	30(1)	1(1)	4(1)	-2(1)
O1	75(1)	53(1)	32(1)	12(1)	1(1)	-13(1)
O2	30(1)	66(1)	62(1)	-18(1)	14(1)	-15(1)
O3	42(1)	64(1)	49(1)	10(1)	3(1)	16(1)
O4	68(1)	51(1)	47(1)	-22(1)	10(1)	-18(1)
O5	55(1)	56(1)	29(1)	-1(1)	6(1)	5(1)
O6	57(1)	76(2)	53(1)	18(1)	14(1)	-17(1)
O7	41(1)	66(1)	56(1)	-3(1)	3(1)	13(1)
O8	60(1)	42(1)	57(1)	-13(1)	-2(1)	3(1)
N1	28(1)	32(1)	38(1)	-9(1)	7(1)	0(1)
N2	29(1)	32(1)	33(1)	-2(1)	5(1)	-2(1)
N3	31(1)	30(1)	27(1)	5(1)	6(1)	5(1)
N4	22(1)	26(1)	21(1)	0(1)	4(1)	3(1)
N5	25(1)	24(1)	21(1)	-2(1)	6(1)	-1(1)
N6	24(1)	25(1)	32(1)	4(1)	6(1)	-1(1)

N7	28(1)	29(1)	31(1)	5(1)	7(1)	4(1)
C1	32(1)	42(1)	36(1)	-4(1)	4(1)	-2(1)
C2	35(1)	55(2)	35(1)	-13(1)	8(1)	-13(1)
C3	33(1)	45(1)	49(1)	-24(1)	16(1)	-9(1)
C4	28(1)	32(1)	54(2)	-17(1)	12(1)	-2(1)
C5	26(1)	30(1)	38(1)	-12(1)	6(1)	-2(1)
C6	32(1)	28(1)	44(1)	-4(1)	7(1)	0(1)
C7	44(1)	33(1)	40(1)	4(1)	12(1)	-2(1)
C8	43(1)	30(1)	33(1)	9(1)	5(1)	5(1)
C9	28(1)	37(1)	25(1)	6(1)	0(1)	3(1)
C10	22(1)	36(1)	29(1)	5(1)	2(1)	4(1)
C11	22(1)	30(1)	22(1)	-2(1)	6(1)	-3(1)
C12	24(1)	25(1)	20(1)	-2(1)	7(1)	-1(1)
C13	32(1)	29(1)	25(1)	1(1)	7(1)	-4(1)
C14	42(1)	31(1)	24(1)	5(1)	8(1)	2(1)
C15	35(1)	35(1)	23(1)	0(1)	-2(1)	6(1)
C16	26(1)	32(1)	28(1)	-4(1)	2(1)	-2(1)
C17	36(1)	40(1)	24(1)	4(1)	7(1)	2(1)
C18	33(1)	34(1)	33(1)	-1(1)	7(1)	4(1)
C19	30(1)	30(1)	36(1)	3(1)	12(1)	3(1)
C20	24(1)	24(1)	38(1)	8(1)	10(1)	0(1)
C21	26(1)	37(1)	53(2)	9(1)	11(1)	1(1)
C22	26(1)	37(1)	60(2)	10(1)	-3(1)	-5(1)
C23	38(1)	29(1)	45(1)	4(1)	-5(1)	-7(1)
C24	33(1)	27(1)	39(1)	1(1)	6(1)	-3(1)

Table 4.30 Hydrogen coordinates ($\times 10^4$) and isotropic displacement parameters ($\text{\AA}^2 \times 10^3$) for **4.20**.

	x	y	z	U(eq)
H1	6237	1347	9129	44
H2	5833	2477	9875	50

H3	5441	4387	9467	49
H4	5489	5150	8336	45
H6	5851	4948	7246	41
H7A	6524	3711	6200	46
H7B	6163	4858	6286	46
H8A	5486	3607	5782	43
H8B	5852	3621	5244	43
H9A	5421	363	5627	37
H9B	5119	1655	5423	37
H10A	5216	2208	6638	35
H10B	4982	807	6525	35
H11	5342	-732	7189	29
H13	5698	-2418	8092	34
H14	6363	-3131	8960	38
H15	7083	-1935	9160	38
H16	7128	-96	8494	35
H17A	6378	2000	5210	39
H17B	5962	992	4893	39
H18A	6240	-438	5829	40
H18B	6698	-42	5496	40
H19	7345	614	6268	38
H21	8090	1162	7236	46
H22	8412	2114	8338	51
H23	7882	2991	9000	47
H24	7050	2918	8551	40

Table 4.31. Torsion angles [°] for **4.20**.

N4-Cu1-N1-C1	82.6(2)	N1-C1-C2-C3	0.9(4)
N6-Cu1-N1-C1	-86.9(2)	C1-C2-C3-C4	-1.2(3)
N2-Cu1-N1-C1	179.0(2)	C2-C3-C4-C5	0.1(3)
N5-Cu1-N1-C1	3.1(2)	C1-N1-C5-C4	-1.9(3)
N4-Cu1-N1-C5	-86.28(14)	Cu1-N1-C5-C4	169.03(17)

N6-Cu1-N1-C5	104.19(14)	C1-N1-C5-C6	177.10(19)
N2-Cu1-N1-C5	10.16(14)	Cu1-N1-C5-C6	-12.0(2)
N5-Cu1-N1-C5	-165.80(14)	C3-C4-C5-N1	1.5(3)
N4-Cu1-N2-C6	80.21(17)	C3-C4-C5-C6	-177.4(2)
N6-Cu1-N2-C6	-100.58(18)	C7-N2-C6-C5	179.05(19)
N5-Cu1-N2-C6	5.8(3)	Cu1-N2-C6-C5	2.9(3)
N7-Cu1-N2-C6	-178.56(17)	N1-C5-C6-N2	7.6(3)
N1-Cu1-N2-C6	-6.99(16)	C4-C5-C6-N2	-173.4(2)
N4-Cu1-N2-C7	-95.76(17)	C6-N2-C7-C8	-102.4(2)
N6-Cu1-N2-C7	83.45(17)	Cu1-N2-C7-C8	73.6(2)
N5-Cu1-N2-C7	-170.21(19)	C9-N3-C8-C7	128.6(2)
N7-Cu1-N2-C7	5.47(18)	C17-N3-C8-C7	-88.2(2)
N1-Cu1-N2-C7	177.04(18)	N2-C7-C8-N3	-55.6(3)
N6-Cu1-N4-C11	21.1(4)	C8-N3-C9-C10	-77.9(2)
N2-Cu1-N4-C11	-163.03(14)	C17-N3-C9-C10	139.03(19)
N5-Cu1-N4-C11	-1.23(14)	C11-N4-C10-C9	-108.7(2)
N7-Cu1-N4-C11	91.34(15)	Cu1-N4-C10-C9	67.0(2)
N1-Cu1-N4-C11	-88.29(15)	N3-C9-C10-N4	-56.2(2)
N6-Cu1-N4-C10	-154.8(3)	C10-N4-C11-C12	179.22(17)
N2-Cu1-N4-C10	21.14(17)	Cu1-N4-C11-C12	3.0(2)
N5-Cu1-N4-C10	-177.07(17)	C16-N5-C12-C13	-1.0(3)
N7-Cu1-N4-C10	-84.49(16)	Cu1-N5-C12-C13	-175.59(16)
N1-Cu1-N4-C10	95.88(16)	C16-N5-C12-C11	176.90(17)
N4-Cu1-N5-C16	-174.36(19)	Cu1-N5-C12-C11	2.3(2)
N6-Cu1-N5-C16	9.82(18)	N4-C11-C12-N5	-3.7(3)
N2-Cu1-N5-C16	-97.3(3)	N4-C11-C12-C13	174.26(19)
N7-Cu1-N5-C16	86.93(18)	N5-C12-C13-C14	1.5(3)
N1-Cu1-N5-C16	-84.96(18)	C11-C12-C13-C14	-176.29(19)
N4-Cu1-N5-C12	-0.73(13)	C12-C13-C14-C15	-0.7(3)
N6-Cu1-N5-C12	-176.55(13)	C13-C14-C15-C16	-0.4(3)
N2-Cu1-N5-C12	76.4(2)	C12-N5-C16-C15	-0.2(3)
N7-Cu1-N5-C12	-99.45(13)	Cu1-N5-C16-C15	173.07(15)
N1-Cu1-N5-C12	88.67(13)	C14-C15-C16-N5	0.9(3)
N4-Cu1-N6-C24	-104.1(4)	C9-N3-C17-C18	-79.8(2)
N2-Cu1-N6-C24	80.01(18)	C8-N3-C17-C18	136.8(2)
N5-Cu1-N6-C24	-82.17(18)	C19-N7-C18-C17	-112.5(2)
N7-Cu1-N6-C24	-176.41(18)	Cu1-N7-C18-C17	62.9(2)
N1-Cu1-N6-C24	4.74(18)	N3-C17-C18-N7	-53.0(2)
N4-Cu1-N6-C20	64.3(4)	C18-N7-C19-C20	176.36(18)
N2-Cu1-N6-C20	-111.64(15)	Cu1-N7-C19-C20	0.2(2)

N5-Cu1-N6-C20	86.18(15)	C24-N6-C20-C21	0.5(3)
N7-Cu1-N6-C20	-8.06(14)	Cu1-N6-C20-C21	-168.53(16)
N1-Cu1-N6-C20	173.09(15)	C24-N6-C20-C19	179.89(19)
N4-Cu1-N7-C19	-165.19(15)	Cu1-N6-C20-C19	10.8(2)
N6-Cu1-N7-C19	4.13(15)	N7-C19-C20-N6	-7.1(3)
N2-Cu1-N7-C19	96.19(16)	N7-C19-C20-C21	172.2(2)
N5-Cu1-N7-C19	-85.19(16)	N6-C20-C21-C22	-0.1(3)
N4-Cu1-N7-C18	19.05(18)	C19-C20-C21-C22	-179.4(2)
N6-Cu1-N7-C18	-171.63(19)	C20-C21-C22-C23	-0.1(4)
N2-Cu1-N7-C18	-79.57(18)	C21-C22-C23-C24	-0.2(4)
N5-Cu1-N7-C18	99.05(18)	C20-N6-C24-C23	-0.8(3)
C5-N1-C1-C2	0.7(3)	Cu1-N6-C24-C23	167.27(17)
Cu1-N1-C1-C2	-167.29(17)	C22-C23-C24-N6	0.7(4)

4.5.4.6. Complex 4.21

Crystals grew as very dark, red plates. The data crystal had approximate dimensions; 0.44 x 0.30 x 0.11 mm. The data were collected on a Rigaku SCX-Mini diffractometer with a Mercury CCD using a graphite monochromator with MoK α radiation ($\lambda = 0.71075\text{\AA}$). A total of 540 frames of data were collected using ω -scans with a scan range of 1° and a counting time of 55 seconds per frame. The data were collected at 153 K using a Rigaku Tech50 low temperature device. Details of crystal data, data collection and structure refinement are listed in Table 1. Data reduction were performed using the Rigaku Americas Corporation's Crystal Clear version 1.40. The structure was solved by direct methods using SIR97 and refined by full-matrix least-squares on F^2 with anisotropic displacement parameters for the non-H atoms using SHELXL-97. Structure analysis was aided by use of the programs PLATON98 and WinGX.

Table 4.32. Crystal data and structure refinement for **4.21**.

Empirical formula	C ₂₄ H ₂₇ Cl ₂ Fe N ₇ O ₈	
Formula weight	668.28	
Temperature	153(2) K	
Wavelength	0.71075 Å	
Crystal system	Monoclinic	
Space group	P21/c	
Unit cell dimensions	a = 10.575(2) Å	α = 90°.
	b = 15.754(3) Å	β = 94.993(5)°.
	c = 17.076(3) Å	γ = 90°.
Volume	2834.0(9) Å ³	
Z	4	
Density (calculated)	1.566 Mg/m ³	
Absorption coefficient	0.781 mm ⁻¹	
F(000)	1376	
Crystal size	0.44 x 0.30 x 0.11 mm	
Theta range for data collection	3.21 to 25.00°.	
Index ranges	-12 ≤ h ≤ 12, -18 ≤ k ≤ 18, -20 ≤ l ≤ 20	
Reflections collected	23764	
Independent reflections	4989 [R(int) = 0.0889]	
Completeness to theta = 25.00°	99.8 %	
Absorption correction	Semi-empirical from equivalents	
Max. and min. transmission	1.00 and 0.626	
Refinement method	Full-matrix least-squares on F ²	
Data / restraints / parameters	4989 / 0 / 379	
Goodness-of-fit on F ²	1.092	
Final R indices [I > 2σ(I)]	R1 = 0.0644, wR2 = 0.1764	
R indices (all data)	R1 = 0.0790, wR2 = 0.1916	
Largest diff. peak and hole	0.678 and -0.905 e.Å ⁻³	

Table 4.33. Atomic coordinates ($\times 10^4$) and equivalent isotropic displacement parameters ($\text{\AA}^2 \times 10^3$) for **4.21**. $U(\text{eq})$ is defined as one third of the trace of the orthogonalized U^{ij} tensor.

	x	y	z	$U(\text{eq})$
Fe1	7909(1)	6087(1)	7997(1)	32(1)
Cl1	7263(1)	3265(1)	6002(1)	53(1)
Cl2	3210(1)	4668(1)	8670(1)	41(1)
O1	7018(5)	2721(3)	5350(2)	86(2)
O2	7588(5)	4071(3)	5733(3)	95(2)
O3	6194(5)	3342(3)	6422(4)	99(2)
O4	8283(6)	2942(5)	6491(3)	131(3)
O5	3320(5)	4659(3)	7842(2)	75(1)
O6	3423(4)	5519(2)	8967(3)	69(1)
O7	4136(3)	4100(2)	9043(2)	51(1)
O8	1960(4)	4388(3)	8817(3)	73(1)
N1	7977(3)	4865(2)	8282(2)	33(1)
N2	6761(3)	6107(2)	8835(2)	34(1)
N3	8134(4)	7672(3)	9428(3)	48(1)
N4	7694(4)	7283(2)	7706(2)	40(1)
N5	6432(4)	5970(2)	7216(2)	39(1)
N6	9472(4)	6246(2)	8675(2)	37(1)
N7	9141(4)	5982(2)	7194(2)	37(1)
C1	8678(4)	4242(3)	7995(3)	38(1)
C2	8650(5)	3417(3)	8273(3)	42(1)
C3	7903(4)	3211(3)	8869(3)	38(1)
C4	7182(4)	3843(3)	9180(3)	36(1)
C5	7234(4)	4662(3)	8871(2)	32(1)
C6	6537(4)	5385(3)	9147(3)	35(1)
C7	6093(5)	6858(3)	9111(3)	43(1)
C8	6942(5)	7385(3)	9694(3)	50(1)
C9	8124(6)	8306(3)	8812(3)	52(1)
C10	8499(5)	7995(3)	8016(3)	45(1)
C11	6798(5)	7440(3)	7168(3)	47(1)

C12	6054(4)	6721(3)	6863(3)	43(1)
C13	5090(5)	6751(4)	6247(3)	56(2)
C14	4517(5)	6003(4)	5971(4)	60(2)
C15	4885(5)	5254(4)	6341(3)	55(1)
C16	5829(5)	5256(3)	6968(3)	46(1)
C17	9309(5)	7311(3)	9749(3)	49(1)
C18	9559(5)	6381(3)	9536(3)	46(1)
C19	10519(4)	6192(3)	8335(3)	42(1)
C20	10376(4)	6065(3)	7491(3)	40(1)
C21	11373(5)	6034(3)	7016(3)	49(1)
C22	11103(6)	5899(3)	6213(4)	57(2)
C23	9864(6)	5803(3)	5906(3)	51(1)
C24	8902(5)	5847(3)	6414(3)	43(1)

Table 4.34. Bond lengths [\AA] and angles [$^\circ$] for **4.21**.

Fe1-N6	1.950(4)	C23-C24	1.395(7)	C8-C7-H7A	109.2
Fe1-N2	1.956(4)	C23-H23	0.95	N2-C7-H7B	109.2
Fe1-N4	1.956(4)	C24-H24	0.95	C8-C7-H7B	109.2
Fe1-N5	1.973(4)	N6-Fe1-N2	96.41(16)	H7A-C7-H7B	107.9
Fe1-N7	1.980(4)	N6-Fe1-N4	95.80(17)	N3-C8-C7	116.3(4)
Fe1-N1	1.986(4)	N2-Fe1-N4	96.02(15)	N3-C8-H8A	108.2
C11-O3	1.397(5)	N6-Fe1-N5	173.71(15)	C7-C8-H8A	108.2
C11-O4	1.401(5)	N2-Fe1-N5	89.51(16)	N3-C8-H8B	108.2
C11-O2	1.402(5)	N4-Fe1-N5	81.41(17)	C7-C8-H8B	108.2
C11-O1	1.412(4)	N6-Fe1-N7	81.18(16)	H8A-C8-H8B	107.4
C12-O5	1.428(4)	N2-Fe1-N7	175.12(15)	N3-C9-C10	116.0(4)
C12-O7	1.435(4)	N4-Fe1-N7	88.47(15)	N3-C9-H9A	108.3
C12-O8	1.436(4)	N5-Fe1-N7	93.08(16)	C10-C9-H9A	108.3
C12-O6	1.444(4)	N6-Fe1-N1	88.18(15)	N3-C9-H9B	108.3
N1-C1	1.347(6)	N2-Fe1-N1	81.28(14)	C10-C9-H9B	108.3
N1-C5	1.369(6)	N4-Fe1-N1	175.44(16)	H9A-C9-H9B	107.4
N2-C6	1.287(5)	N5-Fe1-N1	94.85(16)	N4-C10-C9	112.1(4)
N2-C7	1.476(5)	N7-Fe1-N1	94.36(15)	N4-C10-H10A	109.2
N3-C17	1.432(7)	O3-C11-O4	109.9(4)	C9-C10-H10A	109.2
N3-C8	1.448(6)	O3-C11-O2	108.8(3)	N4-C10-H10B	109.2

N3-C9	1.450(6)	O4-C11-O2	109.0(4)	C9-C10-H10B	109.2
N4-C11	1.286(6)	O3-C11-O1	110.9(3)	H10A-C10-H10B	107.9
N4-C10	1.478(6)	O4-C11-O1	109.2(3)	N4-C11-C12	116.6(4)
N5-C16	1.343(6)	O2-C11-O1	109.0(3)	N4-C11-H11	121.7
N5-C12	1.370(6)	O5-C12-O7	108.8(3)	C12-C11-H11	121.7
N6-C19	1.296(6)	O5-C12-O8	109.0(3)	N5-C12-C13	121.7(5)
N6-C18	1.480(6)	O7-C12-O8	109.5(2)	N5-C12-C11	112.9(4)
N7-C24	1.351(6)	O5-C12-O6	109.5(3)	C13-C12-C11	125.4(5)
N7-C20	1.366(6)	O7-C12-O6	110.1(2)	C14-C13-C12	119.6(5)
C1-C2	1.385(6)	O8-C12-O6	110.0(3)	C14-C13-H13	120.2
C1-H1	0.95	C1-N1-C5	117.8(4)	C12-C13-H13	120.2
C2-C3	1.379(7)	C1-N1-Fe1	128.8(3)	C15-C14-C13	118.2(5)
C2-H2	0.95	C5-N1-Fe1	113.3(3)	C15-C14-H14	120.9
C3-C4	1.387(6)	C6-N2-C7	117.8(4)	C13-C14-H14	120.9
C3-H3	0.95	C6-N2-Fe1	115.9(3)	C14-C15-C16	120.3(6)
C4-C5	1.397(6)	C7-N2-Fe1	126.2(3)	C14-C15-H15	119.9
C4-H4	0.95	C17-N3-C8	120.4(4)	C16-C15-H15	119.9
C5-C6	1.456(6)	C17-N3-C9	120.1(4)	N5-C16-C15	122.0(5)
C6-H6	0.95	C8-N3-C9	119.4(4)	N5-C16-H16	119
C7-C8	1.526(7)	C11-N4-C10	118.3(4)	C15-C16-H16	119
C7-H7A	0.99	C11-N4-Fe1	115.5(4)	N3-C17-C18	116.7(4)
C7-H7B	0.99	C10-N4-Fe1	126.1(3)	N3-C17-H17A	108.1
C8-H8A	0.99	C16-N5-C12	118.2(4)	C18-C17-H17A	108.1
C8-H8B	0.99	C16-N5-Fe1	128.1(3)	N3-C17-H17B	108.1
C9-C10	1.529(7)	C12-N5-Fe1	113.6(3)	C18-C17-H17B	108.1
C9-H9A	0.99	C19-N6-C18	118.2(4)	H17A-C17-H17B	107.3
C9-H9B	0.99	C19-N6-Fe1	116.0(3)	N6-C18-C17	112.0(4)
C10-H10A	0.99	C18-N6-Fe1	125.7(3)	N6-C18-H18A	109.2
C10-H10B	0.99	C24-N7-C20	118.2(4)	C17-C18-H18A	109.2
C11-C12	1.451(7)	C24-N7-Fe1	128.2(3)	N6-C18-H18B	109.2
C11-H11	0.95	C20-N7-Fe1	113.6(3)	C17-C18-H18B	109.2
C12-C13	1.401(7)	N1-C1-C2	122.0(4)	H18A-C18-H18B	107.9
C13-C14	1.389(9)	N1-C1-H1	119	N6-C19-C20	115.8(4)
C13-H13	0.95	C2-C1-H1	119	N6-C19-H19	122.1
C14-C15	1.378(8)	C3-C2-C1	120.3(4)	C20-C19-H19	122.1
C14-H14	0.95	C3-C2-H2	119.9	N7-C20-C21	122.0(5)
C15-C16	1.399(7)	C1-C2-H2	119.9	N7-C20-C19	113.3(4)
C15-H15	0.95	C2-C3-C4	118.9(4)	C21-C20-C19	124.6(5)
C16-H16	0.95	C2-C3-H3	120.6	C20-C21-C22	118.7(5)
C17-C18	1.539(7)	C4-C3-H3	120.6	C20-C21-H21	120.6

C17-H17A	0.99	C3-C4-C5	118.5(4)	C22-C21-H21	120.6
C17-H17B	0.99	C3-C4-H4	120.8	C23-C22-C21	119.9(5)
C18-H18A	0.99	C5-C4-H4	120.8	C23-C22-H22	120.1
C18-H18B	0.99	N1-C5-C4	122.5(4)	C21-C22-H22	120.1
C19-C20	1.450(7)	N1-C5-C6	113.2(4)	C22-C23-C24	118.7(5)
C19-H19	0.95	C4-C5-C6	124.3(4)	C22-C23-H23	120.7
C20-C21	1.386(7)	N2-C6-C5	116.2(4)	C24-C23-H23	120.7
C21-C22	1.393(8)	N2-C6-H6	121.9	N7-C24-C23	122.4(5)
C21-H21	0.95	C5-C6-H6	121.9	N7-C24-H24	118.8
C22-C23	1.376(8)	N2-C7-C8	111.9(4)	C23-C24-H24	118.8
C22-H22	0.95	N2-C7-H7A	109.2		

Table 4.35. Anisotropic displacement parameters ($\text{\AA}^2 \times 10^3$) for **4.21**. The anisotropic displacement factor exponent takes the form: $-2\pi^2 [h^2 a^* U^{11} + \dots + 2 h k a^* b^* U^{12}]$

	U ¹¹	U ²²	U ³³	U ²³	U ¹³	U ¹²
Fe1	33(1)	28(1)	37(1)	4(1)	10(1)	3(1)
Cl1	58(1)	56(1)	45(1)	-15(1)	1(1)	13(1)
Cl2	43(1)	33(1)	49(1)	-3(1)	7(1)	-2(1)
O1	146(5)	62(3)	50(2)	-19(2)	3(3)	-1(3)
O2	110(4)	81(3)	99(4)	-39(3)	31(3)	-40(3)
O3	84(3)	72(3)	148(5)	-38(3)	55(3)	-7(3)
O4	118(5)	180(7)	87(4)	-25(4)	-36(3)	81(5)
O5	118(4)	61(3)	49(2)	11(2)	16(2)	-5(3)
O6	58(2)	41(2)	103(3)	-20(2)	-13(2)	6(2)
O7	50(2)	42(2)	59(2)	-5(2)	6(2)	7(2)
O8	47(2)	73(3)	99(3)	11(3)	17(2)	-8(2)
N1	35(2)	30(2)	34(2)	0(2)	6(2)	2(2)
N2	36(2)	27(2)	40(2)	0(2)	10(2)	6(2)
N3	59(3)	35(2)	51(3)	5(2)	17(2)	0(2)
N4	43(2)	32(2)	47(2)	9(2)	15(2)	4(2)
N5	37(2)	40(2)	42(2)	8(2)	12(2)	2(2)
N6	42(2)	29(2)	40(2)	2(2)	9(2)	1(2)

N7	40(2)	31(2)	43(2)	7(2)	12(2)	0(2)
C1	42(3)	32(2)	41(3)	2(2)	13(2)	8(2)
C2	51(3)	27(2)	50(3)	-1(2)	11(2)	8(2)
C3	47(3)	27(2)	39(3)	3(2)	6(2)	4(2)
C4	41(3)	31(2)	38(3)	4(2)	9(2)	-3(2)
C5	32(2)	31(2)	33(2)	1(2)	6(2)	-1(2)
C6	38(2)	31(2)	38(2)	4(2)	13(2)	4(2)
C7	47(3)	29(2)	57(3)	3(2)	25(2)	8(2)
C8	65(3)	34(3)	54(3)	1(2)	27(3)	6(2)
C9	65(3)	25(2)	68(4)	3(2)	16(3)	-2(2)
C10	45(3)	33(2)	58(3)	11(2)	13(2)	-1(2)
C11	44(3)	42(3)	56(3)	20(2)	12(2)	12(2)
C12	34(2)	45(3)	51(3)	12(2)	15(2)	6(2)
C13	39(3)	76(4)	55(3)	31(3)	10(2)	11(3)
C14	36(3)	87(5)	56(3)	23(3)	3(2)	-2(3)
C15	41(3)	68(4)	56(3)	5(3)	-1(2)	-9(3)
C16	41(3)	48(3)	51(3)	4(2)	10(2)	-3(2)
C17	63(3)	41(3)	44(3)	-5(2)	12(2)	-6(3)
C18	52(3)	46(3)	39(3)	0(2)	1(2)	1(2)
C19	34(3)	36(3)	57(3)	0(2)	7(2)	1(2)
C20	38(3)	31(2)	54(3)	5(2)	12(2)	-1(2)
C21	40(3)	45(3)	64(4)	8(3)	20(2)	3(2)
C22	61(4)	44(3)	73(4)	8(3)	42(3)	8(3)
C23	70(4)	39(3)	48(3)	2(2)	26(3)	5(3)
C24	50(3)	35(2)	45(3)	0(2)	15(2)	-2(2)

Table 4.36. Hydrogen coordinates ($\times 10^4$) and isotropic displacement parameters ($\text{\AA}^2 \times 10^3$) for **4.21**.

	x	y	z	U(eq)
H1	9207	4372	7589	45
H2	9147	2991	8053	51

H3	7883	2647	9062	45
H4	6665	3721	9594	44
H6	5952	5327	9535	42
H7A	5334	6671	9364	52
H7B	5803	7216	8653	52
H8A	6456	7890	9840	60
H8B	7130	7044	10177	60
H9A	8710	8769	8995	62
H9B	7261	8551	8735	62
H10A	8424	8470	7636	53
H10B	9397	7810	8072	53
H11	6631	8000	6980	56
H13	4830	7280	6019	67
H14	3888	6007	5538	72
H15	4497	4735	6169	67
H16	6049	4736	7227	55
H17A	9343	7355	10329	59
H17B	10009	7662	9576	59
H18A	10416	6215	9764	55
H18B	8934	6012	9769	55
H19	11328	6234	8621	50
H21	12224	6104	7234	59
H22	11772	5874	5877	69
H23	9668	5708	5360	62
H24	8046	5780	6203	51

Table 4.37. Torsion angles [°] for **4.21**.

N6-Fe1-N1-C1	-80.0(4)	Fe1-N1-C5-C4	-177.6(3)
N2-Fe1-N1-C1	-176.7(4)	C1-N1-C5-C6	178.9(4)
N5-Fe1-N1-C1	94.5(4)	Fe1-N1-C5-C6	1.2(5)
N7-Fe1-N1-C1	1.0(4)	C3-C4-C5-N1	-0.7(7)
N6-Fe1-N1-C5	97.3(3)	C3-C4-C5-C6	-179.4(4)

N2-Fe1-N1-C5	0.6(3)	C7-N2-C6-C5	-178.8(4)
N5-Fe1-N1-C5	-88.2(3)	Fe1-N2-C6-C5	4.0(5)
N7-Fe1-N1-C5	178.3(3)	N1-C5-C6-N2	-3.4(6)
N6-Fe1-N2-C6	-89.7(4)	C4-C5-C6-N2	175.3(4)
N4-Fe1-N2-C6	173.7(4)	C6-N2-C7-C8	100.9(5)
N5-Fe1-N2-C6	92.4(4)	Fe1-N2-C7-C8	-82.2(5)
N1-Fe1-N2-C6	-2.6(3)	C17-N3-C8-C7	-109.0(5)
N6-Fe1-N2-C7	93.4(4)	C9-N3-C8-C7	68.7(6)
N4-Fe1-N2-C7	-3.2(4)	N2-C7-C8-N3	55.7(6)
N5-Fe1-N2-C7	-84.5(4)	C17-N3-C9-C10	68.1(6)
N1-Fe1-N2-C7	-179.5(4)	C8-N3-C9-C10	-109.6(5)
N6-Fe1-N4-C11	172.4(3)	C11-N4-C10-C9	101.5(5)
N2-Fe1-N4-C11	-90.6(4)	Fe1-N4-C10-C9	-81.9(5)
N5-Fe1-N4-C11	-2.0(3)	N3-C9-C10-N4	56.4(6)
N7-Fe1-N4-C11	91.4(4)	C10-N4-C11-C12	178.2(4)
N6-Fe1-N4-C10	-4.4(4)	Fe1-N4-C11-C12	1.3(6)
N2-Fe1-N4-C10	92.7(4)	C16-N5-C12-C13	-1.7(7)
N5-Fe1-N4-C10	-178.7(4)	Fe1-N5-C12-C13	174.6(4)
N7-Fe1-N4-C10	-85.3(4)	C16-N5-C12-C11	-178.5(4)
N2-Fe1-N5-C16	-85.7(4)	Fe1-N5-C12-C11	-2.3(5)
N4-Fe1-N5-C16	178.1(4)	N4-C11-C12-N5	0.7(6)
N7-Fe1-N5-C16	90.1(4)	N4-C11-C12-C13	-176.0(5)
N1-Fe1-N5-C16	-4.5(4)	N5-C12-C13-C14	-1.5(8)
N2-Fe1-N5-C12	98.5(3)	C11-C12-C13-C14	175.0(5)
N4-Fe1-N5-C12	2.3(3)	C12-C13-C14-C15	2.8(8)
N7-Fe1-N5-C12	-85.7(3)	C13-C14-C15-C16	-1.1(8)
N1-Fe1-N5-C12	179.7(3)	C12-N5-C16-C15	3.5(7)
N2-Fe1-N6-C19	174.0(3)	Fe1-N5-C16-C15	-172.2(4)
N4-Fe1-N6-C19	-89.3(3)	C14-C15-C16-N5	-2.1(8)
N7-Fe1-N6-C19	-1.8(3)	C8-N3-C17-C18	68.9(6)
N1-Fe1-N6-C19	92.9(3)	C9-N3-C17-C18	-108.8(5)
N2-Fe1-N6-C18	-3.1(4)	C19-N6-C18-C17	101.5(5)
N4-Fe1-N6-C18	93.6(4)	Fe1-N6-C18-C17	-81.5(5)
N7-Fe1-N6-C18	-178.8(4)	N3-C17-C18-N6	55.5(6)
N1-Fe1-N6-C18	-84.1(4)	C18-N6-C19-C20	-179.6(4)
N6-Fe1-N7-C24	-179.5(4)	Fe1-N6-C19-C20	3.0(5)
N4-Fe1-N7-C24	-83.4(4)	C24-N7-C20-C21	1.5(6)
N5-Fe1-N7-C24	-2.1(4)	Fe1-N7-C20-C21	-178.1(4)
N1-Fe1-N7-C24	93.0(4)	C24-N7-C20-C19	-179.0(4)
N6-Fe1-N7-C20	0.1(3)	Fe1-N7-C20-C19	1.4(5)

N4-Fe1-N7-C20	96.2(3)	N6-C19-C20-N7	-2.9(6)
N5-Fe1-N7-C20	177.5(3)	N6-C19-C20-C21	176.6(4)
N1-Fe1-N7-C20	-87.4(3)	N7-C20-C21-C22	-1.1(7)
C5-N1-C1-C2	0.7(7)	C19-C20-C21-C22	179.3(5)
Fe1-N1-C1-C2	177.9(4)	C20-C21-C22-C23	0.3(7)
N1-C1-C2-C3	-0.8(8)	C21-C22-C23-C24	0.3(8)
C1-C2-C3-C4	0.2(7)	C20-N7-C24-C23	-0.9(7)
C2-C3-C4-C5	0.6(7)	Fe1-N7-C24-C23	178.6(3)
C1-N1-C5-C4	0.1(6)	C22-C23-C24-N7	0.1(7)

4.5.4.7. Complex 4.23

Crystals grew as colorless prisms. The data crystal was cut from a larger crystal and had approximate dimensions; 0.08 x 0.07 x 0.05 mm. The data were collected on a Rigaku AFC12 diffractometer with a Saturn 724+ CCD using a graphite monochromator with MoK α radiation ($\lambda = 0.71073\text{\AA}$). A total of 1460 frames of data were collected using ω -scans with a scan range of 0.5° and a counting time of 50 seconds per frame. The data were collected at 100 K using a Rigaku XStream low temperature device. Details of crystal data, data collection and structure refinement are listed in Table 1. Data reduction were performed using the Rigaku Americas Corporation's Crystal Clear version 1.40. The structure was solved by direct methods using SIR97 and refined by full-matrix least-squares on F^2 with anisotropic displacement parameters for the non-H atoms using SHELXL-97. Structure analysis was aided by use of the programs PLATON98 and WinGX.

Table 4.38. Crystal data and structure refinement for **4.23**.

Empirical formula	C ₂₉ H ₃₃ F ₆ N ₇ O ₆ S ₂ Zn
Formula weight	819.11
Temperature	100(2) K

Wavelength	0.71075 Å	
Crystal system	Monoclinic	
Space group	P21/n	
Unit cell dimensions	a = 10.8520(15) Å	$\alpha = 90^\circ$.
	b = 10.1814(14) Å	$\beta = 98.631(3)^\circ$.
	c = 31.260(3) Å	$\gamma = 90^\circ$.
Volume	3414.8(7) Å ³	
Z	4	
Density (calculated)	1.593 Mg/m ³	
Absorption coefficient	0.928 mm ⁻¹	
F(000)	1680	
Crystal size	0.08 x 0.07 x 0.05 mm	
Theta range for data collection	3.18 to 25.03°.	
Index ranges	-12 ≤ h ≤ 12, -12 ≤ k ≤ 12, -37 ≤ l ≤ 37	
Reflections collected	40218	
Independent reflections	6017 [R(int) = 0.0929]	
Completeness to theta = 25.03°	99.8 %	
Absorption correction	Semi-empirical from equivalents	
Max. and min. transmission	1.00 and 0.699	
Refinement method	Full-matrix least-squares on F ²	
Data / restraints / parameters	6017 / 103 / 463	
Goodness-of-fit on F ²	1.178	
Final R indices [I > 2σ(I)]	R1 = 0.0669, wR2 = 0.1546	
R indices (all data)	R1 = 0.0934, wR2 = 0.1676	
Largest diff. peak and hole	1.013 and -0.932 e.Å ⁻³	

Table 4.39. Atomic coordinates (x 10⁴) and equivalent isotropic displacement parameters (Å²x 10³) for **4.23**. U(eq) is defined as one third of the trace of the orthogonalized U^{ij} tensor.

	x	y	z	U(eq)
Zn1	2518(1)	7245(1)	6081(1)	19(1)
N1	843(4)	8370(4)	6238(1)	22(1)

N2	1092(4)	5825(4)	6037(1)	23(1)
N3	3346(4)	4302(4)	6580(1)	22(1)
N4	3113(4)	7410(4)	6767(1)	21(1)
N5	3681(4)	9052(4)	6146(1)	22(1)
N6	4085(4)	6313(4)	5851(1)	22(1)
N7	2081(4)	7481(4)	5382(1)	20(1)
C1	761(5)	9613(5)	6362(2)	29(1)
C2	-191(6)	10049(6)	6572(2)	37(1)
C3	-1105(6)	9183(6)	6656(2)	40(2)
C4	-1040(5)	7898(6)	6521(2)	34(1)
C5	-56(5)	7523(5)	6317(2)	25(1)
C6	50(5)	6191(5)	6147(2)	25(1)
C7	1120(5)	4520(5)	5828(2)	24(1)
C8	1373(5)	3398(5)	6154(2)	26(1)
C9	2734(5)	3197(5)	6323(2)	26(1)
C10	2982(5)	4270(5)	7011(2)	30(1)
C11	3290(5)	5491(5)	7282(2)	31(1)
C12	2590(5)	6715(5)	7114(2)	26(1)
C13	3844(5)	8365(5)	6881(2)	23(1)
C14	4289(5)	9199(5)	6552(2)	24(1)
C15	5236(5)	10104(5)	6655(2)	28(1)
C16	5581(5)	10887(5)	6329(2)	29(1)
C17	4933(5)	10763(5)	5917(2)	30(1)
C18	3993(5)	9840(5)	5835(2)	24(1)
C19	4696(5)	4129(5)	6625(2)	25(1)
C20	5275(5)	4414(5)	6224(2)	28(1)
C21	5263(5)	5859(5)	6096(2)	28(1)
C22	4021(5)	6346(5)	5445(2)	25(1)
C23	2937(5)	6904(5)	5171(2)	22(1)
C24	2803(5)	6881(5)	4723(2)	28(1)
C25	1774(6)	7489(5)	4487(2)	30(1)
C26	913(5)	8074(5)	4705(2)	27(1)
C27	1094(5)	8044(5)	5148(2)	25(1)

S1	7437(1)	7343(1)	5034(1)	28(1)
F1	8122(3)	9269(3)	5571(1)	47(1)
F2	6539(3)	8204(3)	5721(1)	37(1)
F3	6330(4)	9544(3)	5187(1)	51(1)
O1	8255(4)	6509(4)	5314(1)	45(1)
O2	6240(4)	6790(4)	4875(1)	41(1)
O3	7994(4)	8062(4)	4718(1)	38(1)
C28	7081(5)	8642(5)	5395(2)	29(1)
S2	6299(2)	8575(2)	8006(1)	46(1)
F4	6625(4)	7831(5)	7219(1)	67(1)
F5	8242(4)	7682(6)	7688(2)	87(2)
F6	6800(6)	6321(4)	7684(2)	101(2)
O4	6649(9)	9853(5)	7911(2)	136(3)
O5	6800(4)	8098(5)	8419(1)	57(1)
O6	5011(4)	8176(7)	7887(2)	89(2)
C29	7026(5)	7592(6)	7633(2)	41(2)

Table 4.40. Bond lengths [\AA] and angles [$^\circ$] for **4.23**.

Zn1-N2	2.108(4)	F4-C29	1.325(6)	H11A-C11-H11B	107.5
Zn1-N4	2.152(4)	F5-C29	1.308(6)	N4-C12-C11	114.9(4)
Zn1-N6	2.162(4)	F6-C29	1.331(6)	N4-C12-H12A	108.5
Zn1-N7	2.178(4)	N2-Zn1-N4	103.03(16)	C11-C12-H12A	108.5
Zn1-N5	2.223(4)	N2-Zn1-N6	106.50(16)	N4-C12-H12B	108.5
Zn1-N1	2.264(4)	N4-Zn1-N6	103.43(16)	C11-C12-H12B	108.5
N1-C1	1.330(7)	N2-Zn1-N7	87.92(16)	H12A-C12-H12B	107.5
N1-C5	1.353(7)	N4-Zn1-N7	168.18(15)	N4-C13-C14	120.2(5)
N2-C6	1.286(6)	N6-Zn1-N7	77.20(16)	N4-C13-H13	119.9
N2-C7	1.483(6)	N2-Zn1-N5	167.16(15)	C14-C13-H13	119.9
N3-C10	1.460(7)	N4-Zn1-N5	76.25(16)	N5-C14-C15	122.3(5)
N3-C19	1.461(6)	N6-Zn1-N5	85.99(15)	N5-C14-C13	115.3(5)
N3-C9	1.481(6)	N7-Zn1-N5	92.08(15)	C15-C14-C13	122.3(5)
N4-C13	1.272(7)	N2-Zn1-N1	75.84(16)	C14-C15-C16	119.0(5)
N4-C12	1.478(6)	N4-Zn1-N1	82.82(15)	C14-C15-H15	120.5
N5-C18	1.342(6)	N6-Zn1-N1	172.39(15)	C16-C15-H15	120.5

N5-C14	1.348(6)	N7-Zn1-N1	95.78(15)	C17-C16-C15	118.5(5)
N6-C22	1.261(6)	N5-Zn1-N1	91.39(15)	C17-C16-H16	120.8
N6-C21	1.464(6)	C1-N1-C5	118.2(5)	C15-C16-H16	120.8
N7-C27	1.332(6)	C1-N1-Zn1	129.4(4)	C16-C17-C18	119.7(5)
N7-C23	1.351(6)	C5-N1-Zn1	110.0(3)	C16-C17-H17	120.1
C1-C2	1.380(8)	C6-N2-C7	117.1(4)	C18-C17-H17	120.1
C1-H1	0.95	C6-N2-Zn1	116.8(3)	N5-C18-C17	122.1(5)
C2-C3	1.381(9)	C7-N2-Zn1	125.4(3)	N5-C18-H18	119
C2-H2	0.95	C10-N3-C19	108.4(4)	C17-C18-H18	119
C3-C4	1.380(8)	C10-N3-C9	108.8(4)	N3-C19-C20	115.6(4)
C3-H3	0.95	C19-N3-C9	108.8(4)	N3-C19-H19A	108.4
C4-C5	1.379(7)	C13-N4-C12	116.9(4)	C20-C19-H19A	108.4
C4-H4	0.95	C13-N4-Zn1	114.9(3)	N3-C19-H19B	108.4
C5-C6	1.466(7)	C12-N4-Zn1	127.2(3)	C20-C19-H19B	108.4
C6-H6	0.95	C18-N5-C14	118.3(5)	H19A-C19-H19B	107.4
C7-C8	1.528(7)	C18-N5-Zn1	129.0(3)	C19-C20-C21	114.5(5)
C7-H7A	0.99	C14-N5-Zn1	111.7(3)	C19-C20-H20A	108.6
C7-H7B	0.99	C22-N6-C21	116.6(4)	C21-C20-H20A	108.6
C8-C9	1.506(7)	C22-N6-Zn1	113.3(3)	C19-C20-H20B	108.6
C8-H8A	0.99	C21-N6-Zn1	129.3(3)	C21-C20-H20B	108.6
C8-H8B	0.99	C27-N7-C23	118.3(4)	H20A-C20-H20B	107.6
C9-H9A	0.99	C27-N7-Zn1	129.3(4)	N6-C21-C20	114.5(4)
C9-H9B	0.99	C23-N7-Zn1	112.3(3)	N6-C21-H21A	108.6
C10-C11	1.513(8)	N1-C1-C2	122.2(6)	C20-C21-H21A	108.6
C10-H10A	0.99	N1-C1-H1	118.9	N6-C21-H21B	108.6
C10-H10B	0.99	C2-C1-H1	118.9	C20-C21-H21B	108.6
C11-C12	1.512(7)	C1-C2-C3	119.7(5)	H21A-C21-H21B	107.6
C11-H11A	0.99	C1-C2-H2	120.1	N6-C22-C23	121.2(5)
C11-H11B	0.99	C3-C2-H2	120.1	N6-C22-H22	119.4
C12-H12A	0.99	C4-C3-C2	118.4(5)	C23-C22-H22	119.4
C12-H12B	0.99	C4-C3-H3	120.8	N7-C23-C24	121.7(5)
C13-C14	1.470(7)	C2-C3-H3	120.8	N7-C23-C22	115.7(4)
C13-H13	0.95	C5-C4-C3	118.9(6)	C24-C23-C22	122.6(5)
C14-C15	1.381(7)	C5-C4-H4	120.5	C23-C24-C25	119.0(5)
C15-C16	1.389(8)	C3-C4-H4	120.5	C23-C24-H24	120.5
C15-H15	0.95	N1-C5-C4	122.5(5)	C25-C24-H24	120.5
C16-C17	1.376(8)	N1-C5-C6	115.2(4)	C26-C25-C24	118.8(5)
C16-H16	0.95	C4-C5-C6	122.2(5)	C26-C25-H25	120.6
C17-C18	1.382(7)	N2-C6-C5	119.0(5)	C24-C25-H25	120.6
C17-H17	0.95	N2-C6-H6	120.5	C25-C26-C27	119.2(5)

C18-H18	0.95	C5-C6-H6	120.5	C25-C26-H26	120.4
C19-C20	1.512(7)	N2-C7-C8	113.0(4)	C27-C26-H26	120.4
C19-H19A	0.99	N2-C7-H7A	109	N7-C27-C26	123.0(5)
C19-H19B	0.99	C8-C7-H7A	109	N7-C27-H27	118.5
C20-C21	1.524(7)	N2-C7-H7B	109	C26-C27-H27	118.5
C20-H20A	0.99	C8-C7-H7B	109	O1-S1-O2	115.2(3)
C20-H20B	0.99	H7A-C7-H7B	107.8	O1-S1-O3	116.0(3)
C21-H21A	0.99	C9-C8-C7	113.8(4)	O2-S1-O3	114.5(3)
C21-H21B	0.99	C9-C8-H8A	108.8	O1-S1-C28	102.8(2)
C22-C23	1.463(7)	C7-C8-H8A	108.8	O2-S1-C28	103.6(2)
C22-H22	0.95	C9-C8-H8B	108.8	O3-S1-C28	102.0(2)
C23-C24	1.384(7)	C7-C8-H8B	108.8	F2-C28-F3	107.3(4)
C24-C25	1.389(8)	H8A-C8-H8B	107.7	F2-C28-F1	106.7(4)
C24-H24	0.95	N3-C9-C8	115.1(4)	F3-C28-F1	106.8(4)
C25-C26	1.372(8)	N3-C9-H9A	108.5	F2-C28-S1	113.1(3)
C25-H25	0.95	C8-C9-H9A	108.5	F3-C28-S1	111.8(3)
C26-C27	1.371(7)	N3-C9-H9B	108.5	F1-C28-S1	110.9(3)
C26-H26	0.95	C8-C9-H9B	108.5	O4-S2-O5	115.8(4)
C27-H27	0.95	H9A-C9-H9B	107.5	O4-S2-O6	119.2(5)
S1-O1	1.430(4)	N3-C10-C11	115.5(4)	O5-S2-O6	111.3(3)
S1-O2	1.435(4)	N3-C10-H10A	108.4	O4-S2-C29	102.7(3)
S1-O3	1.435(4)	C11-C10-H10A	108.4	O5-S2-C29	104.7(3)
S1-C28	1.817(5)	N3-C10-H10B	108.4	O6-S2-C29	100.2(3)
F1-C28	1.342(6)	C11-C10-H10B	108.4	F5-C29-F4	107.0(5)
F2-C28	1.328(5)	H10A-C10-H10B	107.5	F5-C29-F6	104.6(5)
F3-C28	1.330(5)	C10-C11-C12	115.2(5)	F4-C29-F6	104.8(5)
S2-O4	1.400(5)	C10-C11-H11A	108.5	F5-C29-S2	114.0(4)
S2-O5	1.411(4)	C12-C11-H11A	108.5	F4-C29-S2	114.7(4)
S2-O6	1.449(5)	C10-C11-H11B	108.5	F6-C29-S2	110.9(4)
S2-C29	1.805(6)	C12-C11-H11B	108.5		

Table 4.41. Anisotropic displacement parameters ($\text{\AA}^2 \times 10^3$) for **4.23**. The anisotropic displacement factor exponent takes the form: $-2\pi^2 [h^2 a^* U^{11} + \dots + 2 h k a^* b^* U^{12}]$

	U11	U22	U33	U23	U13	U12
Zn1	17(1)	21(1)	20(1)	-1(1)	4(1)	-1(1)
N1	19(2)	22(2)	26(2)	-3(2)	3(2)	4(2)

N2	23(3)	20(2)	24(2)	-1(2)	-1(2)	2(2)
N3	15(2)	25(2)	27(2)	2(2)	4(2)	-1(2)
N4	22(2)	20(2)	20(2)	0(2)	2(2)	3(2)
N5	22(2)	17(2)	28(3)	0(2)	5(2)	4(2)
N6	22(2)	17(2)	27(3)	4(2)	7(2)	-2(2)
N7	19(2)	21(2)	21(2)	0(2)	4(2)	-2(2)
C1	29(3)	29(3)	29(3)	-4(2)	1(3)	5(2)
C2	34(4)	33(3)	42(4)	-11(3)	7(3)	12(3)
C3	28(3)	52(4)	41(4)	-7(3)	9(3)	14(3)
C4	25(3)	45(4)	36(3)	2(3)	13(3)	5(3)
C5	18(3)	31(3)	25(3)	4(2)	1(2)	4(2)
C6	18(3)	28(3)	31(3)	2(2)	5(2)	1(2)
C7	29(3)	19(3)	26(3)	-2(2)	6(2)	0(2)
C8	23(3)	20(3)	34(3)	-1(2)	6(2)	-3(2)
C9	29(3)	18(3)	30(3)	-2(2)	6(2)	3(2)
C10	29(3)	28(3)	33(3)	5(2)	10(3)	-7(2)
C11	32(3)	38(3)	23(3)	6(2)	2(3)	-4(3)
C12	28(3)	31(3)	23(3)	0(2)	11(2)	-2(2)
C13	25(3)	23(3)	20(3)	3(2)	-1(2)	3(2)
C14	24(3)	17(3)	28(3)	2(2)	-3(2)	4(2)
C15	17(3)	25(3)	38(3)	-2(2)	-5(2)	3(2)
C16	21(3)	19(3)	45(4)	-4(2)	1(3)	2(2)
C17	36(3)	21(3)	36(3)	1(2)	15(3)	1(2)
C18	29(3)	17(3)	27(3)	-2(2)	5(2)	1(2)
C19	19(3)	23(3)	33(3)	4(2)	-1(2)	-1(2)
C20	16(3)	27(3)	41(3)	8(2)	1(2)	4(2)
C21	17(3)	32(3)	35(3)	1(2)	4(2)	2(2)
C22	20(3)	16(3)	39(4)	0(2)	8(2)	-1(2)
C23	28(3)	16(3)	24(3)	2(2)	8(2)	-7(2)
C24	34(3)	25(3)	29(3)	-2(2)	13(3)	-5(2)
C25	39(4)	30(3)	20(3)	4(2)	3(3)	-14(3)
C26	23(3)	27(3)	28(3)	5(2)	-1(2)	-5(2)
C27	18(3)	26(3)	29(3)	-1(2)	0(2)	-2(2)

S1	25(1)	27(1)	33(1)	-3(1)	8(1)	0(1)
F1	61(3)	38(2)	43(2)	-4(2)	8(2)	-19(2)
F2	47(2)	35(2)	33(2)	3(1)	19(2)	-5(2)
F3	70(3)	51(2)	34(2)	12(2)	17(2)	36(2)
O1	56(3)	37(2)	40(3)	4(2)	-3(2)	16(2)
O2	32(2)	51(3)	41(3)	-13(2)	10(2)	-16(2)
O3	31(2)	39(2)	48(3)	-1(2)	19(2)	1(2)
C28	32(3)	25(3)	30(3)	3(2)	6(3)	-3(2)
S2	48(1)	59(1)	35(1)	10(1)	16(1)	7(1)
F4	54(3)	114(3)	32(2)	17(2)	9(2)	43(2)
F5	25(2)	162(5)	73(3)	-32(3)	2(2)	-5(3)
F6	163(5)	67(3)	91(4)	0(3)	76(4)	-15(3)
O4	266(9)	48(3)	124(5)	8(3)	127(6)	27(5)
O5	44(3)	95(4)	29(2)	3(2)	-1(2)	-23(3)
O6	33(3)	205(6)	29(3)	-11(3)	0(2)	35(4)
C29	30(3)	57(4)	37(3)	17(3)	8(3)	-5(3)

Table 4.42. Hydrogen coordinates ($\times 10^4$) and isotropic displacement parameters ($\text{\AA}^2 \times 10^{-3}$) or **4.23**.

	x	y	z	U(eq)
H1	1379	10220	6303	35
H2	-218	10942	6659	44
H3	-1763	9466	6804	48
H4	-1663	7282	6569	41
H6	-640	5608	6120	30
H7A	1775	4521	5639	29
H7B	310	4365	5643	29
H8A	925	3577	6401	31
H8B	1032	2575	6015	31
H9A	2822	2397	6505	31
H9B	3182	3039	6074	31

H10A	3395	3510	7170	35
H10B	2071	4121	6979	35
H11A	4194	5665	7302	37
H11B	3114	5315	7578	37
H12A	1717	6471	7004	32
H12B	2575	7329	7359	32
H13	4103	8539	7179	28
H15	5646	10188	6944	34
H16	6249	11495	6389	35
H17	5131	11308	5691	36
H18	3554	9762	5550	29
H19A	4896	3212	6715	30
H19B	5090	4710	6861	30
H20A	4823	3905	5980	34
H20B	6149	4102	6273	34
H21A	5451	6395	6362	33
H21B	5937	6012	5921	33
H22	4689	6002	5315	30
H24	3405	6455	4580	34
H25	1668	7499	4180	36
H26	200	8494	4550	32
H27	488	8444	5296	30

Table 4.43. Torsion angles [°] for **4.23**.

N2-Zn1-N1-C1	175.4(5)	N1-C5-C6-N2	16.7(7)
N4-Zn1-N1-C1	70.0(4)	C4-C5-C6-N2	-166.6(5)
N7-Zn1-N1-C1	-98.2(4)	C6-N2-C7-C8	-85.7(6)
N5-Zn1-N1-C1	-5.9(5)	Zn1-N2-C7-C8	104.4(4)
N2-Zn1-N1-C5	13.8(3)	N2-C7-C8-C9	-82.7(6)
N4-Zn1-N1-C5	-91.7(3)	C10-N3-C9-C8	76.7(5)
N7-Zn1-N1-C5	100.2(3)	C19-N3-C9-C8	-165.4(4)
N5-Zn1-N1-C5	-167.6(3)	C7-C8-C9-N3	64.5(6)

N4-Zn1-N2-C6	73.5(4)	C19-N3-C10-C11	74.8(6)
N6-Zn1-N2-C6	-178.0(4)	C9-N3-C10-C11	-167.1(5)
N7-Zn1-N2-C6	-102.0(4)	N3-C10-C11-C12	66.2(7)
N5-Zn1-N2-C6	-11.8(9)	C13-N4-C12-C11	-95.9(6)
N1-Zn1-N2-C6	-5.5(4)	Zn1-N4-C12-C11	96.9(5)
N4-Zn1-N2-C7	-116.6(4)	C10-C11-C12-N4	-81.6(6)
N6-Zn1-N2-C7	-8.1(4)	C12-N4-C13-C14	-173.0(4)
N7-Zn1-N2-C7	67.9(4)	Zn1-N4-C13-C14	-4.3(6)
N5-Zn1-N2-C7	158.2(6)	C18-N5-C14-C15	-1.7(7)
N1-Zn1-N2-C7	164.4(4)	Zn1-N5-C14-C15	167.9(4)
N2-Zn1-N4-C13	-169.5(4)	C18-N5-C14-C13	176.1(4)
N6-Zn1-N4-C13	79.7(4)	Zn1-N5-C14-C13	-14.3(5)
N7-Zn1-N4-C13	-12.0(10)	N4-C13-C14-N5	13.2(7)
N5-Zn1-N4-C13	-2.7(4)	N4-C13-C14-C15	-169.0(5)
N1-Zn1-N4-C13	-95.9(4)	N5-C14-C15-C16	-0.3(8)
N2-Zn1-N4-C12	-2.1(4)	C13-C14-C15-C16	-178.0(5)
N6-Zn1-N4-C12	-112.9(4)	C14-C15-C16-C17	2.2(7)
N7-Zn1-N4-C12	155.4(7)	C15-C16-C17-C18	-2.2(8)
N5-Zn1-N4-C12	164.7(4)	C14-N5-C18-C17	1.8(7)
N1-Zn1-N4-C12	71.5(4)	Zn1-N5-C18-C17	-165.7(4)
N2-Zn1-N5-C18	-94.1(8)	C16-C17-C18-N5	0.2(8)
N4-Zn1-N5-C18	177.5(4)	C10-N3-C19-C20	-167.9(4)
N6-Zn1-N5-C18	72.7(4)	C9-N3-C19-C20	74.0(5)
N7-Zn1-N5-C18	-4.4(4)	N3-C19-C20-C21	69.3(6)
N1-Zn1-N5-C18	-100.2(4)	C22-N6-C21-C20	-97.1(5)
N2-Zn1-N5-C14	97.7(7)	Zn1-N6-C21-C20	94.0(5)
N4-Zn1-N5-C14	9.4(3)	C19-C20-C21-N6	-82.0(6)
N6-Zn1-N5-C14	-95.5(3)	C21-N6-C22-C23	-173.9(4)
N7-Zn1-N5-C14	-172.5(3)	Zn1-N6-C22-C23	-3.3(6)
N1-Zn1-N5-C14	91.6(3)	C27-N7-C23-C24	-0.5(7)
N2-Zn1-N6-C22	84.2(4)	Zn1-N7-C23-C24	176.7(4)
N4-Zn1-N6-C22	-167.5(3)	C27-N7-C23-C22	177.8(4)
N7-Zn1-N6-C22	0.3(3)	Zn1-N7-C23-C22	-5.1(5)
N5-Zn1-N6-C22	-92.7(4)	N6-C22-C23-N7	5.9(7)
N2-Zn1-N6-C21	-106.6(4)	N6-C22-C23-C24	-175.8(5)
N4-Zn1-N6-C21	1.6(4)	N7-C23-C24-C25	1.3(7)
N7-Zn1-N6-C21	169.5(4)	C22-C23-C24-C25	-176.9(4)
N5-Zn1-N6-C21	76.4(4)	C23-C24-C25-C26	-1.1(7)
N2-Zn1-N7-C27	72.0(4)	C24-C25-C26-C27	0.2(7)
N4-Zn1-N7-C27	-86.1(9)	C23-N7-C27-C26	-0.5(7)

N6-Zn1-N7-C27	179.4(4)	Zn1-N7-C27-C26	-177.1(4)
N5-Zn1-N7-C27	-95.2(4)	C25-C26-C27-N7	0.7(8)
N1-Zn1-N7-C27	-3.6(4)	O1-S1-C28-F2	-59.7(4)
N2-Zn1-N7-C23	-104.8(3)	O2-S1-C28-F2	60.6(4)
N4-Zn1-N7-C23	97.1(8)	O3-S1-C28-F2	179.7(4)
N6-Zn1-N7-C23	2.7(3)	O1-S1-C28-F3	179.0(4)
N5-Zn1-N7-C23	88.1(3)	O2-S1-C28-F3	-60.7(4)
N1-Zn1-N7-C23	179.7(3)	O3-S1-C28-F3	58.5(4)
C5-N1-C1-C2	1.1(8)	O1-S1-C28-F1	60.0(4)
Zn1-N1-C1-C2	-159.3(4)	O2-S1-C28-F1	-179.7(3)
N1-C1-C2-C3	-0.6(9)	O3-S1-C28-F1	-60.5(4)
C1-C2-C3-C4	-0.6(9)	O4-S2-C29-F5	61.4(6)
C2-C3-C4-C5	1.3(9)	O5-S2-C29-F5	-60.0(5)
C1-N1-C5-C4	-0.4(8)	O6-S2-C29-F5	-175.3(5)
Zn1-N1-C5-C4	163.6(4)	O4-S2-C29-F4	-62.4(6)
C1-N1-C5-C6	176.3(5)	O5-S2-C29-F4	176.3(4)
Zn1-N1-C5-C6	-19.7(5)	O6-S2-C29-F4	60.9(5)
C3-C4-C5-N1	-0.8(9)	O4-S2-C29-F6	179.1(6)
C3-C4-C5-C6	-177.3(5)	O5-S2-C29-F6	57.8(5)
C7-N2-C6-C5	-174.2(4)	O6-S2-C29-F6	-57.6(5)
Zn1-N2-C6-C5	-3.4(6)		

4.6. REFERENCES FOR CHAPTER 4

- (1) Rowan, S. J.; Cantrill, S. J.; Cousins, G. R.; Sanders, J. K.; Stoddart, J. F. *Angew Chem Int Ed Engl* **2002**, *41*, 898.
- (2) Corbett, P. T.; Leclaire, J.; Vial, L.; West, K. R.; Wietor, J. L.; Sanders, J. K. M.; Otto, S. *Chem Rev* **2006**, *106*, 3652.
- (3) Lehn, J. M. *Chem Soc Rev* **2007**, *36*, 151.
- (4) Hunta, R. A. R.; Otto, S. *Chem Commun (Camb)* **2011**, *47*, 847.
- (5) Mastalerz, M. *Angew Chem Int Edit* **2010**, *49*, 5042.
- (6) Mohr, G. J. *Chem-Eur J* **2004**, *10*, 1082.
- (7) Meyer, C. D.; Joiner, C. S.; Stoddart, J. F. *Chem Soc Rev* **2007**, *36*, 1705.
- (8) Park, H.; Kim, K. M.; Lee, A.; Ham, S.; Nam, W.; Chin, J. *J Am Chem Soc* **2007**, *129*, 1518.

- (9) Osowska, K.; Miljanic, O. S. *J Am Chem Soc* **2011**, *133*, 724.
- (10) Beeren, S. R.; Sanders, J. K. M. *J Am Chem Soc* **2011**, *133*, 3804.
- (11) You, L.; Long, S. R.; Lynch, V. M.; Anslyn, E. V. *Chem-Eur J* **2011**, *17*, 11017.
- (12) You, L.; Berman, J. S.; Anslyn, E. V. *Nat Chem* **2011**, *3*, 943.
- (13) Kruppa, M.; Konig, B. *Chem Rev* **2006**, *106*, 3520.
- (14) Canary, J. W.; Allen, C. S.; Castagnetto, J. M.; Wang, Y. H. *J Am Chem Soc* **1995**, *117*, 8484.
- (15) Canary, J. W.; Allen, C. S.; Castagnetto, J. M.; Chiu, Y. H.; Toscano, P. J.; Wang, Y. H. *Inorg Chem* **1998**, *37*, 6255.
- (16) Holmes, A. E.; Zahn, S.; Canary, J. W. *Chirality* **2002**, *14*, 471.
- (17) Holmes, A. E.; Das, D.; Canary, J. W. *J Am Chem Soc* **2007**, *129*, 1506.
- (18) Westerhausen, M.; Wieneke, M.; Schwarz, W. *Journal of Organometallic Chemistry* **1996**, *522*, 137.
- (19) Dekker, J.; Boersma, J.; Fernholt, L.; Haaland, A.; Spek, A. L. *Organometallics* **1987**, *6*, 1202.
- (20) Jahn, H. A.; Teller, E. *Proceedings of the Royal Society of London. Series A - Mathematical and Physical Sciences* **1937**, *161*, 220.
- (21) Moore, E. A. A., E. W.; Janes, R. *Metal-Ligand Bonding*; Royal Society of Chemistry, 2004.
- (22) Dragna, J. M.; Pescitelli, G.; Tran, L.; Lynch, V. M.; Anslyn, E. V.; Di Bari, L. *J Am Chem Soc* **2012**, *134*, 4398.
- (23) Kovaricek, P.; Lehn, J.-M. *J. Am. Chem. Soc.* **2012**, *134*, 9446.
- (24) Daigle, D. J.; Decuir, T. J.; Robertson, J. B.; Darensbourg, D. J. In *Inorganic Syntheses*; John Wiley & Sons, Inc.: 2007, p 40.
- (25) Queiroz, M.-J.; Joseph, D.; Kirsch, G. *Organic Preparations and Procedures International* **1995**, *27*, 120.
- (26) Player, T. N.; Shinoda, S.; Tsukube, H. *Org. Biomol. Chem.* **2005**, *3*, 1615.
- (27) Michinobu, T.; Shinoda, S.; Nakanishi, T.; Hill, J. P.; Fujii, K.; Player, T. N.; Tsukube, H.; Ariga, K. *J. Am. Chem. Soc.* **2006**, *128*, 14478.

- (28) Misaki, H.; Miyake, H.; Shinoda, S.; Tsukube, H. *Inorg. Chem. (Washington, DC, U. S.)* **2009**, *48*, 11921.

Chapter 5: Mechanically-Controlled Indicator Displacement Assay

5.1. INTRODUCTION

One of the paramount scientific challenges is the detection and quantification of analytes that are biologically active. These substances can be either harmful or therapeutic. Species of this nature are typically investigated for a variety of properties, including, but not limited to, pharmaceutical activity and chemical toxicity. These analyses find their roots in several disciplines, including drug discovery, pollution monitoring, food safety evaluation, and medical testing. To this end, a great effort has been undertaken to control the selectivity of binding events.¹ This selectivity allows for maximal binding between the receptor and target analyte. Several optical molecular sensors have been introduced that allow for the detection, and quantification, of this binding event.²⁻⁴ One promising approach popularized by the Anslyn group, and discussed previously, is known as an indicator displacement assay (IDA).

IDA has received much research effort, and has achieved broad application in molecular recognition. It does not, however, accurately mimic biological molecular recognition described above. Species in solution equilibria are dispersed throughout the solution, rather than selectively concentrated in an interfacial environment. It would be advantageous to push the scope of this technique from solution phase interactions toward events at an interface for several reasons. Firstly, it would be possible to greatly increase the affinity constant found between the desired receptor and guest. This would greatly increase the sensitivity of this type of analysis, giving more accurate results with smaller amounts of material. Finally, this would open up the application of IDA sensing system to imaging applications within living systems such as tissues or cells. This is currently not feasible since the indicator is present everywhere in solution and not localized to the

spot where imaging is desired. To take steps toward achieving this goal, and expand the capability of the IDA technique, the air-water interface was chosen as a place to localize the host for an IDA.

5.2. INTRODUCTION TO THE AIR-WATER INTERFACE

Molecular recognition is an extremely important chemical task that occurs in biological systems. This event has often been mimicked by supramolecular chemists, as in the creation of artificial enzymes.⁵⁻⁷ This process is typically carried out in a homogeneous solution, where analytes are evenly distributed throughout the bulk medium. While much research effort has been directed toward these systems, the disperse solutions are not an accurate representation of how molecular recognition occurs in biological systems. Within a biological context, many molecular recognition events occur at interfacial environments.⁸ Examples of interfacial environments where molecular recognition occurs include reactive sites on enzymes, interior sites on the DNA double helix, or even the surfaces of membranes. In order to more accurately portray the sophisticated molecular recognition events that occur in biological systems, one must adapt to and mimic the ways that recognition occurs in these systems.

In order to be utilized as the site for preferential molecular recognition events in biological systems, there must be some benefit that comes from constraining these events to an interfacial environment. Kunitake and co-workers have provided seminal work to explore this phenomenon.⁹⁻¹¹ The binding between a guanidinium cation and a phosphate anion in the form of adenosine monophosphate (AMP) was studied in three disparate environments (**Figure 5.1**). When the two species were dispersed in aqueous solution, a relatively small binding constant of 1.4 M^{-1} was calculated. The second study maintained these two ions, but placed them in an aggregated aqueous media such as a micelle- or

liposomal-type structure. In this environment, the binding for these two species was measured to be a few orders of magnitude stronger, at approximately 10^2 - 10^4 M^{-1} . This value represents a significant enhancement over the binding observed in the dispersed solution. The third environment studied was at an interfacial environment, namely the air-water interface. When the cationic guanidinium species was installed at this interface, an additional binding enhancement was found, with values of 10^6 - 10^7 M^{-1} observed.

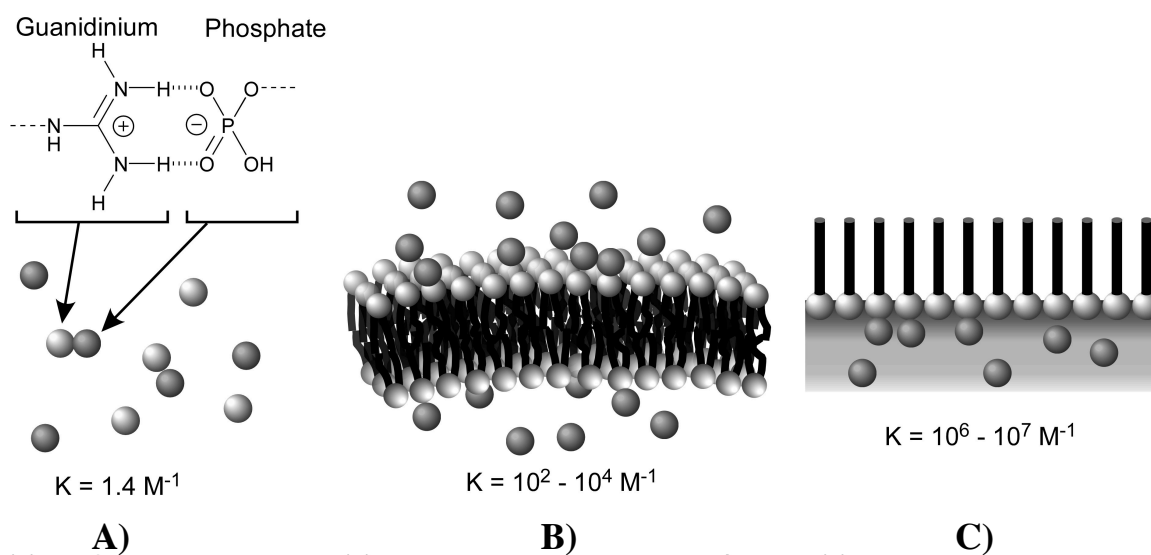


Figure 5.1. Binding constants measured for phosphate and guanidinium (a) in disperse aqueous solutions, (b) at micellar or bilayer surfaces, and (c) at air-water interface.

The previous study illustrates that molecular recognition at an interface can be done with enhanced binding. Binding and dissociation still happen to the same extent, in each case. but the local concentration of the receptor is different. When the guest molecule dissociates from the localized receptor, there are a multitude of other receptors that are located nearby. Thus, the binding of the guest to another molecule of host is relatively facile.

A quantum chemical approach was used by Sakurai and co-workers¹²⁻¹⁴ to understand the theoretical aspects of molecular recognition events at the air-water interface. The researchers modeled an interface occurring between a low dielectric layer, representative of the lipid layer, and a high dielectric layer that represented an aqueous phase. They next placed their binding species, guanidinium and phosphate, at assorted positions with respect to the interface. They found that the modeled binding constants were quite susceptible to their location relative to the phase boundary. Very little binding occurred when the species came together deep within the water layer, while binding was computed to be strong when both species were in the lipid phase. When the guanidinium was positioned at the interface with the binding site directed into the aqueous phase, the binding was affected by the low dielectric lipid layer. The researchers also found enhanced intermolecular hydrogen bonds, as well as more favorable electrostatic interactions. Hence, the binding constant was greatly enhanced at the interfacial environment. These calculations gave credence to the postulated advantages of molecular recognition carried out in interfacial environments.

A variety of monolayer assemblies have been reported that help to facilitate the recognition of substrates that are biologically relevant.¹⁵⁻²⁰ Of the reported strategies, mechanically-controlled interfacial recognition holds much promise for sensor design. Control over molecular conformation, and thus selective recognition, is easily obtained by changing the amount of pressure felt at the sensor interface. A variety of tasks have been carried out using this strategy: binding and release of guests, discriminating subtly different nucleobases, and enantioselectively binding amino acids.²¹⁻²⁹ All of these tasks were achieved using controlled mechanical force.

5.3. DESIGN CRITERIA

In order to address the aforementioned concerns and push the frontiers of the IDA technique even further, the air-water interface was chosen as a medium to perform this analysis. The strategy, mechanically-controlled indicator displacement assay (MC-IDA), was designed as another tool to convert a molecular recognition event with a mechanical force trigger to a sensing system with practical use. The strategy hinges on the use of a monolayer assembly of a fluorescently tagged host molecule, whose emission signal can be modulated by external mechanical force. Compression and expansion of the monolayer in the lateral direction changes the conformation of the monolayer, allowing for appropriate tuning of the sensor. This strategy is represented pictorially in **Figure 5.2**. The signal of the fluorophore can be switched on or off by surface compression. The target substrate, D-glucose, then displaces the indicator into the water solution. This displacement will allow for quantitation of the guest, and thus constitute the MC-IDA.

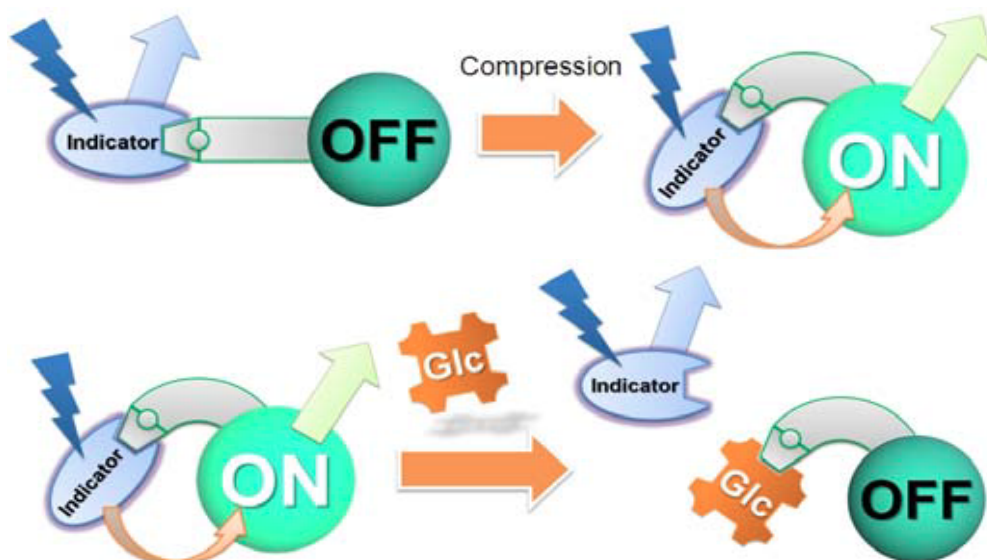
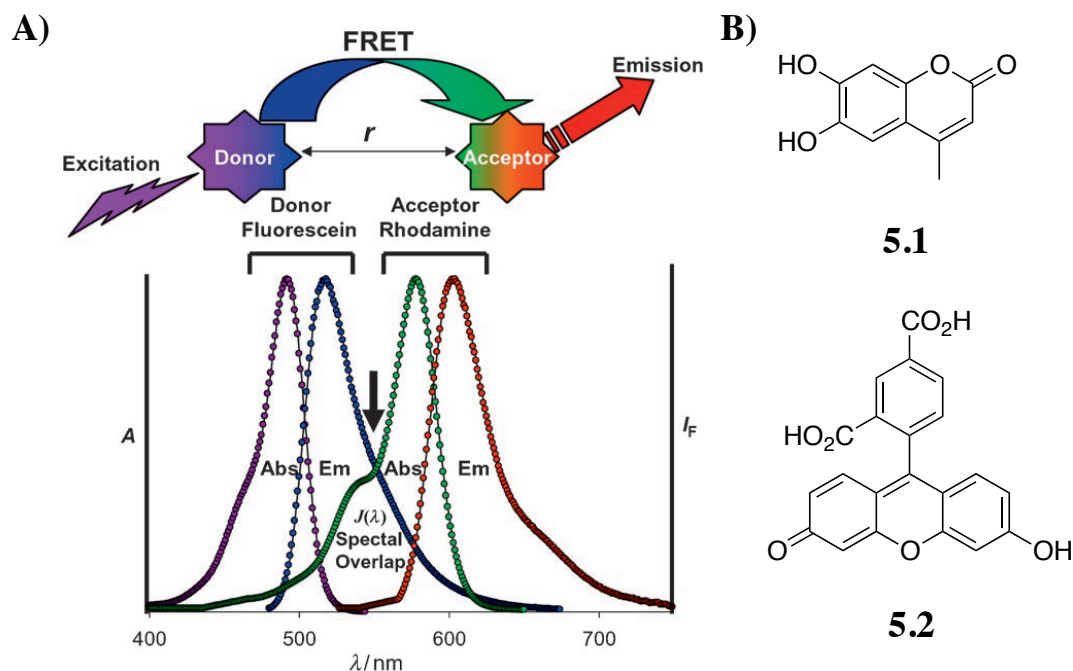


Figure 5.2. Top: Illustration of the FRET signal turned on by external compression. Bottom: Schematic representation of the MC-IDA.

5.4. THE INTERFACIAL RECEPTOR

An amphiphilic dipeptide was envisioned as the base to build the host system applied in this assay. The host was designed to possess three important motifs: a phenylboronic acid, a cholesterol, and a carboxyfluorescein indicator. The boronic acid was chosen since it is known to form reversible covalent bonds with diols and catechols in aqueous media.³⁰ The cholesterol group installs a hydrophobic moiety, making the host compatible for use in organic media. Carboxyfluorescein was chosen as a fluorescent indicator because it has been previously shown to form a FRET pair with coumarin-based indicators such as methylesculetin.³¹⁻³⁵

The process of FRET involves a radiation-less energy transfer between a donor fluorophore and an acceptor fluorophore that are held in close proximity.^{36,37} This strategy relies on the overlap of the emission wavelength of the donor and the excitation wavelength of the acceptor. As shown in **Scheme 5.1A**, the donor is excited at its characteristic excitation wavelength. Instead of emitting the photon it absorbs, this photon is transferred nonradiatively and serves to excite the acceptor fluorophore. The wavelength of emission that is observed from this ensemble is indicative of the acceptor. This is a very sensitive method to probe the distance between two fluorophores, and has been widely used in biology as a sensing paradigm.³⁸⁻⁴¹ In the case at hand, the two molecules are expected to form a FRET pair. Methylesculetin **5.1** is a coumarin-based indicator, known to participate in FRET with fluorescein-based derivatives such as carboxyfluorescein **5.2** (**Scheme 5.1B**). The binding of **5.1** should bring these fluorophores closer together and lead to an observable FRET signal.



Scheme 5.1. A) Schematic representation of the FRET between a fluorescein donor and a rhodamine acceptor. B) Chemical structures of FRET pair methylesculetin **5.1** and carboxyfluorescein **5.2**.

The synthesis of receptor **5.3**, pictured in **Scheme 5.2**, began with Rink Amide Resin. This resin allowed construction of the host from the N-terminus of the peptide. The first step was to add the first lysine residue. The residue that was incorporated was judiciously chosen, with a different protecting group utilized for the type of amine that was present. The N-terminus was protected with 9-fluorenylmethoxycarbonyl (Fmoc), which is stable to acid but removed under basic conditions. The side chain amine was protected with 4-methyltrityl (Mtt), which is cleaved under acidic conditions while remaining stable to base. The orthogonal nature of the protecting groups allowed selective deprotection and reaction of whichever amine is desired. The first lysine residue was attached using standard peptide coupling,⁴² which allowed for homologation of the peptide chain by a single residue.

The side chain amine was selectively deprotected using dilute trifluoroacetic acid, and the boronic acid was coupled in this position through reductive amination. Following the attachment of the boronic acid unit, an additional lysine residue was added as previously described. The side chain amine was used in order to make a carbamate bond and install the cholesterol group, followed by attachment of **5.2** to the N-terminus of the residue by standard peptide coupling conditions. The receptor **5.3** was cleaved from the resin under acidic conditions, isolated and purified. Synthetic details can be found in the experimental section. With the pure receptor in hand, the rest of the experiments could be performed.

5.5. OBSERVATION OF FRET

The efficiency of FRET depends primarily on how well the emission of the donor fluorophore and the excitation of the acceptor overlap. Additionally, efficiency can be affected by orientation of the species in solution, the distance of the chromophores from each other, or the refractive index of the solvent.³⁶ To probe the spectral overlap, both the donor emission and the host excitation were recorded. These signals were then normalized and overlaid (**Figure 5.3A**). Exciting the indicator by itself at 363 nm gave rise to a blue emission, with an emission maximum observed at 436 nm. The absorption by the host was rather broad, possessing maxima at 435, 460, and 492 nm. These spectra show that there is good overlap between the donor emission and acceptor excitation.

When a solution of the host was added to the indicator solution, the low wavelength emission at 436 nm decreased, with concomitant formation of a peak at 522 nm. The longer wavelength peak is indicative of the carboxyfluorescein emission, and these data indicate that a FRET process is taking place. While FRET is occurring, the

remaining peak seen at 436 nm points toward incomplete energy transfer from the indicator to the host.

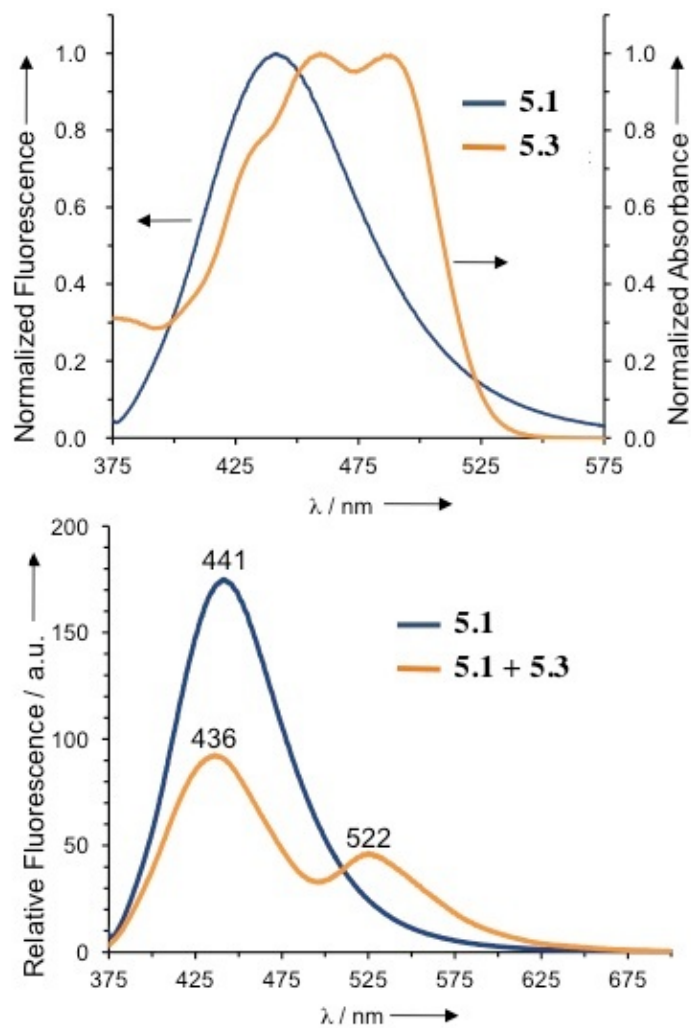


Figure 5.3. (A) Absorption spectrum of the host and fluorescence spectrum of indicator ($\lambda_{\text{ex}}=363\text{nm}$) in chloroform:methanol (4:1 v/v). (B) Fluorescence spectra of indicator ($5\ \mu\text{M}$) before and after addition of host ($\lambda_{\text{ex}}=363\text{nm}$).

In solution, one would expect that the nature of the host would lead to the formation of a higher order structure. It is known that boronic acids aggregate, and this can lead to these higher-order structures.³⁰ Additionally, amphiphilic species are known to form microtubular or vesicular structures. In spite of these types of potentially unfavorable interactions, this species is a good candidate for forming a monolayer.

5.6. MONOLAYER FORMATION

The first step in implementing an IDA at the air-water interface is probing the ability of **5.3** to form a monolayer. A monolayer is shown pictorially in **Figure 5.1C**, where all of the molecules line up in a single well-packed layer. The desired compound is dissolved to a precisely known concentration in an organic solvent such as chloroform, and a known amount of this solution is spread on top of the water layer. As the solvent evaporates, this molecule spreads out across the top of the water. The individual molecules are able to move freely with little restriction, provided that the hydrophilic portion of the molecule is in the water layer and the hydrophobic portion is directed into the air. The compound spread across the water has a high amount of area available per molecule, and this compound exists as a dilute film on the surface of the water. The actual area per molecule is very important, and will be discussed later. At this point, formation of the monolayer is initiated by decreasing the amount of area per molecule using an instrument known as a Langmuir-Blodgett trough (LB) (**Figure 5.4**).⁴³ Following solvent evaporation, the amount of area per molecule is slowly decreased by moving the sidebars toward each other. Eventually, the area per molecule will reach a value indicative of a monolayer, with little gap between each individual molecule. As the pressure continues to increase and lowers the molecular area further, the monolayer

breaks down. Here, the high surface pressure creates insufficient space for each molecule and collapse of the monolayer is observed.

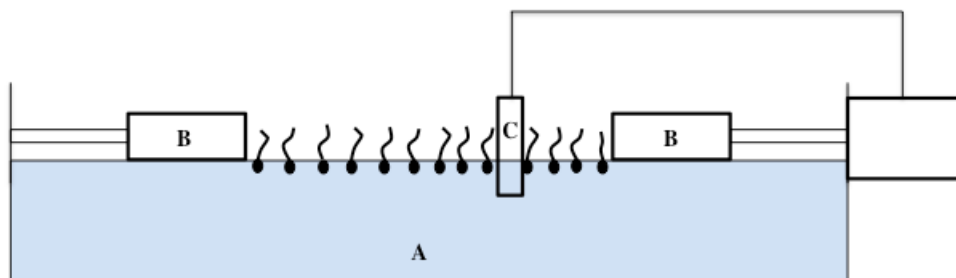


Figure 5.4. Representation of the Langmuir-Blodgett trough, indicating the water subphase (A), the bars to compress the monolayer (B), and the Wilhelmy plate to read the surface pressure (C).

The formation of a monolayer is studied by creating a surface pressure-area isotherm (π - A). The surface pressure is recorded using a Wilhelmy plate as shown in **Figure 5.4**. This apparatus measures the surface pressure that is recorded when the compound of interest is compressed, correcting for the compression on a pure water subphase. The plate consists of filter paper that immersed in the water, and the change in pressure is measured by a coupled electrobalance. As the monolayer begins to form, pressure increases linearly, and this region represents the molecular area in which the compound forms a monolayer. When the lower limit of molecular area for maintaining a monolayer is breached, the pressure drops off and order is no longer maintained. From this graph it is possible to extrapolate the data to the molecular area required for monolayer formation.

Receptor **5.2** was dissolved in an appropriate organic solution (80% chloroform, 20% methanol) and spread on the aqueous subphase. The surface area was steadily

decreased and the isotherm recorded. This was done for several different concentrations of the spreading solution, namely 1.0 mg/mL, 0.5 mg/mL, and 0.25 mg/mL. Different concentrations were used to ensure that no aggregation was taking place, as is known to occur with boronic acids. Any aggregation would have a large negative impact on the isotherms measured, varying the area significantly. The isotherms are shown in **Figure 5.5**. The shape of the isotherm for each concentration of spreading solution looks very similar, indicating that aggregation is not a concern at the concentrations to used. As indicated by the linear increase in surface pressure as a function of decreasing molecular area, the host formed a stable monolayer at the air-water interface. Monolayer formation was not accompanied by a phase transition, and had a high collapse pressure of roughly 40 mN/m.

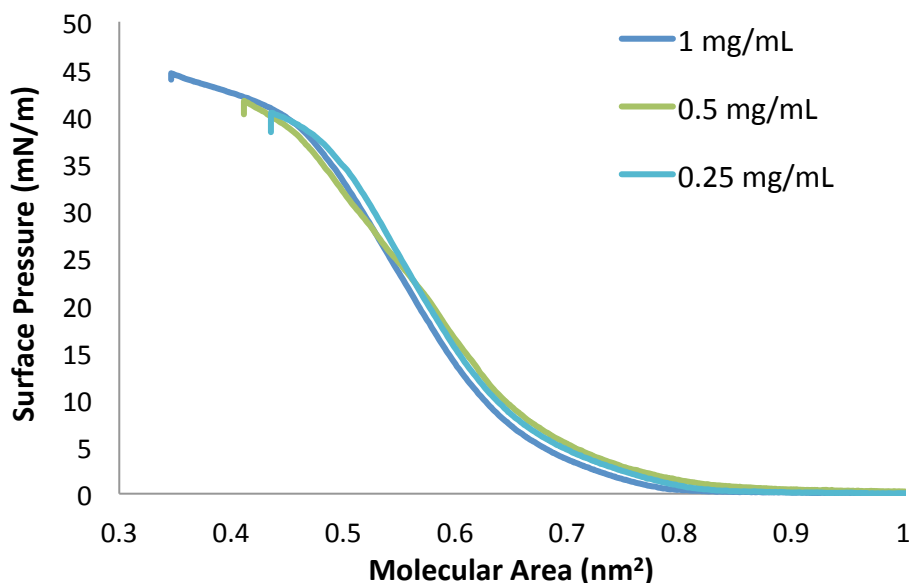


Figure 5.5. Surface pressure-area (π - A) isotherms measured for the host at various concentrations in the spreading solution at 20°C.

An estimation of the limiting molecular area of this monolayer can be made by noting on the x-axis where the curve begins a sharp linear ascent. The limiting molecular area for this monolayer was estimated at $0.61 \text{ nm}^2/\text{molecule}$. This value is much larger than the literature value for pure cholesterol, reported as $0.4 \text{ nm}^2/\text{molecule}$.⁴⁴ The deviation in the molecular area indicates that the structure of the hydrophobic groups affects how the molecule is able to pack at the interface to form a monolayer. Charge state and steric bulkiness is likely responsible for the increase in molecular area.

In order to further characterize the surface morphology of the monolayer, atomic force microscopy (AFM) was used. The monolayer was formed at the air-water interface, and this monolayer was transferred to a freshly cleaved mica substrate. The deposition was done while maintaining a surface pressure of 10 mN/m , a value within the range of stable monolayer formation, demonstrated by the $(\pi\text{-}A)$ isotherm measurement. The monolayer was then dried in a vacuum oven overnight to remove any residual water, and subjected to analysis. The images that were recorded for the monolayer formed by the host are shown in **Figure 5.6**. The images show a smooth, non-characteristic surface. This observation is consistent with the formation of an ideal monolayer. It is noted that the monolayer displayed some holes, indicating that some areas had no complex present. Any number of factors could have led to this observation, such as the presence of a contaminant on the substrate or the spreading solution, or the incomplete transfer of the monolayer. The height of the monolayer was determined from the cross section of one of the holes, indicating a height of approximately 1.2 nm . This value is slightly smaller than expected for cholesterol, indicating a likely tilt in these groups to fill in the space of the bulky head groups. This observation is consistent with the larger molecular area seen for this complex in the $(\pi\text{-}A)$ isotherm.

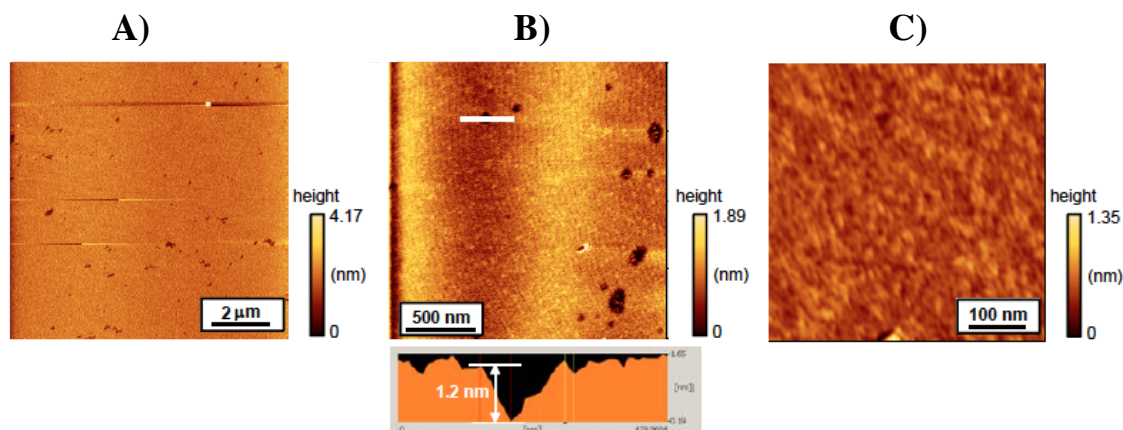


Figure 5.6. AFM height images of the monolayer formed by the host that was transferred to a freshly cleaved mica substrate at a surface pressure of 10 mN/m.

Rather than apply a monolayer composed completely by the host molecule, a lipid matrix was employed in further experiments. This modification was made because the monolayer had a molecular area larger than expected for pure cholesterol at the interface, and this could affect how the analyses were performed. Spreading the receptor molecule over the interface, as opposed to using a layer of pure host molecule, is more consistent with biological systems. In these biological systems, molecular recognition receptors are typically distributed throughout the surface rather than localized in one area of high concentration.

5.7. MATRIX LIPID SELECTION

As mentioned, addition of a lipid matrix agent to pure host was chosen in order to further separate the host molecule and create a better monolayer. This sort of setup is known in the literature, and presents an opportunity to form a more biologically relevant monolayer. Three different lipids that were chosen for matrix formation: cholesteryl acetate (**5.4**), a phospholipid (**5.5**) and methyl stearate (**5.6**). These species were chosen

as they form a variety of matrices, from hard (**5.4**) to soft matrices (**5.6**). The ideal lipid matrix would be one in which there was no interaction between the host and the lipid. Any sort of interaction, such as attraction or repulsion, would change the properties of the monolayer in an undesirable manner. The lipid should function essentially as a space filler, devoid of extraneous interactions with the host molecule. To probe this interaction, monolayers were made at various ratios of host and lipid for each agent selected.

5.7.1. Cholesterol Acetate

Cholesterol acetate **5.4** was initially studied because it is known to be a hard matrix agent that forms hard monolayers. Additionally, the species is identical to the hydrophobic portion of the host molecule, which was postulated to improve the matrix and form a better ideal monolayer. The result of this study is shown in **Figure 5.7**. There appears to be some interaction between the two species, as evidenced by the non-linearity of the best-fit slope of these data points. The likely reason for this deviation is the structural similarity of the matrix lipid to the host. The extent of deviation from linearity is maintained across all surface pressures that were studied. For these reasons, this matrix agent was deemed unfit for future studies. Attention was then turned toward a phospholipid, whose amphiphilic character made it a good candidate for monolayer formation.

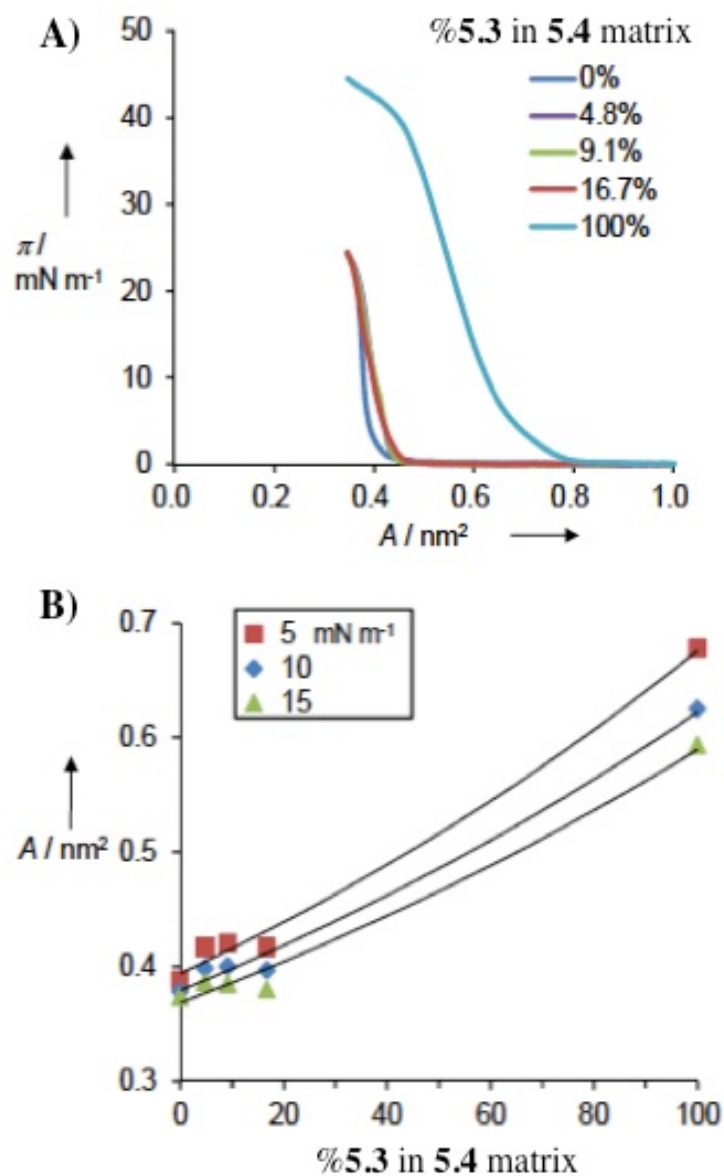


Figure 5.7. A) (π - A) isotherm measured for mixed monolayer of host and cholesterol acetate (**5.4**) on pure water at 20°C. Right: Molecular area as a function of host percent in the matrix at 5 mN/m intervals.

5.7.2. Dipalmitoylphosphatidylcholine

This phospholipid selected was dipalmitoylphosphatidylcholine, (**5.5**). This amphiphilic species was selected because it possesses charged functionalities. These

functionalities were postulated to compliment the charge state of the host molecule. Isotherms were again recorded by varying the amount of host present in the matrix lipid, and molecular area was plotted as a function of the matrix composition. The graphs for this experiment are shown in **Figure 5.8**. The plot shows non-linearity at all recorded surface pressures. The degree of non-linearity, however, increased at higher pressure. Initially the molecular area increased, and then eventually dipped to a much smaller value at low pressure. This initial rise is not present at higher starting pressures. This can be attributed to unfavorable electrostatic interactions between the charged species rather than complementarity. These interactions made it a poor choice of a lipid matrix agent.

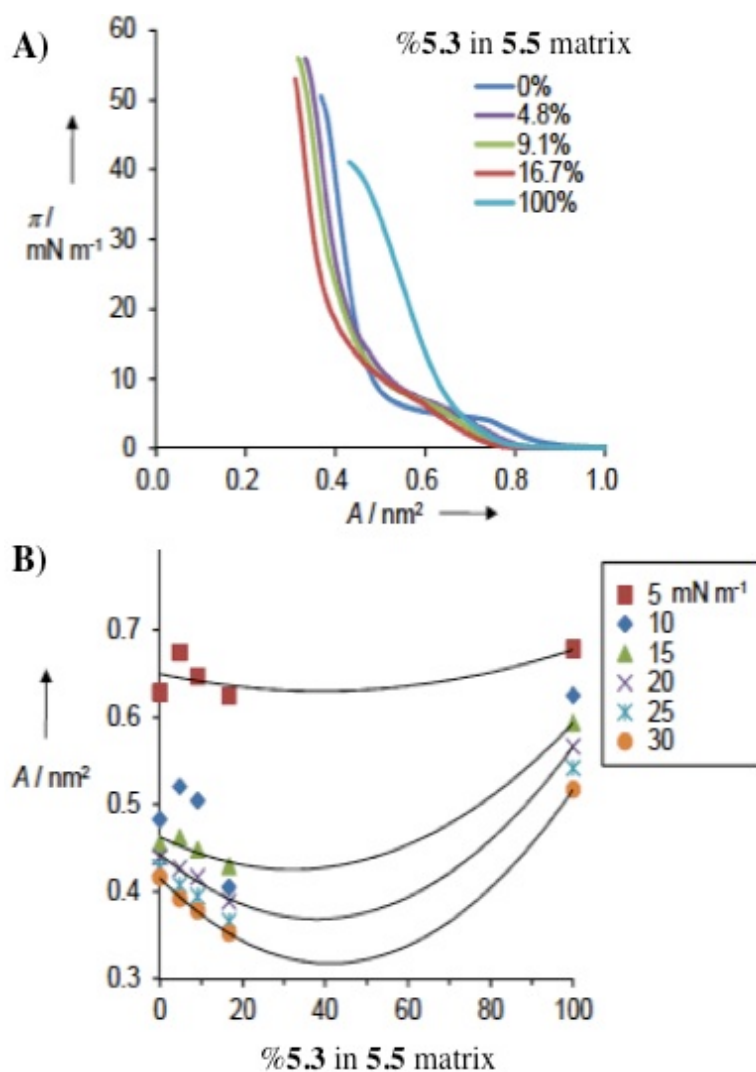


Figure 5.8. Left: (π - A) isotherm measured for mixed monolayer of host and dipalmitoylphosphatidylcholine (5.X) on pure water at 20°C. Right: Molecular area as a function of host percent in the matrix at 5 mN/m intervals.

5.7.3. Methyl Stearate

The final lipid that was chosen to study as a matrix agent was methyl stearate (5.6). This lipid has no structural similarity to the host, and has no charges that could lead to interaction or repulsion with the host. Application of this lipid gave rise to a

linear correlation between the molecular area and the composition of the matrix (**Figure 5.9**). This correlation was present at all studied surface pressures. This observation indicates that no unwanted interactions between the matrix agent and host molecule occurred. Hence, this lipid matrix agent was ideal for use in the monolayer formed with host **5.3**. For this reason, methyl stearate **5.6** was selected as a matrix agent. After determining the best lipid matrix agent, the binding of the desired indicator was studied at the interface.

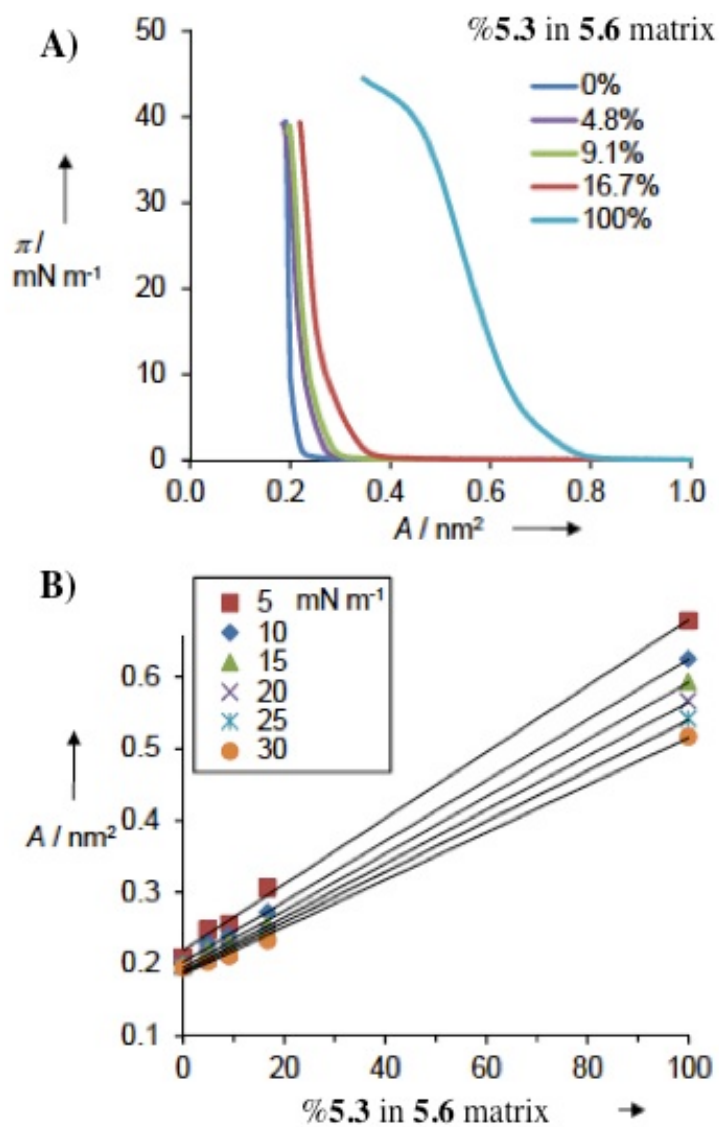


Figure 5.9. Left: (π - A) isotherm measured for mixed monolayer of host and methyl stearate (5.X) on pure water at 20°C. Right: Molecular area as a function of host percent in the matrix at 5 mN/m intervals.

5.8. INDICATOR BINDING

The boronic acid portion of the host was postulated to reside in the water subphase owing to its hydrophilic nature. In this model, binding would occur between this group and an indicator dissolved in the subphase. The indicators used in the

subphase would possess functional groups known to form reversible covalent bonds with boronic acids in aqueous media, namely diols or catechols. This binding would lead to an increase in the molecular area. To this effect, binding of the methylesculetin indicator **5.1** was studied at the interface.

Varying concentrations of the indicator were dissolved in the water subphase. After dissolution, the host was spread on the subphase and the solvent allowed to evaporate. The mechanical force was increased, causing formation of a monolayer. As is shown in **Figure 5.10**, the indicator caused a shift in the molecular area. This shift can be attributed to the bulkiness of the covalent complex formed between the boronic acid and the indicator. Binding constants were calculated for this association, with a value of $K=5.5 \times 10^5 \text{ M}^{-1}$ at a surface pressure of 5 mN/m.^{24,25} These binding constants were attenuated at the interface, with an enhancement of two orders of magnitude over the solution studies.⁴⁵ While this approach was successful in showing the high extent of indicator binding, the lack of solubility of the indicator in water was a major drawback. As the concentration of **5.1** in the subphase was increased, precipitation of this indicator was observed. Hence, effort was directed toward overcoming this drawback.

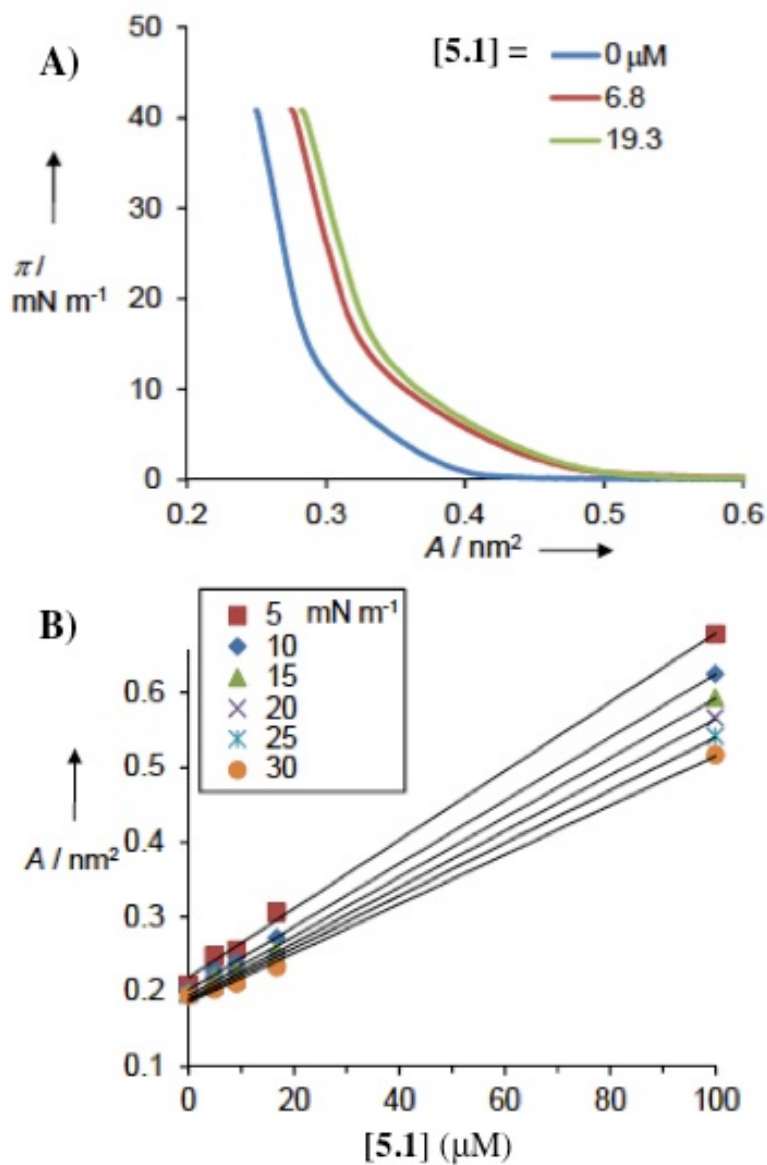


Figure 5.10. Left: (π - A) isotherms of the host matrix with indicator in the water subphase at 20°C . Right: Binding curves for the indicator at indicated surface pressures. The value of ΔA represents the difference between the value with dissolved guest and pure water.

In order to overcome the solubility issue, a strategy to alter the order of addition was envisioned. Since complex formation leads to higher molecular area, this binding

should occur regardless of whether the indicator begins dissolved in the subphase or the spreading solution. Thus, dissolving the indicator in the spreading solution was postulated to lead to the same extent of complex formation as seen for the indicator dissolved in the subphase. As had been observed when the indicator was dissolved in the subphase, the complex was determined to form in the spreading solution by $(\pi-A)$ isotherm measurements. The change in molecular area was observed to saturate at a molar ratio of host to indicator between 1:2 and 1:5 (**Figure 5.11**). The complex caused an increase in the monolayer molecular area, with extensive formation of the complex. It is important to note that the monolayer maintained its robust character, retaining a high collapse pressure of around 30 mN/m.

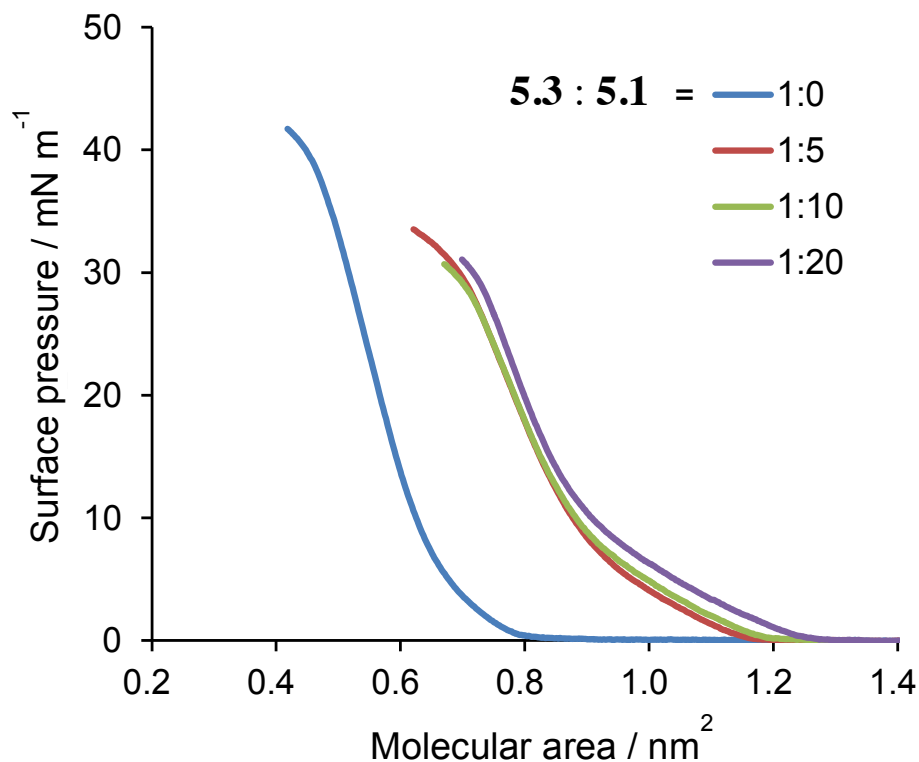


Figure 5.11. (π - A) isotherms of the mixed monolayer with indicator at the noted molar ratio, recorded at 20°C.

In order to confirm the utility of this monolayer, AFM images were recorded for the complex formed from the indicator and the host matrix monolayer. The monolayer was formed at two different surface pressures, namely 10 and 20 mN/m. These monolayers were then transferred to a freshly cleaved mica substrate, as for the pure host monolayer, and evaporated to dryness. The recorded images again show a smooth and non-characteristic surface, even in the presence of the matrix lipid and indicator (**Figure 5.12**). This observation was consistent for monolayers formed at both surface pressures used for deposition. There was again a small fraction of holes present. Estimation of the thickness of the film was done according to the cross-section of the film. The thickness

was estimated to be around 1.3-1.4 nm, in agreement with the trend observed earlier. The external compression seems to have no impact on the surface morphology, but may affect the molecular conformation to some extent.

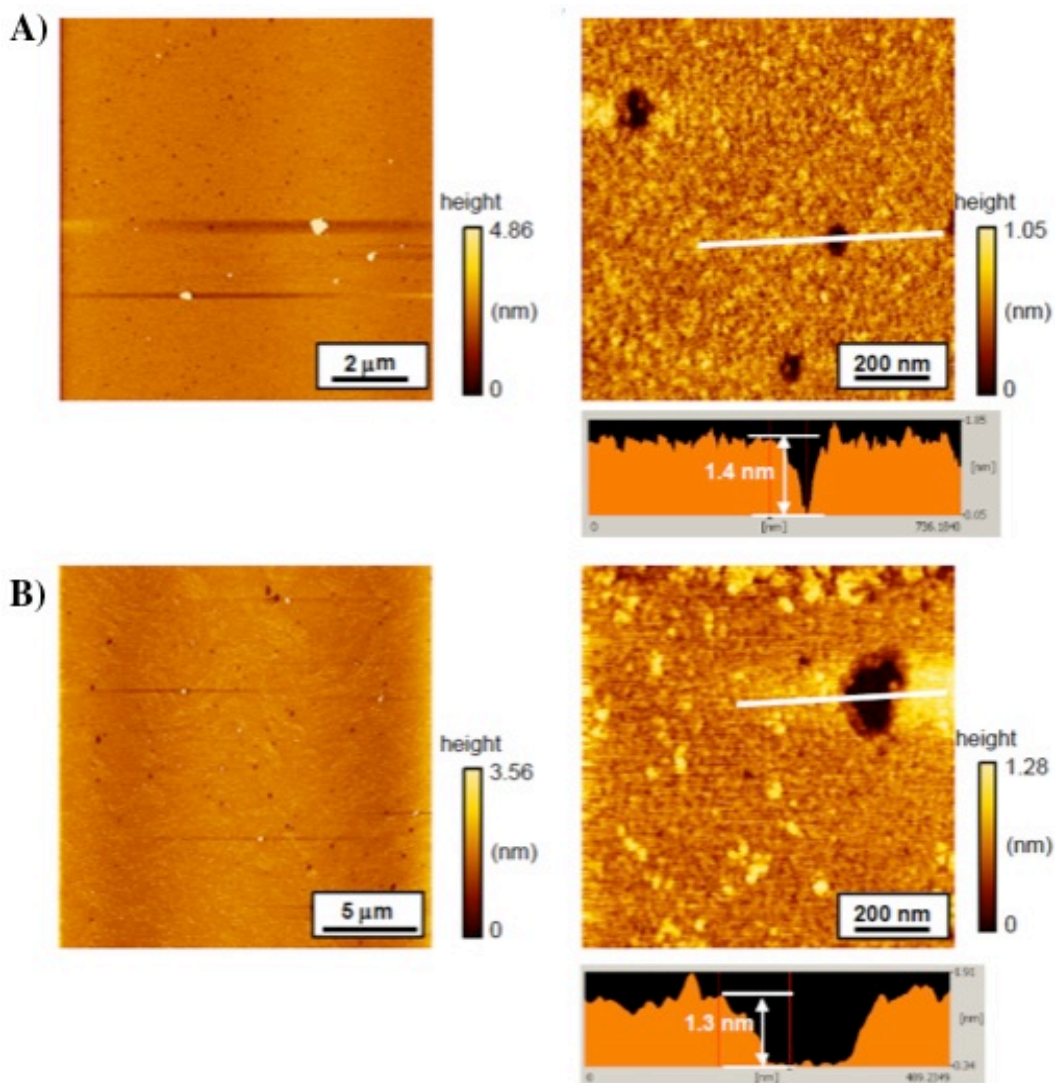
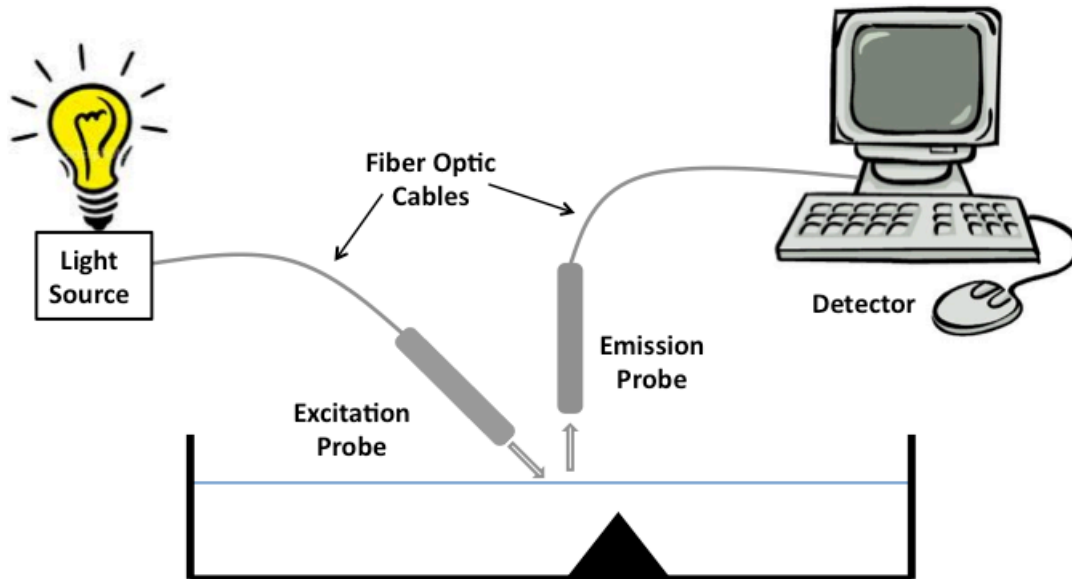


Figure 5.12. AFM height images of monolayer films of host and indicator dissolved in the spreading solution, transferred to a freshly cleaved mica substrate at surface pressures of 10 mN/m (A) or 20 mN/m (B).

5.9. FLUORESCENCE PROPERTIES OF MATRIX MONOLAYERS

In order to measure the fluorescence spectrum at the air-water interface, a multi-channel photo detector (MCPD) was utilized. This instrument, commercially available as Photal MCPD-7000 (Otsuka Instruments), allows both UV/Vis and fluorescence spectra to be recorded in the desired interfacial environment.^{46,47} The experimental setup is shown in **Scheme 5.3**. The light source is supplied to the monolayer using fiber optic cables. The cable is located at a 45° angle with respect to the surface of the water, and a black triangle is placed at the bottom of the trough directly behind the excitation source. This triangle resides entirely below the surface of the water so as not to disturb the monolayer. If left unchecked, extra light may lead to undesirable accidental scatter. The molecules at the interface are excited by light of a particular wavelength, and emit at their characteristic wavelength. This occurs in all directions, including perpendicular to the surface of the water. Thus, the fiber optic cable is designed to monitor emission just above the surface of the water. Monitoring the light in this manner helps to block out extra light that may lead to erroneous readings. The emission information is passed to a detector, and the signal is recorded. This signal allows for assignment of FRET for the sample.



Scheme 5.3. Schematic representation of the multi channel photo detector (MCPD) used to gather UV/Vis or fluorescence data at the air-water interface.

Using this apparatus, fluorescence at the air-water interface was measured for the matrix host monolayer containing the indicator in the spreading solution. At a surface pressure of 10 mN/m, excitation of the monolayer at 363 nm led to emission in the blue portion of the spectrum around 450 nm. This peak can be attributed to fluorescent emission of the indicator. When surface pressure was increased from 10 to 20 mN/m, the same 363 nm excitation produced a new peak in the green portion of the spectrum around 530 nm. This peak is indicative of FRET occurring between the coumarin-based donor **5.1** and fluorescein acceptor **5.3** (**Figure 5.13A**). Indeed, it was possible to effect FRET through application of external mechanical force. Additionally, the proper ratio of the indicator relative to the host was determined. As the ratio of the indicator in the spreading solution increased, the indicator emission began to dominate (**Figure 5.13B**). This is not to say that FRET does not occur, but in this setting the signal was completely overwhelmed by the indicator signal. In contrast, the ratio of 1:2 for the host relative to

the indicator gave the largest amount of carboxyfluorescein emission relative to the emission of indicator **5.1**.

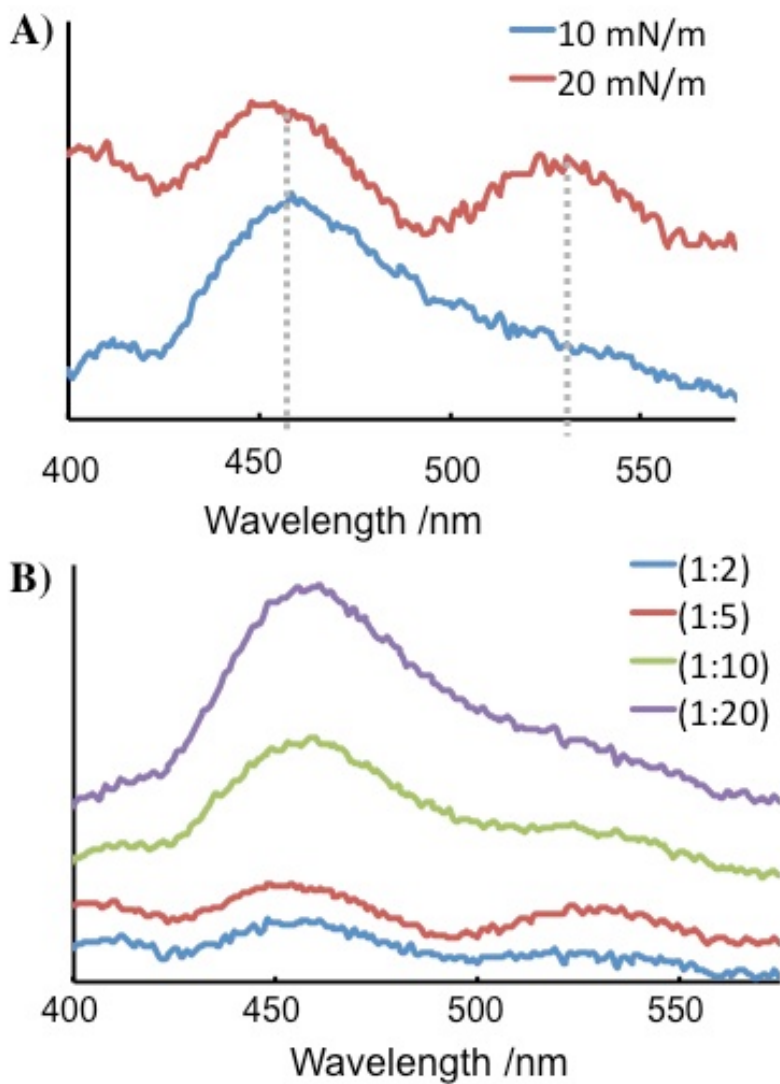


Figure 5.13. Fluorescence spectra of the monolayers of the host indicator complex under various different conditions; (A) 1:5 ratio of host to indicator formed at indicated surface pressures; (B) various ratios of indicator in the spreading solution at a surface pressure of 20 mN/m.

FRET efficiency is generally dependent on the distance and conformation of the fluorophores, as well as the overlap efficiency. As demonstrated previously, there is significant overlap in the donor emission and acceptor excitation for the indicator and host complexes used in this study. Thus, efficiency in this assay should depend on the distance between the chromophores. It is anticipated that higher surface pressure, and thus lower molecular area, will cause those chromophores to be held closer to each other in space. This close arrangement will likely enhance the FRET signal, leading to a better FRET signal observed for higher pressure measurements. The external surface pressure allows for additional experimental control of this sensing system, by switching it “on” and “off.”

5.10. GUEST DISPLACEMENT

After confirming monolayer formation with an appropriate matrix lipid and studying indicator binding to this monolayer, the focus of this study was directed towards displacement of the indicator by an appropriate guest. For this task, D-glucose was selected as an analyte. This important analyte is often used as an analysis target in human blood, and its quantification is routinely performed in a laboratory setting.⁴⁸⁻⁵¹ Glucose, as a solution in water, was added to the subphase below the monolayer. Once addition had occurred, the fluorescence spectrum was recorded. This was done for several concentrations of glucose, and the resultant fluorescence spectra are shown in **Figure 5.14A**. As evidenced in this graph, addition of the guest led to a decrease in the longer wavelength peak corresponding to carboxyfluorescein emission. This decrease was accompanied by very little change in the indicator peak. This trend was general for increasing glucose addition. Hence, the FRET observed between the donor and acceptor had been turned off in a ratiometric fashion at a constant pressure by addition of

increasing concentration of D-glucose. This result clearly indicates that the indicator was displaced by the guest.

To further study this interaction, the ratio of the fluorescence peaks was studied. This ratio was determined by dividing the signal that corresponds to host carboxyfluorescein emission at 525 nm with the methylesculetin indicator emission at 450 nm. This curve is shown in **Figure 5.14B**, and linearly decreases until 190 nM concentration of D-glucose was present in the subphase. This concentration of 190 nM corresponds to the point at which one equivalent of D-glucose guest had been introduced relative to the amount of fluorescent host molecule present in the monolayer. Thus, the data suggest that a very specific binding event takes place between the host monolayer and the D-glucose guest. Saturation was achieved after only one equivalent of guest had been added.

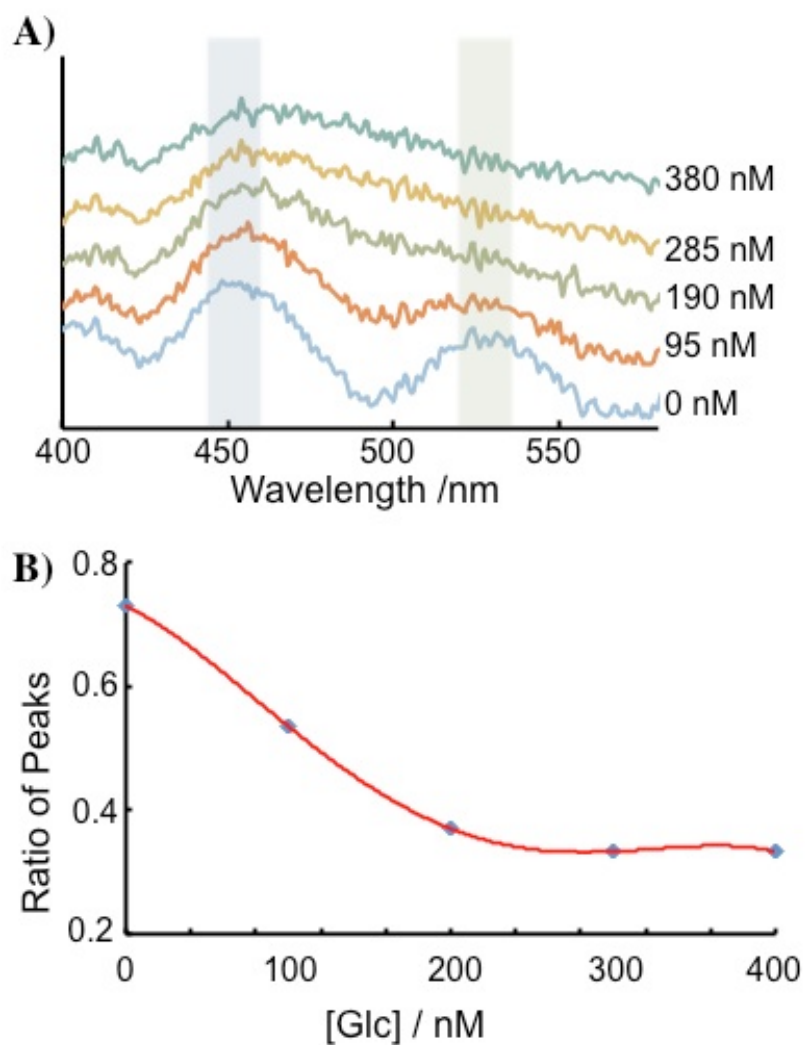


Figure 5.14. (A) Matrix monolayer fluorescence spectra changing upon addition of D-glucose to the subphase. (B) Plot of the fluorescence ratio (I_{525}/I_{450}) with increasing amounts of glucose added.

5.11. CONCLUDING REMARKS

IDA has been expanded past a dispersed solution-based analysis and toward a selective interaction at the air-water interface. Monolayer formation was confirmed by (π -A) isotherm measurements, and morphology understood by images captured by AFM. A strategy was devised to monitor binding between the host and indicator by dissolving

the indicator in the spreading solution before coating the surface of the water. Mechanical control of the FRET signal was confirmed to give the best ratio of carboxyfluorescein emission relative to **5.1** at a surface pressure of 20 mN/m. This pressure was then used to displace the indicator from the monolayer to allow quantitative sensing of a D-glucose guest. This method, using host-indicator complexes at a spatially defined interfacial region, may prove this assay applicable to either biological or environmental analyses.

5.12. EXPERIMENTAL

5.12.1. Materials and Methods

Unless otherwise noted, all solvents and materials were purchased from Aldrich, Tokyo Kasei Chemical Co. and Wako Chemical Co. They were all used without further purification. Water used for the LB subphase was distilled with an Autostill WG220 (Yamato) and deionized with a Milli-Q Lab (Millipore). The specific resistance was greater than 18 M Ω cm. Chloroform in the spreading solution was spectroscopic grade, and purchased from Kanto Chemical Co.

The (π - A) isotherms were measured with a FSD-300 computer controlled film balance (USI System, Fukuoka) at 20.0°C. A dilute solution of the host (approximately 0.5 mg/mL) in a chloroform:methanol mixture (4:1, v/v) was spread onto a water subphase in a Teflon coated trough. Thermostated water was circulated throughout the system in order to keep the temperature of the subphase constant. Any fluctuation was within $\pm 0.2^\circ\text{C}$. A Wilhelmy type film balance was used to measure the surface pressure. A total of 15 minutes were given to allow the solvent to completely evaporate, before the (π - A) isotherms were taken. A constant compression rate of 0.2 mm/s was maintained throughout.

The fluorescence spectra were recorded with a spectrometer equipped with a photodiode array (Otsuka Electronics, MCPD-7000). The wavelength of the excitation light was tuned to 363 nm. The excitation light was introduced to the monolayer through a fiber optic cable directed to the surface at an incident angle of 45°. The emission was recorded by a fiber optic cable placed perpendicular to the water surface. In absence of the host monolayer, the fluorescence reading was negligible.

Binding constants (K) were found for the host and indicator at the interface using a Langmuir type equation. In this approach, it is assumed that a molecular area increase in the (π - A) isotherm is proportional to the amount the indicator that has been absorbed. This assumption is made because of the hydrophobicity of the complex, thus:

$$A_d \propto \Delta A \quad (1)$$

Where A_d is the amount of indicator that has been absorbed relative to the host, and ΔA is the change in molecular area between the subphase as an indicator solution and pure water. The complex ratio (θ) of the indicator species to the binding sites on the host can be shown by the following Langmuir absorption isotherm:

$$\frac{1}{\theta} = 1 + \frac{1}{K [I]} \quad (2)$$

where $[I]$ represents the concentration of indicator that has been added. From equations (1) and (2) it is found that :

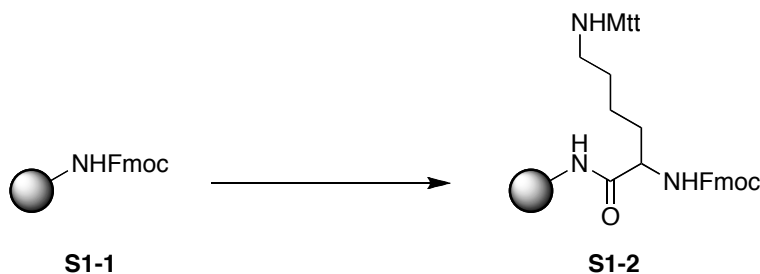
$$\theta = \frac{K [I]}{1+K [I]} = \frac{A_d}{A_{\max}} = \frac{\Delta A}{\Delta A_{\max}} \quad (3)$$

where ΔA_{\max} is the maximum difference in values of molecular area between the subphase as an indicator solution and pure water. From this this equation it is possible to obtain the equation for a linear regression of K - ΔA as follows:

$$\frac{1}{\Delta A} = \frac{1}{\Delta A_{\max}} + \frac{1}{K\Delta A_{\max}} \cdot \frac{1}{[I]} \quad (4)$$

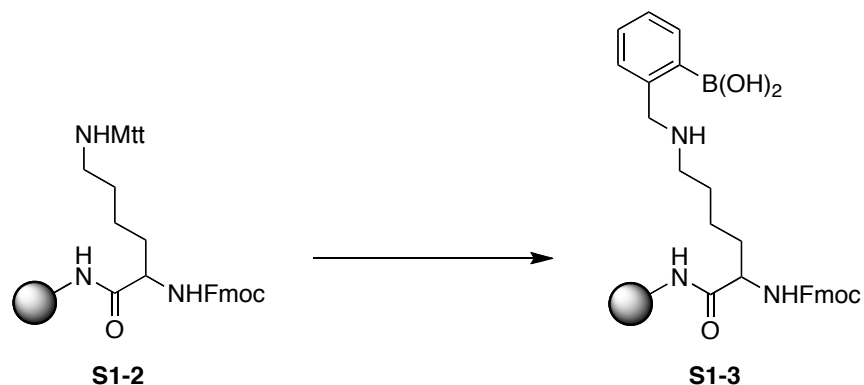
This allows for the creation of a plot of $1/[I]$ versus $1/\Delta A$. In this plot, the y-intercept is calculated to be $1/\Delta A_{\max}$ and a slope of $1/K\Delta A_{\max}$. From this it is possible to calculate the binding constant (K).

5.12.2. Host Synthesis



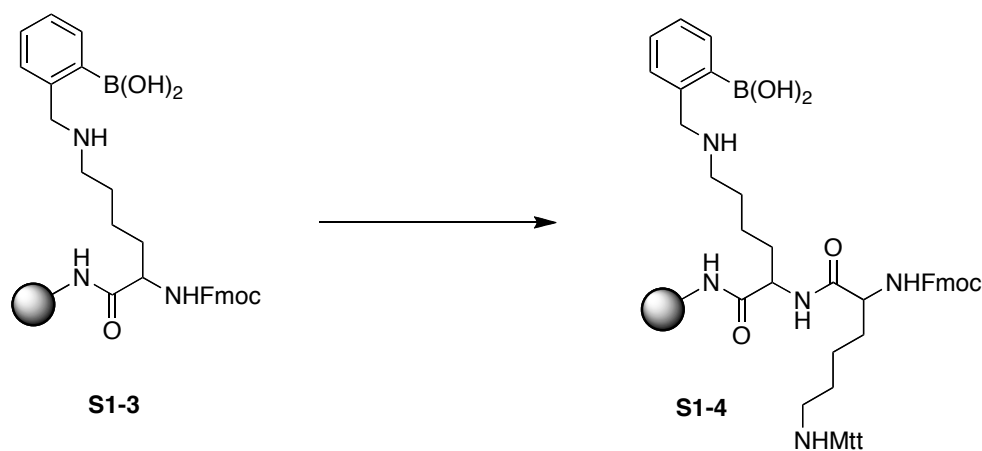
Rink amide resin HL (1.0 g, 1.0 mmol) was shaken with DMF (10 mL) for 30 minutes in order to swell the resin. The resin was then treated with 25 % piperidine in DMF (13 mL) at room temperature. This solution was shaken at room temperature for 1 hour to remove the Fmoc group, then washed with DMF (3×10 mL), DCM (3×10 mL), and then MeOH (3×10 mL). Since the MeOH shrinks the resin, it was subsequently shaken with DMF (10 mL) to ensure it was swelled. Removal of the Fmoc group was confirmed with a ninhydrin test. A separate coupling solution was prepared to contain *N,N,N',N'*-tetramethyl-*O*-(1-*H*-benzotriazol-1-yl)uronium hexafluorophosphate (HBTU) (6.0 mmol, 2.3 g), 1-hydroxybenzotriazol (HOBT) (6.0 mmol, 0.92 g), Fmoc-Lys(Mtt)-OH (6.0 mmol, 3.7 g), and Hünig's base (6.0 mmol, 1.0 mL) in DCM:DMF (10 mL, 1:1). This coupling solution was added to the resin and shaken at room temperature for 4

hours, at which point it was washed with DMF (3 × 10 mL), DCM (3 × 10 mL), and then MeOH (3 × 10 mL). After drying on high vacuum overnight, a small spatula of the resin was placed in a vial that was cooled in an ice bath. The resin was cleaved with TFA (50% in DCM) by stirring for 1 hour and 30 minutes. The beads were filtered away, the solvent evaporated, and the product was analyzed by mass spectrometry. ESI MS: m/z 368.13 (M+H); calculated 368.20 (in the presence of acid, the Mtt protecting group was cleaved to leave a protonated ammonium group).



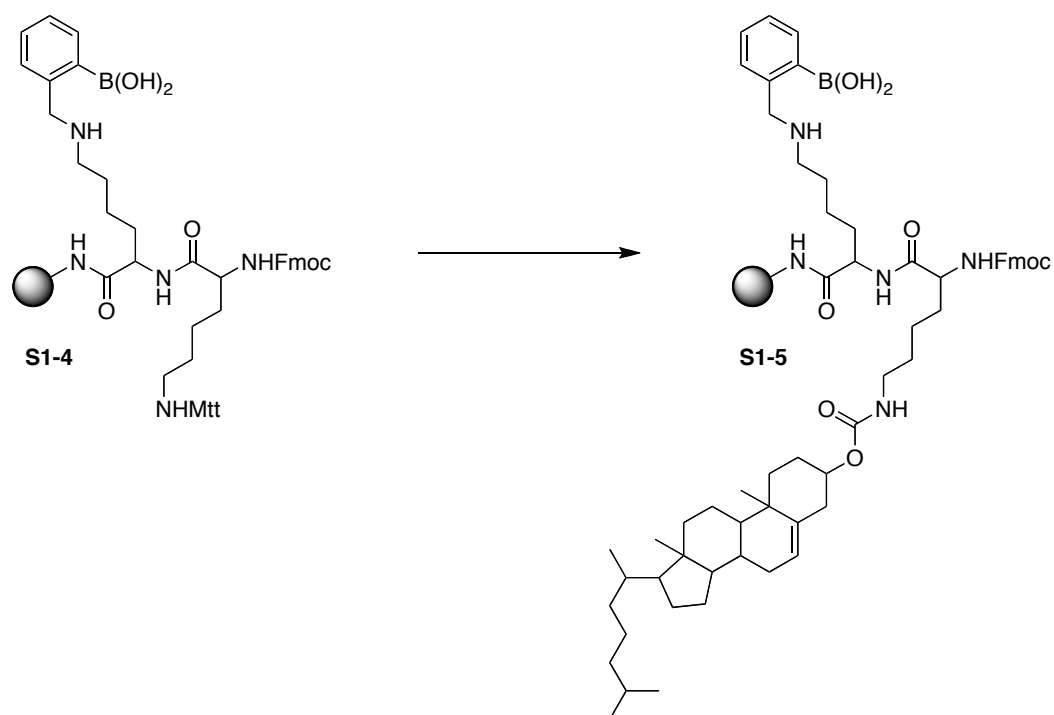
The resin was swelled by shaking with DCM (10 mL) for 10 minutes, and then washed with TFA (9 × 10 mL of 1.8 % TFA in DCM). The resin turned a bright red color, indicating the removal of the Mtt group. Each aliquot of TFA solution was shaken for 2 minutes and filtered off. After the last TFA treatment, the resin was washed with DCM (3 × 10 mL), DMF (3 × 10 mL), DCM (3 × 10 mL), and finally MeOH (3 × 10 mL). Since MeOH shrinks the resin, it had to be swelled again using DMF (10 mL for 10 minutes). The swelled resin was dehydrated by shaking for 30 minutes with a triethyl orthoformate (TeOF) (10 mL) solution that contained 0.1 mL HOAc (glacial). This solution was then drained, and the resin washed with DCM (3 × 10 mL) to remove excess TeOF. To the resin were added MeOH (3 mL), TeOF (3 mL), *N*-methylpyrrolidone

(NMP) (3 mL), HOAc (0.1 mL), and finally 2-formylphenylboronic acid (7.0 mmol, 1.04 g). This mixture was shaken for 6 hours, and the liquid filtered off. Next, MeOH (3 mL), TeOF (3 mL), NMP (3 mL), HOAc (0.1 mL), and NaCNBH₃ (10 mmol, 0.63 g) were added to the resin to reduce the imine and give the desired product. The resin was subjected to the ninhydrin test to confirm the absence of a free amine group, and a small amount cleaved for mass spectrometry as detailed previously. ESI MS: *m/z* 502.54 (M+H); calculated 502.24.



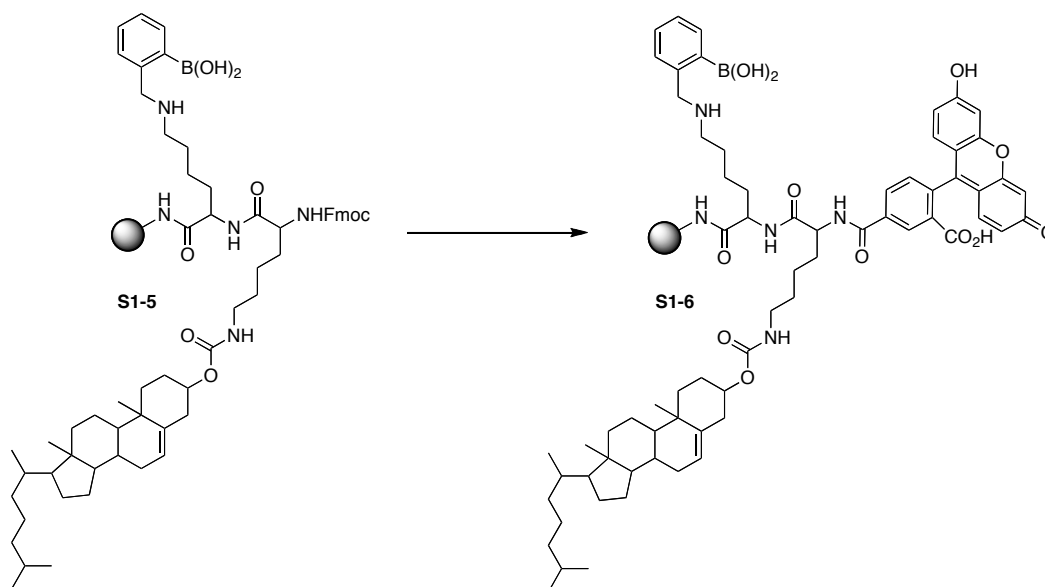
The beads were shaken with DMF (10 mL) for 30 minutes in order to swell the resin. The resin was then treated with 25% piperidine in DMF (13 mL) at room temperature. This solution was shaken at room temperature for 1 hour to remove the Fmoc group, then washed with DMF (3 × 10 mL), DCM (3 × 10 mL), and then MeOH (3 × 10 mL). Since the MeOH shrinks the resin, it was subsequently shaken with DMF (10 mL) to ensure it was swelled. Removal of the Fmoc group was confirmed with a ninhydrin test. A separate coupling solution was made containing HBTU (6.0 mmol, 2.3 g), HOBt (6.0 mmol, 0.92 g), Fmoc-Lys(Mtt)-OH (6.0 mmol, 3.7 g), and Hünig's base (6.0 mmol, 1.0 mL) in DCM:DMF (10 mL, 1:1). This coupling solution was added to the

resin, and shaken at room temperature for 4 hours, at which point the resin was washed with DMF (3 × 10 mL), DCM (3 × 10 mL), and then MeOH (3 × 10 mL). After drying on high vacuum overnight, a small amount of resin was cleaved according to the previous procedure and subjected to mass spectrometry. ESI MS: m/z 630.30 (M+H); calculated 630.35 (in the presence of acid, the Mtt protecting group was cleaved to leave a protonated ammonium group).



Dry DCM (10 mL) was added to the resin to swell it. This solvent was filtered out and followed by addition of an additional amount of DCM (10 mL) containing triethyl amine (1 mL) and cholesteryl chloroformate (6.0 mmol, 2.7 g). This solution was agitated for 4 hours, and the resin was washed with DCM (3 × 10 mL), DMF (3 × 10 mL), and MeOH (3 × 10 mL). A ninhydrin test was performed, confirming the absence of a free

amine. A small amount of resin was cleaved according to the previous procedure and subjected to mass spectrometry. ESI MS: m/z 1042.78 (M+H); calculated 1042.67.



The beads were shaken with DMF (10 mL) for 30 minutes in order to swell the resin. The resin was then treated with 25% piperidine in DMF (13 mL) at room temperature. This solution was shaken at room temperature for 1 hour to remove the Fmoc group, then washed with DMF (3 × 10 mL), DCM (3 × 10 mL), and then MeOH (3 × 10 mL). The MeOH shrinks the resin, so it was subsequently agitated with DMF (10 mL) to ensure it was swelled. Removal of the Fmoc group was confirmed with a ninhydrin test. An activated solution of 5(6)-carboxyfluorescein (CF) was prepared by dissolving CF (3.0 mmol, 1.1 g), diisopropylcarbodiimide (DIC) (3.0 mmol, 470 μ L), and HOBt (3.0 mmol, 0.46 g) in DMF (10 mL). This solution was added to the resin, and allowed to react for 16 hours. The beads were washed with DMF (5 × 10 mL), DCM (5

× 10 mL), MeOH (5 × 10 mL), and finally 20% piperidine solution (10 mL, in DMF) for 1 hour to remove excess CF. After the resin was shaken with piperidine, it was washed with DMF (3 × 10 mL), DCM (3 × 10 mL), MeOH (3 × 10 mL), and dried on high vacuum overnight. The product was cleaved from the resin under acidic TFA conditions (95% TFA, 2.5% triisopropylsilane (TIS), and 2.5% H₂O), which was stirred for 4 hours. The solvent was removed by rotary evaporation, azeotroping with MeOH. The resultant product was dissolved in a solution of THF - H₂O (1:9) and passed through a Sep-Pak Vac 35cc (10 g) tC18 cartridge. The product did not elute until the eluent being passed through was increased to THF - H₂O (1:1), at which point the product was collected and lyophilized to give the target host **1** (147 mg, 12.5%). HR-MS: *m/z* 1178.66 (M+H); calculated 1178.26.

5.13. REFERENCES FOR CHAPTER 5

- (1) Houk, K. N.; Leach, A. G.; Kim, S. P.; Zhang, X. Y. *Angew Chem Int Edit* **2003**, *42*, 4872.
- (2) Lodeiro, C.; Capelo, J. L.; Mejuto, J. C.; Oliveira, E.; Santos, H. M.; Pedras, B.; Nunez, C. *Chem Soc Rev* **2010**, *39*, 2948.
- (3) Dsouza, R. N.; Pischel, U.; Nau, W. M. *Chem Rev* **2011**, *111*, 7941.
- (4) Wu, J.; Liu, W.; Ge, J.; Zhang, H.; Wang, P. *Chem Soc Rev* **2011**, *40*, 3483.
- (5) Ariga, K.; Anslyn, E. V. *J Org Chem* **1992**, *57*, 417.
- (6) Kneeland, D. M.; Ariga, K.; Lynch, V. M.; Huang, C. Y.; Anslyn, E. V. *J Am Chem Soc* **1993**, *115*, 10042.
- (7) Smith, J.; Ariga, K.; Anslyn, E. V. *J Am Chem Soc* **1993**, *115*, 362.
- (8) Kossiakoff, A. A.; Hynes, T.; Devos, A. *Biochem Soc T* **1993**, *21*, 614.

- (9) Springs, B.; Haake, P. *Bioorg Chem* **1977**, *6*, 181.
- (10) Sasaki, D. Y.; Kurihara, K.; Kunitake, T. *J Am Chem Soc* **1991**, *113*, 9685.
- (11) Onda, M.; Yoshihara, K.; Koyano, H.; Ariga, K.; Kunitake, T. *J Am Chem Soc* **1996**, *118*, 8524.
- (12) Sakurai, M.; Tamagawa, H.; Furuki, T.; Inoue, Y.; Ariga, K.; Kunitake, T. *Chem Lett* **1995**, 1001.
- (13) Sakurai, M.; Tamagawa, H.; Inoue, Y.; Ariga, K.; Kunitake, T. *J Phys Chem B* **1997**, *101*, 4810.
- (14) Tamagawa, H.; Sakurai, M.; Inoue, Y.; Ariga, K.; Kunitake, T. *J Phys Chem B* **1997**, *101*, 4817.
- (15) Kitano, H.; Ringsdorf, H. *B Chem Soc Jpn* **1985**, *58*, 2826.
- (16) Taguchi, K.; Ariga, K.; Kunitake, T. *Chem Lett* **1995**, 701.
- (17) Ariga, K.; Kamino, A.; Koyano, H.; Kunitake, T. *J Mater Chem* **1997**, *7*, 1155.
- (18) Izhaky, D.; Addadi, L. *Chem-Eur J* **2000**, *6*, 869.
- (19) Zadnani, R.; Schrader, T. *J Am Chem Soc* **2005**, *127*, 904.
- (20) Wang, C. S.; Zheng, J. Y.; Oliveira, O. N.; Leblanc, R. M. *J Phys Chem C* **2007**, *111*, 7826.
- (21) Ariga, K.; Terasaka, Y.; Sakai, D.; Tsuji, H.; Kikuchi, J. *J Am Chem Soc* **2000**, *122*, 7835.
- (22) Ariga, K.; Nakanishi, T.; Terasaka, Y.; Tsuji, H.; Sakai, D.; Kikuchi, J. *Langmuir* **2005**, *21*, 976.
- (23) Ariga, K.; Nakanishi, T.; Hill, J. P.; Terasaka, Y.; Sakai, D.; Kikuchi, J. *Soft Matter* **2005**, *1*, 132.
- (24) Ariga, K.; Nakanishi, T.; Hill, J. P. *Soft Matter* **2006**, *2*, 465.
- (25) Michinobu, T.; Shinoda, S.; Nakanishi, T.; Hill, J. P.; Fujii, K.; Player, T. N.; Tsukube, H.; Ariga, K. *J Am Chem Soc* **2006**, *128*, 14478.
- (26) Mori, T.; Okamoto, K.; Endo, H.; Hill, J. P.; Shinoda, S.; Matsukura, M.; Tsukube, H.; Suzuki, Y.; Kanekiyo, Y.; Ariga, K. *J Am Chem Soc* **2010**, *132*, 12868.

- (27) Mori, T.; Okamoto, K.; Endo, H.; Sakakibara, K.; Hill, J. P.; Shinoda, S.; Matsukura, M.; Tsukube, H.; Suzuki, Y.; Kanekiyo, Y.; Ariga, K. *Nanoscale Res Lett* **2011**, *6*, 304.
- (28) Michinobu, T.; Shinoda, S.; Nakanishi, T.; Hill, J. P.; Fujii, K.; Player, T. N.; Tsukube, H.; Ariga, K. *Physical chemistry chemical physics : PCCP* **2011**, *13*, 4895.
- (29) Ariga, K.; Mori, T.; Hill, J. P. *Adv Mater* **2012**, *24*, 158.
- (30) Kuivila, H. G.; Keough, A. H.; Soboczanski, E. J. *The Journal of Organic Chemistry* **1954**, *19*, 780.
- (31) Zlokarnik, G.; Negulescu, P. A.; Knapp, T. E.; Mere, L.; Burres, N.; Feng, L. X.; Whitney, M.; Roemer, K.; Tsien, R. Y. *Science* **1998**, *279*, 84.
- (32) Takakusa, H.; Kikuchi, K.; Urano, Y.; Kojima, H.; Nagano, T. *Chemistry* **2003**, *9*, 1479.
- (33) Zhao, Y.; Zheng, Q.; Dakin, K.; Xu, K.; Martinez, M. L.; Li, W. H. *J Am Chem Soc* **2004**, *126*, 4653.
- (34) Furukawa, K.; Nakashima, H.; Kashimura, Y.; Torimitsu, K. *Lab Chip* **2006**, *6*, 1001.
- (35) Zheng, G.; Guo, Y. M.; Li, W. H. *J Am Chem Soc* **2007**, *129*, 10616.
- (36) Lakowicz, J. R. *Principles of fluorescence spectroscopy*; 3rd ed.; Springer: New York, 2006.
- (37) Sapsford, K. E.; Berti, L.; Medintz, I. L. *Angew Chem Int Ed Engl* **2006**, *45*, 4562.
- (38) Sahoo, H. *J. Photochem. Photobiol., C* **2011**, *12*, 20.
- (39) Verma, P. K.; Pal, S. K. *Eur. Phys. J. D* **2010**, *60*, 137.
- (40) Chao, L. K.; Clegg, R. M.; John Wiley & Sons, Inc.: 2009; Vol. 2, p 80.
- (41) Ananthanarayanan, B.; Ni, Q.; Zhang, J. *Methods Cell Biol.* **2008**, *89*, 37.
- (42) Merrifield, R. B. *J Am Chem Soc* **1963**, *85*, 2149.
- (43) Chechel, O. V.; Nikolaev, E. N. *Instrum Exp Tech+* **1991**, *34*, 750.
- (44) Tanaka, K.; Manning, P. A.; Lau, V. K.; Yu, H. *Langmuir* **1998**, *15*, 600.
- (45) Zhu, L.; Zhong, Z.; Anslyn, E. V. *J Am Chem Soc* **2005**, *127*, 4260.

- (46) Li, X. L.; Xu, W. Q.; Jia, H. Y.; Wang, X.; Zhao, B.; Li, B. F.; Ozaki, Y. *J Colloid Interf Sci* **2004**, *274*, 9.
- (47) Bos, M. A.; Kleijn, J. M. *Biophys J* **1995**, *68*, 2566.
- (48) Lim, S. H.; Musto, C. J.; Park, E.; Zhong, W.; Suslick, K. S. *Org Lett* **2008**, *10*, 4405.
- (49) Luo, D.; Wu, L.; Zhi, J. *ACS Nano* **2009**, *3*, 2121.
- (50) Liu, Y.; Deng, C.; Tang, L.; Qin, A.; Hu, R.; Sun, J. Z.; Tang, B. Z. *J Am Chem Soc* **2011**, *133*, 660.
- (51) Zhang, T.; Anslyn, E. V. *Org Lett* **2007**, *9*, 1627.

Bibliography

- Adams, R.; Yuan, H. C. *Chem Rev* **1933**, *12*, 261.
- Ait-Haddou, H.; Wiskur, S. L.; Lynch, V. M.; Anslyn, E. V. *J Am Chem Soc* **2001**, *123*, 11296.
- Alexakis, A.; Chauvin, A. S. *Tetrahedron-Asymmetr* **2000**, *11*, 4245.
- Alexakis, A.; Chauvin, A. S. *Tetrahedron-Asymmetr* **2001**, *12*, 1411.
- Altomare, A.; Giacobazzo, C.; Guagliardi, A.; Moliterni, A. G. G.; Rizzi, R. *J Appl Crystallogr* **1999**, *32*, 963.
- Amendola, V.; Fabbrizzi, L.; Mangano, C.; Pallavicini, P.; Poggi, A.; Taglietti, A. *Coordin Chem Rev* **2001**, *219*, 821.
- Ananthanarayanan, B.; Ni, Q.; Zhang, J. *Methods Cell Biol.* **2008**, *89*, 37.
- Anderson, R. C.; Shapiro, M. J. *J Org Chem* **1984**, *49*, 1304.
- Appella, D. H.; Christianson, L. A.; Klein, D. A.; Powell, D. R.; Huang, X. L.; Barchi, J. J.; Gellman, S. H. *Nature* **1997**, *387*, 381.
- Ariga, K.; Anslyn, E. V. *J Org Chem* **1992**, *57*, 417.
- Ariga, K.; Kamino, A.; Koyano, H.; Kunitake, T. *J Mater Chem* **1997**, *7*, 1155.
- Ariga, K.; Mori, T.; Hill, J. P. *Adv Mater* **2012**, *24*, 158.
- Ariga, K.; Nakanishi, T.; Hill, J. P. *Soft Matter* **2006**, *2*, 465.
- Ariga, K.; Nakanishi, T.; Hill, J. P.; Terasaka, Y.; Sakai, D.; Kikuchi, J. *Soft Matter* **2005**, *1*, 132.
- Ariga, K.; Nakanishi, T.; Terasaka, Y.; Tsuji, H.; Sakai, D.; Kikuchi, J. *Langmuir* **2005**, *21*, 976.
- Ariga, K.; Terasaka, Y.; Sakai, D.; Tsuji, H.; Kikuchi, J. *J Am Chem Soc* **2000**, *122*, 7835.
- Asfari, Z. *Calixarenes 2001*; Kluwer Academic Publishers: Dordrecht ; Boston, 2001.
- Beeren, S. R.; Sanders, J. K. M. *J Am Chem Soc* **2011**, *133*, 3804.
- Berova, N.; Di Bari, L.; Pescitelli, G. *Chem Soc Rev* **2007**, *36*, 914.

- Berova, N.; Nakanishi, K. o.; Woody, R. *Circular dichroism : principles and applications*; 2nd ed.; Wiley-VCH: New York, 2000.
- Bissell, R. A.; De Silva, A. P.; Gunaratne, H. Q. N.; Lynch, P. L. M.; Maguire, G. E. M.; Sandanayake, K. R. A. S. *Chem Soc Rev* **1992**, *21*, 187.
- Bissell, R. A.; De Silva, A. P.; Gunaratne, H. Q. N.; Lynch, P. L. M.; Mccoy, C. P.; Maguire, G. E. M.; Sandanayake, K. R. A. S. *Fluorescent Chemosensors for Ion and Molecule Recognition* **1993**, 538, 45.
- Blaschke, G.; Kraft, H. P.; Fickentscher, K.; Kohler, F. *Arzneimittel-Forsch* **1979**, *29-2*, 1640.
- Bonizzoni, M.; Fabbrizzi, L.; Piovani, G.; Taglietti, A. *Tetrahedron* **2004**, *60*, 11159.
- Bos, M. A.; Kleijn, J. M. *Biophys J* **1995**, *68*, 2566.
- Bressolle, F.; Audran, M.; Pham, T. N.; Vallon, J. J. *J Chromatogr B Biomed Appl* **1996**, *687*, 303.
- Bringmann, G.; Menche, D. *Accounts Chem Res* **2001**, *34*, 615.
- Bringmann, G.; Mortimer, A. J. P.; Keller, P. A.; Gresser, M. J.; Garner, J.; Breuning, M. *Angew Chem Int Edit* **2005**, *44*, 5384.
- Brown, E.; Chevalier, C.; Huet, F. o.; Le Grumelec, C.; Lv/©zv/©, A.; Touet, J. I. *Tetrahedron: Asymmetry* **1994**, *5*, 1191.
- Buryak, A.; Severin, K. *J Am Chem Soc* **2005**, *127*, 3700.
- Cahn, R. S.; Ingold, C.; Prelog, V. *Angew. Chem., Int. Ed. Engl.* **1966**, *5*, 385.
- Canary, J. W.; Allen, C. S.; Castagnetto, J. M.; Chiu, Y. H.; Toscano, P. J.; Wang, Y. H. *Inorg Chem* **1998**, *37*, 6255.
- Canary, J. W.; Allen, C. S.; Castagnetto, J. M.; Wang, Y. H. *J Am Chem Soc* **1995**, *117*, 8484.
- Canary, J. W.; Mortezaei, S.; Liang, J. A. *Coordin Chem Rev* **2010**, *254*, 2249.
- Carballeira, N. M.; Colon, R. *Tetrahedron-Asymmetr* **1999**, *10*, 3785.
- Carballeira, N. M.; Colon, R.; Emiliano, A. *J Nat Prod* **1998**, *61*, 675.
- Carrell, C. J.; Carrell, H. L.; Erlebacher, J.; Glusker, J. P. *J Am Chem Soc* **1988**, *110*, 8651.

Castagnetto, J. M.; Xu, X.; Berova, N. D.; Canary, J. W. *Chirality* **1997**, *9*, 616.

Chang, S. K.; Vanengen, D.; Fan, E.; Hamilton, A. D. *J Am Chem Soc* **1991**, *113*, 7640.

Chao, L. K.; Clegg, R. M.; John Wiley & Sons, Inc.: 2009; Vol. 2, p 80.

Chechel, O. V.; Nikolaev, E. N. *Instrum Exp Tech+* **1991**, *34*, 750.

Chen, Z. H.; He, Y. B.; Hu, C. G.; Huang, X. H.; Hu, L. *Aust J Chem* **2008**, *61*, 310.

Chi, L.; Zhao, J.; James, T. D. *The Journal of Organic Chemistry* **2008**, *73*, 4684.

Chirality **1992**, *4*, 338.

Choi, K.; Hamilton, A. D. *Angew Chem Int Edit* **2001**, *40*, 3912.

Choi, M. K.; Kim, H. N.; Choi, H. J.; Yoon, J.; Hyun, M. H. *Tetrahedron Lett* **2008**, *49*, 4522.

Christmann, M.; Bräse, S. *Asymmetric synthesis : the essentials*; Wiley-VCH: Weinheim, 2007.

Clayden, J.; Fletcher, S. P.; McDouall, J. J. W.; Rowbottom, S. J. M. *J Am Chem Soc* **2009**, *131*, 5331.

Clayden, J.; Moran, W. J.; Edwards, P. J.; LaPlante, S. R. *Angew Chem Int Ed Engl* **2009**, *48*, 6398.

Colladon, M.; Scarso, A.; Strukul, G. *Synlett* **2006**, *2006*, 3515.

Coppola, G. M.; Schuster, H. F. *[Alpha]-hydroxy acids in enantioselective syntheses*; VCH: Weinheim, 1997.

Corbett, P. T.; Leclaire, J.; Vial, L.; West, K. R.; Wietor, J. L.; Sanders, J. K. M.; Otto, S. *Chem Rev* **2006**, *106*, 3652.

Crabtree, R. H. *Chem Commun* **1999**, 1611.

Daigle, D. J.; Decuir, T. J.; Robertson, J. B.; Darensbourg, D. J. In *Inorganic Syntheses*; John Wiley & Sons, Inc.: 2007, p 40.

Dalisay, D. S.; Tsukamoto, S.; Molinski, T. F. *J Nat Prod* **2009**, *72*, 353.

Davydov, A. S. *Theory of molecular excitons*; McGraw-Hill: New York, 1962.

de Vries, J. G.; Lefort, L. *Chem-Eur J* **2006**, *12*, 4722.

de Vries, J. G.; Lefort, L. *Chemistry – A European Journal* **2006**, *12*, 4722.

Dekker, J.; Boersma, J.; Fernholt, L.; Haaland, A.; Spek, A. L. *Organometallics* **1987**, *6*, 1202.

Demirtas, H. N.; Bozkurt, S.; Durmaz, M.; Yilmaz, M.; Sirit, A. *Tetrahedron-Asymmetr* **2008**, *19*, 2020.

Demunari, S.; Marazzi, G.; Forgiione, A.; Longo, A.; Lombardi, P. *Tetrahedron Lett* **1980**, *21*, 2273.

Dhara, K.; Sarkar, K.; Roy, P.; Nandi, M.; Bhaumik, A.; Banerjee, P. *Tetrahedron* **2008**, *64*, 3153.

Dolbier, W. R.; Editor *Guide to Fluorine NMR for Organic Chemists*; John Wiley & Sons, Inc., 2009.

Dragna, J. M.; Pescitelli, G.; Tran, L.; Lynch, V. M.; Anslyn, E. V.; Di Bari, L. *J Am Chem Soc* **2012**, *134*, 4398.

Dreher, S. D.; Katz, T. J.; Lam, K. C.; Rheingold, A. L. *J Org Chem* **2000**, *65*, 815.

Dsouza, R. N.; Pischel, U.; Nau, W. M. *Chem Rev* **2011**, *111*, 7941.

Eliel, E. L.; Wilen, S. H.; Mander, L. N. *Stereochemistry of organic compounds*; Wiley: New York, 1994.

Ema, T.; Tanida, D.; Sakai, T. *Org Lett* **2006**, *8*, 3773.

Erb, S. *Pharmaceut. Technol.* **2006**, *30*, 14.

Fabbrizzi, L.; Marcotte, N.; Stomeo, F.; Taglietti, A. *Angew Chem Int Edit* **2002**, *41*, 3811.

Ferreiro, M. J.; Latypov, S. K.; Quinoa, E.; Riguera, R. *J Org Chem* **2000**, *65*, 2658.

Folmer-Andersen, J. F.; Kitamura, M.; Anslyn, E. V. *J Am Chem Soc* **2006**, *128*, 5652.

Folmer-Andersen, J. F.; Lynch, V. M.; Anslyn, E. V. *Chem-Eur J* **2005**, *11*, 5319.

Folmer-Andersen, J. F.; Lynch, V. M.; Anslyn, E. V. *J Am Chem Soc* **2005**, *127*, 7986.

Frison, J.-C. d.; Palazzi, C.; Bolm, C. *Tetrahedron* **2006**, *62*, 6700.

Fulwood, R.; Parker, D. *Tetrahedron-Asymmetr* **1992**, *3*, 25.

Furukawa, K.; Nakashima, H.; Kashimura, Y.; Torimitsu, K. *Lab Chip* **2006**, *6*, 1001.

Gawronski, J.; Grajewski, J.; Drabowicz, J.; Mikolajczyk, M. *J Org Chem* **2003**, *68*, 9821.

Gennari, C.; Piarulli, U. *Chem Rev* **2003**, *103*, 3071.

Gorenstein, D. G. *Prog Nucl Mag Res Sp* **1983**, *16*, 1.

Griesbeck, A. G.; Hanft, S.; Miara, Y. D. *Photoch Photobio Sci* **2010**, *9*, 1385.

Groger, H. *Chem Rev* **2003**, *103*, 2795.

Gubitz, G. *Chromatographia* **1990**, *30*, 555.

Gübitz, G.; Schmid, M. G. *Chiral separations : methods and protocols*; Humana Press: Totowa, N.J., 2004.

Gustafson, J. L.; Lim, D.; Miller, S. J. *Science* **2010**, *328*, 1251.

Haginaka, J. *Journal of Chromatography A* **2001**, *906*, 253.

Han, M. S.; Kim, D. H. *Tetrahedron* **2004**, *60*, 11251.

Harada, N.; Nakanishi, K. o. *Circular dichroic spectroscopy : exciton coupling in organic stereochemistry*; University Science Books: Mill Valley, CA, 1983.

Hayashi, T.; Hayashizaki, K.; Kiyoi, T.; Ito, Y. *J Am Chem Soc* **1988**, *110*, 8153.

Hintermann, T.; Seebach, D. *Chimia* **1997**, *51*, 244.

Holmes, A. E.; Das, D.; Canary, J. W. *J Am Chem Soc* **2007**, *129*, 1506.

Holmes, A. E.; Simpson, S. A.; Canary, J. W. *Monatsh Chem* **2005**, *136*, 461.

Holmes, A. E.; Zahn, S.; Canary, J. W. *Chirality* **2002**, *14*, 471.

Hong, Y.; Lam, J. W.; Tang, B. Z. *Chem Commun* **2009**, 4332.

Hor, K.; Gimple, O.; Schreier, P.; Humpf, H. U. *J Org Chem* **1998**, *63*, 322.

Houk, K. N.; Leach, A. G.; Kim, S. P.; Zhang, X. Y. *Angew Chem Int Edit* **2003**, *42*, 4872.

Hughes, G.; Kimura, M.; Buchwald, S. L. *J Am Chem Soc* **2003**, *125*, 11253.

Hunta, R. A. R.; Otto, S. *Chem Commun (Camb)* **2011**, *47*, 847.

Ikeda, A.; Shinkai, S. *Chem Rev* **1997**, *97*, 1713.

Izhaky, D.; Addadi, L. *Chem-Eur J* **2000**, *6*, 869.

Jahn, H. A.; Teller, E. *Proceedings of the Royal Society of London. Series A - Mathematical and Physical Sciences* **1937**, *161*, 220.

Jakel, C.; Paciello, R. *Chem Rev* **2006**, *106*, 2912.

Jakobsche, C. E.; Peris, G.; Miller, S. J. *Angew Chem Int Ed Engl* **2008**, *47*, 6707.

- James, T. D.; Sandanayake, K. R. A. S.; Shinkai, S. *Angewandte Chemie-International Edition in English* **1994**, *33*, 2207.
- James, T. D.; Sandanayake, K. R. A. S.; Shinkai, S. *J Chem Soc Chem Comm* **1994**, 477.
- James, T. D.; Sandanayake, K. R. A. S.; Shinkai, S. *Nature* **1995**, *374*, 345.
- Johnson, F. *Chem Rev* **1968**, *68*, 375.
- Johnson, R. A. W., D. W. *Applied Multivariate Statistical Analysis*; Prentice-Hall: New Jersey, 1982.
- Joyce, L. A.; Maynor, M. S.; Dragna, J. M.; da Cruz, G. M.; Lynch, V. M.; Canary, J. W.; Anslyn, E. V. *J Am Chem Soc* **2011**, *133*, 13746.
- Kacprzak, K.; Grajewski, J.; Gawronski, J. *Tetrahedron-Asymmetr* **2006**, *17*, 1332.
- Kaiser, E.; Colescott, R. L.; Bossinger, C. D.; Cook, P. I. *Anal Biochem* **1970**, *34*, 595.
- Kakiuchi, F.; Le Gendre, P.; Yamada, A.; Ohtaki, H.; Murai, S. *Tetrahedron-Asymmetr* **2000**, *11*, 2647.
- Karlin, K. D.; Wei, N.; Jung, B.; Kaderli, S.; Niklaus, P.; Zuberbuhler, A. D. *J Am Chem Soc* **1993**, *115*, 9506.
- Katsuki, T. *Russian Chemical Bulletin* **2004**, *53*, 1859.
- Kenner, J.; Stubbings, W. V. *J. Chem. Soc., Trans.* **1921**, *119*, 593.
- Kitano, H.; Ringsdorf, H. *B Chem Soc Jpn* **1985**, *58*, 2826.
- Klapötke, T. M.; Broschag, M. *Compilation of reported ⁷⁷Se NMR chemical shifts : up to the year 1994*; Wiley: Chichester ; New York, 1996.
- Kneeland, D. M.; Ariga, K.; Lynch, V. M.; Huang, C. Y.; Anslyn, E. V. *J Am Chem Soc* **1993**, *115*, 10042.
- Knobel, A. K. H.; Escher, I. H.; Pfaltz, A. *Synlett* **1997**, 1429.
- Konig, W.; Geiger, R. *Chem Ber* **1970**, *103*, 788.
- Kossiakoff, A. A.; Hynes, T.; Devos, A. *Biochem Soc T* **1993**, *21*, 614.
- Kovaricek, P.; Lehn, J.-M. *J. Am. Chem. Soc.* **2012**, *134*, 9446.
- Krauthauser, S.; Christianson, L. A.; Powell, D. R.; Gellman, S. H. *J Am Chem Soc* **1997**, *119*, 11719.
- Krow, G. R. In *Organic Reactions*; John Wiley & Sons, Inc.: 2004.

Kruppa, M.; Konig, B. *Chem Rev* **2006**, *106*, 3520.

Kubo, Y.; Maeda, S. y.; Tokita, S.; Kubo, M. *Nature (London)* **1996**, *382*, 522.

Kuivila, H. G.; Keough, A. H.; Soboczenski, E. J. *The Journal of Organic Chemistry* **1954**, *19*, 780.

Kuntz, K. W.; Snapper, M. L.; Hoveyda, A. H. *Curr Opin Chem Biol* **1999**, *3*, 313.

Lakowicz, J. R. *Principles of fluorescence spectroscopy*; 3rd ed.; Springer: New York, 2006.

Lavigne, J. J.; Anslyn, E. V. *Angew Chem Int Edit* **2001**, *40*, 3119.

Lee, D. H.; Lee, K. H.; Hong, J. I. *Org Lett* **2001**, *3*, 5.

Lee, S. J.; Lin, W. B. *J Am Chem Soc* **2002**, *124*, 4554.

Lefort, L.; Boogers, J. A. F.; de Vries, A. H. M.; de Vries, J. G. *Top Catal* **2006**, *40*, 185.

Lehn, J. M. *Chem Soc Rev* **2007**, *36*, 151.

Lelais, G.; Seebach, D. *Biopolymers* **2004**, *76*, 206.

Leung, D.; Anslyn, E. V. *Org Lett* **2011**, *13*, 2298.

Leung, D.; Folmer-Andersen, J. F.; Lynch, V. M.; Anslyn, E. V. *J Am Chem Soc* **2008**, *130*, 12318.

Li, D. M.; Zheng, Y. S. *Chem Commun* **2011**, *47*, 10139.

Li, X. L.; Hewgley, J. B.; Mulrooney, C. A.; Yang, J. M.; Kozlowski, M. C. *J Org Chem* **2003**, *68*, 5500.

Li, X. L.; Xu, W. Q.; Jia, H. Y.; Wang, X.; Zhao, B.; Li, B. F.; Ozaki, Y. *J Colloid Interf Sci* **2004**, *274*, 9.

Li, Y.; Miller, S. J. *The Journal of organic chemistry* **2011**, *76*, 9785.

Lichter, P. A.; Miller, S. J. *ACS Comb Sci* **2011**, *13*, 321.

Lim, S. H.; Musto, C. J.; Park, E.; Zhong, W.; Suslick, K. S. *Org Lett* **2008**, *10*, 4405.

Lin, G.-Q.; Li, Y.-M.; Chan, A. S.-C. *Principles and applications of asymmetric synthesis*; John Wiley & Sons: New York, 2001.

Lin, G.-Q.; You, Q.-D.; Cheng, J.-F. *Chiral drugs : chemistry and biological action*; Wiley: Hoboken, N.J., 2011.

Lin, J.; Rajararn, A. R.; Pu, L. *Tetrahedron* **2004**, *60*, 11277.

Lin, J.; Zhang, H. C.; Pu, L. *Org Lett* **2002**, *4*, 3297.

Liu, S. L.; Pestano, J. P. C.; Wolf, C. *J Org Chem* **2008**, *73*, 4267.

Liu, Y.; Deng, C.; Tang, L.; Qin, A.; Hu, R.; Sun, J. Z.; Tang, B. Z. *J Am Chem Soc* **2011**, *133*, 660.

Lodeiro, C.; Capelo, J. L.; Mejuto, J. C.; Oliveira, E.; Santos, H. M.; Pedras, B.; Nunez, C. *Chem Soc Rev* **2010**, *39*, 2948.

Lohray, B. B. *Curr. Sci.* **2001**, *81*, 1519.

Luo, D.; Wu, L.; Zhi, J. *ACS Nano* **2009**, *3*, 2121.

Luthra, N. P.; Dunlap, R. B.; Odom, J. D. *J Magn Reson* **1982**, *46*, 152.

Ma, F. N.; Ai, L.; Shen, X. M.; Zhang, C. *Org Lett* **2007**, *9*, 125.

Ma, J. A. *Angew Chem Int Ed Engl* **2003**, *42*, 4290.

Malkov, A. V.; Friscourt, F.; Bell, M.; Swarbrick, M. E.; Kocovsky, P. *The Journal of Organic Chemistry* **2008**, *73*, 3996.

Maruoka, K.; Ooi, T. *Chem Rev* **2003**, *103*, 3013.

Mastalerz, M. *Angew Chem Int Edit* **2010**, *49*, 5042.

Mateos, J. L.; Cram, D. J. *J Am Chem Soc* **1959**, *81*, 2756.

Matile, S.; Berova, N.; Nakanishi, K.; Fleischhauer, J.; Woody, R. W. *J Am Chem Soc* **1996**, *118*, 5198.

Matile, S.; Berova, N.; Nakanishi, K.; Novkova, S.; Philipova, I.; Blagoev, B. *J Am Chem Soc* **1995**, *117*, 7021.

McCarpa, F.; Long, P. V. *Tetrahedron Letters* **1981**, *22*, 3009.

Mei, X.; Wolf, C. *J Am Chem Soc* **2004**, *126*, 14736.

Mei, X.; Wolf, C. *Tetrahedron Lett* **2006**, *47*, 7901.

Merrifield, R. B. *J Am Chem Soc* **1963**, *85*, 2149.

Meyer, C. D.; Joiner, C. S.; Stoddart, J. F. *Chem Soc Rev* **2007**, *36*, 1705.

Michinobu, T.; Shinoda, S.; Nakanishi, T.; Hill, J. P.; Fujii, K.; Player, T. N.; Tsukube, H.; Ariga, K. *J. Am. Chem. Soc.* **2006**, *128*, 14478.

Michinobu, T.; Shinoda, S.; Nakanishi, T.; Hill, J. P.; Fujii, K.; Player, T. N.; Tsukube, H.; Ariga, K. *Physical chemistry chemical physics : PCCP* **2011**, *13*, 4895.

Mihovilovic, M. D. *Current Organic Chemistry* **2006**, *10*, 1265.

Misaki, H.; Miyake, H.; Shinoda, S.; Tsukube, H. *Inorg Chem* **2009**, *48*, 11921.

Mohr, G. J. *Chem-Eur J* **2004**, *10*, 1082.

Moore, E. A. A., E. W.; Janes, R. *Metal-Ligand Bonding*; Royal Society of Chemistry, 2004.

Mori, T.; Okamoto, K.; Endo, H.; Hill, J. P.; Shinoda, S.; Matsukura, M.; Tsukube, H.; Suzuki, Y.; Kanekiyo, Y.; Ariga, K. *J Am Chem Soc* **2010**, *132*, 12868.

Mori, T.; Okamoto, K.; Endo, H.; Sakakibara, K.; Hill, J. P.; Shinoda, S.; Matsukura, M.; Tsukube, H.; Suzuki, Y.; Kanekiyo, Y.; Ariga, K. *Nanoscale Res Lett* **2011**, *6*, 304.

Murahashi, S.; Ono, S.; Imada, Y. *Angew Chem Int Ed Engl* **2002**, *41*, 2366.

Nagai, Y.; Kusumi, T. *Tetrahedron Lett* **1995**, *36*, 1853.

Najera, C.; Sansano, J. M. *Chem Rev* **2007**, *107*, 4584.

Nguyen, B. T.; Anslyn, E. V. *Coordin Chem Rev* **2006**, *250*, 3118.

Nicolaou, K. C.; Snyder, A. *Classics in Total Synthesis II: Targets, Strategies, Methods*; John Wiley & Sons, 2003.

Nicolaou, K. C.; Sorensen, E. J. *Classics in total synthesis : targets, strategies, methods*; VCH: Weinheim ; New York, 1996.

Nieto, S.; Dragna, J. M.; Anslyn, E. V. *Chem-Eur J* **2010**, *16*, 227.

Nieto, S.; Lynch, V. M.; Anslyn, E. V.; Kim, H.; Chin, J. *J Am Chem Soc* **2008**, *130*, 9232.

Nieto, S.; Lynch, V. M.; Anslyn, E. V.; Kim, H.; Chin, J. *Org Lett* **2008**, *10*, 5167.

Noyori, R.; Takaya, H. *Accounts Chem Res* **1990**, *23*, 345.

Onda, M.; Yoshihara, K.; Koyano, H.; Ariga, K.; Kunitake, T. *J Am Chem Soc* **1996**, *118*, 8524.

Osowska, K.; Miljanic, O. S. *J Am Chem Soc* **2011**, *133*, 724.

Otwinowski, Z.; Minor, W. *Macromolecular Crystallography, Pt A* **1997**, 276, 307.

Pamies, O.; Dieguez, M. *Chem-Eur J* **2008**, *14*, 944.

Park, H.; Kim, K. M.; Lee, A.; Ham, S.; Nam, W.; Chin, J. *J Am Chem Soc* **2007**, *129*, 1518.

Parker, D. *J Chem Soc Perk T 2* **1983**, 83.

Patai, S.; Rappoport, Z.; Editors *The Chemistry of Organic Selenium and Tellurium Compounds, Vol. 1*; John Wiley and Sons, 1986.

Peris, G.; Miller, S. J. *Org Lett* **2008**, *10*, 3049.

Pescarmona, P. P.; van der Waal, J. C.; Maxwell, I. E.; Maschmeyer, T. *Catal Lett* **1999**, *63*, 1.

Pfeiffer, P.; Quehl, K.; Tappermann, F. *Ber. Dtsch. Chem. Ges. B* **1930**, *63B*, 1301.

Pirkle, W. H.; Hauske, J. R. *The Journal of Organic Chemistry* **1977**, *42*, 2436.

Player, T. N.; Shinoda, S.; Tsukube, H. *Org. Biomol. Chem.* **2005**, *3*, 1615.

Poleschner, H.; Radeglia, R.; Meyer, H. *Org Magn Resonance* **1984**, *22*, 480.

Pu, L. *Accounts Chem Res* **2011**, *45*, 150.

Pu, L. *Chem Rev* **1998**, *98*, 2405.

Pu, L. *Chem Rev* **2004**, *104*, 1687.

Qing, G. Y.; He, Y. B.; Zhao, Y.; Hu, C. G.; Liu, S. Y.; Yang, X. *Eur J Org Chem* **2006**, 1574.

Queiroz, M.-J.; Joseph, D.; Kirsch, G. *Organic Preparations and Procedures International* **1995**, *27*, 120.

Raban, M.; Mislow, K. *Tetrahedron Lett* **1965**, 4249.

Rabenstein, D. L.; Tan, K. S. *Magn Reson Chem* **1988**, *26*, 1079.

Reetz, M. T. *Angew Chem Int Edit* **2001**, *40*, 284.

Rowan, S. J.; Cantrill, S. J.; Cousins, G. R.; Sanders, J. K.; Stoddart, J. F. *Angew Chem Int Ed Engl* **2002**, *41*, 898.

Rukachaisirikul, V.; Koert, U.; Hoffmann, R. W. *Tetrahedron* **1992**, *48*, 4533.

Sahoo, H. *J. Photochem. Photobiol., C* **2011**, *12*, 20.

Sajonz, P.; Gong, X.; Leonard, W. R., Jr.; Biba, M.; Welch, C. J. *Chirality* **2006**, *18*, 803.

Sajonz, P.; Schafer, W.; Gong, X.; Shultz, S.; Rosner, T.; Welch, C. J. *J Chromatogr A* **2007**, *1145*, 149.

- Sakurai, M.; Tamagawa, H.; Furuki, T.; Inoue, Y.; Ariga, K.; Kunitake, T. *Chem Lett* **1995**, 1001.
- Sakurai, M.; Tamagawa, H.; Inoue, Y.; Ariga, K.; Kunitake, T. *J Phys Chem B* **1997**, *101*, 4810.
- Salvatore, B. A.; Smith, A. B. *Tetrahedron Lett* **1994**, *35*, 1329.
- Sapsford, K. E.; Berti, L.; Medintz, I. L. *Angew Chem Int Ed Engl* **2006**, *45*, 4562.
- Sasaki, D. Y.; Kurihara, K.; Kunitake, T. *J Am Chem Soc* **1991**, *113*, 9685.
- Schurig, V. *J Chromatogr A* **2001**, *906*, 275.
- Seebach, D.; Beck, A. K. *Chimia* **1997**, *51*, 293.
- Seebach, D.; Gademann, K.; Schreiber, J. V.; Matthews, J. L.; Hintermann, T.; Jaun, B.; Oberer, L.; Hommel, U.; Widmer, H. *Helv Chim Acta* **1997**, *80*, 2033.
- Seebach, D.; Jaeschke, G.; Gottwald, K.; Matsuda, K.; Formisano, R.; Chaplin, D. A.; Breuning, M.; Bringmann, G. *Tetrahedron* **1997**, *53*, 7539.
- Seebach, D.; Matthews, J. L. *Chem Commun* **1997**, 2015.
- Seyden-Penne, J. *Chiral auxiliaries and ligands in asymmetric synthesis*; Wiley: New York, 1995.
- Shimizu, K. D.; Snapper, M. L.; Hoveyda, A. H. *Chem-Eur J* **1998**, *4*, 1885.
- Shindo, M.; Koga, K.; Tomioka, K. *J Am Chem Soc* **1992**, *114*, 8732.
- Silks, L. A.; Dunlap, R. B.; Odom, J. D. *J Am Chem Soc* **1990**, *112*, 4979.
- Silks, L. A.; Peng, J.; Odom, J. D.; Dunlap, R. B. *J Chem Soc Perk T 1* **1991**, 2495.
- Silks, L. A.; Peng, J.; Odom, J. D.; Dunlap, R. B. *J Org Chem* **1991**, *56*, 6733.
- Smith, J.; Ariga, K.; Anslyn, E. V. *J Am Chem Soc* **1993**, *115*, 362.
- Sogah, G. D. Y.; Cram, D. J. *J Am Chem Soc* **1979**, *101*, 3035.
- Song, F.; Wei, G.; Wang, L.; Jiao, J.; Cheng, Y.; Zhu, C. *The Journal of Organic Chemistry* **2012**, *77*, 4759.
- Springs, B.; Haake, P. *Bioorg Chem* **1977**, *6*, 181.
- Stambuli, J. P.; Hartwig, J. F. *Curr Opin Chem Biol* **2003**, *7*, 420.
- Stoughton, R. W.; Adams, R. *J Am Chem Soc* **1932**, *54*, 4426.

- Subramanian, G. *Chiral separation techniques : a practical approach*; 2nd completely rev. and updated ed.; Wiley-VCH: Weinheim ; New York, 2001.
- Tabei, J.; Shiotsuki, M.; Sanda, F.; Masuda, T. *Macromolecules* **2005**, *38*, 9448.
- Taft, R. W., Jr. *Steric effects in organic chemistry* **1956**, 556.
- Taguchi, K.; Ariga, K.; Kunitake, T. *Chem Lett* **1995**, 701.
- Takakusa, H.; Kikuchi, K.; Urano, Y.; Kojima, H.; Nagano, T. *Chemistry* **2003**, *9*, 1479.
- Tamagawa, H.; Sakurai, M.; Inoue, Y.; Ariga, K.; Kunitake, T. *J Phys Chem B* **1997**, *101*, 4817.
- Tanaka, K.; Fukuda, N. *Tetrahedron-Asymmetr* **2009**, *20*, 111.
- Tanaka, K.; Manning, P. A.; Lau, V. K.; Yu, H. *Langmuir* **1998**, *15*, 600.
- Tanaka, K.; Tsuchitani, T.; Fukuda, N.; Masumoto, A.; Arakawa, R. *Tetrahedron-Asymmetr* **2012**, *23*, 205.
- Tarasow, T. M.; Tarasow, S. L.; Eaton, B. E. *Nature* **1997**, *389*, 54.
- ten Brink, G. J.; Arends, I. W. C. E.; Sheldon, R. A. *Chem Rev* **2004**, *104*, 4105.
- Terrett, N. K.; Gardner, M.; Gordon, D. W.; Kobylecki, R. J.; Steele, J. *Tetrahedron* **1995**, *51*, 8135.
- Traverse, J. F.; Snapper, M. L. *Drug Discov Today* **2002**, *7*, 1002.
- Verma, P. K.; Pal, S. K. *Eur. Phys. J. D* **2010**, *60*, 137.
- Voet, D.; Voet, J. G. *Biochemistry*; 4th ed.; John Wiley & Sons: Hoboken, NJ, 2011.
- von Baeyer, A. V., V. *Berichte der Deutschen Chemischen Gesellschaft* **1899**, *32*, 3625.
- Wahler, D.; Reymond, J. L. *Curr Opin Biotech* **2001**, *12*, 535.
- Wang, C. S.; Zheng, J. Y.; Oliveira, O. N.; Leblanc, R. M. *J Phys Chem C* **2007**, *111*, 7826.
- Wang, D. Z. G.; Katz, T. J. *J Org Chem* **2005**, *70*, 8497.
- Wang, W.; Ma, F.; Shen, X.; Zhang, C. *Tetrahedron: Asymmetry* **2007**, *18*, 832.
- Wang, Y.; Mosher, H. S. *Tetrahedron Lett* **1991**, *32*, 987.
- Ward, T. J.; Farris, A. B., 3rd *J Chromatogr A* **2001**, *906*, 73.
- Watanabe, A.; Uchida, T.; Irie, R.; Katsuki, T. *Proc Natl Acad Sci U S A* **2004**, *101*, 5737.

Wei, N.; Murthy, N. N.; Karlin, K. D. *Inorg Chem* **1994**, *33*, 6093.

Weix, D. J.; Dreher, S. D.; Katz, T. J. *J Am Chem Soc* **2000**, *122*, 10027.

Wenzel, T. J. *Discrimination of chiral compounds using NMR spectroscopy*; Wiley-Interscience: Hoboken, N.J., 2007.

Westerhausen, M.; Wieneke, M.; Schwarz, W. *Journal of Organometallic Chemistry* **1996**, *522*, 137.

Winschel, C. A.; Kalidindi, A.; Zgani, I.; Magruder, J. L.; Sidorov, V. *J Am Chem Soc* **2005**, *127*, 14704.

Wipf, P.; Miller, C. P. *Tetrahedron Lett* **1992**, *33*, 907.

Wiskur, S. L.; Ait-Haddou, H.; Lavigne, J. J.; Anslyn, E. V. *Accounts Chem Res* **2001**, *34*, 963.

Wolf, C.; Liu, S. L.; Reinhardt, B. C. *Chem Commun* **2006**, 4242.

Wu, J.; Liu, W.; Ge, J.; Zhang, H.; Wang, P. *Chem Soc Rev* **2011**, *40*, 3483.

Yabuuchi, T.; Kusumi, T. *J Org Chem* **2000**, *65*, 397.

Yashima, E. *J Chromatogr A* **2001**, *906*, 105.

Yin, J.; Buchwald, S. L. *J Am Chem Soc* **2000**, *122*, 12051.

You, L.; Berman, J. S.; Anslyn, E. V. *Nat Chem* **2011**, *3*, 943.

You, L.; Long, S. R.; Lynch, V. M.; Anslyn, E. V. *Chem-Eur J* **2011**, *17*, 11017.

Zadmard, R.; Schrader, T. *J Am Chem Soc* **2005**, *127*, 904.

Zahn, S.; Canary, J. W. *Org Lett* **1999**, *1*, 861.

Zhang, J.; Holmes, A. E.; Sharma, A.; Brooks, N. R.; Rarig, R. S.; Zubieta, J.; Canary, J. W. *Chirality* **2003**, *15*, 180.

Zhang, T.; Anslyn, E. V. *Org Lett* **2007**, *9*, 1627.

Zhao, Y.; Zheng, Q.; Dakin, K.; Xu, K.; Martinez, M. L.; Li, W. H. *J Am Chem Soc* **2004**, *126*, 4653.

Zheng, G.; Guo, Y. M.; Li, W. H. *J Am Chem Soc* **2007**, *129*, 10616.

Zhu, L.; Anslyn, E. V. *J Am Chem Soc* **2004**, *126*, 3676.

Zhu, L.; Zhong, Z. L.; Anslyn, E. V. *J Am Chem Soc* **2005**, *127*, 4260.

Vita

Leo A. Joyce was born in Madison, Wisconsin on September 9, 1983 to parents Leo W. Joyce and Mary Ann Etling. After graduating from Sauk Prairie High School in May 2002, he attended the University of Wisconsin-Madison. While at UW, Leo was introduced to organic chemistry research in Professor Samuel H. Gellman's laboratory. There he worked on small molecule synthesis, creating enantioenriched unnatural amino acids to incorporate into peptides. He graduated with a Bachelor of Science degree in Chemistry in December 2006. After graduating from UW, Leo enrolled in the Ph.D. program at the University of Texas at Austin in the fall of 2007 and joined Professor Eric V. Anslyn's research group. During his time at UT, Leo received the Organic Lab TA of the Semester (2007), H. R. Henze Teaching Excellence Award (2009), and Welch Service Awards (2009, 2010). After graduation, Leo will be joining Merck as a Senior Research Chemist. In his free time, he enjoys running, hiking with his wife Katie and their dog Sadie, and playing video games with Pedro.

Permanent address: S10395 Leuders Road, Sauk City, WI 53583

This dissertation was typed by Leo A. Joyce.